Universitá degli Studi di Torino
Facoltá di Scienze M.F.N.

Tesi di Dottorato di Ricerca del XIII ciclo

Study of the phase transition to QGP at the CERN SPS with the NA50 multiplicity detector

Francesco Prino

Dipartimento di Fisica Sperimentale dell'Università di Torino
Istituto Nazionale di Fisica Nucleare, Sezione di Torino
via P.Giuria 1, I-10125 Torino, Italia

Relatore:
Prof. A. Marzari-Chiesa

Co-relatore:
Prof. L. Ramello

Contro-relatore:
Prof. B. Chaurand

Coordinatore del Dottorato di Ricerca in Fisica:
Prof. R. Garfagnini

Introduzione

La materia nucleare è caratterizzata dal fatto che i quark e i gluoni sono confinati all'interno dei nucleoni. Calcoli di cromodinamica quantistica non perturbativa prevedono che, quando la temperatura supera un certo valore critico ($T_c \sim$ 150-180 MeV), la materia nucleare subisca una transizione di fase ad uno stato in cui i quark e i gluoni non sono più confinati all'interno degli adroni, ma sono liberi di muoversi in volumi più estesi. Questo stato della materia viene denominato Plasma di Quark e Gluoni (QGP).

La ricerca sperimentale si basa principalmente sullo studio di collisioni di ioni pesanti nelle quali è previsto che si possano raggiungere le condizioni di temperatura e densità di energia necessarie per la formazione del QGP. La transizione di fase dovrebbe essere favorita in collisioni a piccolo parametro d'urto (collisioni centrali), in cui il volume della regione interagente è maggiore e la temperatura più elevata.

Nel 1986, all'SPS del CERN è iniziato un programma sperimentale volto a fornire evidenze sperimentali della formazione del QGP. Dapprima si accelerarono ioni ossigeno e ioni zolfo ad un'energia di 200 GeV per nucleone, poi, a partire dal 1994, si è lavorato con un fascio di ioni piombo a 158 GeV/nucleone. Particolare attenzione è stata rivolta alla ricerca dei segnali previsti nel caso di transizione a QGP.

Diversi segnali sono stati proposti come "segnature" della formazione del QGP. In particolare, Matsui e Satz hanno previsto che la produzione di mesoni J/ψ sia soppressa in un mezzo deconfinato a causa dell'effetto dello "screening di Debye" sulla forza attrattiva di colore che lega i quark c e $\bar{c}$. La soppressione di J/ψ costituisce una segnatura di particolare interesse perché dipende dallo stato della materia presente nelle prime fasi della collisione, cioè nei momenti in cui possono avvenire le collisioni "dure" tra partoni che danno origine alle coppie $c\bar{c}$. Inoltre, la J/ψ è uno stato fortemente legato che non può essere facilmente dissociato in interazioni con gli adroni creati nella collisione e pertanto conserva pressochè intatta l'informazione sui primi istanti della collisione.

Gli esperimenti NA38, NA51 e NA50 hanno iniziato nel 1986 all'SPS uno studio sistematico della produzione di J/ψ e ψ' (rivelate attraverso il decadimento in $\mu^+\mu^-$) con fasci di protoni, ossigeno, zolfo e piombo su diversi bersagli. I dati raccolti da NA38 e NA51 evidenziano che la produzione di

J/ψ segue un andamento decrescente e continuo a partire da collisioni p-p fino alle collisioni centrali S-U. Questo risultato è spiegabile con l'assorbimento della coppia $c\bar{c}$ nella materia nucleare prima che dia origine alla J/ψ. Questo "assorbimento normale" costituisce il riferimento a cui paragonare i dati raccolti dall'esperimento NA50 in collisioni Pb-Pb in cui si raggiungono valori più elevati di temperatura e densità di energia. La transizione di fase dovrebbe apparire come un effetto a soglia nell'andamento della soppressione di J/ψ in funzione della centralità della collisione.

E' quindi importante determinare con precisione la geometria (centralità) della collisione. Perciò, l'apparato sperimentale di NA50 è dotato di tre rivelatori di centralità indipendenti: un calorimetro elettromagnetico che serve per determinare l'energia trasversa neutra, un rivelatore di molteplicità per misurare il numero e la distribuzione angolare delle particelle cariche prodotte nell'interazione e un calorimetro a zero gradi che raccoglie l'energia dei nucleoni del proiettile che non hanno interagito.

Il rivelatore di molteplicità dell'esperimento NA50 consente anche di misurare la distribuzione delle particelle cariche in funzione della pseudorapidità e di valutare la densità di particelle nella regione di rapidità centrale. Quest'ultima variabile è legata alle condizioni iniziali (in particolare alla densità di energia) della materia creata nell'interazione e permette di quantificare la frazione di energia incidente utilizzata per produrre nuove particelle.
Inoltre, la molteplicità di particelle cariche è utile per discernere tra diversi modelli di produzione di particelle, valutando, ad esempio, l'importanza relativa dei processi "soffici" (che dipendono dal numero di nucleoni partecipanti, N_{part}) e dei processi "duri" (che, al contrario, sono proporzionali al numero di collisioni tra nucleoni, N_{coll}).

Il primo capitolo di questa tesi è una breve introduzione alla fisica degli ioni pesanti e ai principali risultati sperimentali.

I capitoli 2 e 3 sono dedicati alla descrizione dell'apparato dell'esperimento NA50 e ad una presentazione dettagliata della struttura e del funzionamento del rivelatore di molteplicità (MD).

Nel capitolo 4 sono descritti i metodi utilizzati per la ricostruzione degli eventi e la selezione dei dati, il calcolo della molteplicità e l'algoritmo di identificazione della posizione dell'interazione a partire dai dati di MD.

I capitoli 5 e 6 riguardano lo studio della produzione di particelle cariche

in collisioni Pb-Pb. I principali concetti di fisica sono introdotti nel capitolo 5. Il sesto capitolo è dedicato ad una spiegazione dettagliata dell'analisi riguardante le distribuzioni di particelle cariche in funzione della pseudorapidità in collisioni Pb-Pb a due diverse energie (40 e 158 GeV per nucleone), con particolare attenzione alla dipendenza della densità di particelle nella regione di rapidità centrale dalla centralità e dall'energia nel centro di massa. Le particelle cariche mostrano un andamento lineare in funzione di N_{part}, evidenziando che i meccanismi di produzione di particelle alle energie dell'SPS sono dominati dalle interazioni "soffici".

I capitoli 7, 8 e 9 sono dedicati alla soppressione di J/ψ e alla sua interpretazione come segnatura della formazione del QGP. Nel settimo capitolo sono discusse le previsioni teoriche e i risultati ottenuti dagli esperimenti NA38, NA51 e NA50 con fasci di protoni, ossigeno, zolfo e piombo.
Il capitolo 8 riguarda lo studio della produzione di J/ψ in collisioni Pb-Pb in funzione dell'energia trasversa. L'analisi è svolta sui dati raccolti nel 1998 e si avvale dell'algoritmo di identificazione della posizione dell'interazione basato su MD. I risultati sono in accordo con quelli ottenuti in precedenza da NA50 con un diverso metodo di riconoscimento delle interazioni e hanno inoltre il vantaggio di essere estratti da un unico campione di dati.
Il nono capitolo è dedicato all'analisi della produzione di J/ψ in funzione del numero di particelle cariche prodotte nella collisione. L'uso di una diversa variabile di centralità permette di confermare i risultati ottenuti utilizzando l'energia trasversa e, inoltre, di studiare la soppressione di J/ψ in funzione di una variabile misurata nella stessa accettanza angolare in cui è misurata la J/ψ.
Tutte queste analisi mostrano chiaramente un effetto "a soglia" nella produzione di J/ψ in funzione della centralità della collisione Pb-Pb e rivelano la presenza di un meccanismo di soppressione "anomala". Secondo alcune interpretazioni, ciò è dovuto al raggiungimento delle condizioni necessarie alla transizione di fase (o ad un avvicinamento ad esse). Esistono però anche modelli diversi che assumono che la J/ψ sia dissociata in interazioni con gli adroni prodotti nella collisione. Il fatto che la produzione di particelle in collisioni Pb-Pb mostri una dipendenza lineare dal numero di partecipanti riduce le possibilità di dissociazione dovuta alle interazioni adroniche e fa pensare che il sistema prodotto nelle collisioni Pb-Pb soddisfi le condizioni di temperatura e densità di energia necessarie alla transizione di fase (o sia per lo meno assai vicino ad esse).

Introduction

In ordinary nuclear matter, quarks and gluons are confined inside nucleons. Non-perturbative calculations of Quantum Chromo Dynamics predict that, when temperature exceeds a critical value $T_c \sim$ 150-180 MeV, nuclear matter should undergo a phase transition into a state of matter in which quarks and gluons are no more confined into hadrons and behave as free particles. Such a state of matter is named Quark-Gluon Plasma (QGP).

Heavy-ion collisions are a powerful experimental tool to investigate nuclear matter under extreme conditions: the formation of the QGP is expected to occur in these collisions if the critical temperature and energy density required for the phase transition are attained. The transition to QGP is expected to be favored in collisions with small impact parameter (central collisions), where the volume of the interaction region is larger and the energy density and the temperature can reach higher values.

An experimental program aimed at providing evidence of QGP formation started at the CERN SPS in 1986, when oxygen and sulphur ions were first accelerated at 200 GeV per nucleon energy. Since 1994, a 158 GeV per nucleon lead beam is provided by the SPS. The experiments involved in the heavy ion program are searching for the signals foreseen in the case of phase transition to a deconfined state.

Several probes have been proposed as signatures of QGP formation. In particular Matsui and Satz predicted that the J/ψ yield would be suppressed in a deconfined medium due to the Debye screening of the attractive colour force which binds the c and $\bar{c}$ quarks together. The J/ψ suppression is a particularly interesting signature because it probes the state of matter in the earliest stages of the collision, since $c\bar{c}$ pairs can only be produced in hard parton interactions occurring at that time. Moreover the J/ψ is a tightly bound state that can not be easily broken by interactions with the hadronic medium created in the collision and therefore it carries its original message through the different stages of the reacting medium.

Since 1986, at the CERN SPS, the NA38, NA51 and NA50 experiments have studied J/ψ and ψ' production using the $\mu^+\mu^-$ decay channel with incident proton, oxygen, sulphur and lead ions on several targets. The data collected by the NA38 and NA51 experiments show a continuous and monotonic J/ψ suppression pattern from p-p up to central S-U collisions. This

result can be understood in terms of absorption of the $c\bar{c}$ pair in nuclear matter before it forms the J/ψ state. This "ordinary nuclear absorption" sets the baseline for the study, carried on by the NA50 experiment, of J/ψ production in Pb-Pb collisions, where higher temperatures and energy densities are reached. The occurrence of the transition from hadronic matter towards QGP should manifest itself as a threshold effect in the J/ψ suppression pattern as a function of the centrality of the Pb-Pb collision.

Consequently, it is important to determine with good precision the geometry (centrality) of the collision. In particular, the NA50 experiment is equipped with three independent centrality detectors: an Electromagnetic Calorimeter for neutral transverse energy determination, a Multiplicity Detector measuring the number and the angular distribution of the charged particles produced in the interaction and a Zero Degree Calorimeter which detects the forward energy carried by the non-interacting projectile nucleons.

The multiplicity detector of the NA50 experiment, with its good granularity, allows also to measure the charged particle distribution as a function of pseudorapidity, thus providing the particle density at midrapidity. This observable gives information about the initial conditions (in particular the energy density) of the system created in the reaction, quantifying to which extent the incoming beam energy is released to produce new particles. Furthermore, the charged multiplicity information may help constrain different models of particle production by evaluating the relative importance of soft processes (which are expected to scale with the number of participant nucleons, N_{part}) and hard processes (which, on the contrary, should scale with the number of nucleon-nucleon collisions, N_{coll}).

In the first chapter of this thesis a brief overview of the physics of heavy ion collisions is presented together with a survey of the most important experimental results.

Chapters 2 and 3 are devoted to the general description of the NA50 experimental apparatus and to a detailed discussion of the characteristics and the operation of the silicon strip Multiplicity Detector (MD).

In chapter 4 the event reconstruction and the data selection criteria are summarized. The multiplicity calculation and the target identification algorithm based on MD data are also described.

Chapters 5 and 6 are dedicated to the study of charged particle production in Pb-Pb collisions. The main physical concepts are briefly introduced

in chapter 5, while chapter 6 presents the detailed analysis of charged particle pseudorapidity distributions in Pb-Pb collisions at two different energies (40 and 158 GeV per nucleon). The scaling of charged particle density at midrapidity with centrality and with energy is also considered. As a result, charged particles are found to scale linearly with N_{part}, indicating that particle production mechanisms at SPS energies are dominated by soft interactions.

In chapters 7, 8 and 9 the attention is focused on the J/ψ suppression as a signature of QGP formation. Chapter 7 describes the theoretical expectations and the experimental results obtained by NA38, NA51 and NA50 experiments with proton, oxygen, sulphur and lead beams.
In chapter 8, J/ψ production in Pb-Pb collisions is studied as a function of the neutral transverse energy. The analysis is performed on the data collected in 1998 and uses the MD based target identification algorithm. The results are in agreement with the ones previously obtained by NA50 using a different target identification method and have the advantage of being extracted from a single year data sample.
In chapter 9, J/ψ yield is analyzed as a function of the charged multiplicity of the collision. The use of a different centrality estimator allows to cross-check the results obtained as a function of the transverse energy and, besides, to evaluate J/ψ production as a function of a variable measured in the same angular acceptance in which the J/ψ itself is measured.
All these analyses clearly show a "threshold" effect in the J/ψ suppression pattern in Pb-Pb collisions, indicating the presence of an "anomalous" suppression mechanism. This can be interpreted as due to the reaching (approaching) of the critical conditions for deconfinement. Alternative models assuming J/ψ dissociation by interactions with the hadrons produced in the collision (co-movers) also exist. The experimental observation that particle production in Pb-Pb collisions scales linearly with the number of participant nucleons leaves little room for explanations based on J/ψ absorption by co-movers and suggests that the system produced in Pb-Pb collisions is beyond (or at least very close to) the energy density and temperature conditions required for the occurrence of the phase transition to a deconfined state.

Contents

List of Figures

Chapter 1

The quest for the Quark-Gluon Plasma

In ordinary nuclear matter, quarks and gluons are confined inside nucleons. Non-perturbative calculations of Quantum Chromo Dynamics predict that, at large energy density, or baryon density, nuclear matter should undergo a phase transition into a state of matter in which quarks and gluons are deconfined from their individual nucleons and free to move over larger space–time volumes. Such a state of matter is named Quark-Gluon Plasma (QGP).

Furthermore, the verification of the existence of the QGP state is also of cosmological and astrophysical interest because it is expected that the QGP was the state of matter in the first instants ($t < 10^{-6}$ s) of the Universe after the "big-bang". Moreover, a low temperature and high baryon density plasma of quarks and gluons could be present in the core of neutron stars.

High energy heavy-ion collisions are a powerful experimental tool to investigate nuclear matter under extreme conditions: the formation of the QGP, as a transient state, is expected to occur in these collisions if the critical temperature and energy density required for the phase transition are reached.

1.1 The phase transition

The strong interaction between quarks and gluons inside hadrons is characterized by the behaviour of the coupling constant α_s which increases with growing distance between the interacting quarks. For this reason, the binding force is negligible at small distance ("asymptotic freedom") and has a steep

growth as the distance between the constituents becomes larger, causing the quarks to be confined inside hadrons.

This colour confinement should disappear at sufficiently high temperature and/or density values, as it can be argued from the analogy with the Debye charge screening phenomenon in atomic matter. In a dense atomic medium, as a consequence of the overlapping of the atomic orbits, the charge of a nucleus is partially screened by the electronic orbits of other atoms which generate a high density of negative charge around the positively charged nucleus. The Coulomb potential between two electric charges consequently changes:

$$V(r) = \frac{e}{r} \rightarrow \frac{e}{r} \cdot e^{-\frac{r}{r_D}} \tag{1.1}$$

where r_D is the Debye radius. In a conductor r_D is smaller than the distance between the center of the atom and the outermost electrons which feel a smaller electric field so that they behave as deconfined from the atom and are free to move inside the material. In an insulator material r_D is larger than the radius of the atom, so that the electrons are confined. Since r_D is inversely proportional to the matter density ρ and to the temperature T, increasing ρ or T, r_D becomes smaller and smaller and the insulator material may undergo a phase transition to conductor (Mott transition [1])

For the same reason, in a medium characterized by a very high density of colour charge, a screening effect should affect the colour interquark potential, which is composed of a short-range coulombic term $\propto 1/r$ and of a long-range string-tension term $\propto r$ responsible for confinement of quarks inside hadrons:

$$V(r) = \sigma \cdot r - \frac{\alpha}{r} \rightarrow \sigma \cdot r_D \left(1 - e^{-r/r_D}\right) - \frac{\alpha}{r} \cdot e^{-\frac{r}{r_D}} \tag{1.2}$$

When, with increasing colour charge density, the colour screening Debye radius (r_D) becomes smaller than the radius of the hadron, the binding force can not hold the quark inside the hadron anymore, and therefore the deconfinement occurs. Hence, if the hadronic matter is sufficiently dense and/or hot, a phase transition from a "colour insulator" phase (the hadron gas made of colourless hadrons) to a "colour conductor" phase where the coloured quarks and gluons are deconfined can occur. The state of matter in which quarks and gluons are not confined inside hadrons, but are free to move over larger space–time volumes is called Quark Gluon Plasma (QGP).

The theoretical study of the conditions for the phase transition and of the properties of the QGP state can not be performed using perturbative QCD

calculations, because the perturbative approach can only be applied for small values of the QCD coupling constant. When studying nuclear matter under extreme density and/or temperature conditions, the perturbative approach has to be substituted by phenomenological models or by lattice QCD calculations, which are numerical simulations of the QCD equation of state on a finite discretized volume of space–time.

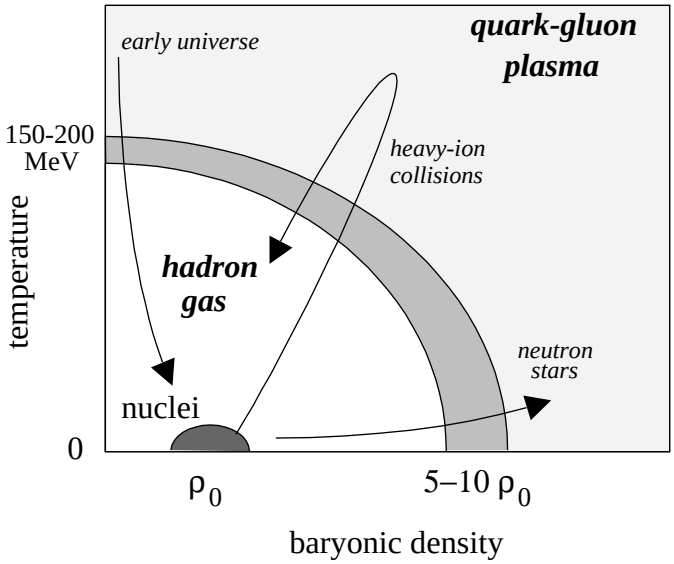

Figure 1.1: *Phase diagram of strongly interacting matter.*

The phase diagram of strongly interacting matter obtained from thermodynamical models [2] is represented in fig. 1.1 in the plane of temperature and net baryon density. The transition temperature (T_c) from hadron matter to QGP varies from $T_c \simeq 140 - 200$ MeV at zero baryon density, to zero temperature at a critical baryon density $\simeq 5 - 10$ times the density of ordinary nuclear matter ($\rho_o = 0.15$ nucleons/fm^3). More reliable predictions concerning the phase transition can at present only be obtained from lattice calculations, which indicate that the phase transition should occur at a critical temperature $T_c = 154 \pm 8$ MeV for a 3 flavour QCD [3] , while the critical energy density is $\varepsilon \simeq 2 - 3$ GeV/fm^3 [4] (the relative uncertainty on ε_c is larger than the one on T_c because $\varepsilon \propto T^4$). The nature of the phase transition results to be dependent on the quark masses: a first order phase transition should occur in the case of statical ($m_q = \infty$) and dynamical mass-

less ($m_q = 0$) quarks, while, if the physical values of the quark masses are considered, a second order phase transition is expected.

Lattice QCD calculations predict also that the phase transition to QGP should be accompanied by the chiral symmetry restoration. Quarks confined in a hadron have non-zero mass because of their interaction with the other quarks and gluons: a non zero quark mass destroys the symmetry of the QCD Lagrangian under chiral tranformation of the quark spinor, while the chiral symmetry is valid in the case of zero quark masses. When quarks become free in the deconfined phase, their masses drop to smaller values ($m_u \simeq 1-5$ MeV, $m_d \simeq 3-9$ MeV, $m_s \simeq 75-170$ MeV [5]), causing the restoration of the chiral symmetry which is spontaneously broken in ordinary nuclear matter. In fact, interactions are never really turned off and therefore only a partial chiral symmetry restoration is expected.

1.2 Heavy ion collisions

To explore experimentally the possible existence of the QGP, it is mandatory to create a strongly interacting system which satisfies the following requirements:

- The system should be studied using macroscopic variables. This means that big systems (with a size much larger than the confinement scale) consisting of many particles are required.

- The system should be studied using thermodynamics, and so it must be in equilibrium. To reach the equilibrium condition, the system must be long-lived, with a lifetime greater than the relaxation time (usually defined as the time needed to a particle to travel a 1 fm distance at the speed of light, $\tau_o \approx 1$ fm/c). To remain in equilibrium, the system must be sufficiently interacting, which means that the mean free path of the constituents (which is ≈ 0.5 fm for quarks at densities of ≈ 2 GeV/fm^3) must be smaller than the system dimensions, so that several collision per particle can occur.

- The system must have large energy density and/or temperature, greater than the critical energy density and/or temperature required for the phase transition to QGP.

Nucleus–nucleus collisions at very high energy provide the means of creating hadronic states with high energy density and/or high temperature fulfilling all these demanding requirements. For example, the system created in a Pb-Pb collision can reach a volume of the order of 1000 fm^3, consisting of $\approx$ 1000 hadrons, and, at SPS energies, can reach an energy density $\approx$ 20 times larger than in a nucleus and $\approx$ 4 times larger than in a hadron.

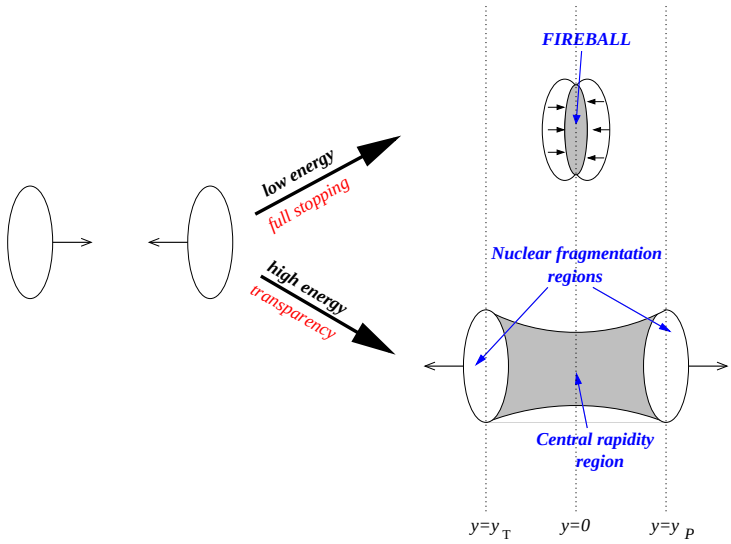

Figure 1.2: *Scheme of a relativistic heavy-ion collision.*

A schematic drawing of a relativistic heavy ion collision is shown in fig. 1.2. The two Lorentz contracted nuclei collide giving rise to a very high number (up to 800 in Pb–Pb) of elementary inelastic nucleon–nucleon collisions, causing a large loss of energy and momentum of the colliding baryon matter, which is slowed down. The loss of kinetic energy is accompanied by the production of a large number of particles (mostly pions), so that a large fraction of the longitudinal energy is converted into the energy of hot hadronic matter produced in the vicinity of the center of mass of the colliding system (central region).

It is useful to introduce the rapidity variable which transforms additively under a Lorentz transformation:

$$y = \frac{1}{2} \ln \left(\frac{E + p_L}{E - p_L} \right) \tag{1.3}$$

where p_L is the longitudinal momentum and E the energy of the particle. For a given incident energy, the rapidity of the projectile (y_P) and of the target (y_T) particles can be easily determined; the greater the incident energy, the greater is the separation between y_P and y_T. Since the rapidity variable depends on the longitudinal momentum p_L, the loss of energy and momentum in the collision appears as a modification of the rapidity of the colliding baryon matter. The rapidity region about midway between the projectile rapidity and the target rapidity is called central rapidity region; most of the produced particles lie in this central rapidity region. In the center-of-mass reference frame $y_T = -y_P$ and the central rapidity region is located around $y = 0$.

The amount of energy lost by the projectile is defined by the stopping power: the degree of stopping reveals whether the energy density attained is high enough to allow a phase transition leading to the formation of a QGP. Two energy regimes are discussed: at low $\sqrt{s}$ (full-stopping regime) the formation of a baryon-rich QGP is expected, while at high energies (transparency regime) a baryon-free QGP should be produced. Both models seem to be inadequate to fit the experimental data at SPS energies, which lies somewhere between the applicability ranges of these two models.

1.2.1 Low energy regime: the Fireball model

At low energies ($\sqrt{s} \sim 5 - 10$ GeV per nucleon, typical of the AGS), the colliding nuclei are expected to completely stop each other, leading to a baryon rich system. In this regime, no fragments are found in the rapidity regions of the projectile and of the target because most of the colliding baryons are stopped in the central region and pile-up to form a fireball of high baryon density.

The degree of stopping determines how many nucleons are stopped, allowing to estimate the temperature, the baryon density and the energy density of the large volume of the hot and compressed nuclear matter stopped in the collision. For large values of stopping power, the energy density attained could be high enough to lead to the formation of a QGP with a large baryon density. Successively the fireball explodes isotropically producing a large number of particles symmetrically distributed around the center of mass of the fireball [6].

1.2.2 High energy regime: the Bjorken hydrodynamical model

At very high energies ($\sqrt{s} \sim 100 - 200$ GeV per nucleon), the slowed down baryons after the collision can still have enough momentum to proceed forward and escape from the central region, resulting in a situation with nuclear fragments well separated from the central region of particle production. The beam and target fragments after the collision lie in rapidity regions (called nuclear fragmentation regions) located respectively close to the beam and target rapidities.

In such a collision, a large amount of energy is deposited in a small region of space in a short duration of time. The matter created in the central region has therefore a very high energy density, but a small net baryon content, giving possibly rise to a baryon free QGP. As the net baryon content of the early universe was very small, this kind of QGP is of astrophysical interest.

The system after the collision should evolve according to the space–time scenario proposed by Bjorken [7] and represented in fig. 1.3.

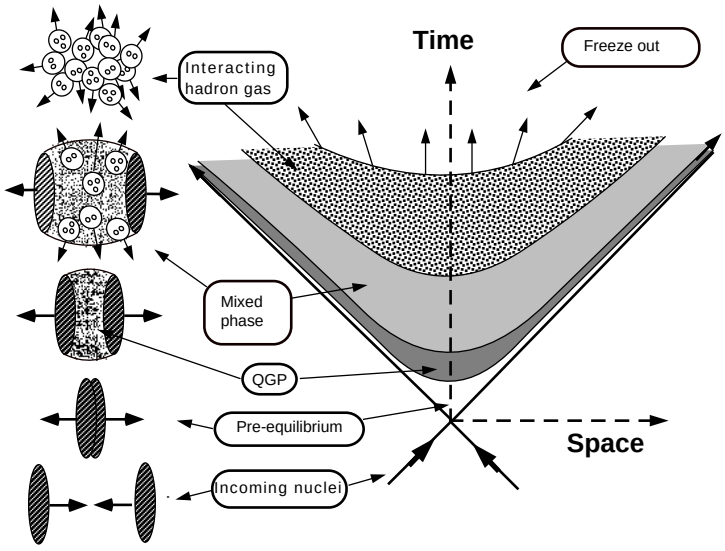

Figure 1.3: *Space-time diagram for nucleus-nucleus collision, showing the various stages of the evolution of the expanding matter.*

The quanta of energy deposited in elementary nucleon-nucleon collisions materialize, after a time $\tau_o \approx 1$ fm/c (formation time), into partons or into

hadrons, depending on the energy density reached in the collision: if the energy density is sufficiently high, the system should be in a QGP state, while for lower energy densities, the system should be made of hadronic matter. The plasma initially may not be in thermal equilibrium, but parton-parton interactions might then lead it into local thermal equilibrium after a proper time τ_e (equilibration time). It is important to stress that thermal equilibration does not always imply chemical equilibration at the parton level: gluons reach the chemical equilibrium faster than quarks and light quarks faster than heavy quarks [8].

Once the QGP has reached local thermal equilibrium, its further evolution can be described in the framework of relativistic hydrodynamics [7]: the system expands and cools until at a proper time τ_{QGP} (lifetime of the QGP) it reaches the critical temperature T_c. At this point the system should undergo a phase transition from QGP to ordinary nuclear matter, going through a "mixed phase" in which hadrons and "blobs" of plasma would coexist. After a proper time τ_h, the system reaches the hadron phase and can still be described by the laws of hydrodynamics, with the appropriate hadron equation of state. The temperature of the expanding hadronic matter decreases until it reaches the freeze–out temperature: first the chemical freeze–out is reached, then the thermal freeze–out. After the chemical freeze-out no more inelastic interactions between hadrons can occur and the relative abundance of the different particle species are defined, while after the thermal freeze–out neither the elastic collisions between hadrons can occur and the final state particles are completely decoupled and fly towards the detectors. The final state reflects the complex evolution of the system and the experimental observables correspond to values integrated over the whole space-time evolution of the system until freeze-out. Since a system that evolves through equilibrium states does not have memory of the earlier stages, to obtain information about the different stages of the evolution, it is necessary (similarly to big bang cosmology) to find observables that decouple from the system in different moments, carrying information of the status of the system at the moment of their decoupling.

1.3 Global features of the system

Since a huge number of particles is produced in heavy ion collisions (more than 1000 secondaries in Pb-Pb), it would be a daunting task to study the

system produced in these reactions by measuring the physical interesting quantities of all the produced particles. Consequently, it is more common to use inclusive (global) variables, performing a kind of QCD thermodynamical study.

1.3.1 Geometry of the collision

The thermodynamical properties of the initial state and, consequently, the global features of the system are strictly connected with the geometry of the collision and in particular with the impact parameter b, defined as the distance between the centers of the colliding nuclei. A schematic picture of a collision between two relativistic nuclei is shown in fig. 1.4. The incoming nuclei are Lorentz-contracted: their transverse size is equal to the nuclear section, while their thickness is ≈ 1 fm.

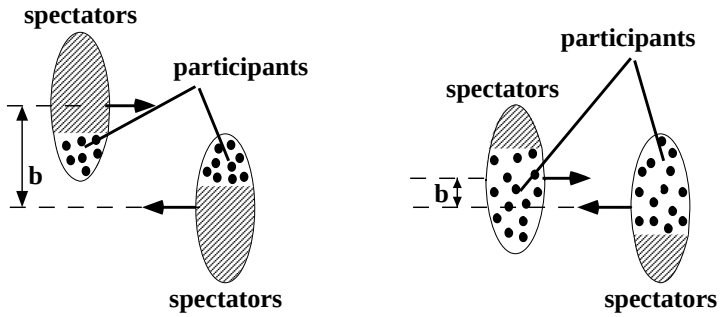

Figure 1.4: *Schematic representation of nucleus-nucleus peripheral and central collisions.*

Depending on the value of the impact parameter b, it is possible to distinguish between central and peripheral collisions. Peripheral collisions are characterized by an impact parameter which can be as large as the sum of the two radii ($b \approx r_1 + r_2$): the two nuclei glance each other and only few nucleons of both nuclei do participate in the interaction, while most of the nucleons do not participate, remaining as spectators. In central collisions the impact parameter is zero or close to zero ($b \approx 0$). If the two nuclei have different radii, the smaller one makes a hole in the larger one and almost all the nucleons of the smaller nucleus can participate in the interaction. If

the two colliding nuclei are equal, almost all the nucleons of both nuclei are involved in the collision, while the number of spectator nucleons is small.

Therefore, given an impact parameter b, the nucleons can be separated into participants, which undergo primary nucleon-nucleon collisions, and spectators, which continue along their original direction with modest perturbation. The number of participant nucleons N_{part} grows with the centrality of the collision (inversely proportional to b), while the number of the spectator nucleons N_{spect} is directly proportional to b and decreases with increasing centrality.

1.3.2 Initial conditions: energy density and baryon content

The initial conditions of the system are defined by the geometry of the collision, by the energy density reached in the collision and by the baryon content in the interaction volume. The measurement of the energy carried by the spectators, emitted at almost zero degrees in the forward direction, can be used to define the collision geometry, while the number of participants defines the amount of energy released in the collision (see fig. 1.5).

The energy lost in the collision reappears mainly in the form of many "soft" mesons, mostly pions. The number of particles produced (multiplicity) and the transverse energy E_T (component of the "energy vector" in the plane orthogonal to the beam direction) of these particles are directly measurable and closely related to the energy density produced.

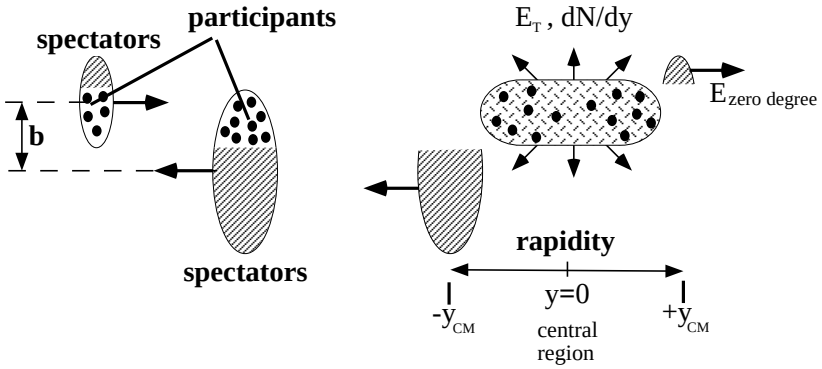

Figure 1.5: *Schematic representation of a collision of two relativistic nuclei.*

The energy density ε can be estimated through the measurement of the transverse energy or of the multiplicity, making geometrical and dynamical assumptions which are different in the case of low energy and high energy regimes.

- In the case of low energy regime, the maximum energy released in the fireball equals the kinetic energy of the stopped nucleons:

$$E^{max} = \sqrt{s} - m(n_P + n_T) \tag{1.4}$$

  where n_P and n_T are respectively the number of projectile and target nucleons stopped in the collision. From this value E^{max}, under the assumption that this energy is emitted isotropically in the explosion of the fireball, it is possible to calculate the maximum transverse energy E_T^{max} and to evaluate the fraction of energy stopped in the collision (stopping power) as the ratio between the maximum experimentally observed E_T and E_T^{max}. Knowing E^{max} and the stopping power S, it is possible, with simple geometrical assumptions for the volume of the fireball V_{FB}, to calculate the energy density of the fireball as:

$$\varepsilon_{FB} = \frac{\gamma E^{max}}{V_{FB}} \cdot S \tag{1.5}$$

  where the γ factor takes into account the Lorentz contraction of the fireball.

- In the opposite case of ultrarelativistic regime, the Bjorken formula [7] allows to estimate, under the assumption of a longitudinal expansion of the system, the energy density ε reached in the collision from the rapidity density of transverse energy (dE_T/dy) or particle multiplicity (dN/dy):

$$\varepsilon_{BJ} = \frac{1}{\mathcal{A} c \tau_o} \left(\frac{dE_T}{dy} \right)_{y=0} = \frac{< m_T >}{\mathcal{A} c \tau_o} \left(\frac{dN}{dy} \right)_{y=0} \tag{1.6}$$

  where $\mathcal{A}$ is the transverse overlapping area in the collision of the two nuclei, τ_o is the formation time and $m_T = \sqrt{m^2 + p_T^2}$ is the so-called transverse mass.

It has been verified that none of these two models is adequate to describe collisions at SPS energy. Nevertheless, the energy densities reached at the

System	Beam energy (GeV per nucleon)	ε_{BJ} (GeV/fm^3)
S–S	200	1.2
S–Au	200	2.6
Pb–Pb	158	3.2

Table 1.1: *Energy density reached at SPS for various systems.*

SPS are usually roughly estimated by means of Bjorken's formula, obtaining the values reported in table 1.1. The critical values of energy density indicated by QCD lattice calculations for the phase transition are around 1-2 GeV/fm^3, so the energy density reached at the SPS in Pb–Pb collisions should be sufficient to observe the phase transition.

Like the energy density, the baryon content of the system immediately after the collision depends on the degree of stopping. In case of full-stopping a baryon rich hadron gas is expected, while at very high energy, the central rapidity region should be populated only by mesons, giving rise to a baryon-free hadron gas.

1.3.3 Space–time evolution and freeze-out

The temperature at thermal freeze-out ($T_{f.o.}$) can be extracted from two different measurements: the transverse mass distributions for identified particles and the two-pion correlation functions.

The transverse mass (or transverse momentum) distributions, in the p_T range 0.2 GeV/c $< p_T <$1 GeV/c, exhibit a typical thermal spectrum:

$$f(m_T) \propto exp(-m_T/T) \tag{1.7}$$

where the transverse mass m_T is defined as $m_T = \sqrt{m^2 + p_T^2}$.

The inverse slope of the transverse mass distributions is connected to the temperature of the system at the time of decoupling. The measured inverse slope, as shown in fig. 1.6 grows linearly with the particle mass. Such a behaviour is expected in a scenario where a transverse collective expansion (flow) of the system is superimposed to the thermal motion. The anomalously low inverse slope of the Ω may be explained in this context by the fact that the Ω does not have any strong scattering resonance with pions and therefore

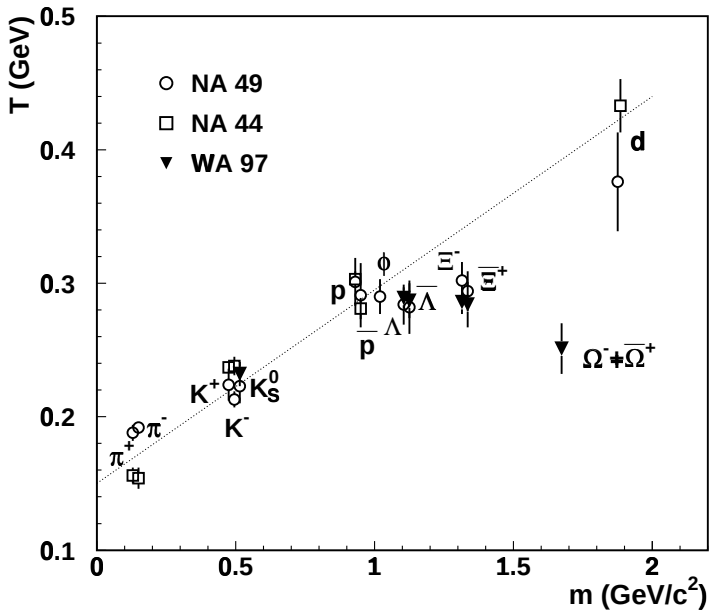

Figure 1.6: *Dependence of the inverse slope of the transverse mass distribution on the particle mass at SPS energy.*

freezes-out rather early from the hot and dense expanding system, before most of the transverse flow has developed [9].

The two-pion correlation analysis allows a direct measurement of the emitting source geometry, whose gaussian radius for central Pb-Pb events results to be $R_G = 6.5 \pm 0.5$ fm, which corresponds to an effective radius of $\sqrt{5} \cdot R_G$ [10] giving rise to a volume of the system at thermal freeze-out of $\approx$13000 fm^3. The gaussian radius of the system immediately after the collision is estimated to be 2.7 fm, so the source expands by a factor 2.4 between the initial maximum energy density state and the final hadronic decoupling.

The combined information from two-pion correlation functions and from single-particle transverse mass spectra makes it possible to separate the collective flow and the temperature contributions to the "apparent temperature" obtained from the m_T inverse slopes, determining both the expansion velocity, $\beta_T = 0.55 \pm 0.12$, and the thermal freeze-out temperature, $T_{f.o.} = 120 \pm 12$ MeV [10]. The system therefore grows transversely by a factor 2.4 with a transverse velocity greater than half the speed of light.

1.3.4 Final state particles and chemical equilibrium

The observed final state hadrons reflect the space-time evolution of the system and therefore provide clues as to the state of the system prior to hadronization. The relative abundance of different particle species in the final state is remarkably well described (as it can be seen in fig. 1.7) in the framework of a simple statistical model [11] which assumes a system in thermal and chemical equilibrium at the point of hadro-chemical freeze-out. This result is quite natural if the system before hadronization consists of largely uncorrelated quarks and gluons, like in a QGP, with hadronization filling statistically the hadronic phase-space.

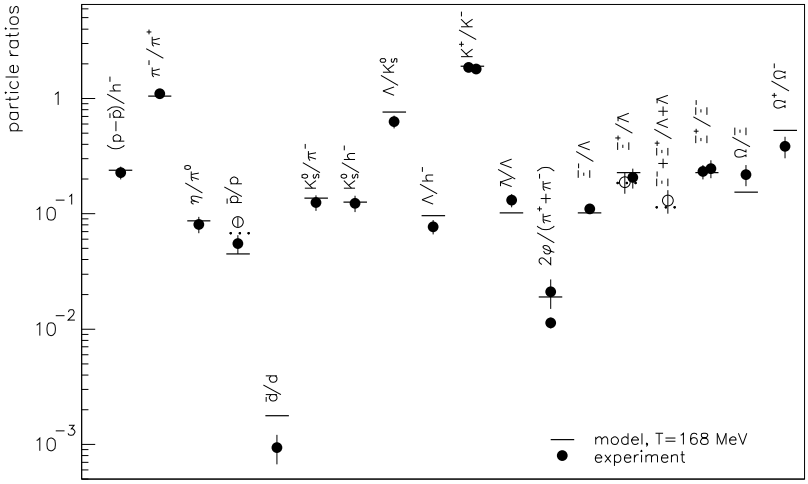

Figure 1.7: *Comparison between experimental particle ratios and the thermal model.*

The good agreement between the predictions of this thermal model and the measured particle ratios implies that thermal and chemical equilibrium is established in the system at the chemical freeze-out. The model uses only two parameters: the temperature T at the chemical freeze-out and the baryon chemical potential μ_B. The temperature in the model is about 160-170 MeV, higher than the freeze-out one, as one would expect in the progressive cooling-expansion process, in which the chemical freeze-out, with the consequent definition of the particle species, comes earlier than the thermal freeze-out when the collisions cease to occur. Furthermore, it is interesting to note that the resulting temperature value is very close to the critical temperature T_c

which separates hadronic matter and QGP. It is therefore quite probable that the system undergoes the phase transition from QGP to hadron gas shortly before it freezes-out chemically.

1.4 Signatures of the phase transition

A signature of the QGP formation is an experimental tool acting as deconfinement probe: it is used to check if the medium produced in the early stages of the collision evolution was deconfined or not. A good signature should fulfill these requirements:

1. It must distinguish between confined and deconfined matter
2. It must be present in the initial stages of the collision evolution
3. It must preserve the memory about the earlier stages of the system during its space-time evolution

Several factors complicate the task of these deconfinement probes:

- At SPS energies, the size of the QGP volume is expected to be small (at most few fermis in diameter) and it does not live long (between 5 and 10 fm/c) [8].
- All signals coming from the QGP phase compete with backgrounds emitted from the hot hadronic gas phase that follows the hadronization of the plasma phase.
- Signals coming from the QGP phase can be modified or destroyed by final state interactions in the hadronic phase.

Consequently, there are several arguments against the existence of unambiguous signatures of the phase transition to QGP and it is generally recognized that there is no single unique signal which allows an unequivocal identification of the plasma phase. Several signatures have been proposed, and most of them were searched for, in order to gather several pieces of evidence which, taken together, may indicate the presence of a deconfined phase.

The up to now proposed signatures can be divided, depending on the scale of the probing phenomenon, into two main classes (hard probes and soft probes), providing information about different stages of the collision evolution [12].

1.4.1 Hard probes of the QGP

Hard probes are related to signals produced in physical processes with large momentum transfer (hard processes), so that the associated length scale is much less than the confinement scale (≈ 1 fm). Hence such probes, coming from partonic processes, are well suited to study directly the short distance features of a hot deconfined medium and to probe the very early stages of a high-energy heavy-ion collision. The main phenomena predicted to constitute direct hard probes of the QGP are briefly discussed in the following.

Hard thermal photon/dilepton emission
Photons and lepton pairs (dileptons) should be copiously produced in a QGP via $q\bar{q}$ annihilations and "Compton" scattering of gluons on quarks. The production rate and the momentum distribution of the produced photons and dileptons depend on the momentum distribution of quarks and gluons in the plasma, which are governed by the thermodynamic condition of the plasma. Direct photons and dileptons from the early hot and dense stages of the system evolution would leave the hot plasma with a small probability of interaction in the outer low temperature region and therefore they would keep the memory of the temperature in which they were created, giving rise to a thermal spectrum which should serve as a thermometer of the medium from which they were emitted [13].

Since they carry direct information from the possible QGP phase, thermal dileptons and photons have been the subject of intensive experimental studies, but, due to the huge background coming from hadron (π and η) decays, there is up to now no real evidence for their production. The observed intermediate mass dilepton enhancement [14] may turn out to be a first indication of thermal dileptons, but, so far, its origin remains completely open [12].

Jet quenching
In the case of QGP formation, a suppression of the yield of large transverse momentum jets (or particles) with respect to proton-proton collisions is expected [15]. This is due to the fact that the energy loss of fast coloured partons passing through a deconfined medium (composed of coloured particles) should exceed the one suffered in the passage through hadronic matter. First indication of jet quenching are coming from the results of the first RHIC (Relativistic Heavy Ion Collider) run in year 2000 concerning Au–Au colli-

sions at $\sqrt{s} = 130$ GeV. Due to the lower rate of jet production, this hard probe is probably not visible at SPS energies.

Charmonium suppression
In 1986 Matsui and Satz [16] predicted that the production of J/ψ and other charmonium states would be suppressed in a QGP environment by Debye screening of the quark colour charge. Given the mass of charm quarks, at SPS energies charmonium states can only be produced in the first stages of the collision, when two gluons interact to produce a $c\bar{c}$ pair. In the QGP the attractive potential which is necessary to bind the c and $\bar{c}$ quarks is screened, so that the c and the $\bar{c}$ would go their separate ways and eventually pick up other quarks in the hadronization phase giving rise to open charm production. When, increasing the temperature, the "Bohr radius" of the charmonium state is larger than the Debye screening radius, the charmonium would disintegrate in the plasma and the $c\bar{c}$ bound state would not exist. Therefore a pattern as a function of temperature would emerge once the critical temperature for deconfinement is reached: the ψ' resonance, which is the largest and the more loosely bound, would melt immediately, the χ_c at somewhat higher temperature and finally, at even higher temperatures, also the more tightly bound J/ψ resonance would be suppressed.

In reality other competing processes (such as absorption in ordinary nuclear matter of $c\bar{c}$ preresonant states) are involved, making the interpretation of the data not straightforward. However an anomalous J/ψ suppression effect, which finds a natural interpretation assuming QGP formation, has been observed in Pb–Pb collision at SPS [17, 18, 19].

1.4.2 Soft probes of the hadronic state

Soft probes are connected to processes with small momentum transfer (soft processes) and therefore they are of hadronic size and they appear when the density of the medium has dropped sufficiently to allow the existence of hadrons. Hence, they naturally provide information about the hadronic stages of the system evolution, but they may carry also indirect information about earlier (deconfined) stages. Some of the proposed soft probes are described in the following.

Transverse momentum broadening and flow
Compared to proton-proton interactions, a hot initial QGP could lead to

more pronounced transverse expansion, causing a broadening of the transverse momentum spectrum, and/or to specific expansion patterns.

It has been suggested [20] that the form of the broadening might reflect the phase transition to QGP, leading to a temperature-entropy curve with the typical feature of a phase transition: the transverse momentum $< p_T >$, proportional to the temperature, increases with increasing entropy (dN/dy) up to the critical point; then, during the phase transition, the temperature $(< p_T >)$ remains constant and begins rising again when the transition to the new phase is complete (see fig 1.8).

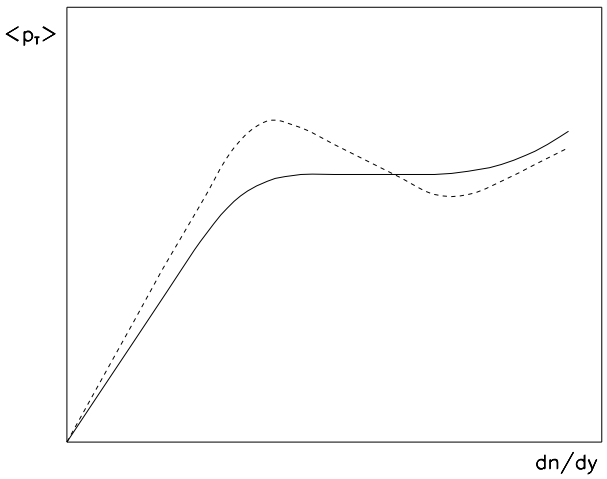

Figure 1.8: *Characteristic temperature-entropy curve for phase transition.*

Moreover, indirect signals of the phase transition can be found in specifical expansion patterns, such as the so-called elliptic flow which is driven by the azimuthal anisotropy of the transverse pressure gradient caused by geometrical shape of the reaction region in the transverse plane. Since elliptic flow should be established quite early in the collision evolution, it probes the equation of state at high energy density: the phase transition to QGP would lead to a non-monotonic behaviour in the impact parameter dependence of the elliptic flow component [21].

In-medium modification of resonances

The production of mesons provide the opportunity to observe in medium modification of the resonance properties (mass and/or width) which may be connected with chiral symmetry restoration. In particular, the interest is

concentrated on the ρ mesons because, due to their short lifetime ($\tau \sim 1.3$ fm/c), most of the ρ mesons decay inside the interaction region which can modify the particle properties. An anomalous shape of the ρ peak has been observed by the NA45 experiment in S-Au and Pb–Au collisions, together with an enhancement of e^+e^- pairs for masses lower than the ρ mass [22]. This effect can be explained both by a ρ mass shift due to partial chiral symmetry restoration and by a broadening of its width resulting from hadronic interactions [12].

Strangeness enhancement

One of the first proposed signatures of the phase transition to QGP was the enhancement of the production of strange particles [23]. The production probability of a $s\bar{s}$ in hadronic matter is small due to the high mass of the strange quark ($m_s \sim$450 MeV/c^2). On the contrary, in a QGP environment, strange quarks would be more abundantly produced due to the lower mass of the s quark induced by the (partial) restoration of chiral symmetry ($m_s \sim$150 MeV/c^2, comparable to the transition temperature T_c) and to the Pauli blocking of u and d quark states.

In particular, the strangeness enhancement should manifest itself in the production of multi-strange hyperons which can hardly be produced by hadron rescattering in a confined medium due to the low cross section and high production thresholds. On the contrary, in the case of QGP formation with a strangeness content enhanced by a factor E_s, hadrons containing N strange quarks should be enhanced by a factor E_s^N, leading to a enhancement hierarchy $E_{\Omega(s=3)} > E_{\Xi(s=2)} > E_{\Lambda(s=1)}$, which is the opposite of what should be expected in absence of phase transition. As it can be seen in fig. 1.9, the experimental results [24] show that the hierarchy expected in the case of QGP is indeed observed at the SPS.

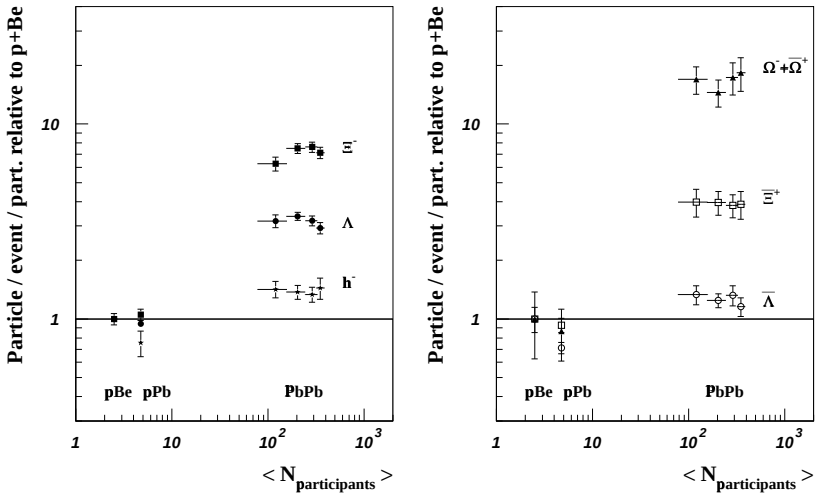

Figure 1.9: *Hadrons and hyperons yields as a function of centrality (number of participants) normalized to p-Be results as measured by WA97/NA57 experiment.*

Bibliography

[1] N.F. Mott, Rev. Mod. Phys. 10 (1968),677.

[2] C.Y. Wong, Introduction to High-Energy Heavy-Ion Collisions, World Scientific, 1994.

[3] F.Karsch et al., Nucl. Phys. B605 (2001) 579.

[4] E. Laermann, Nucl. Phys. A610 (1996) 1c-12c.

[5] Review of particle physics, The Eur. Phys. Journal C15 (2000)

[6] M.J. Tannenbaum, in Sinha, Pal, Raha, Quark-Gluon Plasma, Springer-Verlag (1990), 108.

[7] J.D. Bjorken, Phys. Rev. D 27 (1983) 140.

[8] B.Muller, Rept.Prog.Phys.58 (1995) 611.

[9] F.Antinori et al., NA57 collaboration, Eur. Phys. J. C14 (2000) 633.

[10] H.Appelshauser et al., NA49 collaboration, Eur. Phys. J. C2 (1998) 661.

[11] P.Braun-Munzinger et al., Phys. Lett. B465 (1999) 15.

[12] H.Satz , Nucl.Phys.Proc.Suppl.94 (2001) 204.

[13] E.V. Shuryak, Phys. Lett. B78 (1978) 150.

[14] L.Kluberg, Nucl.Phys. A661 (1999) 300c.

[15] M. Gyulassy and M. Plumer, Phys. Lett. B243 (1990) 432.

[16] T. Matsui and H. Satz, Phys. Lett. B178 (1986) 416.

[17] M.C. Abreu et al., NA50 Collaboration, Phys.Lett. B410 (1997) 337.

[18] M.C. Abreu et al., NA50 Collaboration, Phys.Lett. B450 (1999) 456.

[19] M.C. Abreu et al., NA50 Collaboration, Phys.Lett. B477 (2000) 28.

[20] L. Van Hove, Phys. Lett. B118 (1982) 138.

[21] P.F. Kolb et al., Phys. Rev. C62 (2000) 054909.

[22] B.Lenkeit for the NA45 collaboration, Nucl. Phys. A661 (1999) 23c.

[23] P. Koch, B.Muller and J. Rafelski, Phys. Rep. 142 (1986) 167.

[24] F.Antinori et al., NA57 collaboration, Nucl. Phys. A661 (1999) 130c.

Chapter 2

The NA50 Experiment

The NA50 experiment is a fixed target experiment which uses the CERN SPS proton and lead ion ($^{208}_{82}$Pb) beams provided by the CERN SPS accelerator. It started to take data in 1994 with the aim of extending the NA38 physics program focused on the study of the production of muon pairs in ultrarelativistic interactions of protons and ions. The experimental set–up is based on the old NA10 spectrometer, upgraded at the end of the 80's for the NA38 experiment which took data from 1986 to 1992 using lighter projectiles ($^{16}_{8}$O and $^{32}_{16}$S) which did not allow to reach the conditions of initial temperature, energy density and reaction volume (i.e. thermalization) expected for a central Pb–Pb collision.

The main goal of NA50 experiment [1] is to detect those signals which are accessible in the muon pair channel and which are related to the phase transition of ordinary nuclear matter into the QGP state. In particular the following signatures are searched for:

- Thermal dimuons production in the mass range $1.4 < M_{\mu\mu} < 2.4\,\mathrm{GeV}/c^2$, where other dimuon sources are less important.
- Anomalous suppression of the production of vector mesons J/ψ and ψ'
- Enhancement of the production of ϕ mesons with respect to ρ and ω mesons which is related to the strangeness enhancement expected for dense media

Since all these processes have small cross-section, it is mandatory to reach high values of luminosity, which are obtained with high beam intensity (I$\sim$

$5 \cdot 10^7$ ions per burst) and adequate target thickness. As a consequence, some constraints in the detector design criteria (such as radiation hardness and pile–up detection) are needed.

The experimental set–up is represented in figure 2.1. The Pb projectiles are focused on the Pb target and a fraction of them interacts producing a large number of particles (mostly pions). Since the phase transition from hadronic matter towards QGP can occur only if a high enough energy density is reached and since the energy density grows with the centrality of the Pb–Pb interaction, the determination of the centrality of the collision turns out to be very important. For this reason in the NA50 set–up three different detectors are used to measure event by event the centrality of the collision: the Electromagnetic Calorimeter (which measures the electromagnetic transverse energy, mostly due to $\pi^0 s$, released in the interaction), the Multiplicity Detector (which measures the number of charged particles produced in the collision) and the Zero Degree Calorimeter which measures the energy of the beam fragments which continue to travel in the forward direction.

Since π and K mesons decay with a high branching ratio into muons giving rise to a combinatorial background under the dimuon signals, an absorber has been placed very close to the target ($\approx$ 20 cm), with the aim of stopping most of the hadrons before they decay.

Downstream of the absorber there is the muon spectrometer, which measures the momenta of the muons produced in the target. It is the same spectrometer used in NA38 experiment, except for a slight acceptance modification which allows to cover the pseudorapidity range 2.7< η <3.9, where the highest energy densities are expected.

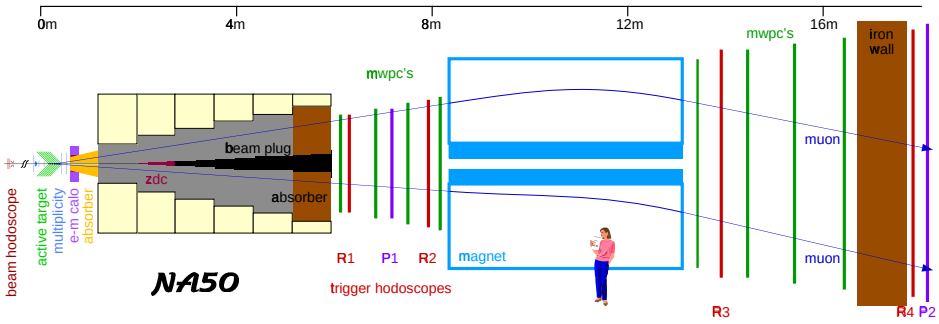

Figure 2.1: *The NA50 experimental set–up.*

2.1 Beam and beam detectors

2.1.1 The SPS beams

The NA50 experiment is placed in the ECN3 hall, at the end of a high-intensity beam line. Two kinds of primary beam are delivered from the SPS: a proton beam with a momentum of 450 GeV/c and an ion (Pb^{82+}) beam. The momentum of the lead beam is normally 158 GeV/c per nucleon (158·A GeV/c), but data with a 40·A GeV/c beam have also been taken.

The intensity of the Pb beam is chosen to fulfill both the requirement of high luminosity and the conditions for a good detector operation. The beam intensity should be high enough to allow to accumulate the high statistics required for the study of processes with small cross section. At the same time, a limit is imposed by the fact that increasing the beam intensity causes a deterioration of detector operation induced by the increase of pile-up events. Pile-up contamination is due to events occurring so close in time, that they mix up inside the integration time of the detectors giving thus rise to two signals that can not be distinguished. Of course, pile-up events have to be identified and rejected.

The cycle is different for the proton beam and the lead beam; its main characteristics - the total cycle duration (t_{cycle}) and the effective spill duration (t_{spill}) - constrain the data acquisition timing and the maximum time available for the data transfer between consecutive spills.

In tab. 2.1 are shown the specifications of each beam.

Beam		Momentum	intensity	t_{cycle}	t_{spill}
Type	Year	(GeV/c per nucleon)	(part/spill)	(s.)	(s.)
Pb	1994-1998	158	$5 \cdot 10^7$	19.2	5
Pb	1999	40	$\sim (0.7 - 1.2) \cdot 10^6$	19.2	5
Pb	2000	158	$7 \cdot 10^7$	19.2	5
p	1994-2000	400 and 450	10^{11}	14	2.5

Table 2.1: *Characteristics of the SPS primary beams.*

2.1.2 The beam hodoscope

The beam hodoscope (BH) is located 33 m upstream from the target, in a region where the beam spot is large enough to allow the tagging of individual incoming ions. It is made of one plane of 16 quartz blades associated with photomultipliers detecting the Cerenkov light produced by incident ions in the quartz. Each blade is 1 mm thick, and has a transverse size adapted to the beam intensity profile so that each counter sees about 1/16 of the total beam intensity.

Standard TDCs record the time of arrival of the ions for each blade with respect to the ion that triggered the apparatus. The information is used to tag beam pile-up which occurs when the ion triggering the apparatus is accompanied by a second ion within a short time interval.

During the data taking with proton beam, the quartz BH is replaced by a conventional scintillator and three ionization chambers filled with argon are used to measure the beam intensity.

2.1.3 Other beam detectors

Three detectors (BHI, BHInew and BAH) made of scintillating blades and placed off the beam axis are used to tag possible interactions of the projectile in the BH or somewhere else upstream from the target. The BHI and BHInew are located 19 cm and $\approx$ 100 cm downstream of the BH, while the BAH is located immediately upstream from the target system.

Approximately 50 cm upstream from the target there are two pairs of small wire proportional chambers (named GANIL chambers) which are used for an on-line monitoring of the beam profile during beam tuning sessions.

Finally, there are the two anti-halo detectors located respectively 44 and 11 cm upstream from the target, each of them consisting in a square shaped quartz blade with a central 3 mm diameter hole centered on the beam axis (the beam dimensions are $\sigma_x \approx \sigma_y \approx 0.4$ mm). These detectors allow to identify both the events in which the Pb projectile is more than 1.5 mm far from the beam axis, and the events for which an interaction occurred upstream from the target giving rise to a Pb fragment crossing one antihalo detector out of the central hole. For the 1999 and 2000 data taking, only one antihalo detector, located 8 cm upstream from the target, was present.

2.2 The target system

The target configuration varied in the different data taking periods. The main characteristics of the various target setups are reported in table 2.2.

Year	Number of subtargets	Target thickness (mm)	Target environment
1995	7	7	air
1996	7	12	air
1998	1	3	air
1999	1	3	vacuum
2000	1	4	vacuum

Table 2.2: *Main characteristics of the different target configurations for the standard data taking conditions.*

2.2.1 The multitarget system

The NA50 Pb multi-target has been originally designed in order to satisfy the following requirements:

- Maximize the number of interactions (luminosity)
- Minimize the interactions inside the target of the particles produced in the Pb-Pb interaction
- Have a good identification of the vertex position
- Identify the re-interactions of fragments of the projectile
- Be radiation resistant

A segmented target, made of 7 subtargets, each of them being sufficiently thin to minimize re-interactions, has therefore been implemented. Moreover, it was chosen to use an active target, featuring detectors to identify the subtarget in which the primary interaction (or possibly the re-interaction) took place. This is done by means of radiation resistant quartz blades placed off the beam axis on both sides of each subtarget (see fig. 2.2). These quartz

blades collect the Cerenkov light produced by the passage of fast charged particles (mostly pions) produced in the collision. Thanks to the geometry of the system, the two blades placed immediately downstream of the subtarget where the interaction occurred give the highest signal [2, 3]. A couple of blades placed before the first target is used to recognize interactions which took place in the region upstream from the target system.

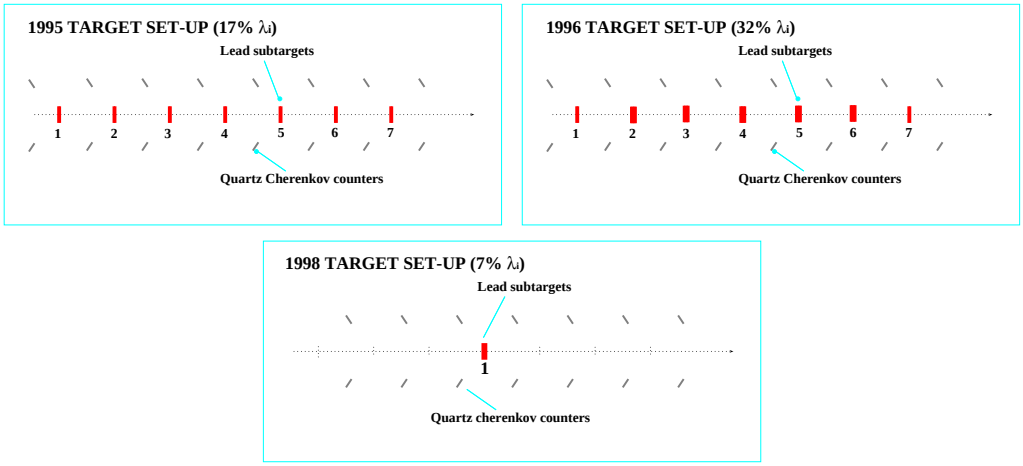

Figure 2.2: *The multitarget system for 1995, 1996 and 1998 data taking periods.*

The subtargets (Pb blades with a transverse area of 1.5×1.5 mm^2) are placed along the beam line at regular intervals of 25 mm. The number of subtargets used and the total target thickness varied in the different data taking periods, as it is shown in fig. 2.2. In 1995 data taking, 7 subtargets of 1 mm thickness were used, for a total target thickness of 17% of an interaction length (λ_I). In 1996 data taking, to collect larger statistics, 5 subtargets 2 mm thick and 2 subtargets 1 mm thick were used, the total target thickness being 32% λ_I. In 1998, to minimize the probability of fragments re-interactions, only one subtarget 3 mm thick (7% λ_I) was used.

2.2.2 The single target in vacuum system

A completely new target system has been implemented on the NA50 beam line for the 1999 and 2000 data taking periods with the aim of getting rid of the contamination coming from Pb-air interactions. For this reason, the

beam vacuum tube has been extended up to the multiplicity detector, so that the Pb projectile travels in vacuum and can interact only with the target nuclei.

A new mechanical target support has been designed to fit inside the vacuum tube (see fig. 2.3). It can hold up to 3 different targets on a rotating device which puts one (and only one) of them on the beam line. Two quartz blades are located off the beam axis 6 cm downstream of the target and are used to identify the interacting ions by detecting the Cerenkov light produced by the crossing particles.

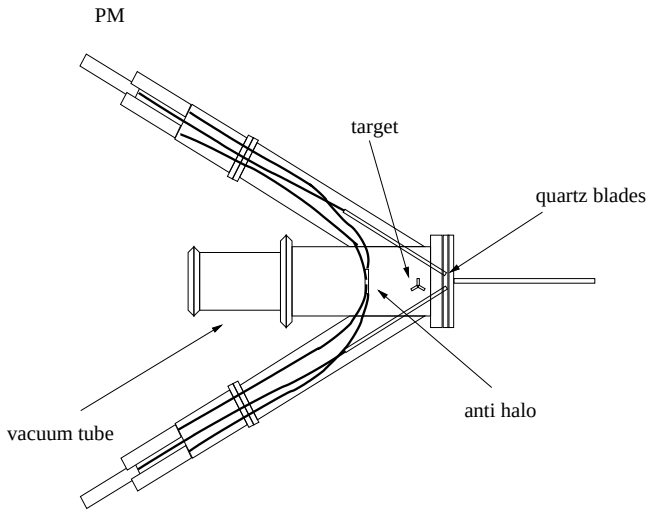

Figure 2.3: *The target in vacuum system for 1999 and 2000 data taking periods.*

2.3 Centrality detectors

Since it is expected that some effects under study, such as the J/ψ suppression, depend on the temperature (or the energy density) of the system, it is of crucial importance to precisely measure the centrality of the collision, which is strictly connected with the thermodynamical properties of the initial state.

The centrality of an event is defined by the impact parameter b of the collision and can not be directly measured. It can, however, be deduced from the measurement of some centrality-related observables. In the NA50

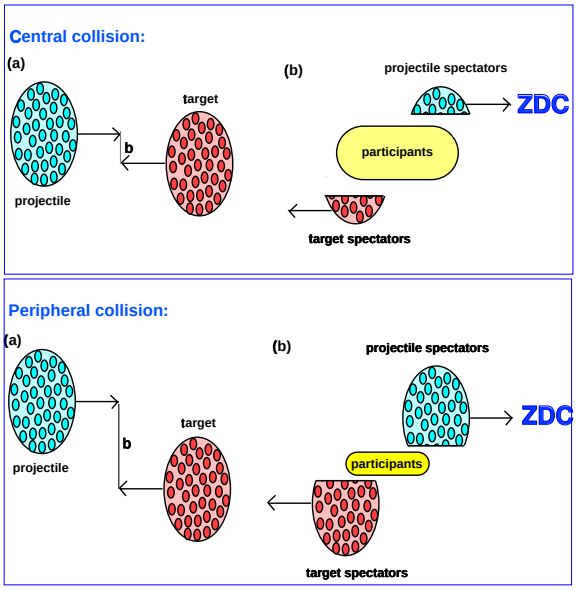

Figure 2.4: *Scheme of central (top panel) and peripheral (bottom panel) collisions.*

experiment, the centrality of the collision can be estimated on an event by event basis using three independent detectors:

- the Multiplicity Detector (MD) which measures the total number of charged particles produced in the interaction (N_{ch})
- the Electromagnetic Calorimeter (EMC), which measures the transverse neutral energy produced in the interaction (E_T)
- the Zero Degree Calorimeter (ZDC), which measures the residual energy of projectile fragments (E_{ZDC})

E_T, E_{ZDC} and N_{ch} are all related to the impact parameter of the collision, b. Actually, the number of interacting nucleons grows with centrality. Hence, also E_T and the multiplicity grow with centrality, being themselves approximately proportional to the number of participant nucleons. On the opposite, the number of nucleons in the projectile which do not interact (spectator nucleons) and reach the ZDC decreases with increasing centrality, and so does the forward energy E_{ZDC}.

The correlations among the variables measured by these three detectors are a powerful tool used to clean the sample of the collected events by rejecting events originating both upstream and downstream of the target region.

2.3.1 The multiplicity detector

The multiplicity detector is used to measure the number and the angular distribution of the charged particles produced in the collision and therefore it is placed immediately downstream of the target. It is made of two identical discs of silicon strip detectors and it covers the pseudorapidity interval $1.0 < \eta < 4.4$. The next chapter is devoted to a detailed description of this detector.

2.3.2 The electromagnetic calorimeter

The electromagnetic calorimeter (EMC) is located downstream of the second disc of the multiplicity detector ($\approx$32 cm downstream of the target region) and it is used to measure event by event the transverse energy E_T carried by neutral particles produced in the interaction (mostly due to $\pi^0 \rightarrow \gamma\gamma$ and to direct γ).

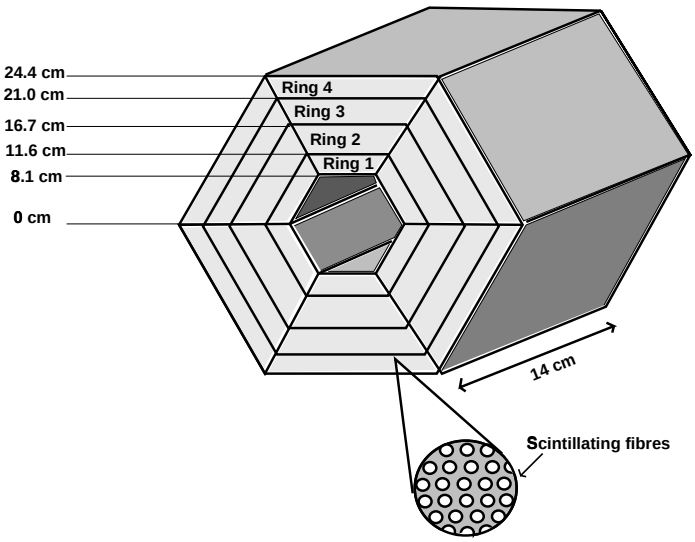

Figure 2.5: *The electromagnetic calorimeter.*

It is made of 2 mm diameter scintillating fibers placed parallel to the beam direction and embedded into a 14 cm thick lead converter. The ratio between the fiber volume and the passive volume is 1:2. The thickness of the lead converter corresponds to $\sim$ 15 interaction lengths ($X_0 = 0.95$ cm). Therefore, to avoid the deterioration of the mass resolution of the muon spectrometer, the EMC is placed out of the spectrometer acceptance and covers the pseudorapidity interval $1.1 < \eta < 2.3$. This location far from the beam axis has also the advantage that the fibers can work in an environment where the radiation level does not affect dramatically the calorimeter operation.

The EMC is divided in six azimuthal sectors (it has the same hexagonal azimuthal geometry of the spectrometer) and each sextant is further subdivided into four radial rings (see fig. 2.5), each of them covering different pseudo-rapidity ranges. The neutral transverse energy is obtained from the energy measured in each calorimeter ring multiplied by the sine of the angle subtended by the ring and corrected by subtracting the charged particle contribution evaluated with a GEANT-based simulation [4]. The resolution on the measured E_T is 5% for central Pb–Pb collisions.

2.3.3 The Zero–Degree Calorimeter

The Zero–Degree Calorimeter (ZDC) [5] measures the energy E_{ZDC} emitted in a narrow angular interval around zero degrees. This energy is mostly due to the projectile nucleons which have not taken part to the collision (spectator nucleons) and continued to travel in the forward direction. From the measured E_{ZDC} it is possible to evaluate the number of projectile participant nucleons:

$$N^P_{part} = 207 - \frac{E_{ZDC}(GeV)}{158\ GeV}$$

It is also possible, assuming a spherical geometry for the nuclei, to estimate the transverse area involved in the collision.

The ZDC is located along the beam axis 165 cm downstream of the target, inside the hadron absorber. In order to stand the huge radiation dose, it is based on the quartz fiber technique: 900 quartz fibers with a diameter of 365 μm are embedded in a tantalum converter with a volume ratio fiber/Ta equal to 1:17 [6]. The calorimeter measures the Cerenkov light produced by beam spectators showering in the tantalum converter. The converter is 65 cm long and it has a cross section of 5×5 cm^2. The fibers are 1.8 m long; the first part (65 cm) of them is placed inside the tantalum, parallel to the beam

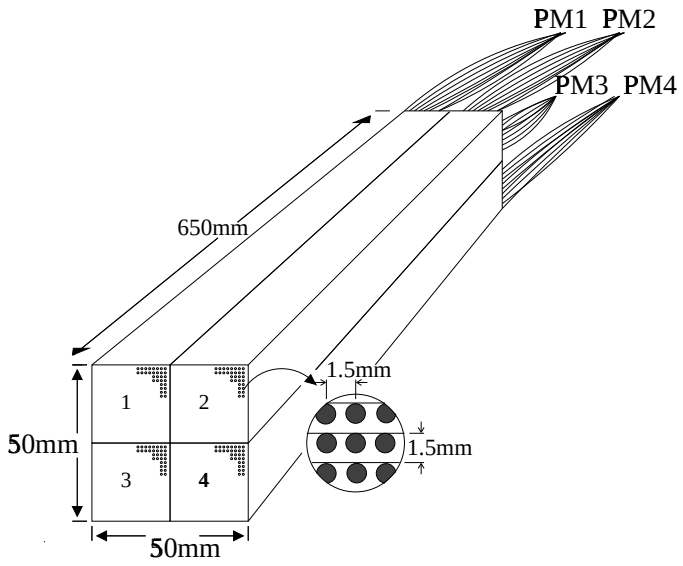

Figure 2.6: *The Zero Degree Calorimeter.*

axis, and constitute the active part of the detector; the rest (1.15 m) is bent and used as a light guide towards 4 photomultipliers (see fig. 2.6). The fibers are divided into 4 groups each one read by one of the 4 photomultipliers in order to have a beam position sensitive detector.

2.4 The muon spectrometer

The muon spectrometer, which constitutes the main body of NA50, measures the kinematic variables which characterize the muons produced in the interaction of a proton or of a lead ion in the target.

The spectrometer set-up is shown in fig. 2.7. It is made of a toroidal field magnet which bends the muon tracks which are reconstructed by 8 three-plane multi-wire proportional chambers (PC1-PC8). Four plastic scintillator hodoscopes (R1-R4) are placed both upstream and downstream of the magnet to provide the muon pair trigger. Muon pairs are detected in the pseudorapidity interval $2.7 < \eta < 3.9$ [1]. Two additional hodoscopes (P1 and P2) are used to measure the trigger efficiency. Upstream from these detectors there is the hadron absorber which stops all the particles produced in the interaction except for the muons.

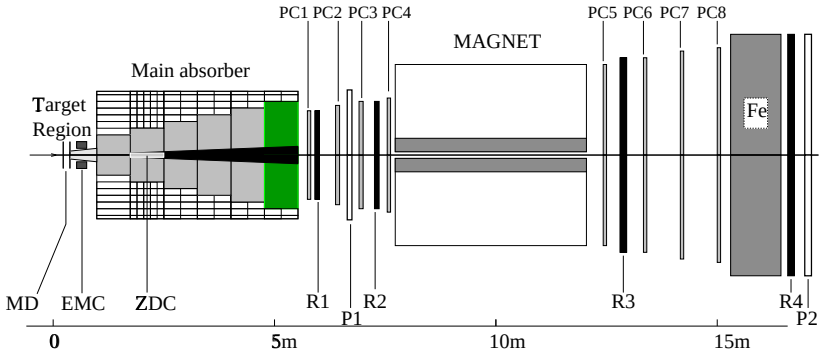

Figure 2.7: *The muon spectrometer.*

The resulting J/ψ mass resolution is 3.1% (r.m.s.) and the acceptance for muon pairs is of the order of 15% for invariant masses above 3 GeV/c^2 [4].

2.4.1 The hadron absorber

An hadron absorber has been placed upstream from the muon tracking detectors, very close to the target region ($\approx$ 20 cm). It is used to stop the hadrons (mostly π and K mesons) generated in the Pb–Pb interaction before they decay into muons, so as to avoid that a huge number of muons coming from hadron decays reach the spectrometer giving rise to a background to the muons originated by the interesting signals.

Since the absorber must stop most of the hadrons coming from the target, the absorption probability should be maximized. To obtain this, a material with short interaction length λ_I (high mass number A) must be used. On the other hand, highly penetrating muons, which are not stopped by the absorber, should not suffer too much multiple Coulomb scattering, because this would cause a deterioration of the mass resolution of the spectrometer. In order to minimize multiple scattering, the material of the absorber should have long radiation length X_0, which means small atomic number Z.

For these reasons an hadron absorber composed of different layers of materials has been chosen (see fig. 2.8). It is composed of:

- the BeO preabsorber: it has conical shape and it is located in the center of the electromagnetic calorimeter $\approx$ 20cm downstream of the

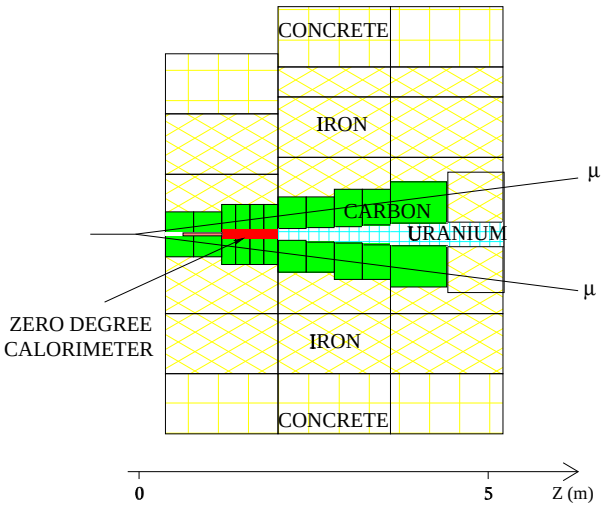

Figure 2.8: *The absorber.*

target. It has a central hole along the beam axis to allow the projectile fragments to travel towards the ZDC

- the carbon absorber: it is located immediately downstream of the pre-absorber. It is 4 m long and it is composed composed of a central cone of carbon surrounded by iron and concrete blocks. The carbon cone covers the spectrometer acceptance (32-116 mrad) where it is mandatory to minimize the multiple scattering, while iron and concrete are meant to stop all the particles out of the spectrometer acceptance.

- the iron absorber: it is an 80 cm thick wall of iron placed immediately downstream of the carbon absorber and it is used to reduce the illumination of the most upstream detectors of the spectrometer [1].

- the plug: a central hole along the beam axis allows to the fragments of the projectile to reach the ZDC which measures their energy and acts also as a plug. Moreover downstream of the ZDC there is a 4 m long block of Uranium and Tungsten which stops all the fragments which continue to travel along the beam axis.

Finally, a second absorber (a wall of iron 1.2 m thick) has been placed between the last set of MWPC and the last hodoscope R_4 (see fig. 2.7) with the aim of absorbing the mesons which entered in fake a dimuon trigger .

2.4.2 The magnet

The magnetic field used to bend the muon tracks is generated by a 480 cm long toroidal magnet placed approximately 10.5 m downstream of the target. It has hexagonal shape, as it can be seen in fig. 2.9a, and this fact influences also the geometry of the hodoscopes and of the proportional chambers.

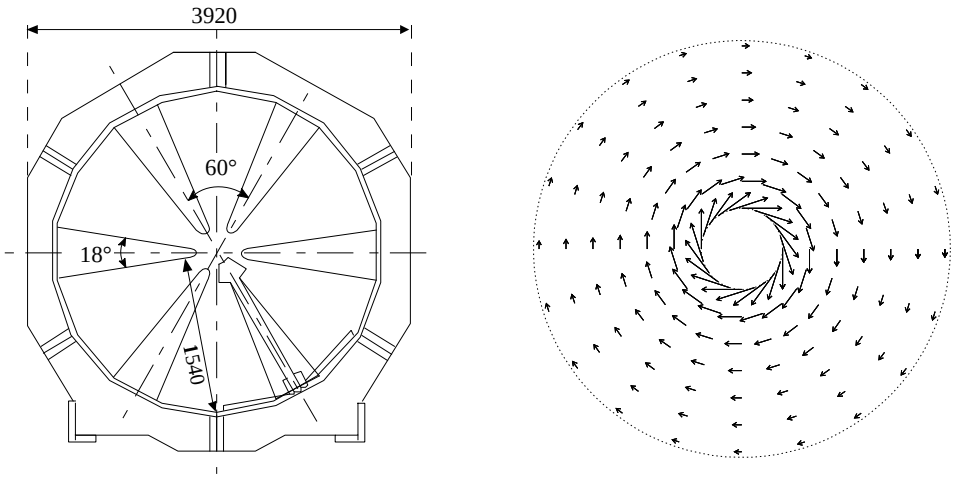

Figure 2.9: *(a)View of the magnet* *(b) Shape of the magnetic field.*

The magnetic field is generated by a pulsed current, synchronized with the SPS cycle, circulating in 6 coils, mounted on 6 supports, each of them occupying an azimuthal angle of 18^o. Muon pairs for which one of the muons went through one of these iron supports, suffering a severe multiple scattering, are rejected in the offline analysis.

The magnetic field inside the magnet is essentially toroidal (see fig. 2.9b), it is symmetric around the beam line and its strength is inversely proportional to the distance r from the beam axis:

$$\vec{B}(r) = \frac{B_0}{r}\vec{e}_\Phi \tag{2.1}$$

where B_0 depends on the current intensity (B_0 = 0.383 T·m, for I=7000 A which is the current value commonly used in NA50 to study high mass muon pairs). Crossing such a magnetic field, a charged particle generated

in the target remains in the same azimuthal plane and is deflected by an angle inversely proportional to its transverse momentum $\Delta\theta \propto 1/p_T$. To prevent any systematic effect related to the sign of the magnetic field, the polarity of the magnet is reversed every few hours. The intensity of the field is continuously checked by means of a Hall-probe.

2.4.3 The trigger hodoscopes

Two sets of scintillator hodoscopes provide the signal that triggers the data acquisition system and allow a first determination of the muon trajectories. Each set is made of two hodoscopes, which are hexagonal planes of plastic scintillator blades, designed to provide a fast response. The light produced in each blade by crossing particles is collected via plastic light-guides and read by two photomultipliers.

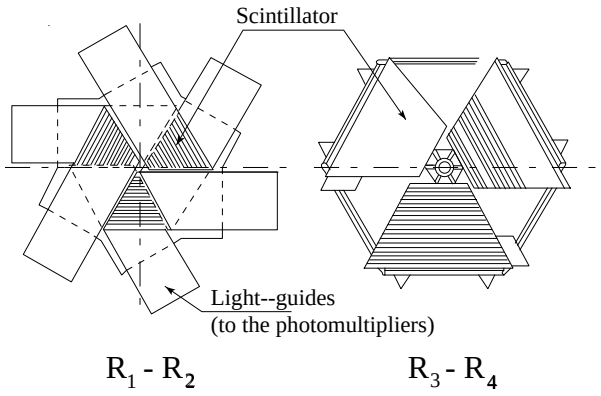

Figure 2.10: *The trigger hodoscopes.*

The two first hodoscopes, called R_1 and R_2, are placed between the main absorber and the magnet, while the other two - R_3 and R_4 - are placed downstream of the magnet, one before and the other after the iron wall. R_1 and R_2 are made of 6 azimuthal units and are radially divided in 30 scintillator blades (fig. 2.10). The width of the blades increases gradually with the distance from the beam axis.

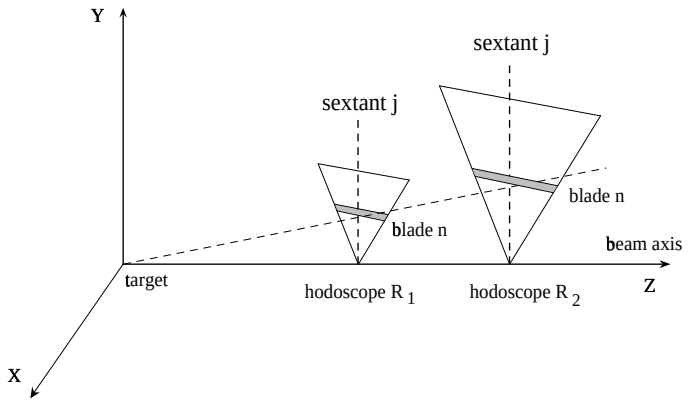

Figure 2.11: *The V coincidence selection.*

According to this geometry, a coincidence $V = R_1^i \times R_2^i$ identifies the trajectory of a particle coming directly from the target, as it can be seen in fig. 2.11. To take into account also the longitudinal size of the target, also the coincidences $V = R_1^i \times R_2^{(i-1)}$ are accepted.

The hodoscopes R_3 and R_4 of the second set are made respectively of 24 and 32 scintillator blades for each sextant; all the blades have the same width (5.5 cm), The coincidence between R_3 and R_4 blades and R_1 and R_2 blades provide the trigger and allow also to estimate the transverse momentum of the muons by measuring the deflection angle through the magnet.

Two other hodoscopes, named P_1 and P_2, are used to check the trigger efficiency. They are divided in six azimuthal sectors, each of them composed of 8 scintillator blades. P_1 is located between the main absorber and the magnet, while P_2 is placed after R_4, downstream of the iron absorber wall. Each P_1 scintillator is read by one PM, while the P_2 scintillator blades are connected to 2 PM's whose signals are averaged by a "mean timer".

2.4.4 The multi wire proportional chambers

The reconstruction of the muon tracks is done by means of two sets of four Multi Wire Proportional Chambers (MWPC). The first set of chambers ($PC_{1,2,3,4}$), is placed immediately after the absorber and reconstructs the segment of the track pointing to the interaction vertex. The second set

($PC_{5,6,7,8}$) is placed downstream of the magnet, and is used to reconstruct the trajectory after the deflection due to the magnetic field. The precision of such a measurement is of the order of some tenth of mrad.

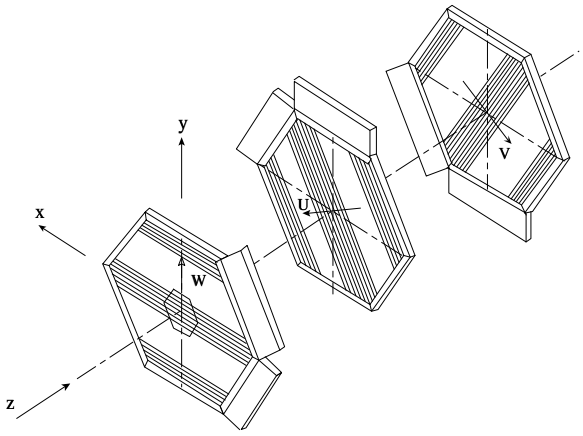

Figure 2.12: *The Multi Wire Proportional Chambers.*

Each chamber has hexagonal geometry and is composed of 3 independent anode wire planes rotated respectively by 0, 60 and 120 degrees with respect to the horizontal axis, as it can be seen in fig. 2.12. All the wire planes are made of 20μm gold-plated tungsten wires with a wire spacing of 3 mm, immersed within a gas mixture of Argon (80%), Isobutane (19.8%) and Freon (0.2%). The upstream chambers have a radius of 1.3 m and are equipped with 749 wires per plane, while for the downstream ones the radius is 3 m and each plane contains 1229 wires.

2.5 Trigger selection and Data Acquisition

In the NA50 experiment three different types of trigger are used to select the events that are to be acquired and recorded by the data acquisition system.

2.5.1 Dimuon trigger

The main trigger of the NA50 experiment has been developed to select events in which a pair of muons (dimuon) has been produced in the Pb–Pb interaction, while the muons originating from interactions in the absorber should be rejected.

There are 2 levels of trigger; the first level trigger selects events in which 2 tracks coming from the target region have crossed the spectrometer in 2 different sextants. The identification of a single muon is based on the V coincidence between the n^{th} blades of the hodoscopes R_1 and R_2. In this way, muons not coming from the target region and muons which suffered strong multiple scattering in the absorber are rejected. This V signal is then put in coincidence with R_4 ($V * R_4$), while R_3 is used to confirm the trigger and to reduce the rate of accidental tracks.

This system provides also a rough estimation of the deflection angle of the muon and, consequently, of its transverse momentum p_T. On the basis of their p_T, single muon signals are grouped in 4 classes (namely A, B, C and D) and sent to a programmable unit (named "Magic Box") which gives an output signal each time two muons are detected in different sextants of the hodoscopes.

The output signal of the "Magic Box" is then put in coincidence with the V signal, generating a trigger signal called "Trigger Sans Jitter" (TSJ) which has a time instability of about 1 ns. A further synchronization of the TSJ with the BH signals allows to reduce the jitter to 0.5 ns, giving rise to the so-called "Trigger Zero Jitter" (T0J).

Events fulfilling the conditions for this first level trigger, can be further selected with a second level trigger according to their kinematical and dynamical characteristics.

2.5.2 Minimum Bias trigger

The Minimum Bias (MB) trigger signal is generated when the ZDC signal is higher than a fixed threshold. A very low value (50 mV, lower than the minimum energy detectable by the ZDC [6]) has been chosen for the trigger threshold, in order to a have a trigger signal each time some particle enters the ZDC and to avoid any trigger bias. Most of these MB triggers are events in which a lead ion did not interact in the target and then deposited all its energy (33 TeV) in the ZDC.

2.5.3 Laser trigger

The third trigger used by NA50 is the so-called laser trigger, which is obtained by means of a pulse generator which sends a laser pulse to the EMC photomultipliers. It is used to check the gain stability of the photomultipliers of the EMC. At the same time, it allows to evaluate the pedestal values for the other detectors whose PM's are not connected to the laser.

2.5.4 Data acquisition system

For the events fulfilling the trigger requirements, the data of each detector is acquired in local memories, then transferred to the final memory devices and recorded on tape. This data transfer is done burst by burst and not event by event. During the 5 s spill, the data from the different detectors are stored into temporary memories, which can stack the information of a whole burst (i.e. up to 5000 events, corresponding to 17 Mbytes [4]). At the end of the burst, the data of the whole burst is transferred via transputer links (10-20 Mbits/s) to the final acquisition memories connected to the tape recording system. Simultaneously, a copy of the data collected during the whole burst is sent to "SPY" memories, which allow a continuous on-line monitoring of the detector operation without any interference with the activity of the acquisition.

Bibliography

[1] Study of Muon Pairs and Vector Mesons Produced in High Energy Pb-Pb Interactions, Proposal CERN/SPSLC 91-05, SPSLC/P 265, October 1991.

[2] F.Bellaiche, PHD thesis, Apr. 1997, Universitè de Lyon.

[3] F.Bellaiche et al.,. Nucl. Instr. and Meth. in Phys. Res. A398 (1997) 180.

[4] M.C. Abreu et al., NA50 Collaboration, *Phys.Lett.* **B410**(1997)327.

[5] R.Arnaldi et el,. Nucl. Instr. and Meth. in Phys. Res. A411 (1998) 1-16.

[6] R. Arnaldi, PHD thesis, Dec. 2000, Universitè Blaise Pascal, Clermont-Ferrand.

Chapter 3

The NA50 multiplicity detector

3.1 Introduction

The multiplicity detector (MD) of the NA50 experiment [1, 2] is a silicon microstrip detector used to measure the number and the angular distribution of the charged particles produced in Pb–Pb collisions. Since the number of particles (multiplicity) produced in the interaction depends on the centrality of the collision, the measurement of the charged multiplicity with a good resolution allows to characterize the events according to their centrality.

It is important that this measurement is performed over a wide angular range including the muon spectrometer acceptance for all the targets; for this reason the MD has been organized in two identical detector planes (named MD1 and MD2) located 10 cm apart, each of them serving one half of the targets. This two–plane structure allows to use the multiplicity detector also as a target recognition system, by means of an algorithm which reconstructs particle "tracks" by matching the hits on the two detector planes.

The layout of the NA50 experiment has put several important constraints on the design of the multiplicity detector. As it can be seen in figure 3.1, the MD is located in a very small space (about 10 cm in the longitudinal direction), because the absorber has to be placed very close to the target in order to limit the background due to muons coming from π and K decays. Moreover, the very high rate at which NA50 takes data constraints the dead-time of the readout electronic to be very short (< 50 ns) and the sampling frequency very high (50 MHz). This high data taking rate, in addition to the location close to the target, cause the MD to operate in a high–radiation

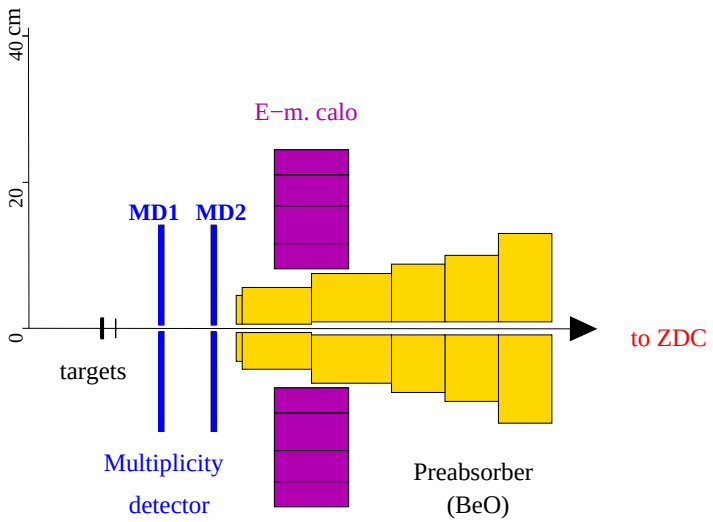

Figure 3.1: *Scheme of the NA50 target region.*

environment: during two months of Pb-Pb data taking the radiation level reaches approximately 10^{14} equivalent neutrons/cm^2 of fluence and 10 Mrad of dose for the most irradiated part of the detector. Finally, since a huge number of particles ($\sim$ 1000) is produced in central Pb–Pb collisions, to achieve a good resolution, a good granularity is required.

The detector, therefore, has to be very fast, radiation resistant and of high granularity. The conditions on speed and radiation hardness are comparable to the ones foreseen for the inner trackers of the future Large Hadron Collider experiments at CERN [3].

To reduce the data volume and simplify the design and the operation of the electronic readout chain, a binary readout scheme has been implemented for the MD: the analog signal from the strip is immediately discriminated and only the hit/no hit information is stored for each channel.

3.2 Structure of the Multiplicity Detector

The two multiplicity detector planes (MD1 and MD2) have been designed to be modular, which means that they are made of many identical pieces, in order to allow easy replacement of damaged parts.

Each detecting plane is composed of silicon microstrip detector wafers of trapezoidal shape placed on both sides of a stesalite disk made and arranged to form two circular crowns (inner crown and outer crown) centered on the beam axis. A whole detecting plane is therefore a circle with a central hole where the beam fragments and the non–interacting ions pass through, as it can be seen in figure 3.2.

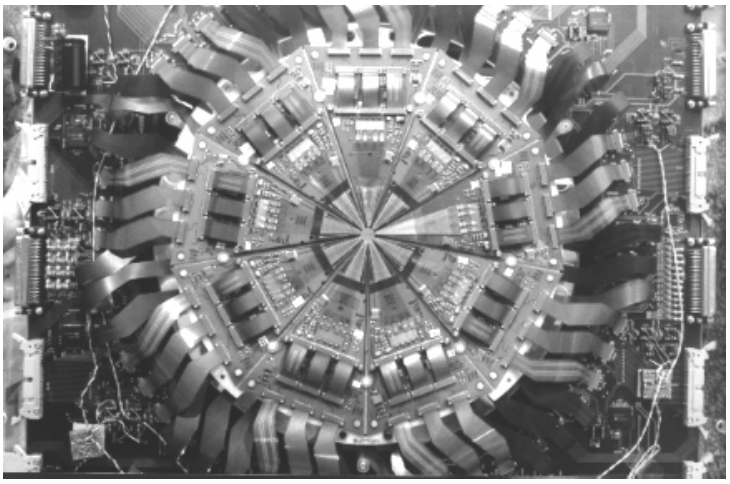

Figure 3.2: *Picture of one plane of the multiplicity detector.*

Each detector wafer of the inner crown of the MD covers a 20^o azimuthal angle and it is segmented azimuthally in 2 sectors of $\Delta\phi$=10^o and radially in 128 strips with different dimensions, so as to have almost constant occupancy per sensitive element. The granularity of the MD was chosen to match at the same time with the requirements of good angular resolution and of a reasonably low occupancy per sensitive element, and with the uncertainties on the angle due to the beam spot size and to the multiple scattering in the target, which limit the azimuthal resolution. An average pseudorapidity step of $\Delta\eta \approx 0.02$ has therefore been implemented for the strips; this granularity gives about 30% occupancy for "quasicentral" Pb–Pb collisions (impact parameter < 2 fm), according to VENUS simulations [4]. According

to the original design, the inner radius of the sensitive part of the innermost detector (r_{min}) should have been 4.4 mm and the outer radius (r_{max}) 34.4 mm, but, for mechanical reason, this range was shifted by 2.1 mm and therefore the innermost strips lie at 6.5 mm distance from the beam axis and the outermost ones at 36.5 mm. The pseudorapidity (η) coverage for a target located at 11.65 cm upstream from MD1 is therefore $1.93 < \eta < 3.51$ for MD1 and $2.47 < \eta < 4.13$ for MD2.

The outer crown is composed of detecting units covering an azimuthal angle of 20^o segmented in two 10^o azimuthal sectors and in 64 radial strips with the same average granularity of the inner crown ones ($\Delta\eta \approx 0.02$). The sensitive part of the outer crown detectors extends itself from r_{min}=36.5 mm to r_{max}=88.5, so that it covers a pseudorapidity range $1.11 < \eta < 1.85$ for MD1 and $1.61 < \eta < 2.43$ for MD2 in the case of a target located at 11.65 cm upstream from MD1.

Since each unit covers a 20^o azimuthal angle, 18 units are needed to cover the full 2π azimuth. Therefore a single MD plane (MD1 or MD2) consists of 6912 microstrips (4608 on the inner crown and 2304 on the outer crown) and the total number of strips on the two MD planes is 13824. The main characteristics of the detectors are summarized in table 3.1.

Detector layer	Crown	# of azim. sectors	# of strips per sector	r_{min} (mm)	r_{max} (mm)
MD1	Inner	36	128	6.5	36.5
MD1	Outer	36	64	36.5	88.5
MD2	Inner	36	128	6.5	36.5
MD2	Outer	36	64	36.5	88.5

Table 3.1: *Characteristics of the silicon detectors.*

A scheme of the MD structure is reported in figure 3.3. The detectors are glued on multilayer circuits, which work also as a mechanical support, called BOARDs. The BOARD which accommodates an inner crown detector is named BOARD1, while the one for an outer crown detector is named BOARD2. The BOARDs have triangular shape covering an azimuthal extension of 40^o and they hold, besides the silicon detector, also the front–end VLSI chips, some filter capacitors and the signal and power lines.

The modular structure of MD is based on the BOARD1+BOARD2 cou-

ple: each of the two MD planes (MD1 and MD2) is composed of two layers (called UP and DOWN) made of 9 BOARD1+BOARD2 couples fixed on a stesalite plane; the DOWN layer is rotated by 20^o with respect to the UP layer, so that the full 2π azimuth is covered by the silicon detectors. The pseudorapidity coverages of the four MD1 layers in the case of a target located 11.65 cm upstream from the MD1 stesalite disc are listed in table 3.2.

Detector layer	Crown	distance (mm) from target	r_{min} (mm)	r_{max} (mm)	η_{min}	η_{max}
MD1 UP	Inner	108.6	6.5	36.5	1.81	3.51
MD1 UP	Outer	112.6	36.5	88.5	1.06	1.85
MD1 DOWN	Inner	123.5	6.5	36.5	1.93	3.64
MD1 DOWN	Outer	120.4	36.5	88.5	1.11	1.91
MD2 UP	Inner	201.8	6.5	36.5	2.41	4.13
MD2 UP	Outer	205.1	36.5	88.5	1.58	2.43
MD2 DOWN	Inner	215.3	6.5	36.5	2.47	4.19
MD2 DOWN	Outer	212.9	36.5	88.5	1.61	2.46

Table 3.2: *Pseudorapidity coverage of the different MD layers in the case of a target located 11.65 cm upstream from the MD1 stesalite disc.*

Mechanically the BOARD1 is mounted on top of a BOARD2 to which it is electrically connected by means of a set of three kapton cables. The BOARD2 then is connected, by means of three kapton cables, to an external distribution card, named EXTCARD, which is used to collect the data from all the silicon detectors, to provide the interconnections with the outside and to supply the power voltage and the control signals to the detectors and the front–end chips. One EXTCARD can serve 18 BOARD1+BOARD2 couples, i.e. one MD plane. MD1 and MD2, with their respective EXTCARDs, are mounted on a mechanical support, so that the whole system can be moved vertically with a remote–controlled stepper motor.

3.3 The Silicon Microstrip Detectors

To detect the charged particles produced in the Pb–Pb collision, single side silicon strip detectors, where the strips are made of p^+ implantation on a n

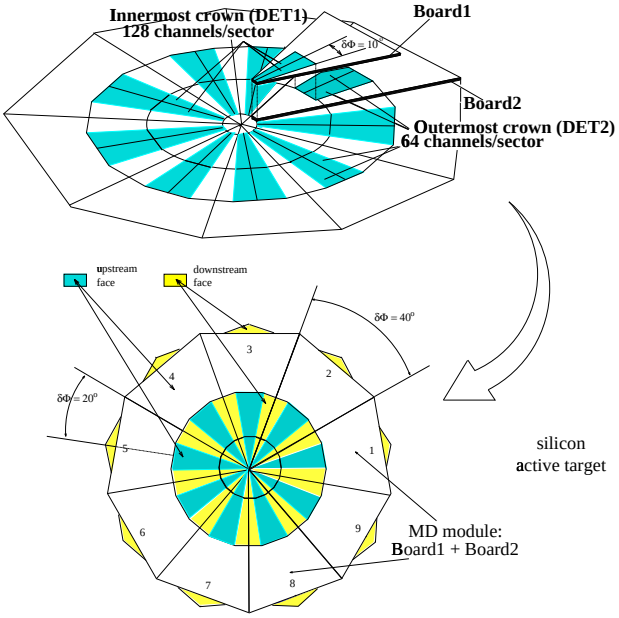

Figure 3.3: *The Multiplicity Detector structure: a) superposition of BOARD1 and BOARD2 to form a complete module b) different position of the modules on the UP and DOWN layers.*

bulk, are used. In order to have the same pseudorapidity coverage for all the strips of the detector, the area of the strips grows when going from the beam axis to the outer part of the MD, as it can be seen if fig. 3.4. The strip pitch ranges from 90 μm at the tip of the detector to 700 μm in the outermost part of the inner crown. Outer crown strips are larger (up to 980 μm pitch).

Two different detector types are used for the inner crown and for the outer crown: the inner crown detectors consist of 128 strips AC-coupled (with integrated capacitors) to the readout electronic chain, while the outer crown detectors consist of 64 strips directly (DC) coupled to the electronics.

In both cases, the detector production process begins with the oxidation of a 300 μm thick, n doped silicon wafer, so that a passivated SiO_2 layer is produced on the whole surface of the silicon bulk. The geometry of the strip pattern is defined by means of a mask of inactive material. Using photolithographic techniques, windows are opened in the oxide areas not

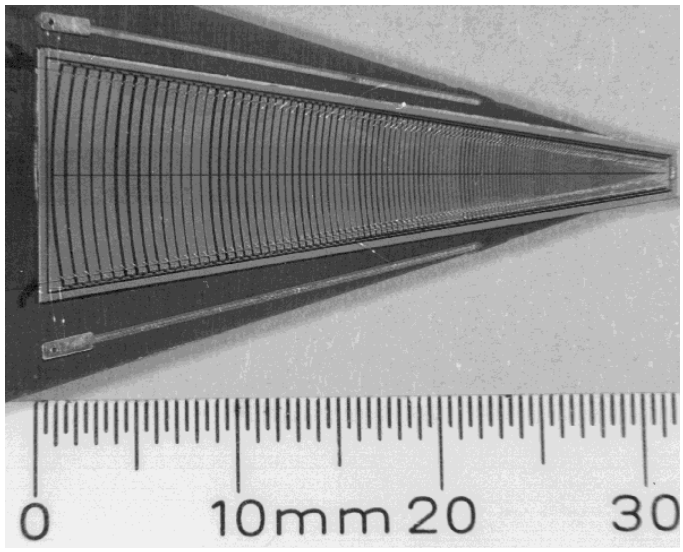

Figure 3.4: *Picture of an inner crown silicon detector.*

protected by the mask (the strips) to enable ion implantation, while in the areas protected by the mask (which will constitute the interstrip regions) the oxide layer remains on the surface of the silicon. In the strip windows boron ions are implanted, creating the p^+ regions. On the opposite side of the silicon bulk, a diffusion of phosphorus is made to create a n^+ region, called backplane, which provides the ohmic contact with the bias voltage supply.

The production process proceeds differently for the AC-coupled detectors of the inner crown detectors, and for the DC-coupled detectors of the outer crown. For the DC-coupled detectors an aluminum layer is deposited on the silicon strips, thus obtaining a direct (ohmic) contact between the metal and the semiconductor. For the AC-coupled detectors, a second oxidation is performed to let grow a 250 nm layer of silicon dioxide on the p^+ strips. Afterwards the aluminum is deposited on the oxide in correspondence of the strips, creating a MOS (Metal-Oxide-Semiconductor) capacitor directly integrated on the surface of the detector. In both AC and DC coupled detectors, the aluminum layer is bonded to aluminum-on-glass fanouts which provide the connection with the readout chips.

The MOS contact realized for the inner crown detectors prevents the detector current to flow inside the first stage of the preamplifier. The choice of DC-coupling for the outer crown is imposed by the fact that, due to difficulties

in the SiO_2 deposition process on silicon wafers, it is not possible to produce a homogeneously thick and defect free SiO_2 layer on big surfaces, as the ones of the outermost strips of the outer crown detectors.

The $p^+ - n$ junction between the strip and the bulk is reverse biased by applying a negative voltage between the backplane and a bias bus, which surrounds the sensitive area and is connected to each strip by means of integrated polysilicon resistors of about 200 kΩ. The reverse bias reduces the number of majority carriers in the region close to the junction, causing an extension of the depletion region, which, in the case of full depletion, reaches the n^+ backplane giving rise to an electric field between the backplane itself and the strips.

In this bias condition, only a small current flows across the junction, the so-called leakage current, which is usually due to both surface and bulk effects. The bulk leakage current is mainly due to the thermal generation of electron-hole pairs in the depletion region and to minority carriers drifting across the junction. The other component of the leakage current, the surface current, occurs at the edge of the junction where relatively high voltage gradients must be supported over small distances. The surface leakage current is collected by the guard ring, a p^+ implantation which limits the sensitive area defining the shape of the electric field close to the physical edge of the detector.

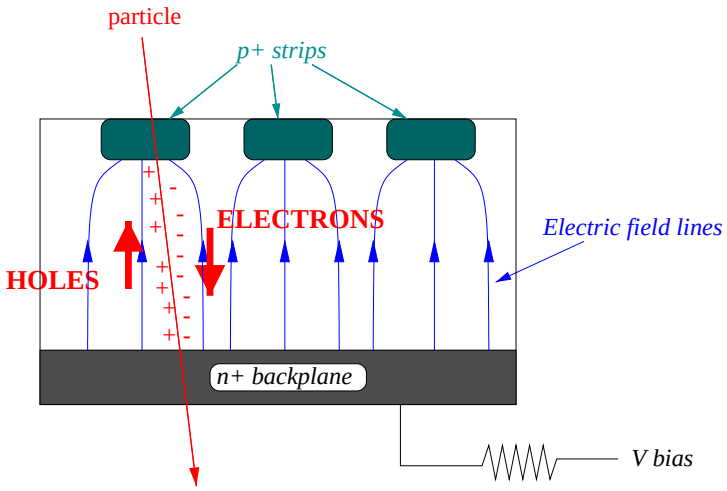

Figure 3.5: *Transverse section of a silicon strip detector.*

As illustrated in figure 3.5, when a charged particle passes through the

detector, electron–hole pairs are created along the path of the particle track. The created electron and holes separate in the electric field and induce signals at the electrodes: the electrons drift to the backplane of the detector with velocity $v_e = \mu_e \cdot E$, while the holes drift to the p^+ strips with velocity $v_h = \mu_h \cdot E$. Since in silicon $\mu_e \approx 3 \cdot \mu_h$, the resulting signal is made of a fast component due to the electrons and a slow component due to the holes. As a consequence, the duration of the current signal induced in the strips is equal to the hole collection time. For a 300 μm thick detector biased at 1.5 times the full depletion voltage, the collection time for the holes is approximately 25 ns, but half of the charge is collected within the first 5 ns [5].

As electrons and holes drift in the depletion region, they also diffuse sideways, resulting in a charge cloud at the collection surface of the order of 5-10 μm wide. Depending on the pitch of the strips and on the angle at which the particle traversed the detector, the holes may drift to one or more strips, giving possibly rise to groups (clusters) of contiguous firing strips.

The collection of holes or electrons appears as a current pulse on top of the leakage current; the integration of this pulse signal equals the total charge deposited in the silicon, which is proportional to the energy deposited by the ionizing particle. To have good detection efficiency, the reverse bias voltage should be high enough to completely deplete the $p^+ - n$ junction from majority carriers, in order to minimize the probability of recombination between the electrons (or the holes) generated by the ionizing particle and the free carriers in the silicon bulk.

3.4 The Front–end VLSI circuits

A binary readout scheme, in which only the digital information (hit/no hit) is stored for each strip, has been designed with the aim of limiting the amount of data coming from the 13824 strips of the two MD planes.

Each strip of the MD is connected to a readout chain based on two full-custom VLSI chips. The analog signal generated by the charge released by a ionizing particle traversing a strip is transferred via aluminum-on-glass fanouts to the input of the first VLSI chip, named FABRIC [6], which preamplifies, shapes and discriminates the input signal giving a digital output signal. The output signal of the FABRIC is sent to the second VLSI chip, called CDP [7], which is a clock driven digital buffer, providing the storage of the information in the trigger latency period (about 1 μs).

These two VLSI chips are located on the BOARD, close to the silicon detectors, and therefore they must be very compact and have narrow channel pitch (50 μm), low–power consumption (so that on-BOARD cooling could be avoided) and be radiation resistant. The radiation resistance requirement is due to the fact that these chips operate at few cm distance from the beam axis and therefore they are exposed to high levels of radiation, resulting in a ionizing radiation dose of more than 200 krad and displacement damage equivalent to 1 MeV neutron fluence of more than $5 \cdot 10^{11}$ eq. neutrons/cm^2 during two months of data taking with Pb beam [8]. Both chips provide test–mode operation, allowing full test and calibration of the system.

3.4.1 The FABRIC analog chip

The FABRIC is a 64 channel chip specifically designed for the binary readout of silicon strips fulfilling the requirements of the NA50 experiment, which call for an exceptionally fast front–end electronics.

In particular, given the high foreseen rates of $\sim 10^7$ beam particles/s which, combined with a target thickness of $18\% \cdot \lambda_I$, lead to $\sim 2 \cdot 10^6$ interactions/s, the dead time and the time resolution result to be of primary importance for the front–end electronics. Regarding the dead time, the design aimed at a value below 50 ns, based on the maximum the experiment can tolerate as loss of events for pileup protection [4]. The goal for the time resolution was to keep the time walk (difference between the discriminator output delays for different amplitude input signals) below 8 ns, to guarantee that no losses occur in the digital buffer which works at a frequency of 50MHz [7]. Moreover, to have good detection efficiency, a signal/noise ratio of 20 for minimum ionizing particles for an input capacitance of 5 pF is required. Other fundamental issues are the radiation resistance and the limited power consumption, which should stay below 100 mW per chip (i.e. 1.5 mW/channel) to avoid the installation of cooling devices.

Taking into account all these demanding requirements, the bipolar (Tektronix [9]) technology was chosen for the FABRIC design. The chip has an area of 4 mm $\times$ 3.2 mm. Each channel has a pitch of 42 μm and treats the signal of one strip of the detector. Therefore, each FABRIC can treat the data of 64 strip elements, so 216 FABRICs are necessary to serve the 13824 channels of the MD.

The working scheme of the FABRIC is shown in fig. 3.6. The analogic signal from the strip is amplified by a preamplifier in the configuration of

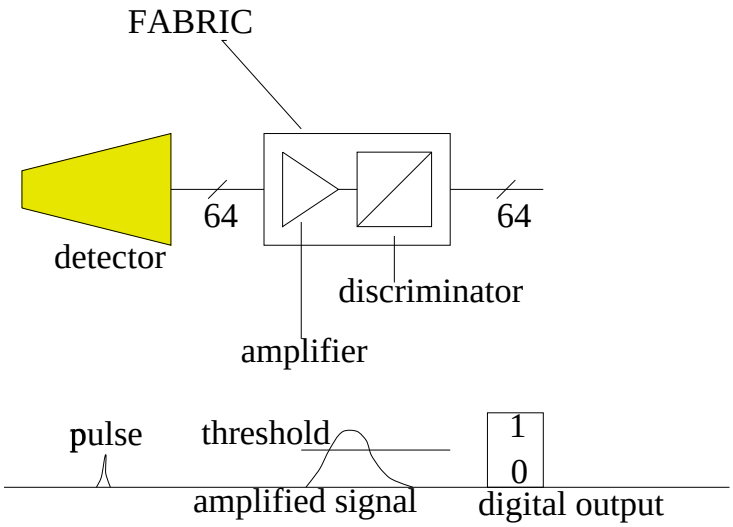

Figure 3.6: *Scheme of the FABRIC.*

a transimpedance amplifier, giving an output signal which is successively shaped by an integrator circuit and discriminated. In this way a output signal in a current mode is obtained each time the voltage produced by the preamplifier is above the discrimination threshold.

The basic parameters of the FABRIC were measured during the test period, obtaining the values reported in table 3.3 which resulted to satisfy the design requirements [6].

Parameter	**Value**
Equivalent noise charge (electrons)	$476+63 \cdot C_{in}$ (pF)
Time walk (for input signals 2 fC <Q< 8 fC)	5 ns
Dead time (for two 4 fC signals)	42 ns
Gain	100 mV/fC
Spread of gain values	5%
Spread of the threshold values	2.4%
Power consumption	1.3 mW/channel

Table 3.3: *Basic parameters of FABRIC operation.*

3.4.2 The CDP digital chip

The digital chip CDP [7] is a Clock Driven Pipeline, i.e. a digital data buffer that stores the data during the trigger latency period ($\sim 1\mu$s) and then sends it asynchronously to the data acquisition system.

It is a 81 column, 64 row RAM memory realized in 0.8 μm CMOS technology. Each row reads and stores the data from one FABRIC channel, which is 0 if no particle hit the strip and 1 if the strip was hit. Therefore, each CDP can store the data of 1 FABRIC (64 strips), so 216 CDPs are necessary to serve the whole MD.

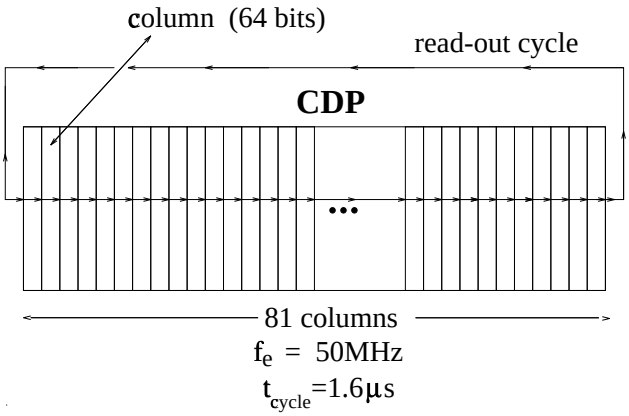

Figure 3.7: *Scheme of the CDP.*

The CDP functions logically as a storage pipeline, its functional diagram is shown in figure 3.7. A column pointer is driven by a 50 MHz clock so that at every clock cycle (=20 ns) the CDP reads the hit pattern from the output of the FABRIC, writes the data in that column and then points to the next column. After 80 clock cycles (=1.6 μs) the CDP overwrites the first column. When the CDP receives a trigger signal, writing is disabled and the hit-pattern of the appropriate column is read back and transmitted to the data acquisition system. Additionally, the chip provides a "timestamp" consisting of the pipeline column being read-out, which is sent to the data acquisition system together with the data and which is useful as a debugging utility for system timing.

To properly operate, the CDP must receive four control signals, encoded into a command word CMD[3:0], along with the clock and the bus interface.

The command word specifies the actions the chip will execute on the clock cycle following its receipt and determines how data will be dealt with.

The distribution of the main power supply of the CDPs (V_{DD}) has been designed in such a way that there are three V_{DD} lines ($V_{DD_{123}}$, $V_{DD_{456}}$ and $V_{DD_{789}}$) for MD1 and three for MD2, therefore each V_{DD} line supplies the power to 36 CDPs.

The prototypes used for the first tests were processed at Hewlett-Packard through the MOSIS facility and they were not made using radiation hardened technology. After some changes in the design, mainly meant to ensure radiation resistance, the CDP for the data taking were produced by Honeywell using their 0.8 μm, three-metal rad–hard process. The external dimensions of the Honeywell chips are 3.2 x 2.95 mm^2, and they are guaranteed for radiation dose levels up to 1 Mrad. Of the 216 CDPs used during the 1996 data taking (the one corresponding to the largest fluence), 5 were HPMOSIS prototypes and the other 211 were Honeywell radiation-hardened CDPs. In the successive data taking periods, no HPMOSIS prototype has been used.

3.5 The BOARD and the EXTCARD

The BOARD is a multilayer printed circuit acting as a support on which are placed one silicon detector, the front-end electronics and electrical components, such as filter capacitors and other surface mounted components, as well as signal and power lines. The BOARD1 (see fig. 3.8) holds the inner crown detector, which is divided in 256 strips (128 for each of the two 10^o sectors), so that the front–end electronics for a BOARD1 is constitued of 4 FABRIC analogic chips and 4 CDP digital chips. The BOARD2 (see fig. 3.9) holds the outer crown detectors which have only 128 strips and therefore only 2 FABRICs and 2 CDPs are necessary. Both types of BOARDs have been designed in Torino and produced at CERN. The detectors and the chips are stuck on the BOARD using radiation–resistant glues.

The detecting strips are connected to FABRIC channels by means of fanout aluminum lines realized on a 300 μm thick glass support; the connections between strips and fanout lines and between fanout lines and FABRIC channels are provided by micro–bondings.

The BOARD1 is placed on top of a BOARD2 and fixed to it with precision pins. Each BOARD1 is connected to the underlying BOARD2 via a set of three short kapton cables inserted into surface–mounted connectors

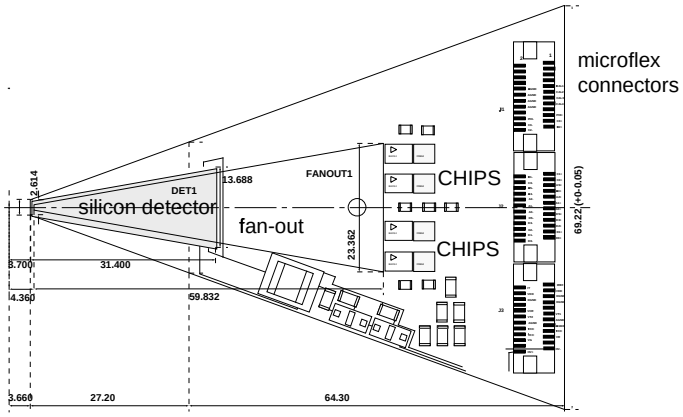

Figure 3.8: *Scheme of the BOARD1.*

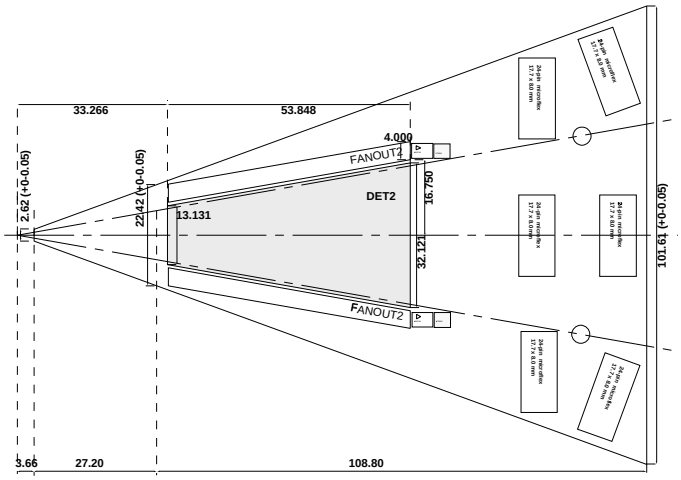

Figure 3.9: *Scheme of the BOARD2.*

(MICROFLEX from DuPont). The BOARD2 is then connected to the external distribution card (EXTCARD) via a set of three long kapton cables and surface–mounted connectors.

The EXTCARD, whose geometrical layout is shown in fig. 3.10, is used to:

- collect the data of all the CDPs and send them to the data acquisition

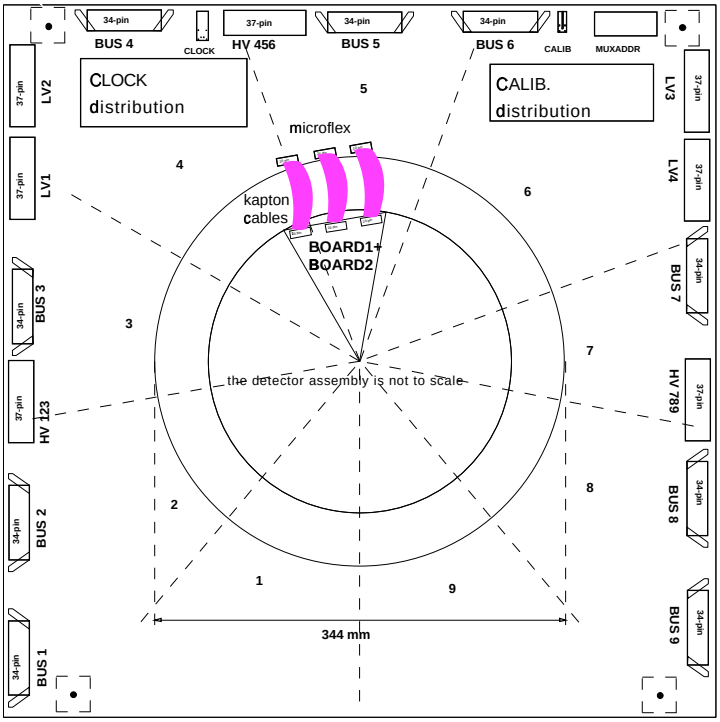

Figure 3.10: *Scheme of the EXTCARD.*

- distribute the high and low voltages of the detectors and of the chips
- distribute command, control and calibration signals
- distribute the clock signal

Practically, the BOARD2 relays all the signals from the overlying BOARD1 to the EXTCARD, which provides the interconnections with the data acquisition system. On the contrary, the power supply voltages and the control signals distibuted by the EXTCARD are relayed to the BOARD1 by the underlying BOARD2.

3.6 The readout chain

The readout chain of the MD consists in two full-custom VME modules (BUSIF and CCTD) and a commercial memory device (B016 from INMOS).

The BUSIF and the CCTD modules are placed in one double–depth VME crate located in the experimental area a few meters away from the detector units, while the B016 modules are placed in the counting room ($\approx$ 80 m distant from the experimental area).

Each of these modules contains a transputer which is a microprocessor featuring a local memory and four high bit–rate (10-20 Mbits/s) transmission lines, named links. The MD readout chain is therefore based on a transputer network: the communication among BUSIF, CCTD and B016 occurs via transputer links and not via the VME protocol. A block diagram of the MD readout chain is shown in fig. 3.11

When the system is in acquisition mode, the data of the MD are written on the CDP columns: at each clock cycle (=20 ns) a column is written and then the pointer steps on the successive column; after 80 clock cycles a column is overwritten. When the BUSIFs receive the trigger signal from the CCTD, they send to the CDPs the command of disabling acquisition, so that the columns of each CDP are ready to be read back.

The binary data of the appropriate column is sent from the front-end electronics through 5 m cables to the BUSIFs, which are memories used to store the data during the burst (up to 5000 events). Each BUSIF is divided in three slots (A, B and C) and each slot collects the data of 12 CDPs (i.e. six BOARD1+BOARD2 couples), so 6 BUSIFs are necessary to store all the data of the two MD units. A code in the range 1-12 is hard wired on each CDP, so that the 12 CDPs on the same BUSIF slot are identified by hardware with a 4-bit code, which constitutes the address of the chip.

At the end of the burst, the BUSIF transmits via optical links the data of the whole burst to the B016 modules which collect the data of the 6 BUSIFs and make them available for writing on tape.

The CCTD module generates the clock signal that drives the CDP operation and provides the calibration signals and the proper synchronization of the trigger signals.

3.6.1 The BUSIF module

The BUSIF (BUS Interface), developed at L.A.P.P. (Annecy) specifically for the NA50 experiment, is the interface between the front–end electronics of the MD and the transputers of the data acquisition system [10].

The BUSIF provides the read and write commands to the digital chips (CDPs) and collects from them the data. The data of a single CDP are

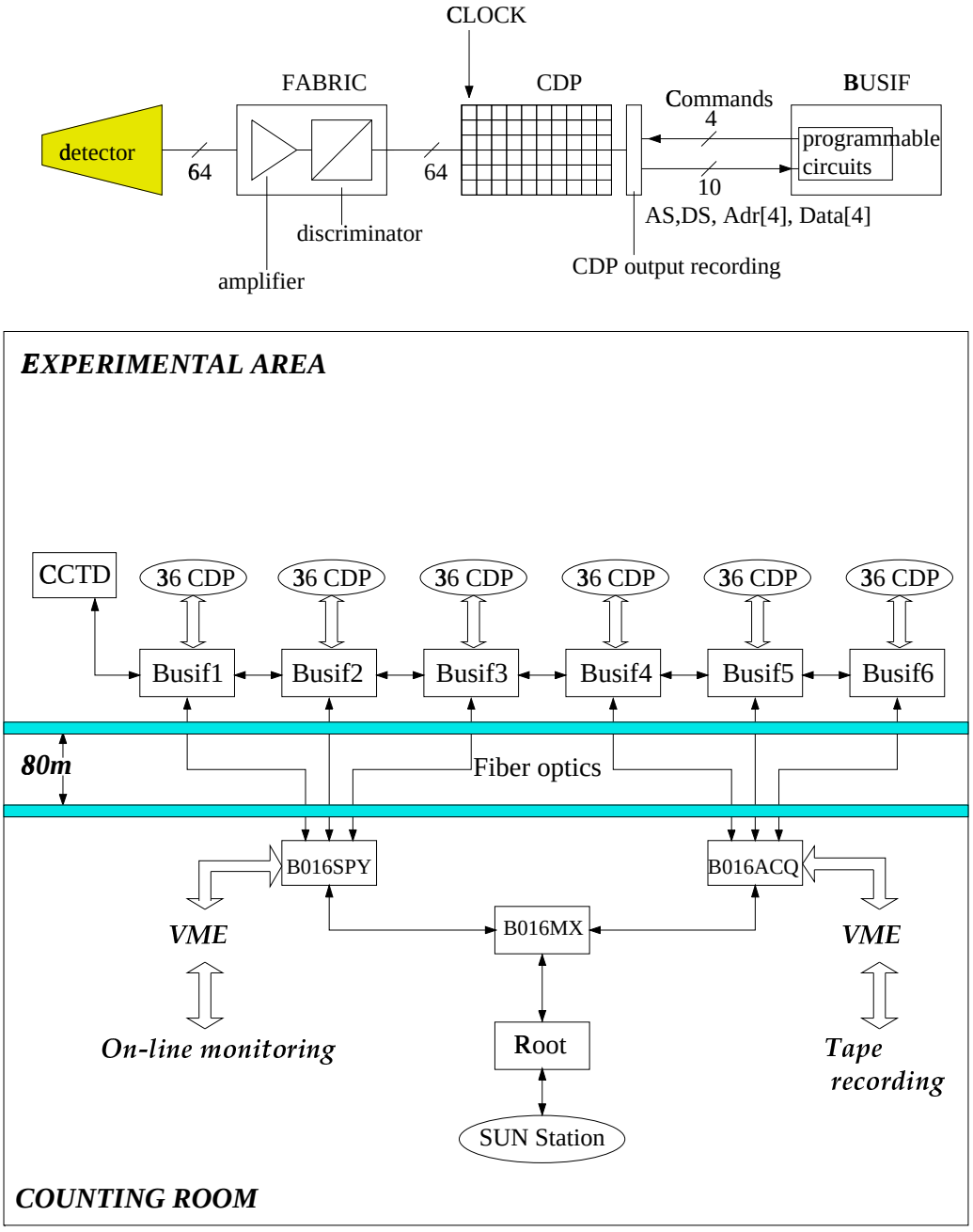

Figure 3.11: *Block diagram of the MD read–out chain.*

grouped for each event in three words: two of them are 32-bit words containing the digital outputs of the 64 channels of the FABRIC, while the third one (named "timestamp word") is a 12-bit word containing the address of the CDP (4 bits), the number of the CDP column from which comes the data (7 bits), ans the information about the quality of the data transmission (1 bit). The timestamp word is stored in separate fast memories located in the BUSIF and is analyzed on–line by means of a filter algorithm which provides a 1 bit flag (named "time-out flag") used to validate the data of each CDP. In this way, the timestamp word information is compressed into 1 bit, thus reducing the data volume and the time needed for data transfer.

The BUSIFs are connected to the EXTCARD via 5 m long twisted pair cables for the control and bus signals, and to the CCTD from which they receive the trigger signal of the experiment. Each BUSIF module is dedicated to 12 CDPs and provides enough FIFO storage for a whole burst. The 6 BUSIF are numbered from 1 to 6; BUSIFs 1, 2 and 3 serve the CDPs of MD1, while BUSIFs 4, 5 and 6 serve the CDPs of MD2.

3.6.2 The CCTD module

The CCTD module (Calibration, Clock and Trigger Distribution) has been developed by INFN Torino, and it is used for the following purposes:

- generate a clock signal of frequency f_e (variable from 391 kHz to 50 MHz) which is responsible for the incrementation of the column pointer in the CDP;
- provide the calibration signals to the FABRIC;
- relay to the BUSIFs the trigger signal that it receives from the general trigger system of the experiment.

The clock signal is sent to each EXTCARD where it is translated from the ECL standard to the non–standard levels needed by the digital chip and distributed to each of the 18 BOARD1+BOARD2 couples.

The amplitude of the calibration signal is expressed in terms of fraction of charge released in the detector by Minimum Ionizing Particles (MIP): the equivalent charge of 0.5, 1.0 and 1.5 MIP can be sent to the FABRIC input.

The trigger signal of the experiment should be appropriately delayed before sending it to the BUSIFs, so that the data transmitted by the CDPs are

read back from the column in which the signals generated by the particles produced in the Pb–Pb interaction which triggered the NA50 apparatus were written.

The clock frequency, the amplitude of the calibration signals and the delay applied to the trigger signal can be controlled by the T425 transputer mounted on the CCTD module.

3.6.3 Data synchronization

The read–out chain must be exactely synchronized to read the appropriate column of the RAM memory of the CDP. A scheme of the read–out synchronization is reported in fig. 3.12.

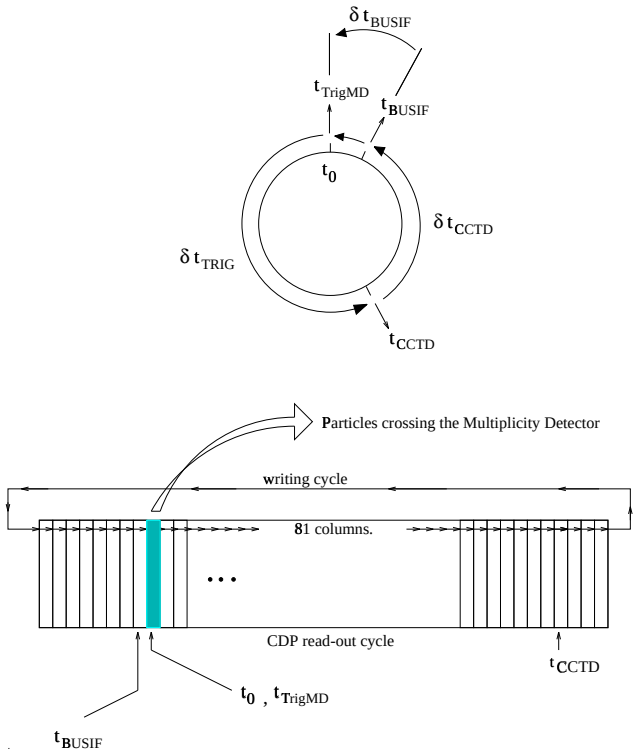

Figure 3.12: *Scheme of the read–out synchronization.*

Since the CDP has been designed in such a way that only the data of the column where the pointer is positioned can be read back, a time interval of 80 clock cycles (i.e. 1.6 μs for a clock frequency of 50 MHz) should pass

between the writing of the data and the reading back of the data. Therefore, if the products of the collision cross the MD at $t = t_0$, the trigger signal should arrive to the CDPs at the time $t_{trigMD} = t_0 + 1.6\mu$s.

The generation of the T0J trigger signal defined by the hodoscopes R_1, R_2, R_3 and R_4 requires a time interval given by:

$$t_{gen} = t_{flight} + t_{R1} + t_{trig} \simeq 580ns$$

where:

- t_{flight} $\simeq$20 ns is the time of flight of muons between the target and the trigger hodoscopes;
- t_{R1} $\simeq$260 ns is the time between data output from R-hodoscopes and input to discriminators (including cables to the counting room);
- t_{trig} $\simeq$300 ns is the time between discriminators output and production of trigger signal in the counting room.

Successively, a time interval t_{send} $\simeq$356 ns is needed to bring the signal via an 80 m long optical fiber from the counting room to the CCTD which is located downstairs in the experimental area. Therefore the trigger signal arrives to the CCTD at the time :

$$t_{CCTD} = t_0 + t_{gen} + t_{send} = t_0 + \delta t_{trig}$$

The time interval $\delta t_{trig} \approx 1000$ ns between the passage of the particles in the MD and the moment when the signal arrives to the CCTD is called trigger latency period. The trigger signal is then delayed in the CCTD for a programmable time interval δt_{CCTD} and successively distributed to the BUSIFs which receive the trigger signal at the time:

$$t_{BUSIF} = t_{CCTD} + \delta t_{CCTD} = t_0 + \delta t_{trig} + \delta t_{CCTD}$$

After another delay of about 20 ns (δt_{BUSIF}) the trigger signal is sent to the CDPs where it stops the sampling of the FABRICs output. As a consequence δt_{CCTD} should be fixed to have:

$$t_{TrigMD} = t_0 + \delta t_{trig} + \delta t_{CCTD} + \delta t_{BUSIF} = t_0 + 1.6\mu s$$

In practice, the programmable time interval δt_{CCTD} is fixed (and periodically verified) on the basis of data collected in "delay scan" runs.

3.6.4 The B016 card

The B016 card is a commercial VME module featuring a T800 transputer and 16 Mbytes of RAM memory. It is used to interface the transputer network with the VME bus. At the end of each burst, the data stored in the BUSIF is transmitted to the B016 via the optical fibers connecting the respective transputers. Other parameters, such as the burst number, the event number, the trigger type, are added to the data of each event. Two B016 modules (named B016SPY and B016ACQ) are used to serve the 6 BUSIFs: the B016SPY collects the data from BUSIFs 1, 2 and 3 (MD1), while the B016ACQ collects the data from BUSIFs 4, 5 and 6 (MD2). A third B016 card (B016MX) is used for the data exchange between B016ACQ and B016SPY, so that the B016ACQ data are copied in the memory of the B016SPY and vice versa. After this operation each B016 module holds the data of the two MD planes for all the events of the burst. The data of the B016ACQ are sent via the VME bus to the tape recording system, while the same data, present on the B016SPY, are available for the on–line monitoring of the detector operation.

3.7 Power supply

The power is supplied to the detectors and to the chips by means of a CAEN SY527 mainframe which is located in the experimental area a few meters away from the detector units and which can host up to 10 modules for low or high voltage power supply. The whole system can be remotely controlled from a PC located in the counting room.

The low voltage power is supplied to the chips by means of A516 plug–in modules. Each module is composed of 8 channels at 12 V, 1.5 A. Two A516 modules are needed to supply the power to the chips of a single MD plane. The high voltage power is supplied to the detectors with A520 plug–in modules, each of them composed of 16 channels at 200 V, 1 mA. Each detector is biased independently by a single channel of the A520 module, so that three A520 modules are necessary to supply the power to the 36 detectors of a single MD plane. Therefore to power the two MD planes 6 HV modules (A520) and 4 LV modules (A516) are needed.

3.8 On–line monitoring

The data acquired by the Multiplicity Detector can be continuously monitored on–line to check the quality of the system operation and the efficiency of the detector strips and of the read-out chain. The on–line monitoring is based on a C++ program running on a MVME2604 card featuring a PowerPC microprocessor and a 32 MB memory. This program reads the data from the B016SPY card and organizes it in histograms displaying the main characteristics of the system performance:

- The hit-maps of the detectors and the multiplicity distributions (used to control the efficiency of the strips)
- The number of "time-out" events for each CDP, which gives information about its efficiency
- The distribution of the MD-TDC, which measures event-by event the time interval between the NA50 trigger signal and the beginning of the clock-cycle when the CDP columns are read back, in order to correct off–line for possible variations of sampling efficiency.
- The Trigger type distribution and the ZDC spectrum.

Bibliography

[1] B. Alessandro et al., Nucl. Instr. and Meth. A360 (1995),189.

[2] S. Beolè, Ph.D. thesis, Università di Torino, 1998.

[3] ATLAS Inner Tracker Technical Design Report, vol. 2, CERN/LHCC/97-17, p. 394.

[4] Study of Muon Pairs and Vector Mesons Produced in High Energy Pb-Pb Interactions, Proposal CERN/SPSLC 91-05, SPSLC/P 265, October 1991.

[5] W. Dabrowski and M. Idzik, Technical Note RD20/TN/15, CERN, 1993.

[6] W. Dabrowski et al., Nucl. Instr. and Meth. A350 (1994) 548.

[7] Joel DeWitt, A pipeline and bus interface chip for silicon strip detector read–out, Internal Note, SCIPP, Santa Cruz, CA.

[8] B.Alessandro et al., Observation of radiation induced latchup in the readout electronics of NA50 multiplicity detector, presented by F.Prino at F2K conference, to be published on Nucl. Instr. and Meth. A.

[9] Tektronix INC., Beaverton, OR 97077.

[10] V.Capony, Ph.D. Thesis, Savoy University, Annecy-Le-Vieux Cedex, France (1996).

Chapter 4

Event reconstruction and selection

The NA50 experiment acquires data using two different types of trigger: the Minimum Bias (MB) trigger and the dimuon (2μ) trigger, collected simultaneously and independently. While all the events which fulfill the 2μ trigger requirements are recorded on tape, the MB events are prescaled by a factor which brings their rate down to 10% of the total number of recorded events.

The Raw Data Tapes written by the acquisition system are read and processed off-line by means of a specific program, named DIMUREC [1], which extracts the interesting physical variables from the recorded detector signals.

Depending on the trigger type, different reconstruction and selection algorithms are applied to the data. For dimuon events, DIMUREC reconstructs the tracks of the muons and provides all the useful information on the related kinematic quantities, on the interaction vertex and on the response of all the detectors of the experimental apparatus. For MB events, muon track reconstruction is not done and only the information from beam detectors (BH, BHI, antihalo...), target detectors and centrality detectors (the Multiplicity Detector, the Electromagnetic Calorimeter and the Zero Degree Calorimeter) is used. The reconstructed variables for dimuon events with at least 2 fully reconstructed muon tracks ($\sim 35-40\%$ of all 2μ triggers) and for all MB events are written to "μDST" (micro Data Summary Tape) for later analysis.

4.1 Dimuon reconstruction

4.1.1 Muon tracks reconstruction

The tracks of the muons detected by the NA50 spectrometer are reconstructed by associating for each muon two track "segments" defined from the hits in two sets of MWPCs. The first segment is defined by the four MWPCs located downstream of the magnet ($PC_5 - PC_8$), for which the number of hit wires is smaller because the magnet sweeps away the low momentum particles emerged from the absorber. The second track segment is reconstructed by the four MWPCs ($PC_1 - PC_4$) placed upstream from the magnet. The association of the two segments is done according to particular criteria of deflection angle and of relative distance and allows to calculate the kinematical quantities related to each muon [2]. Each reconstructed track is then validated by hits in the corresponding scintillators of hodoscopes R_1-R_4.

4.1.2 Muon tracks selection

The two reconstructed muon tracks which constitute the dimuon are then selected according to the following criteria [3]:

- **Fiducial cut**: the tracks crossing the iron supports of the magnet coils are rejected as well as the tracks crossing inefficient regions of the chambers.

- **Image cut**: it consists in the rejection of all the events which would have not been accepted if at least one of the detected muons had the opposite charge. This selection is aimed at getting rid of the systematic effects due to the magnetic field, so as to ensure that the spectrometer acceptance is the same for positive and negative tracks.

- **Global cut**: it is used to select only the muons coming from the target region. The tracks not pointing to the target, which would be reconstructed with wrong values of the kinematic variables, are rejected. This cut operates, event by event, on the χ^2 probability of the $p \times d_{targ}$ variable [4]. The quantity d_{targ} is the distance from the beam axis of the intersection point of the reconstructed muon track with the target plane. This distance d_{targ} is sensitive to multiple scattering in the absorber which depends on the muon momentum p ($d_{targ} \propto 1/p$). A

cut on d_{targ} variable would therefore introduce a bias because it would affect differently tracks with different momenta: for this reason the product $p \times d_{targ}$ is used. The cut level varies for different samples between 1% and 18% on the value of Prob(χ^2).

4.1.3 Kinematical cuts

After assigning the vertex of the muon tracks to the center of the identified sub-target, DIMUREC performs the calculation of the interesting kinematical parameters, which are mainly the invariant mass $M_{\mu\mu}$, the rapidity y, the transverse momentum p_T and the polar and azimuthal angles in the Collins-Soper reference frame [5] (θ_{CS} and ϕ_{CS}).

In order to eliminate dimuons coming from regions where the spectrometer acceptance is very small, a further selection, based on kinematical variables, is performed on the data. Since the acceptance of the apparatus is nearly constant all over the p_T and ϕ_{CS} range, the kinematic selection is done on rapidity and θ_{CS} by requiring:

$$2.9 < y_{lab} < 3.9 \qquad -0.5 < \cos\theta_{CS} < 0.5$$

where y_{lab} is the muon rapidity in the laboratory system. If expressed in terms of rapidity in the center-of-mass reference frame (y^*) at 158 GeV/nucleon beam energy, the accepted rapidity range would be $0 < y^* < 1.0$.

4.2 Multiplicity reconstruction

The Multiplicity Detector (MD) is made up of two identical planes of silicon detectors (namely MD1 and MD2, placed respectively 11.65 cm and 20.90 cm downstream of the target in the 1998 setup) and therefore it allows to define particle "tracklets" by matching the hits recorded on each of them.

The track reconstruction (see figure 4.1) is based on "correspondences" between MD1 and MD2 strips. A correspondence defines in which strip (or range of strips) of MD2 one expects to detect the signal of a particle that has been produced in the target and has traversed a selected strip on MD1. A list of such correspondences for all the MD1 strips is called Strip Correspondence Map (SCM). A SCM can be easily built by means of geometrical calculations based on tracks (lines) starting from the target and passing through the two MD planes.

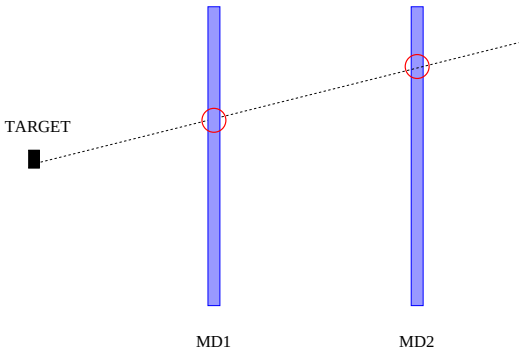

Figure 4.1: *Scheme of the geometry of target and MD.*

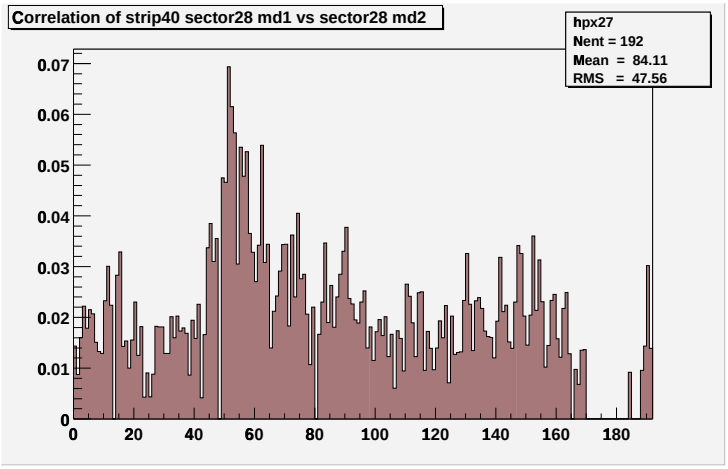

Figure 4.2: *Hit map on a MD2 sector (n.28) when a MD1 ($n_1 = 40$) selected strip has fired.*

It is also possible to obtain a SCM from the experimental data. This is accomplished by selecting a strip (n_1) on MD1 and analyzing the hit map of the corresponding azimuthal sector on MD2 for the events in which the n_1 strip is firing. A typical example of such an hit map is plotted in figure 4.2 where it is possible to distinguish, over a flat distribution of strips with relatively small occupancy of about 1.5%, an approximately gaussian peak given by a group of $\sim 8 - 10$ strips with higher occupancy. This peak can be interpreted as due to the big amount of particles coming from the target:

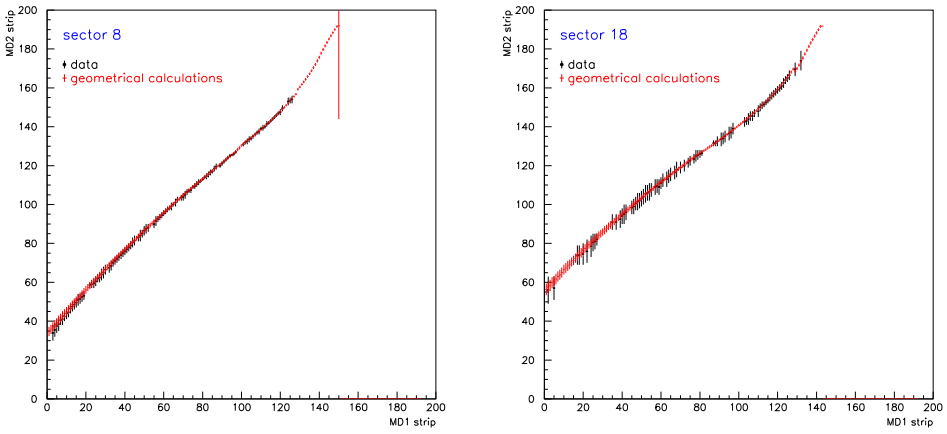

Figure 4.3: *Correspondences between strips on MD1 and MD2 for particles coming from the target for two azimuthal sectors.*

a particle produced in the target, after traversing the n_1 strip, gives a signal on one of the MD2 strips inside the peak, which, therefore, can be considered as the region which is in correspondence with the selected strip n_1 on MD1.

The comparison between the SCMs obtained from the geometrical calculations and the one extracted from the experimental data for two azimuthal sectors is shown in the plots of figure 4.3, where on the x-axis the selected strip on MD1 is reported, and on the y-axis, the corresponding range of strips on MD2 for particles coming from the target. It can be seen that the agreement between the two SCMs is very good. This agreement was obtained after an optimization of the beam offset in the transverse plane, resulting in a most probable offset in the vertical direction of +1 mm for 1998 (+2 mm for 1999).

On the basis of these strip correspondences, a track can be defined as a matching pair of firing channels on MD1 and MD2. In other words, when a MD1 strip and one of the corresponding strips of MD2 are simultaneously on, a "tracklet" is identified. The charged multiplicity is then calculated event-by-event as the number of detected tracks. Three different multiplicity variables are defined by counting the tracks in different angular (pseudorapidity) ranges:

- **MDMUL1**: charged multiplicity per 10^o sector in the pseudorapidity range $2.8 < \eta < 3.7$ (approximately coincident with the spectrometer acceptance window)
- **MDMUL2**: charged multiplicity per 10^o sector in the pseudorapidity range $2.3 < \eta < 2.8$
- **MDMUL3**: charged multiplicity per 10^o sector in the pseudorapidity range $1.15 < \eta < 2.3$ (within the acceptance of the electromagnetic calorimeter); this variable in the subrange $1.15 < \eta < 1.52$ is based only on hits on MD1 for a lack of geometrical coverage by MD2.

These three variables are calculated event-by event by averaging over the 36 azimuthal sectors, excluding, for all the events, sectors with many bad channels (inefficient or noisy strips) and, for single events, sectors for which in the event under analysis the number of firing strips is more than 2.5 standard deviations away from the mean number of hits on the other sectors.

4.3 Event selection

4.3.1 Run selection

The acquired data are written on tape in samples of events, called runs. During the whole 1998 data taking period ≈ 700 runs were collected, each of them consisting of ≈ 350000 events and corresponding to a period of data acquisition of $\approx 1 - 1.5$ hours. Runs characterized by bad beam quality (e.g. huge fluctuations in the beam intensity), hardware problems or other anomalies in the detector performance are rejected off-line.

4.3.2 Beam cleaning cuts

The selection criteria meant to reject events with possible biases on the projectile ions are called beam cleaning cuts. In particular, the following set of cuts is usually applied [3]:

1. **Pile-up rejection**: it is intended to get rid of the events with two or more ions arriving so close-in-time that the detectors can not resolve them. It is defined by requiring that one and only one incident ion is detected by the BH within the 20 ns gate opened by the trigger signal.

2. **Parasitic interactions rejection**: this cut is applied to remove all the events in which the Pb projectile underwent an interaction in the BH. Such events are identified on the basis of the signals in the BHI, BHINEW and BAH detectors.

3. **Beam halo rejection**: in order to eliminate the Pb ions which are far from the beam axis and also the ones which have undergone an interaction upstream from the target (between the BH and the target), events for which a signal is present in the anti-halo detectors are rejected.

4.3.3 Cut on the correlation between E_T and E_{ZDC}

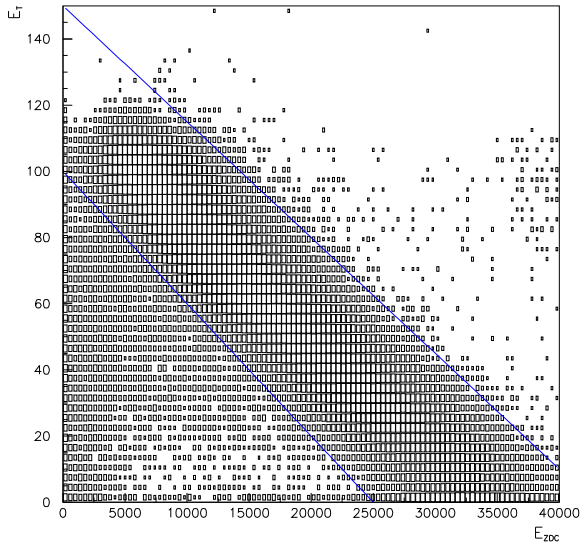

Figure 4.4: *E_T versus E_{ZDC} for 1998 dimuon data sample after the application of the beam cleaning cuts.*

After the application of the beam cleaning cuts, the correlation between E_T and E_{ZDC} appears like the one shown in figure 4.4. For most of the events the measured values of the two centrality variables are located inside a correlation band defined by the two lines superimposed on the plot, but there are also events out of this band.

It is expected that, in nucleus-nucleus interactions, the transverse energy (proportional to the number of participant nucleons N_{part}) and the forward energy (which scales as the number of spectators) are correlated. Therefore, the Pb-Pb interaction events should stay inside the diagonal band region, while the events out of this correlation band are affected by some kind of bias and should be rejected. In fact, these events are mostly due to Pb-air interactions and to residual pile-up (i.e. events characterized by the superposition of the signals of two projectile ions which are not rejected by the cut based on the BH signals).

A cut on the correlation between E_T and E_{ZDC} is applied in order to select the events which stay inside the diagonal band defined by the two lines superimposed on the plot in figure 4.4.

4.3.4 Special MD pile-up rejection

Since the dead time of the MD (≈ 42 ns) is higher than the BH time window used to define pile-up, an additional cut is needed to avoid "MD pile-up", i.e. to exclude the events whose measured multiplicity results from particles generated by more than one ion. In order to eliminate this pile-up contamination, a very severe cut on the TDCs of the BH has been developed, but it turned out that with such a selection too many good events were rejected. Hence, similarly to what it is done for the E_T-E_{ZDC} correlation, a cut on the correlation between the measured multiplicity and the transverse energy E_T has been developed with the aim of rejecting "MD pile-up" events.

In Pb-Pb interactions, multiplicity and transverse energy should be correlated, because both of them are expected to be proportional to the number of participant nucleons. On the contrary, in the case of MD pile-up, there would be on the multiplicity detector a superposition of the hits of the particles produced by two or more ions and consequently the measured multiplicity would result to be larger and uncorrelated with the transverse energy. Events for which the multiplicity and the transverse energy are uncorrelated are therefore rejected by means of a cut on the distribution of MDMUL1 as a function of E_T, as shown in figure 4.5. This cut rejects also events with very small MDMUL1 and $E_T > 20 - 25$ GeV which are probably due to inefficiencies of the MD detector or to badly-synchronized data read-out.

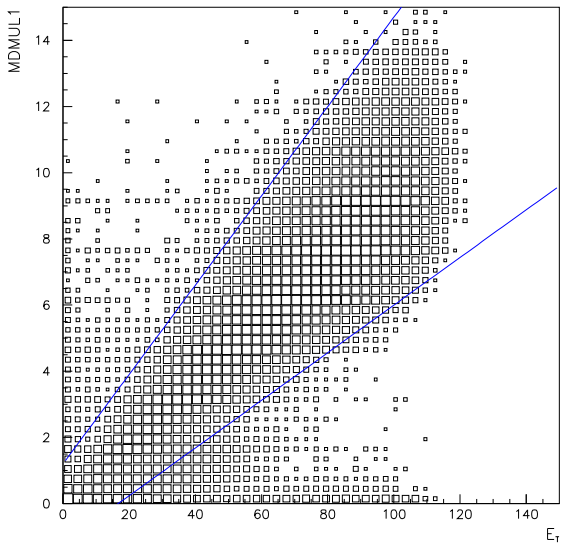

Figure 4.5: *Multiplicity measured in the spectrometer pseudorapidity region versus E_T for 1998 dimuon events after the application of the beam cleaning cuts and of the cut on the $E_T - E_{ZDC}$ correlation.*

4.4 Target identification

The usual target identification system is based on the quartz blades located downstream of each subtarget and allows to identify, both for dimuon and MB events, the subtarget where the primary interaction has taken place. The interaction is assigned to a certain subtarget if the signals in both the correspondent quartz blades are above a fixed threshold [2, 6]. The threshold is fixed so as to separate the interacting events from the peak at lower signal amplitude due to the δ rays produced in the target.

The efficiency of this identification is strongly dependent on the centrality of the collision (i.e. on E_T). In the case of peripheral Pb-Pb collisions (low E_T), few particles are produced in the interaction and consequently the signal induced in the quartz blades could be so small that it would not pass the threshold, causing a loss of efficiency. On the other hand, if events where only one of the two blades gave a signal over the threshold were also accepted, the statistics of dimuon events would increase by $\sim$ 20% [7] (not enough

to recover completely the loss of peripheral events), but a possible bias in the target recognition could be introduced by fluctuations of the signal in a single blade. Furthermore, it is not possible to distinguish a Pb-Pb in target interaction from a Pb-air interaction occurred slightly upstream the target and central enough to induce in the quartz blades a signal over the threshold.

Most of this off-target contamination can be rejected by means of the cut on the correlation between E_T and E_{ZDC}, which therefore serves also as a target selection cut. The use of the cut on the $E_T - E_{ZDC}$ correlation alone for target identification, in alternative to the method based on the quartz blades, has also the advantage that it allows to recover the target identification efficiency for peripheral events [8].

4.4.1 Vertex reconstruction with the Multiplicity Detector

For the 1998 (single target) data sample, an independent method of target recognition, based on the data recorded by the multiplicity detector, has been developed, with the aim of recovering the target identification efficiency for the peripheral events and of eliminating the Pb-air contamination.

The interaction vertex is reconstructed by means of an algorithm based on a statistical approach, consisting in the calculation of the likelihood of a certain hypothesis about the place where the interaction took place. In particular, four hypotheses are taken into account:

0) Pb-Al interaction in the target box entrance window ($\approx$ 66.5 cm upstream from the target)

3) Pb-air interaction $\approx$ 2.5 cm upstream from the target

4) Pb-Pb interaction in the target

5) Pb-air interaction $\approx$ 2.5 cm downstream of the target

For each of these four hypotheses a different map of strip correspondences has been built. Then, event by event, the number of tracks pointing to the interaction vertex being considered is counted according to the following procedure. A scan on all the MD1 strips is performed: if the selected strip is firing and if there is at least one good strip in the corresponding region on MD2, the number of possible coincidences (N_{pos}) is incremented by one.

The corresponding region of strips on MD2 is then analyzed: if one of these strips is firing, then the number of found coincidences (N_{track}) is incremented by one. The number of possible coincidences (N_{pos}) is therefore the number of firing strips on MD1 with at least one corresponding good strip on MD2, while N_{track} is the number of matching pairs of strips on MD1 and MD2, i.e. the number of detected tracks which has passed through the two MD planes.

If $N_{track} \leq 6$, the event is marked as non interacting. Otherwise, for each of the four hypothesis described above, a statistical estimator is calculated as:

$$est_n = \frac{N_{track}}{N_{pos}} = \frac{number\ of\ found\ coincidences}{number\ of\ possible\ coincidences} \tag{4.1}$$

where n=0, 3, 4 or 5 according to the corresponding hypothesis.

The largest of the four estimators is taken as the winning estimator. If the winning estimator is est_4, the event is a candidate in-target interaction, if est_3 or est_5 is the winner the event is a candidate Pb-air interaction, while if est_0 wins, the event is considered as a possible upstream (in the entrance window of the target box) interaction.

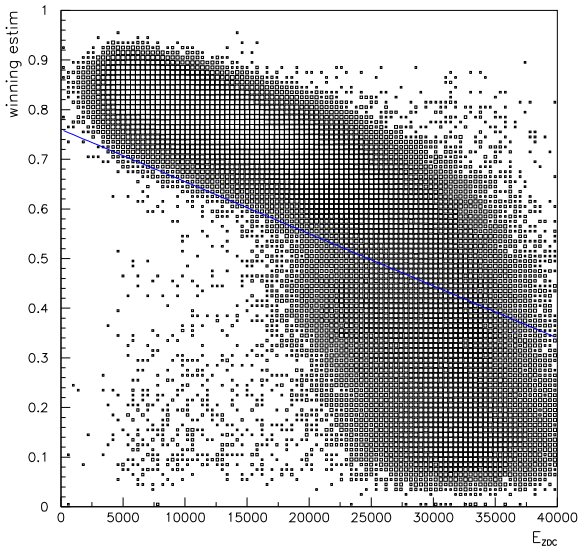

Figure 4.6: *Distribution of the winning estimator as a function of E_{ZDC}.*

Successively, a cut on the winning estimator as a function of centrality is

applied according to the line plotted in figure 4.6 which shows the winning estimator distribution as a function of E_{ZDC}. The slope of the line reflects the increase of the occupancy (i.e. of the number of found coincidences and consequently of the winning estimator) with increasing centrality. The events which stay below the line are marked as non-interacting ions which have produced few delta rays in air and in the target, giving thus rise to a small number of tracks (i.e. small values of the winning estimator). On the basis of this algorithm, a variable called NOCIMD has been defined according the criteria listed in table 4.1.

NOCIMD	**interaction**	**conditions**
0	Pb-Al $\approx$ 66.5 cm upstream	est_0 > all other estimators AND est_0 > threshold
3	Pb-air $\approx$ 2.5 cm upstream	est_3 > all other estimators AND est_3 > threshold
4	Pb-Pb in target	est_4 > all other estimators AND est_4 > threshold
5	Pb-air $\approx$ 2.5 cm downstream	est_5 > all other estimators AND est_5 > threshold
8	no interaction	$N_{track} \leq 6$ OR all estimators below the threshold

Table 4.1: *Definition of NOCIMD variable. The threshold is defined by the cut on the winning estimator as a function of E_{ZDC} plotted in fig. 4.6.*

The results obtained using NOCIMD for target recognition should be compared with the ones given by the usual variable (NOCIBI) based on the quartz blades system, in order to verify if the MD based algorithm guarantees a gain of efficiency for peripheral events. In figure 4.7 the E_T distribution of events from the Minimum Bias sample with NOCIBI=4 (interactions in target recognized by a pair of quartz blades) and NOCIMD=4 (interactions in target according to the algorithm based on MD data) is shown. It can be seen that, while at high E_T the number of in target events recognized by the two different algorithms is the same, at low E_T (peripheral events), the MD based method is much more efficient than the quartz blades.

The absolute efficiency of NOCIMD recognition as a function of centrality (E_T) has been evaluated by comparing the E_T spectra obtained for interacting events and E_T spectra for events tagged with NOCIMD=4. At first, the

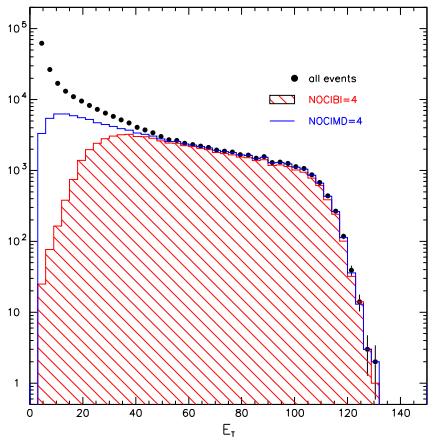

Figure 4.7: *E_T spectra for all MB events (closed circles), events in target according to NOCIBI (hatched area) and events in target according to NOCIMD (empty area histogram).*

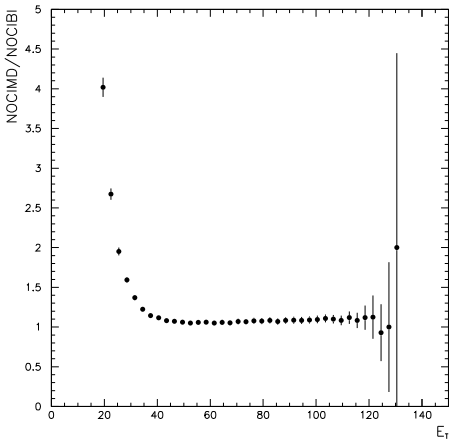

Figure 4.8: *ratio of number of events selected by NOCIMD and NOCIBI target identification methods.*

E_T spectrum of interacting events has been extracted from special runs collected in 1998 at low beam intensity and with an interaction trigger based on a cut on the ZDC signal (fig. 4.9). A second evaluation of the interacting event spectrum, has been obtained from a Glauber calculation [11] including the experimental smearing on the measured transverse energy (fig. 4.10). Both the results indicate that the efficiency of NOCIMD is $\approx 100\%$ for $E_T > 30$ GeV.

It is also important to verify that the events tagged with NOCIMD=4 are real Pb-Pb in target interactions and not Pb-air collisions occurring close to the target. For this reason, Monte Carlo simulations have been performed using VENUS 4.12 [9] for particle generation in Pb-N and Pb-O interactions and the GEANT 3.21 [10] package for track propagation, δ rays generation and detector response simulation. The results confirm that for $E_T > 15$ GeV the number of Pb-air events tagged as NOCIMD=4 is negligible.

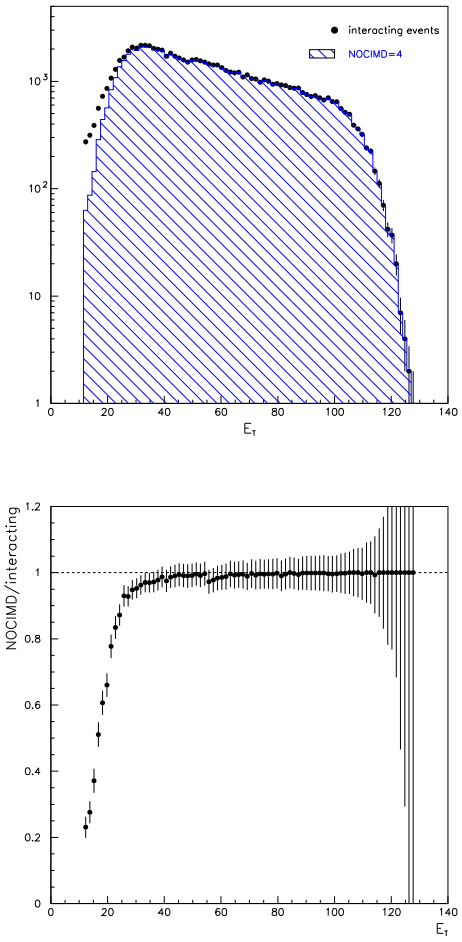

Figure 4.9: *E_T spectra (top) and ratios (bottom) for interacting events (closed circles) from special runs, and events in target according to NOCIMD (hatched histogram).*

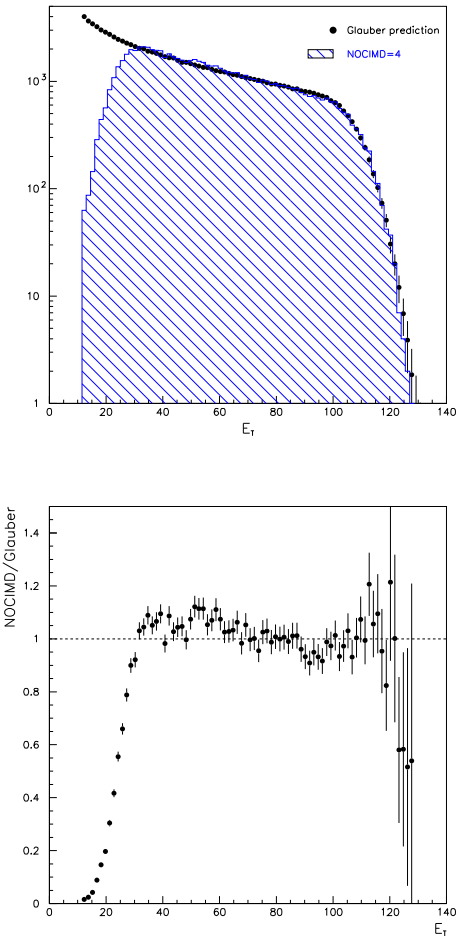

Figure 4.10: *E_T spectra (top) and ratios (bottom) for interacting events (closed circles) from Glauber calculations, and events in target according to NOCIMD (hatched histogram).*

Bibliography

[1] DIMUREC USER GUIDE 2.00/02 (1997).

[2] F.Bellaiche, PhD thesis, Apr. 1997, Universitè de Lyon.

[3] M.C. Abreu et al. (NA50 Collaboration), Phys.Lett. B410 (1997) 327.

[4] L. Villatte, PhD Thesis, Universite' Paris7 (2001).

[5] J. C. Collins and D. E. Soper, Phys. Rev. D16 (1977) 2219.

[6] F.Bellaiche et al.,. Nucl. Instr. and Meth. in Phys. Res. A398 (1997) 180.

[7] R. Arnaldi, Ph.D. thesis, Dec. 2000, Universitè Blaise Pascal, Clermont-Ferrand.

[8] M.C. Abreu et al. (NA50 collaboration), Phys.Lett. B450 (1999) 456.

[9] K. Werner, Phys. Rep. 32 (1993) 87.

[10] R. Brun et al., GEANT3, CERN/DD/cc/84-1.

[11] R.J. Glauber, Lectures in Theoretical Physics, Vol. 1, Interscience publishers, NY 1959, 315.

Chapter 5

Particle production in nucleus-nucleus collisions

High energy collisions of two nuclei are generally described as superpositions of many independent (incoherent) collisions between nucleons. This hypothesis relies on the consideration that the distance between nucleons in a nucleus ($\sim$ 1.8 fm) is much greater than their De Broglie wave length ($\lambda \sim 0.2$ fm for a nucleon with p$\sim$1 GeV/c), so that each nucleus sees the other nucleus as an object composed of independent nucleons. Consequently, the fundamental features of the collision are usually extended from proton-proton to proton-nucleus and nucleus-nucleus collisions taking into account the geometry of the nucleus.

The nucleon–nucleon total cross section is dominated by the inelastic cross section and the probability for the colliding nucleons to lose a large fraction of their energy is quite substantial. This energy is predominantly used to produce particles: the higher the energy available in the interaction, the higher the number of particles produced.

In proton-nucleus interactions, the projectile undergoes many interactions with the target nucleons, losing energy and momentum and emerging from the other side of the target nucleus with much lower energy and momentum. The number of proton-nucleon collisions suffered by the projectile proton depends on the thickness of the target nucleus: the greater the radius of the target nucleus, the greater the number of binary proton-nucleon collisions and consequently the loss of energy and momentum and the number of particles produced.

A nucleus-nucleus interaction can be described in terms of single nucle-

ons of the projectile nucleus making many nucleon-nucleon collisions with the target nucleons. It is important to remark that these naive multicollision models neglect the contribution of collective effects in the nucleus, and therefore they are only approximately valid, if such collective effects are present.

5.1 Particle multiplicity

The total number of particles produced in an inelastic collision is called multiplicity of the collision. Since experimental detection methods are usually sensitive to ionizing (charged) particles, it is useful to introduce the charged multiplicity (N_{ch}) of the collision defined as the total number of charged particles produced in the interaction.

Experimental data show that about 80-90% of the charged particles produced in an inelastic nucleon-nucleon collision are pions; the rest consists of kaons, baryons, anti–baryons and other particles. Therefore, assuming that most of the neutral particles produced are π^0s and that equal numbers of π^+, π^- and π^0 are produced, the total number of particles produced can be estimated from the measured number of charged particles as about $\frac{3}{2} \cdot N_{ch}$.

The multiplicity of charged particles produced in nulceus-nucleus collisions is a global variable that is essential for their characterization, because it is connected with the impact parameter of the collision and can therefore be used as a centrality estimator (the larger the multiplicity, the larger the centrality). Moreover, the number of produced particles quantifies to which extent the incoming beam energy is distributed to produce new particles and gives information about initial conditions, such as the energy density and the entropy. According to thermodynamics, the entropy is connected to the number of degrees of freedom inside a given system: the larger the number of degrees of freedom, the larger the entropy of the system. In the collisions of two nuclei, the available energy is distributed among the existing degrees of freedom, i.e. the different particle species, giving rise to particle production. The multiplicity can thus be an observable related to the entropy of the system [1]. The estimation of the entropy of the system may also give information about the phase of the matter created in the collision. It is expected [2] that the QGP phase would have an entropy content per baryon a few times higher than the hadron gas phase, due to the fact that the colour degrees of freedom become available after the colour deconfinement. The hadronization of the QGP would then release a considerable amount of en-

ergy and entropy, which in the case of plasma droplets deflagration, might cause collective fluctuations in the momentum distribution of particles, which would appear as large fluctuations in the number of particles produced and in their rapidity distribution.

5.2 Distribution of momenta of the produced particles

The momenta of the produced particles are usually analyzed in the component transverse to the beam axis (p_T) and in the one along the beam axis (p_L). In this way, all the information about the velocity of the particle-emitting source is contained in the longitudinal momentum, while the transverse momentum is free from kinematic effects and is governed only by the internal characteristics of the system which emits the particles.

The transverse momentum distribution of the produced particles (dN/dp_T), usually represented as a function of the transverse mass $m_T = \sqrt{m^2 + p_T^2}$ has approximately an exponential shape in the region $p_T < 1$ GeV/c (soft p_T region), with an inverse slope reflecting the combined effects of temperature and transverse expansion of the system.

The longitudinal momentum distribution of the produced particles can be inferred from their distribution in rapidity y, defined as:

$$y = \frac{1}{2} ln \left(\frac{E + p_L}{E - p_L} \right) \tag{5.1}$$

To characterize the rapidity of a particle it is therefore necessary to measure two quantities: its energy and its longitudinal momentum. For this reason it is convenient to introduce the pseudorapidity variable, defined as:

$$\eta = -ln \left[tan \left(\frac{\vartheta}{2} \right) \right] = \frac{1}{2} ln \left(\frac{|\mathbf{p}| + p_L}{|\mathbf{p}| - p_L} \right) \tag{5.2}$$

which coincides with the rapidity variable when the momentum is large, that is when $|\mathbf{p}| \approx E$. The pseudorapidity of a particle requires the measurement of only one kinematic quantity, the angle ϑ of emission of the particle relative to the beam axis, so that it is easier to experimentally measure the pseudorapidity rather then the rapidity of a particle.

The rapidity (or pseudorapidity) distributions of the produced particles dN/dy (or $dN/d\eta$) play an important role in defining the features of the

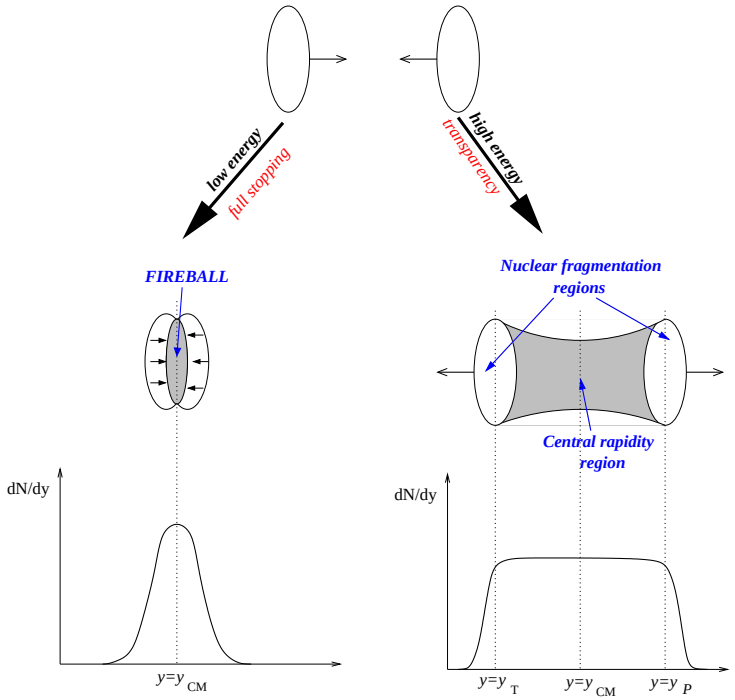

Figure 5.1: *Rapidity distributions of produced particles in the two different energy regimes: full stopping regime and Bjorken (transparency) regime.*

collision, carrying information about the energy lost by the projectile, the total energy deposition, the longitudinal expansion of the system created in the collision and the issue of the "stopping power".

In the case of the Bjorken high energy regime particles are expected to be produced with limited transverse momentum ($< p_T > \simeq \frac{1}{3}$ GeV/c) and very broad and flat rapidity distributions, because of the mainly longitudinal expansion of the hadronic matter and to the almost constant particle production per rapidity unit in the central rapidity region. This features generate dN/dy distribution with a broad plateau centered on the rapidity of the center of mass of the nucleus-nucleus system.

Three distinct regions in the particle rapidity distributions can be considered (see figure 5.1), connected with three distinct aspects of the collisions: the fragmentation of the target, the fragmentation of the projectile and the production of particles in the central region. The fragments of the projectile are found in the forward fragmentation region, which is populated by parti-

cles with high y values, close to the rapidity of the projectile. The backward fragmentation region consists of particles with small rapidity values, close to the rapidity of the target. The greater the incident energy, the greater the separation between the projectile and the target rapidity regions. The produced particles are concentrated in the central rapidity region around the rapidity of the center of mass of the system, where the energy deposition occurs. The energy density of the system created in the interaction is connected with the energy deposition in the center of mass of the system and can be estimated from the particle rapidity density in the central rapidity region by means of the Bjorken formula [3], under the assumption of purely longitudinal expansion of the system:

$$\varepsilon_{BJ} = \frac{< m_T >}{\mathcal{A} c \tau_o} \left(\frac{dN}{dy} \right)_{y=y_{cm}}$$

where $\mathcal{A}$ is the transverse overlapping area in the collision of the two nuclei, τ_o is the formation time and m_T is the transverse mass.

The estimation of the energy density in the fragmentation regions, which contains information about the energy transfer between the projectile and its fragments, is more complicated.

On the contrary, in the "full stopping" regime with formation of a hadronic fireball, the relevant symmetry point is the rapidity of the fireball center of mass and no particles are found in the nuclear fragmentation regions because all the projectile and target nucleons are stopped in the collision. Furthermore, the isotropic explosion of the fireball gives rise to an isotropic emission of particles from a single source at rest in the center-of-mass system, which has the neat and striking consequence that the particle rapidity distributions would be universal bell-shaped curves around the symmetry point, with the same FWHM ($\Delta\eta = 1.41$ or 1.75 [4], depending on model assumptions) for all projectiles, targets and incident energies.

It is expected that the fireball model works well at the energies attained at the AGS (i.e. $\sqrt{s}$ in the range 3-5 GeV). Experimental AGS results [5] show that, while the rapidity dependence of the inverse slopes of proton m_T spectra are in agreement with the prediction of the fireball model (see right panels of fig. 5.2), the dN/dy distributions of protons, which contain the most relevant information about stopping power, are inconsistent with isotropic emission from a single source at rest in the center-of-mass system, as it can be seen in the left panels of fig. 5.2. This disagreement indicates that the

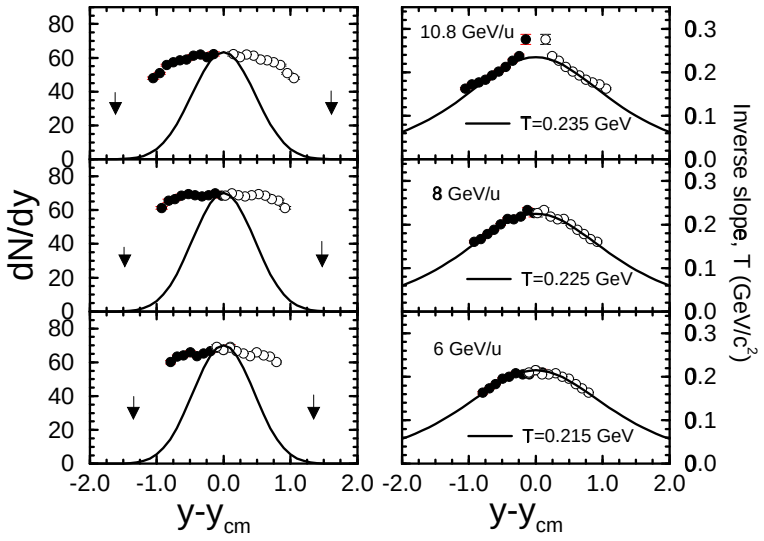

Figure 5.2: *Proton rapidity distributions in the center-of-mass system (left panels) and inverse slopes (right panels) compared to the expected distributions for isotropic emission from a thermal source at rest in the center of mass system ($y = y_{cm}$). The arrows indicate target and beam rapidities.*

protons retain a fair quantity of their longitudinal motion and implies that the degree of stopping of the incident baryons is far from complete already at AGS energies.

The dN/dy distributions observed at SPS (typical ones for negative hadrons and different colliding systems are reported in figure 5.3) do not show a broad plateau at central rapidity and, at the same time, are not in agreement with the FWHM predictions of the fireball model, indicating that at SPS energies (i.e. $\sqrt{s}$ in the range 17-20 GeV) none of these two models is adequate to fit the experimental data.

5.3 Particle production mechanisms

The produced particles are usually classified according to their transverse momentum p_T in two categories: particles with p_T much below 1 GeV/c are called "soft" particles, while particles with $p_T \gg 1$ GeV/c are classified as "hard" particles.

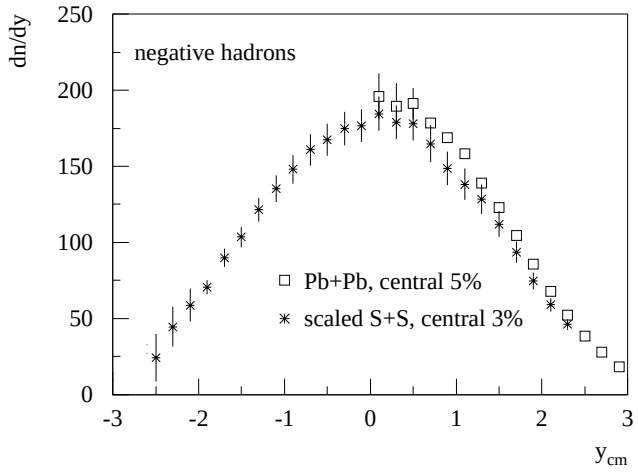

Figure 5.3: *Rapidity distributions of negative hadrons in S-S and Pb-Pb collisions at CERN SPS, as measured by the NA49 experiment [6].*

Hard particles (with $p_T \gg 1$) originate from hard processes, which involve large momentum transfer, corresponding to small length scale, much below the confinement scale. These processes, therefore, occur at parton level and can be treated very precisely in the framework of perturbative QCD since they are associated with small values of the QCD coupling constant α_s.

Most of the interactions are indeed processes characterized by a small momentum transfer, which lead to the production of particles with a transverse momentum in the soft p_T region. These are called soft processes and are associated with a large length scale and with large values of the strong coupling constant. As a consequence, soft processes can not be described by perturbative QCD and require non-perturbative techniques, so that, at present, no analytical calculations exist: the knowledge about them is limited to a phenomenological description of the observations, with some features that can be qualitatively understood on the basis of QCD.

Nuclear collisions are generally described in the framework of multicollision models as a superposition of elementary collisions. In the case of soft processes, the elementary collisions occur at large distances (small momentum transfer), i.e. between nucleons; while in the case of hard processes the elementary collisions are characterized by small distances (large momentum transfer) and they occur at the parton level.

5.3.1 Hard processes

Hard processes are characterized by a transverse distance scale of the collision ($\sim 1/p_T$) so small that the elementary collisions occur at the parton level, giving rise to the production of jets with large transverse momentum. Since high p_T partons are produced on a very short timescale compared to the low p_T partons in the same collision, such jets provide a probe of the matter in the initial stages of the collision.

As far as hard processes are concerned, the nucleons inside the colliding nuclei act independently, giving a cross section proportional to the total number of constituents in the projectile and target nuclei, i.e. to $A \times B$, where A and B are respectively the mass numbers of the two nuclei. In such a scenario, nuclear collisions can be modeled as a superposition of independent binary collisions between nucleons and the physically relevant quantity is the number of nucleon-nucleon collisions (N_{coll}). A scaling with N_{coll}, therefore, arises naturally in a regime of nuclear reactions where hard processes dominate over the soft particle production.

Hard processes are rather accurately described by QCD-based Monte Carlo generators like PYTHIA [7].

5.3.2 Soft processes

In the "soft" regime, the dynamics of the nucleus-nucleus collision can be described considering elementary collisions at the baryon (nucleon) level and the underlying quark-gluon structure of hadrons is not revealed and does not play a significant role in the multiple baryon collisions.

The simplest model of "soft" particle production is the Wounded Nucleon Model (WNM) [8]. The projectile nucleon, after the first interaction with a nucleon of the target nucleus, goes into an excited state and remains in that state during all its path inside the nucleus because the uncertainty principle and time dilation prevent it from fragmenting into particles until it is well outside the nucleus. This feature eliminates the possibility of a cascade in the nucleus from the re-interaction of the secondary fragments. [1]

[1] This assumption is true only in the rapidity regions where the partonic constituents of the excited state have enough velocity to hadronize outside the nucleus. On the contrary, partons with $v \cdot \gamma\tau_o < L$ (where v is the velocity, τ_o the hadron formation time and L the length of nuclear matter to be traversed), can re-interact within the nucleus and produce a cascade [9].

After the first interaction, the resultant excited nucleon continues to make further collisions along the direction of the projectile; it is assumed that the excited nucleon interacts with the same cross section as an unexcited nucleon and the successive collisions do not affect its state. In this scenario the elementary process for particle production is the excitation of the nucleon and the multiplicity results to be proportional to the number of "wounded" nucleons defined as the number of nucleons which underwent at least one inelastic collision, i.e. the number of projectile and target participant nucleons (N_{part}). This means that each wounded nucleon contributes only once to the particle production, no matter how many times it is successively struck.

This picture implies that, since a proton-proton collision has 2 wounded nucleons, while for a proton-nucleus interaction with N_{coll} collisions it is $N_{part} = N_{coll} + 1$ (the incident proton plus the N_{coll} nucleons struck in the target nucleus), the average multiplicity in collisions of a proton with a target nucleus of mass number A (p-A collisions) is approximately given by:

$$< N_{pA} >= \frac{1}{2}\,(N_{coll} + 1) < N_{pp} >$$

where $< N_{pp} >$ is the average multiplicity in proton-proton collisions. This approximation turns out to be in good agreement with the experimental data.

In the case of nucleus-nucleus collisions there is no unique relation between N_{part} and N_{coll}, which are usually computed from the nuclear geometry in the framework of the Glauber model [10], and the multiplicity is given by:

$$< N_{AB} >= \frac{1}{2} N_{part} \cdot < N_{pp} >$$

A scaling with the number of participants N_{part} is therefore expected in a regime of nuclear reactions dominated by soft particle production.

5.3.3 Particle production during the system evolution

The observed final state particles reflect the space-time evolution of the system created in the collision between the nuclei, and therefore they are the outcome of all the particle production processes which occur in different stages of the system expansion.

Initial state interactions

Immediately after the two Lorentz contracted nuclei have collided, a large

number of elementary inelastic interactions between nucleons (or partons) takes place, resulting in a large energy deposition in a small volume. Particle production mechanisms in these first stages of the system evolution depend on the energy of the colliding nuclei: soft interactions between nucleons are expected to dominate at low energies, while with increasing energy, the contribution from hard processes at the parton level could become more and more important.

Later on, the quanta of energy deposited in the elementary collisions materialize, depending on the energy density attained in the collision, into partons or into hadrons. If the energy density is sufficiently high, the system should be composed of partons and the interactions among these partons should lead the system to the thermal equilibrium (in a QGP state). There are mainly two approaches to describe the system in the first stages of its evolution until it reaches the thermal equilibrium: the QCD string breaking and the partonic cascade.

The QCD string breaking approach, developed from models of soft hadron-hadron interaction, assumes that the production of particles originates from the independent fragmentation of several color flux tubes (strings) exchanged by the partons of the excited (wounded) nucleons. The two main models based on the string approach are the Lund Model [11] and the Dual Parton Model [12]. The difference between these two models consists in the fact that in the Lund Model the strings are formed between partons of the same nucleon and so there is no colour exchange between the colliding nucleons, while in the Dual Parton Model strings are formed between constituents of the two colliding hadrons, which therefore exchange colour. Both these approaches have been cast into Monte-Carlo event generator form: the Monte-Carlo implementation of the Lund model is called FRITIOF [13], while VENUS [14] is one of the existing event generators based on the Dual Parton Model.

Experimental data at low energies are well explained in the framework of QCD string breaking. With increasing energy hard processes are expected to play an important role in particle production: it has been evaluated that jets could produce up to 50% of the transverse energy per unit rapidity in heavy nuclei collisions at RHIC energies and up to 80% at LHC energies. For this reason, a Monte Carlo event generator incorporating soft particle production based on the string phenomenology and multiple jet processes has been developed: it is called HIJING [15] and it should be well suited for the description of the RHIC and LHC experimental data.

A completely different description of the system evolution is the parton cascade approach [16], which is based on the concept that the colliding nuclei can be decomposed into their parton substructure. The hard interactions among these partons can be precisely described by perturbative QCD (if the momentum transfer is sufficiently high) and followed until they lead the system to thermalization. Whereas the string picture runs into conceptual difficulties at very high energy, when the string density becomes too large, the parton cascade becomes invalid at low energy, where most partonic scatterings are too soft to be described by perturbative QCD.

Expansion and hadronization
The thermalized quark-gluon-plasma, if formed, then evolves according to the laws of relativistic hydrodynamics, until it cools down to the critical temperature T_c, when it begins to hadronize, i.e. partons combine to form hadrons.

The hadronization phase is usually described as a stochastic process dominated by soft interactions. It is usually assumed that the plasma converts into a hadronic gas via a mixed phase, while maintaining thermal and chemical equilibrium. This treatment of the phase transition is probably quantitatively correct if the transition is of the second order or weak first order. If there is a truly first-order transition from QGP to hadron gas, this approach may be invalidated by supercooling of the plasma and by the presence of various deflagration and detonation singularities. If the system does not thermalize, its behaviour can be studied by following the partonic reactions at a microscopic level, until the parton density has become sufficiently low to allow the formation of individual hadrons [9, 17].

In the hadronic stage of the collision evolution, before the system freezes-out, the produced particles could undergo a strong rescattering which can cancel the memory of the initial stages in which hard processes were present.

5.3.4 Interplay between soft and hard processes

The measurement of the charged multiplicity, and in particular of its dependence on the centrality (impact parameter) of the collision in heavy ion reactions, may help constrain different models of particle production, and quantify the relative importance of soft versus hard processes in the particle production mechanisms. On this respect, an important test for models of particle production is the study of its scaling properties with respect both

to the number of participant nucleons (N_{part}) and to the number of binary collisions (N_{coll}), because a scaling with N_{part} is expected in scenarios dominated by soft processes, while a scaling with N_{coll} is expected to be observed in a regime where hard processes dominate over the soft particle production.

Models based on the assumption that the multiplicity is proportional to the number of participant nucleons describe very well the multiplicity distributions in Pb-Pb collisions observed at SPS energies, as it can be seen in figure 5.4. This result indicates that particle production at SPS energies is due dominantly to soft processes and that the Wounded Nucleon Model offers a good description of the collision. At higher energies, like the ones reached at RHIC and at LHC, the contribution from hard processes should become more and more relevant.

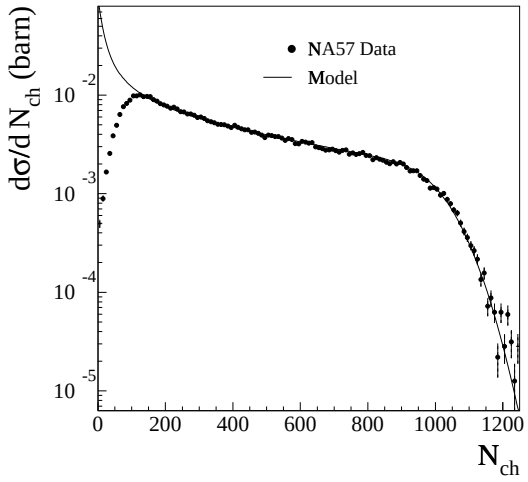

Figure 5.4: *Charged multiplicity distribution in Pb-Pb collisions at 158 GeV per nucleon beam energy fitted with the Wounded Nucleon Model, as measured in the range* $2 < \eta < 4$ *by the NA57 experiment [18].*

5.3.5 Energy dependence of particle production

The dependence of the average multiplicity on the center-of-mass energy ($\sqrt{s}$) contains information on the scaling properties of the collision dynamics and therefore can contribute to the understanding of particle production mechanisms. A simple scaling law for the energy dependence of particle

production was proposed by Feynman [19], who predicted that the average multiplicity should increase logarithmically with the center of mass energy $\sqrt{s}$. In fact, the observed multiplicity in p-p and p-$\bar{\text{p}}$ collisions can not be well reproduced by a linear dependence on (ln s) and the best fit to the data is given by [20, 21]:

$$< N_{ch} >= a + b \cdot \ln\, s + c \cdot (\ln\, s)^2$$

The non-linear dependence of $< N_{ch} >$ on (ln s) suggests that the Feynman scaling is only approximately valid.

Important information can be extracted also from the energy dependence of the momenta distributions of produced particles. It has been observed that, in the transverse momentum distributions, the hard p_T region ($p_T \gg 1$ GeV/c) shows a strong dependence on the center-of-mass energy, while the soft physics region (with p_T below 1 GeV/c), which dominates the spectrum, remains essentially unchanged [4]. Therefore, as $\sqrt{s}$ increases, the $< p_T >$ remains practically constant and the energy is mostly used for the longitudinal expansion of the system.

In p-p and p-A collisions, two main features have been observed in the dN/dy distributions with increasing $\sqrt{s}$: an extension of the rapidity plateau and an increase of the particle density in the central region [20]. The broadening of the central plateau with increasing energy reflects the extension of the available phase space in rapidity due to the greater longitudinal expansion of the system. The available rapidity range increases with $\sqrt{s}$ as [4]:

$$\Delta y \mid_{max} = \ln \frac{\sqrt{s}}{m}$$

This result implies that, in the case of exact Feynman scaling, the dN/dy distribution should reach a constant or limiting value in the rapidity plateau, so that the multiplicity, which is the integral of the particle rapidity distribution, would result to be proportional to Δy and would increase logarithmically with $\sqrt{s}$. The observation that the dN/dy value at midrapidity is not constant, but rises steadily gives further evidence for a substantial violation of Feynman scaling in the central region and accounts for the non-linear dependence of $< N_{ch} >$ on (ln s).

The $\sqrt{s}$ dependence of multiplicity in proton-nucleus and nucleus-nucleus collisions can be compared with proton-proton data by means of a normalization to the number of participant nucleons. This is justified in the framework

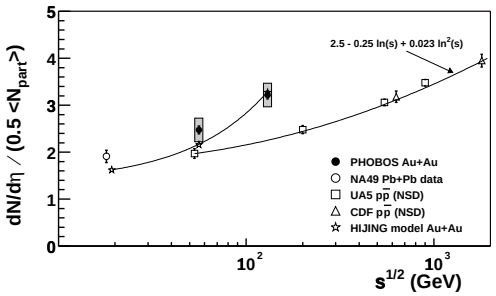

Figure 5.5: *Particle pseudorapidity density at midrapidity per participant pair as a function of $\sqrt{s}$ for different colliding systems.*

of the Wounded Nucleon Model which assumes that for soft processes each participant nucleon gives a constant contribution to the production of particles. In particular, taking into account that in p-p collisions it is $N_{part} = 2$, nucleus-nucleus data can be scaled to proton-proton results by calculating the mean charged multiplicity per participant pair, or, equivalently, the particle rapidity density at midrapidity per participant pair, defined as:

$$\frac{\left(\frac{dN}{dy}\right)_{y=0}}{< \frac{1}{2} \cdot N_{part} >}$$

which allow a direct comparison of the data about particle production for different colliding systems. In figure 5.5 the values for particle pseudorapidity density per participant pair for p-$\bar{\text{p}}$ collisions and also for central Pb-Pb collisions at CERN SPS and Au-Au collisions at RHIC are reported. These results show that in central Au-Au collisions at $\sqrt{s} = 130$ GeV the particle density per participant pair is significantly larger than for nucleon-nucleon collisions and is compatible with the prediction of HIJING, indicating that at such energies simple multicollision models (such as the WNM) are inadequate and that hard processes may play an important role [22].

Bibliography

[1] L. Van Hove, Phys. Lett. B118 (1982), 138.

[2] L. Van Hove, CERN-TH-3623, June 1983.

[3] J.D. Bjorken, Phys. Rev. D 27 (1983), 140.

[4] M.J. Tannenbaum, in Sinha, Pal, Raha, Quark-Gluon Plasma, Springer-Verlag (1990), 108.

[5] B.B. Back et al., E917 Collaboration, Phys. Rev. Lett. 86 (2001), 1970.

[6] H. Appelshauser et al., NA49 Collaboration, Phys. Rev. Lett. 82 (1999), 2471.

[7] T. Sjostrand, Comput. Phys. Commun. 82 (1994) 74.

[8] Bialas, Bleszynski and Czyz, Nucl. Phys. B111 (1976), 461.

[9] K. Kajantie and L. McLerran, Ann. Rev. Nucl. Sci. 37 (1987) 293.

[10] R.J. Glauber, Lectures in Theoretical Physics, Vol. 1, Interscience publishers, NY 1959, 315.

[11] B. Andersson et al, Phys. Rep. 97 (1983), 31.

[12] A. Capella and J. Tran Thanh Van, Phys. Lett. B93 (1980), 146.

[13] B. Nilsson-Almsquist and E. Stenlund, Computer Phys. Comm 43 (1987), 387.

[14] K. Werner et al., Phys.Rep. 32 (1993), 87.

[15] M. Gyulassy and X.N.Wang, Phys.Rev. D44 (1991), 3501.

[16] K. Geiger and B.Müller, Nucl. Phys. B369 (1992), 600.

[17] B. Muller, Rept.Prog.Phys.58 (1995) 611.

[18] F. Antinori et al., WA97 and NA57 collaborations, Eur. Phys. Journ. C18 (2000), 57.

[19] R. Feynman, Phys. Rev. Lett. 23 (1969), 1415.

[20] W. Thome et al., Nucl. Phys. B129 (1977), 365.

[21] Busza and Ledoux, Ann. Rev. Nucl. Part. Sci. 38 (1988), 119.

[22] B.B. Back et al., PHOBOS Collaboration, Phys. Rev. Lett. 85 (2000), 3100.

Chapter 6

Charged particle multiplicity in Pb-Pb collisions at SPS energies

The multiplicity detector of the NA50 experiment, with its good granularity, allows to measure the charged particle multiplicity as a function of pseudorapidity in Pb-Pb collisions at ultra–relativistic energies.

Data collected at two different energies of the SPS Pb beam have been used for the analysis presented here: the first data sample was taken in 1998 at 158 GeV per nucleon beam energy, corresponding to $\sqrt{s} = 17.3$ GeV, the second in 1999 at 40 GeV per nucleon energy ($\sqrt{s} = 8.77$ GeV).

The analysis has been performed on the data of some special runs taken with the minimum bias (MB) trigger at low beam intensity (about 1/10 of the standard intensity) to minimize pile–up effects. The average Pb beam intensity, the thickness and the position of the targets used in 1998 and 1999 are listed in table 6.1.

The pseudorapidity distributions of primary charged particles are studied as a function of the centrality of the collision. It is important, to avoid autocorrelations, that the centrality selection is made using observables which are independent of the multiplicity detector itself. On this respect, two independent centrality-related observables can be used: the energy of the projectile spectator nucleons (E_{ZDC}) measured by the Zero Degree Calorimeter and the neutral transverse energy (E_T) measured by the Electromagnetic Calorimeter.

	Pb beam		Pb target		
Year	energy per nucleon (GeV)	intensity (ions/burst)	thickness (mm)	distance from MD1 (cm)	# of events analyzed
1998	158	$3.2 \cdot 10^6$	3 mm	11.65	48000
	158	$3.9 \cdot 10^6$	1 mm	9.15	18000
1999	40	$1 \cdot 10^6$	3 mm	12.55	35000

Table 6.1: *Data taking conditions.*

6.1 Centrality selection

The aim of the analysis is to study the properties of the pseudorapidity distributions of primary charged particles ($dN_{ch}/d\eta$) for different classes of events selected according to the centrality of the collision, using two independent centrality estimators (E_{ZDC} and E_T).

To allow a comparison of the results obtained with these two centrality selections, centrality intervals have been defined in terms of fractions of the total inelastic cross section calculated by integrating the minimum bias (MB) dN/dE_{ZDC} and dN/dE_T distributions.

Since the MB spectra contain also events from non-interacting Pb projectiles, to obtain the number of interactions (N_{int}), the integral of the MB spectra (N_{Pb}) has to be normalized taking into account the interaction probability P_{int}:

$$N_{int} = N_{Pb} \cdot P_{int} = N_{Pb} \cdot \left(1 - e^{-L_T/\lambda_{int}}\right) \tag{6.1}$$

where L_T is the target thickness (see table 6.1) and λ_{int} is the interaction length, which can be expressed as:

$$\lambda_{int} = \frac{A_{targ}}{\rho_{Pb} \cdot N_A \sigma_{inel}} \tag{6.2}$$

where $A_{targ} = 207.2$ is the atomic mass of the target (Pb) nucleus, N_A is the Avogadro number, $\rho_{Pb} = 11.35$ g/cm^3 and σ_{inel} is the total inelastic cross section, given by:

$$\sigma_{inel} = \sigma_0 (A_{proj}^{1/3} + A_{targ}^{1/3} - \delta)^2 \tag{6.3}$$

Assuming $\sigma_0 = 68.8$ mb and $\delta = 1.32$ (obtained interpolating from the

values given in [1, 2], taken respectively as lower and upper limit) one obtains:

$$\sigma_{inel} = 7.62^{+0.54}_{-1.23} \text{ barn}$$

$$\lambda_{int} = 3.98^{+0.21}_{-0.27} \text{ cm}$$

$$P_{int}(L_T = 3 \text{ mm}) = 7.26^{+0.51}_{-0.35} \cdot 10^{-2}$$

6.1.1 Data at 158 GeV/nucleon

The E_{ZDC} and E_T spectra for MB events at 158 GeV/nucleon beam energy are reported in fig. 6.1.

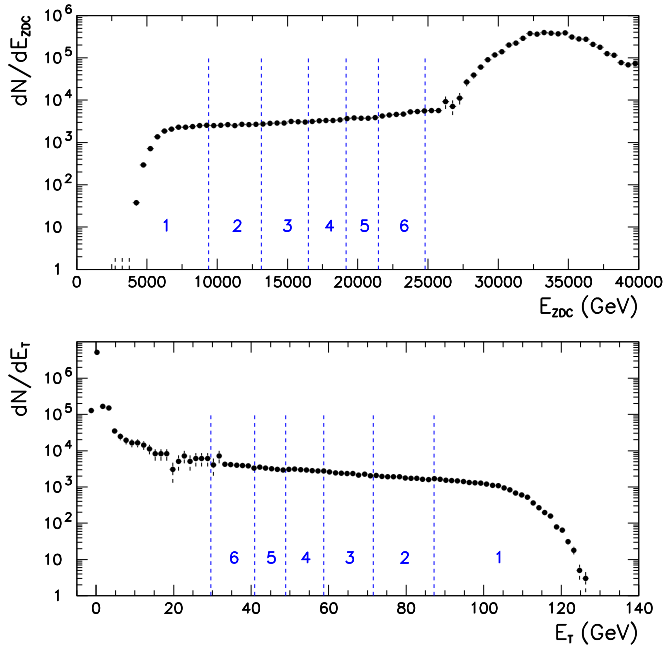

Figure 6.1: *Distributions of the forward energy E_{ZDC} and of the transverse energy E_T in 158·A GeV/c Pb–Pb Minimum Bias collisions.*

The limits of each centrality class have been fixed so as to have classes with a width corresponding to 5% of the total inelastic cross section σ_{inel}. When the 5% class would have been too narrow with respect to the E_{ZDC} or

E_T resolution giving thus rise to possible biases in the centrality selection, a class with a width corresponding to $10\% \cdot \sigma_{inel}$ has been defined. In this way, 6 centrality classes have been defined for both centrality estimators. The E_{ZDC} and E_T limits for the different centrality classes are plotted in fig. 6.1 and are listed in table 6.2 together with the mean E_{ZDC} and E_T value for each class.

The $\simeq 5\%$ uncertainty on the value of P_{int} is reflected in a $\simeq 5\%$ uncertainty in the evaluation of the total inelastic cross section fraction. This corresponds to uncertainties of $\sim 300 - 500$ GeV on the E_{ZDC} limits of each class and $\sim 2 - 3$ GeV on the E_T limits, which give the systematic errors on $< E_{ZDC} >$ and $< E_T >$ quoted in table 6.2.

CLASS	% of c.s. ($\pm 5\%$)	E_{ZDC}^{min}-E_{ZDC}^{max} (GeV)	$< E_{ZDC} >$ (GeV)	Syst. err. $< E_{ZDC} >$ (GeV)
1	0-5	0-9385	7500	130
2	5-10	9385-13150	11280	380
3	10-15	13150-16490	14790	620
4	15-20	16490-19180	17790	770
5	20-25	19180-21475	20250	650
6	25-35	21475-24790	23110	650

CLASS	% of c.s. ($\pm 5\%$)	E_T^{min}-E_T^{max} (GeV)	$< E_T >$ (GeV)	Syst. err. $< E_T >$ (GeV)
1	0-5	87.2-140.	98.3	1
2	5-10	71.5-87.2	78.6	2
3	10-15	58.7-71.5	64.5	2
4	15-20	48.9-58.7	53.4	2
5	20-25	40.9-48.9	44.4	2
6	25-35	29.6-40.9	34.9	2

Table 6.2: *E_{ZDC} and E_T limits for the different centrality classes at 158 GeV/nucleon.*

6.1.2 Data at 40 GeV/nucleon

The same method has been applied to the data sample collected in 1999 at 40 GeV per nucleon incident energy. Due to the worse performance of the

ZDC at such a low beam energy, it was not possible to use both centrality estimators and only the analysis with the E_T based centrality selection has been performed. The E_T spectrum of Minimum Bias events is shown in fig. 6.2. The limits of the centrality classes (indicated by vertical bars on the spectrum in fig. 6.2 and listed in table 6.3) correspond to the same intervals of total inelastic cross-section fraction used for the 158 GeV/nucleon data sample.

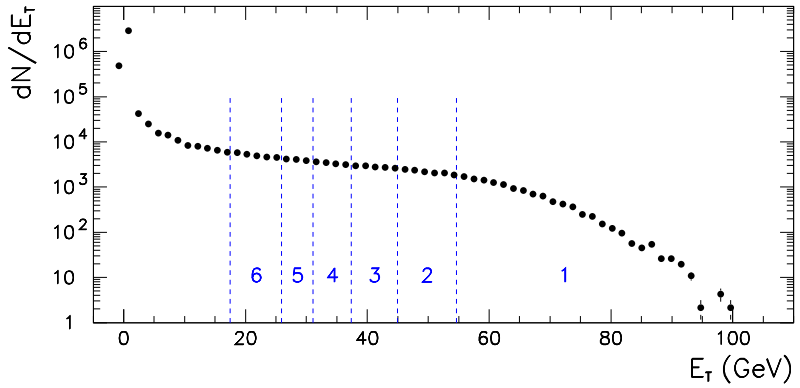

Figure 6.2: *E_T in Pb–Pb collisions at 40 GeV per nucleon incident energy. The limits of the 6 centrality classes are superimposed.*

CLASS	% of c.s. (±5%)	E_T^{min}-E_T^{max} (GeV)	$< E_T >$ (GeV)	Syst. err. $< E_T >$ (GeV)
1	0-5	54.6-100.	63.1	0.7
2	5-10	44.7-54.6	49.2	0.8
3	10-15	37.2-44.7	40.4	0.8
4	15-20	31.1-37.2	33.9	0.8
5	20-25	25.9-31.1	28.2	0.8
6	25-35	17.9-25.9	21.7	1.5

Table 6.3: *E_T limits for the different centrality classes at 40 GeV/nucleon.*

6.2 Event analysis

In each of the centrality classes defined in tables 6.2 and 6.3, the multiplicity detector data have been analyzed according to the following procedure:

1. Data selection on the basis of quality cuts
2. Calculation of the "raw" $dN_{ch}/d\eta$ distribution in each centrality class
3. Extraction of the primary $dN_{ch}/d\eta$ distribution by subtracting the delta electron contribution and then by correcting for secondary processes.

Gamma conversions and other processes of secondary particle production or primary particle decay have been evaluated with a complete Monte Carlo simulation based on the VENUS 4.12 [3] event generator and on the GEANT 3.21 [4] package for track propagation and detector response simulation.

6.2.1 Data selection

Events collected in special low-intensity runs with the MB trigger have been selected according to the criteria explained in chapter 4. In particular, usual beam cleaning cuts have been applied, the events lying out of the chosen E_T versus E_{ZDC} correlation band have been rejected to eliminate off-target contamination and residual pile–up, and NOCIMD target identification has been used as a further constraint to select in target events.

6.2.2 Raw multiplicity evaluation

The main difficulty in the extraction of particle multiplicity from the observed detector occupancy is connected to the presence of many strip clusters, i.e. groups of 2 or more contiguous detector strips firing at the same time.

The origin of clusters could be both physical and instrumental. The physical cluster mechanism is due to particles crossing contiguous strips and to the effects of particle energy deposition process inside the detector. By instrumental origin we refer to all clustering sources connected to a deteriorated performance of the detector and front–end electronics, such as crosstalk between channels in the front–end electronics system which gives rise to clustering effects similar to the ones coming from physical processes.

In figure 6.3, the cluster size distributions observed in the experimental data sample are shown both for a typical MD1 sector and for a typical MD2

sector. As expected, larger clusters are found on the higher occupied MD1 plane. The cluster distributions observed in a VENUS+GEANT Monte Carlo simulation of the full detector system for the same MD1 and MD2 sectors are displayed in fig. 6.4 and present clusters of smaller size with respect to the experimental data. Since the VENUS+GEANT Monte Carlo simulation, which includes only clusters of physical origin, does not reproduce the cluster distributions observed in the experimental data, a correction to account for clusters of instrumental origin is needed.

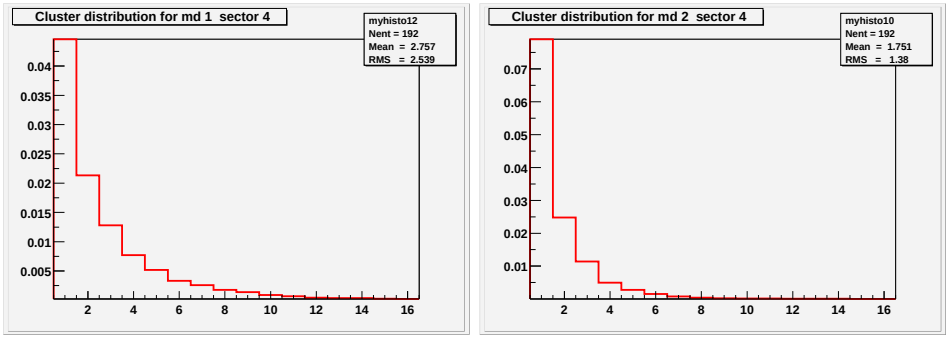

Figure 6.3: *Cluster size distributions observed in the experimental data sample for a typical MD1 sector (left panel) and a typical MD2 sector (right panel) for the 158 GeV/nucleon data sample with a 3 mm thick target.*

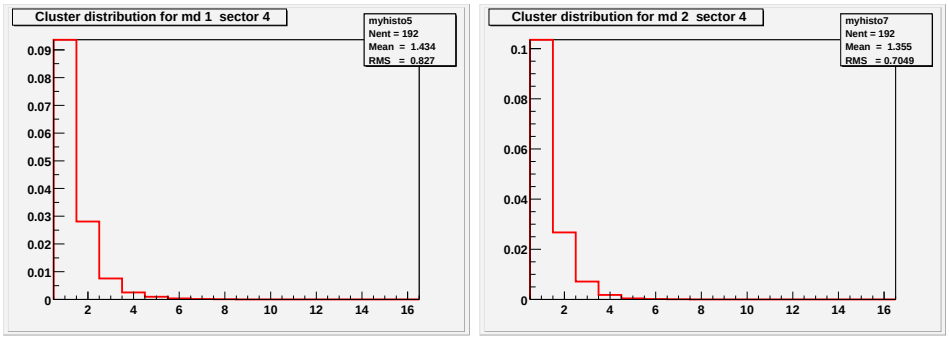

Figure 6.4: *Cluster size distributions observed in the VENUS+GEANT data sample for a typical MD1 sector (left panel) and a typical MD2 sector (right panel) for the 158 GeV/nucleon data sample with a 3 mm thick target.*

The method used to get the true particle occupancy from the measured strip occupancy is based on minimization techniques aimed at reproducing

the cluster distribution of the experimental data. The strip occupancy is simulated by generating the particle distributions in the detector and afterwards including the effects responsible for clustering. The particles are generated in each pseudorapidity bin according to a Poissonian distribution whose mean equals the particle occupancy. The clustering mechanisms are modeled by means of coefficients describing the probability that the strips in the vicinity of real particle tracks are firing. First, three coefficients (namely P_1, P_2 and P_3) accounting for processes in which one particle induces a signal on 1, 2 or 3 adjacent strips are introduced. Then, three other parameters (P_4, P_5 and P_6) representing the probability of filling a gap of 1, 2 or 3 non-firing strips located between two firing strips are evaluated. The parameter used are listed in table 6.4.

Param.	clustering process	order of magnitude	
	particle occup. $\rightarrow$ strip occup.	Data	VENUS+GEANT
P_1	10 $\rightarrow$ ff	0.15-0.25	0.05-0.12
P_2	010 $\rightarrow$ fff	0.04-0.10	0.-0.01
P_3	0100 $\rightarrow$ ffff	0.005-0.02	0.
P_4	f0f $\rightarrow$fff	0.4-0.9	0.05-0.15
P_5	f00f $\rightarrow$ffff	0.1-0.35	0.03
P_6	f000f $\rightarrow$fffff	0.03-0.07	0.

Table 6.4: *Parameters used to model clustering effects (1=particle in the strip, 0= no particle in the strip, f=firing strip).*

Afterwards, for a given particle occupancy (P_0) and probability coefficients ($P_1 - P - 6$), the cluster distribution is calculated and compared to the observed one. This procedure is applied iteratively, changing the particle occupancy and the probability coefficients, until the generated cluster distribution reproduces the experimental one. Typical results are shown in fig. 6.5 for two η bins (one on MD1 and the other on MD2) in the $5 - 10\%$ centrality class .

The particle occupancy per strip (P_0) obtained in this way is then used to calculate the raw $dN_{ch}/d\eta$ distributions, taking into account the geometrical acceptance of the strips in each η bin.

The stability of reconstructed particle occupancies against the initial parameters values has been checked. For testing purposes the method has been applied to VENUS+GEANT generated data in the complete detector sys-

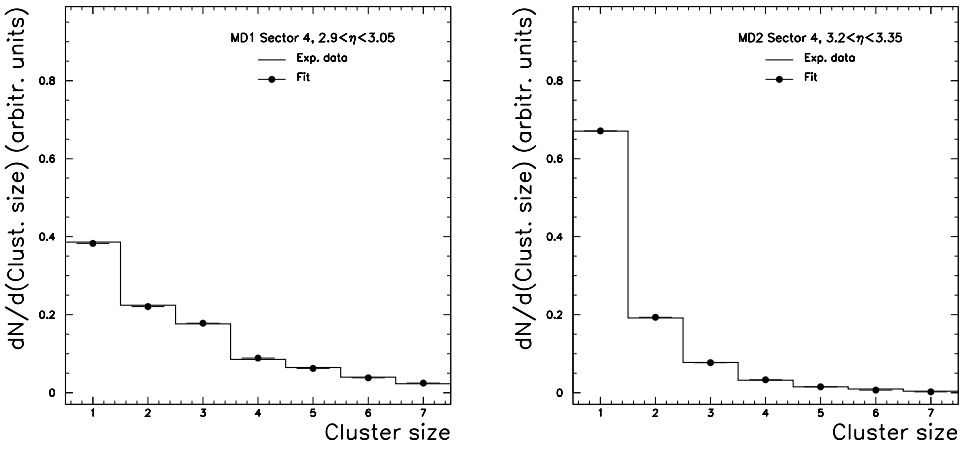

Figure 6.5: *Cluster size distributions observed in the experimental data sample for a typical MD1 η bin (left panel) and a typical MD2 η bin (right panel). The generated cluster distribution resulting from the minimization procedure are superimposed (full circles).*

tem for different centrality classes. It has been found that the reconstructed $dN_{ch}/d\eta$ distributions are in agreement with the generated ones within 5%. For experimental data samples we checked that in each centrality class the reconstructed occupancy for a given pseudorapidity bin agrees within 6% among adjacent azimuthal sectors of the detector. The ratio between the observed detector occupancy and the real particle occupancy ranges from ~ 1 for peripheral (low multiplicity) events to ~ 1.8 for central (high multiplicity) events.

6.2.3 Primary particle multiplicity evaluation

The δ ray contribution to the detector occupancy is evaluated by means of a GEANT 3.21 simulation, taking into account the effects of the target and of all the other materials, including the mechanical support of the detectors. This contribution reaches a maximum of 5% of the true occupancy in the most peripheral sample considered in this paper.

The VENUS+GEANT $dN_{ch}/d\eta$ distributions for different centrality classes, selected using the number of projectile participants as given by VENUS, are

reconstructed with the same method as the one used for the experimental data. This is done in order to keep exactly the same treatment for experimental and Monte Carlo data, so that possible systematics are canceled. The secondary/primary correction factors are obtained dividing for each centrality class the VENUS+GEANT reconstructed $dN_{ch}/d\eta$ distributions by the primary VENUS $dN_{ch}/d\eta$ distributions. We have run VENUS 4.12 with the default setting for decays of unstable particles, except for neutral pions (whose decay has been taken in charge by GEANT), meaning that charged particles from decays of K_0's, Λ's and other hyperons are considered as primary. The resulting secondary/primary ratio does not depend on centrality and therefore the correction factors obtained for the different centrality classes are averaged together. However, these correction factors depend on target thickness, on target position and on the particular multiplicity detector plane. The secondary/primary ratios at 158 GeV/nucleon beam energy as a function of pseudorapidity for the MD1-UP and MD2-UP planes in the case of a 3 mm target are displayed in fig. 6.6.

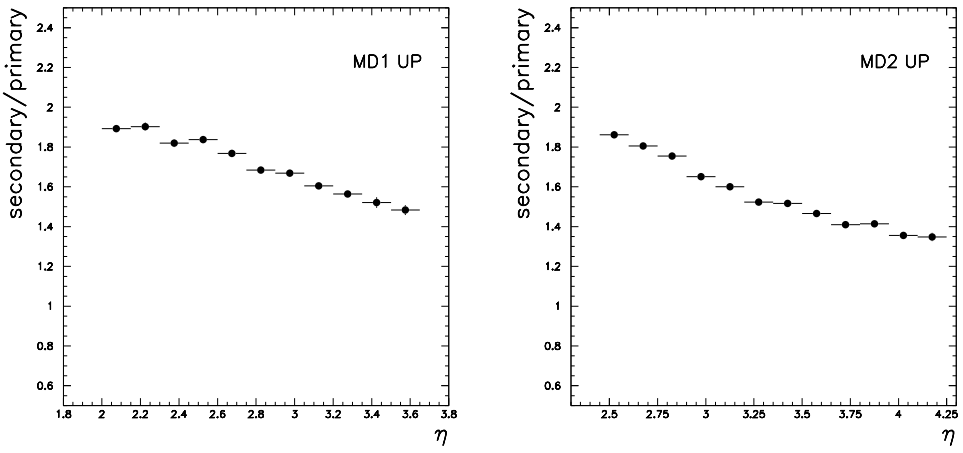

Figure 6.6: *Secondary/primary ratios for MD1-UP and MD2-UP layers for the 158 GeV/nucleon data sample with a 3 mm thick target.*

The primary experimental $dN_{ch}/d\eta$ distributions are obtained dividing the raw $dN_{ch}/d\eta$ distributions after δ subtraction by the secondary/primary correction factors. In this way, the $dN_{ch}/d\eta$ particle distributions from each of the four MD layers (MD1-UP, MD1-DOWN, MD2-UP and MD2-DOWN),

each of them extending over a different η region, are obtained. These distributions result to be in good agreement in their common η range, as it can be seen in fig. 6.7 and are therefore merged together, providing a wider η coverage.

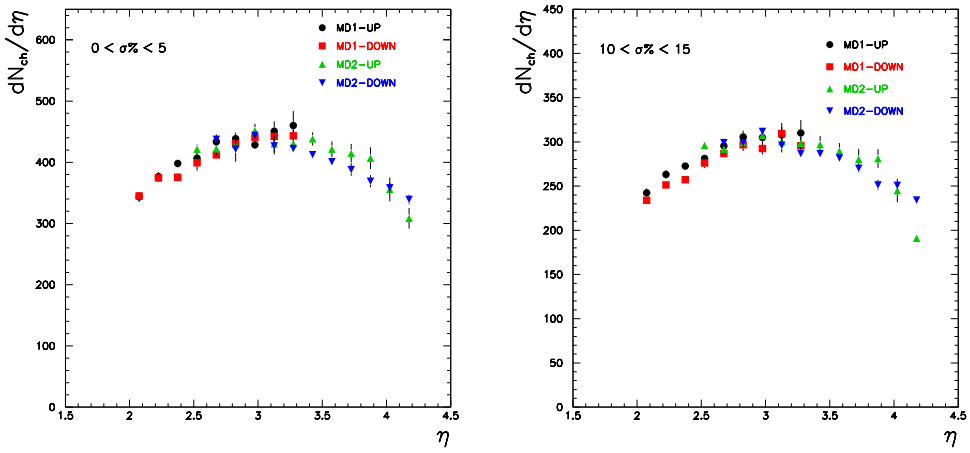

Figure 6.7: *$dN_{ch}/d\eta$ particle distributions obtained from the 4 MD layers, for the 0-5% and the 10-15% centrality classes of the 158 GeV/nucleon data sample with a 3 mm thick target.*

As a final check, for the 158 GeV/nucleon data sample, the complete procedure is applied to two data samples with different target thickness and position: the results agree, as shown in Fig. 6.8.

Including other error sources not discussed so far, as uncertainties on the discrimination threshold of the front-end electronics channels, possible misalignments of the detectors and influence of the primary particle composition (depending on the VENUS model) on the Monte Carlo secondary/primary correction factor, we estimate the overall systematic error on the evaluated multiplicity to be below 8%. For the 40 GeV/nucleon data, since only one centrality estimator is used, a larger systematic error (10%) is estimated.

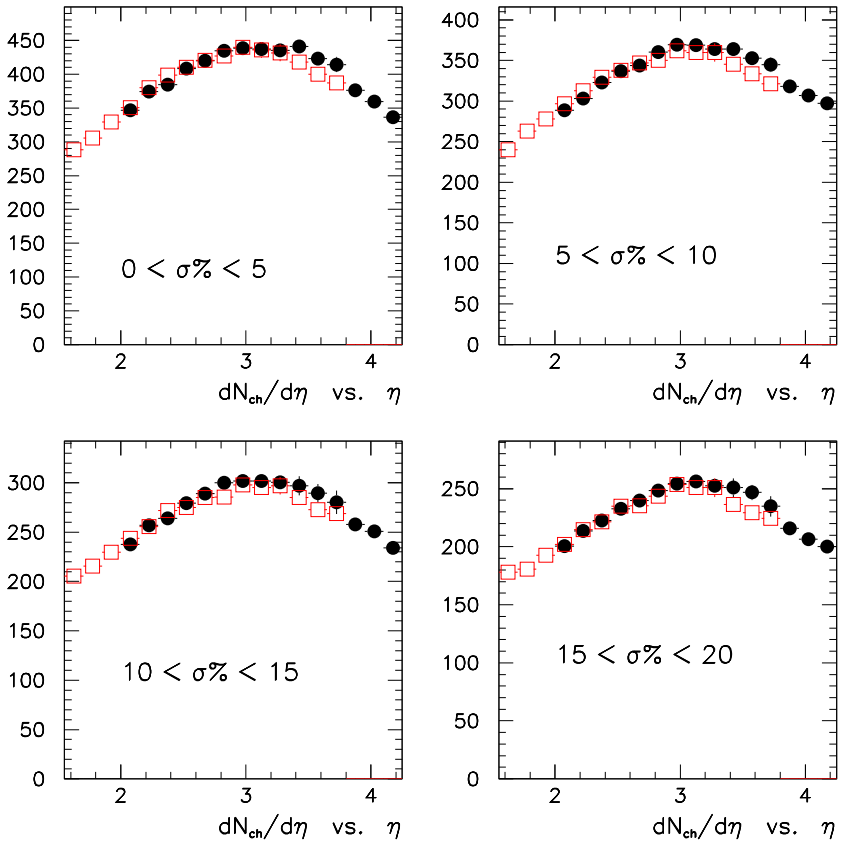

Figure 6.8: *Comparison of corrected pseudorapidity distributions for the 1 mm (open squares) and the 3 mm (closed circles) targets; the two targets were placed 2.5 cm apart and lead to different η regions covered by MD.*

6.3 Charged particle pseudorapidity distributions

6.3.1 Results at 158 GeV/nucleon

The pseudorapidity distributions of charged particles obtained using E_{ZDC} and E_T as centrality estimators are shown respectively in fig. 6.9 and 6.10.

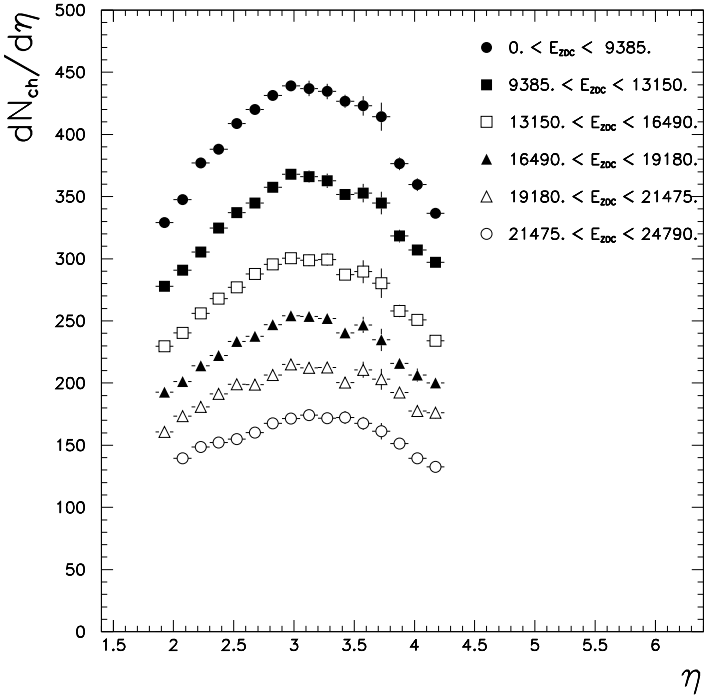

Figure 6.9: *$dN_{ch}/d\eta$ distributions at 158 GeV per nucleon, obtained using E_{ZDC} as centrality estimator. The 8% systematic error on the multiplicity evaluation is not included in the data points.*

The pseudorapidity coverage is approximately centered at midrapidity and extends over $\sim$ 2.2 units, so that the $dN_{ch}/d\eta$ peak is visible in the pseudorapidity distributions without any reflection around midrapidity. The

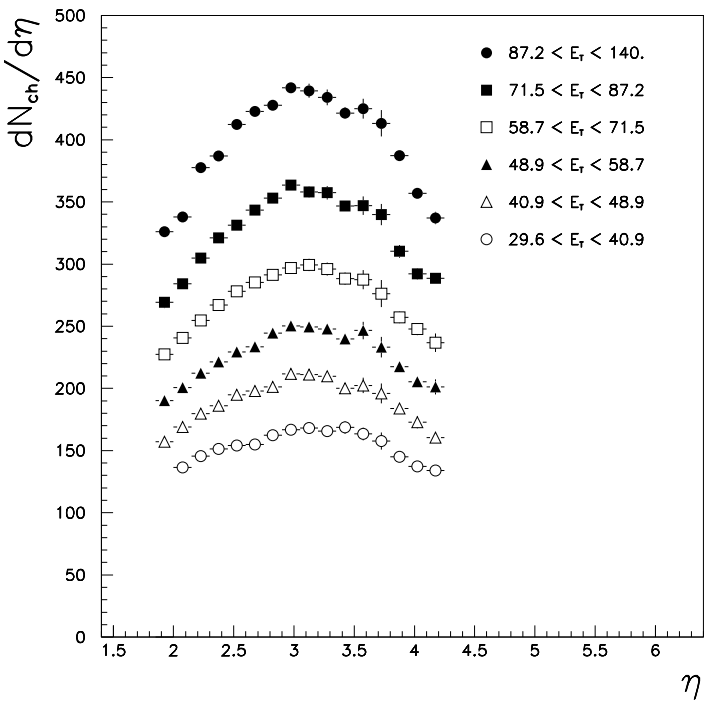

Figure 6.10: *$dN_{ch}/d\eta$ distributions at 158 GeV per nucleon, obtained using E_T as centrality estimator (8% systematic error not included in the data points).*

peak of the distributions is expected at:

$$y_{max} = 0.5 \cdot y_{beam} = 0.5 \cdot \frac{1}{2} \cdot \ln\left(\frac{1+\beta_{beam}}{1-\beta_{beam}}\right) = 2.91$$

where $\beta_{beam} = p_{beam}/E_{beam} = 0.99998$. Then, according to VENUS, a shift of $\approx$0.2 units between y_{max} and η_{max} has to be applied, obtaining $\eta_{max} \simeq 3.1$, in good agreement with what is observed in the experimental distributions. The $dN_{ch}/d\eta$ distributions are rather symmetrical around the peak and their heights increase steadily with increasing centrality.

The $dN_{ch}/d\eta$ distributions have been integrated in the range $2.45 < \eta < 3.65$ (approximately symmetric around midrapidity) and divided by the width of the pseudorapidity interval considered ($\Delta\eta = 1.2$), to obtain the

average value of the charged particle pseudorapidity density at midrapidity ($< dN_{ch}/d\eta >|_{mid}$).

Depending on the variable (E_T or E_{ZDC}) used as centrality estimator, two different values of $< dN_{ch}/d\eta >|_{mid}$ have been obtained. The relative difference between these two estimations amounts to $\simeq 1.5\%$ for the five most central classes, while for the most peripheral class it is below 3%.

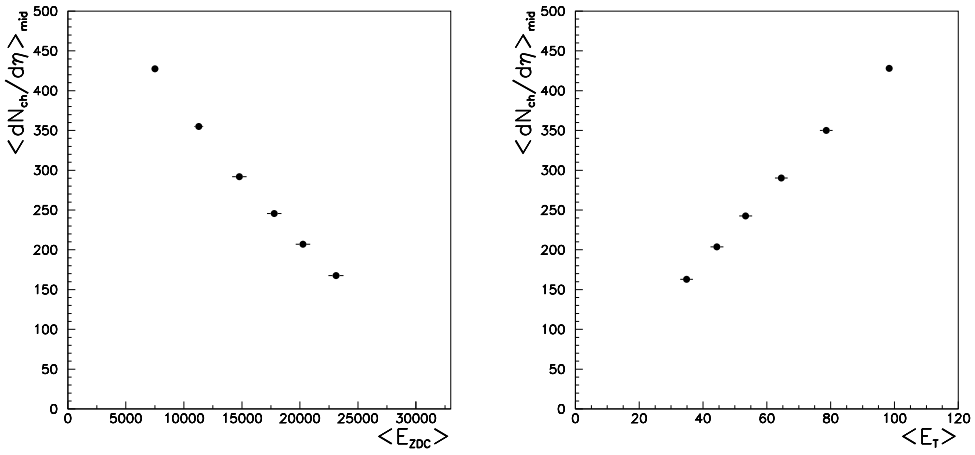

Figure 6.11: *Average charged particle pseudorapidity density at midrapidity as a function of E_{ZDC} (left panel) and E_T (right panel). The 8% systematic error on the charged multiplicity evaluation is not included. The statistical error bars on $< dN_{ch}/d\eta >|_{mid}$ are smaller than the symbol sizes.*

In fig. 6.11 the value of $< dN_{ch}/d\eta >|_{mid}$ as a function of centrality is plotted, showing an approximately linear dependence of the charged multiplicity on both E_T and E_{ZDC}. The average value of charged particle pseudorapidity density for the most central class of events (0-5% of the total inelastic cross-section) results to be:

$$< dN_{ch}/d\eta >|_{mid} = 428 \pm 1(stat) \pm 34(syst)$$

averaged over the values obtained using E_{ZDC} and E_T as centrality estimators. This result can be compared with the corresponding one extracted from a VENUS 4.12 simulation, which is:

$$< dN_{ch}/d\eta^{VENUS} >|_{mid} = 465 \pm 6.$$

and turns out to be 8% higher than our measured value.

The average primary charged multiplicity in the pseudorapidity range $2.75 < \eta < 3.95$ (approximately equal to the muon spectrometer acceptance) has been calculated by integrating the $dN_{ch}/d\eta$ distributions, obtaining for the 5% most central events:

$$< N_{ch} >|_{2.75<\eta<3.95} = 508 \pm 2(stat) \pm 40(syst)$$

The corresponding VENUS 4.12 prediction is:

$$< N_{ch}^{VENUS} >|_{2.75<\eta<3.95} = 550 \pm 7$$

and overestimates the charged multiplicity by $\approx 8\%$.

6.3.2 Results at 40 GeV/nucleon

The same analysis has been performed on data collected at 40 GeV per nucleon beam energy. The $dN_{ch}/d\eta$ distributions are shown in fig. 6.12.

At this energy, the midrapidity point is given by:

$$y_{max} = 0.5 \cdot y_{beam} = 0.5 \cdot \frac{1}{2} \cdot \ln\left(\frac{1+\beta_{beam}}{1-\beta_{beam}}\right) = 2.27$$

where $\beta_{beam} = p_{beam}/E_{beam} = 0.9997$. Applying the 0.2 unit shift from y_{max} to η_{max} extracted from VENUS, we obtain:

$$\eta_{max} \approx y_{max} + 0.2 \approx 2.47$$

In this case, the MD acceptance is not symmetrical around the peak and covers only the forward rapidity region. Nevertheless, the midrapidity point is inside the η coverage and, as it can be seen in fig. 6.12, the charged particle pseudorapidity distributions reach the maximum in correspondence with the η_{max} expected value.

The average value of the charged particle pseudorapidity density at midrapidity has been evaluated over the interval $2.15 < \eta < 2.90$ approximately symmetric around the midrapidity value $\eta_{max} \approx 2.47$ extracted from VENUS. It scales linearly as a function of E_T, as it can be seen in fig. 6.13.

For the most central class (0-5% of the total inelastic cross-section) it is:

$$< dN_{ch}/d\eta >|_{mid} = 207 \pm 1(stat) \pm 16(syst)$$

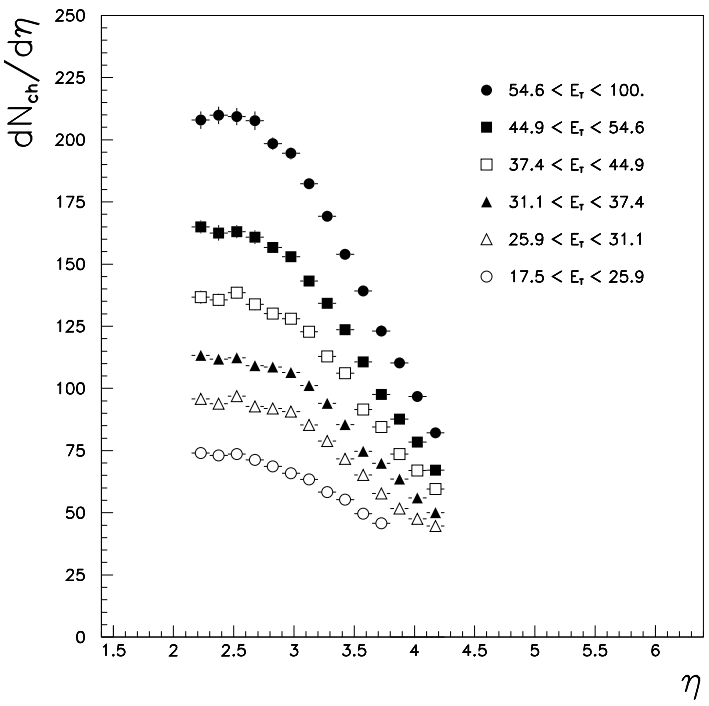

Figure 6.12: *$dN_{ch}/d\eta$ distributions at 40 GeV per nucleon, obtained using E_T as centrality estimator (8% systematic error not included in the data points).*

approximately 2 times smaller than the value measured at 158 GeV per nucleon incident energy.

Furthermore, the average primary charged multiplicity in the NA50 spectrometer acceptance can be evaluated by integrating the the $dN_{ch}/d\eta$ distributions in the range $2.75 < \eta < 3.95$, obtaining for the 5% most central events:

$$< N_{ch} >|_{2.75<\eta<3.95} = 191 \pm 1(stat) \pm 15(syst)$$

which is ≈ 2.9 times smaller than the value measured at 158 GeV/nucleon. The observed difference in the scaling of multiplicity with energy at the peak and in the η range of the spectrometer is due to the fact that at 158 GeV/nucleon the spectrometer acceptance is approximately centered at midrapidity, while at 40 GeV/nucleon it is located beyond the peak in the forward rapidity region which is less populated.

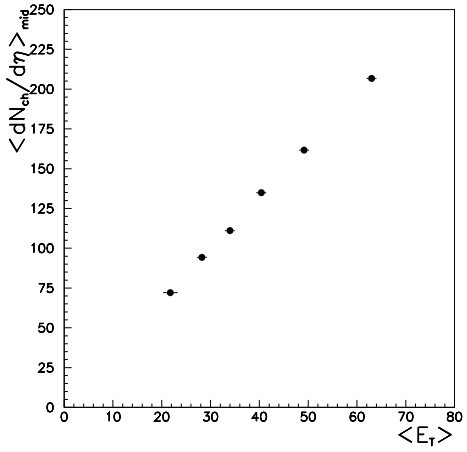

Figure 6.13: *Average charged particle pseudorapidity density at midrapidity as a function of E_T for Pb-Pb collisions at 40 GeV/nucleon beam energy. The 8% systematic error on the charged multiplicity evaluation is not included.*

6.3.3 Gaussian fits to particle pseudorapidity distributions

The $dN_{ch}/d\eta$ distributions thus obtained have been fitted with gaussian functions, to obtain an estimate of the charged particle pseudorapidity density at the peak ($dN_{ch}/d\eta\ |_{max}$), of the peak position (η_{max}) and of the gaussian width (σ_{gaus}). We emphasize that, thanks to the wide η coverage ($\sim$ 2.2 units) approximately symmetric around the peak, the mid-rapidity point η_{max} is not fixed at the theoretical value, but is left as a free parameter of the fit.

The results of the fits for the 158 GeV data sample with the two independent centrality selections are shown in fig. 6.14 (E_{ZDC} selection) and in fig. 6.15 (E_T selection), together with tables listing the resulting fit parameters. The results obtained with the two independent centrality estimators are in agreement within 1.5% except for the most peripheral class where the difference between the $dN_{ch}/d\eta\ |_{max}$ values amounts to $\simeq$ 2.5%.

In fig. 6.16, the particle pseudorapidity distributions obtained for the data collected at 40 GeV per nucleon beam energy are shown, as well as the values of η_{max}, σ_{gaus} and $dN_{ch}/d\eta\ |_{max}$ resulting from the gaussian fits.

The midrapidity values resulting from the fit to data at 158 GeV/nucleon

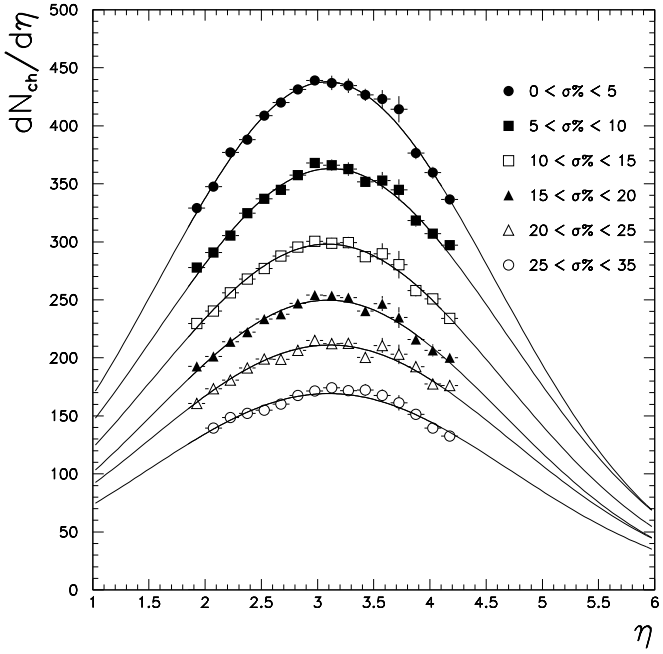

Class	% of c.s.	η_{max}	σ_{gaus}	$dN_{ch}/d\eta\mid_{max}$
1	0-5	3.08 ± 0.01	1.50 ± 0.03	438 ± 4
2	5-10	3.12 ± 0.01	1.56 ± 0.02	363 ± 3
3	10-15	3.09 ± 0.02	1.57 ± 0.04	298 ± 3
4	15-20	3.09 ± 0.02	1.56 ± 0.04	250 ± 3
5	20-25	3.11 ± 0.02	1.62 ± 0.04	211 ± 3
6	25-35	3.10 ± 0.02	1.62 ± 0.05	169 ± 3

Figure 6.14: *Pseudorapidity distributions of charged particles in* $158\,A\,GeV/c$ *Pb–Pb collisions obtained using* E_{ZDC} *as centrality estimator. Gaussian fits are superimposed.*

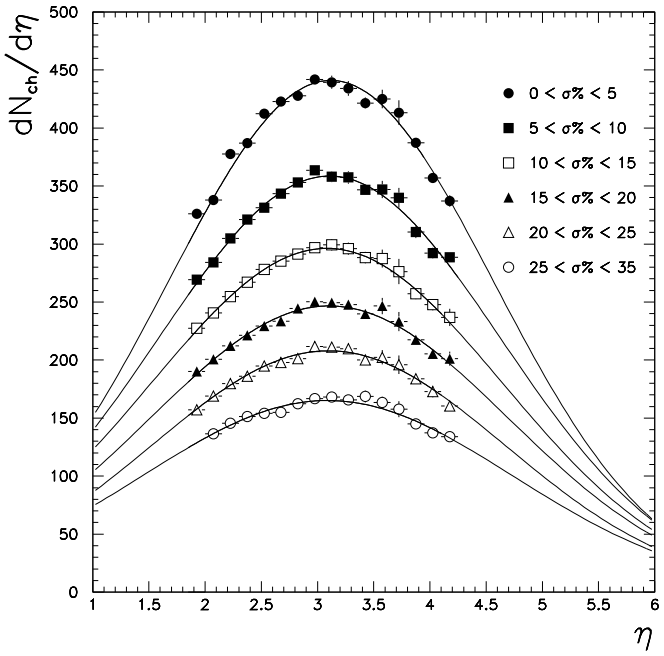

Class	% of c.s.	η_{max}	σ_{gaus}	$dN_{ch}/d\eta \mid_{max}$
1	0-5	3.12 ± 0.01	1.45 ± 0.02	441 ± 4
2	5-10	3.11 ± 0.01	1.53 ± 0.03	359 ± 4
3	10-15	3.08 ± 0.02	1.57 ± 0.04	296 ± 3
4	15-20	3.10 ± 0.02	1.60 ± 0.04	247 ± 3
5	20-25	3.10 ± 0.02	1.58 ± 0.04	208 ± 2
6	25-35	3.09 ± 0.03	1.65 ± 0.06	165 ± 3

Figure 6.15: *Pseudorapidity distributions of charged particles in* $158\,A\,GeV/c$ *Pb–Pb collisions obtained using* E_T *as centrality estimator.*

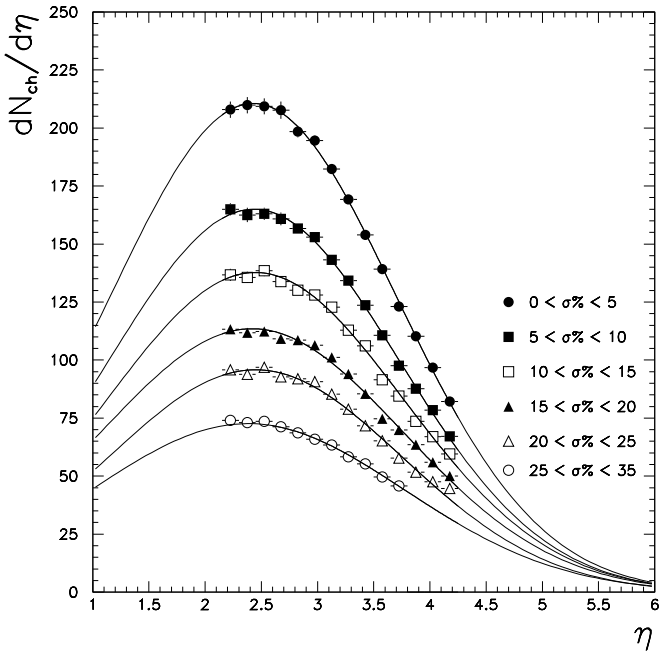

Class	% of c.s.	η_{max}	σ_{gaus}	$dN_{ch}/d\eta \mid_{max}$
1	0-5	2.43 ± 0.03	1.27 ± 0.02	211 ± 4
2	5-10	2.43 ± 0.03	1.29 ± 0.02	165 ± 3
3	10-15	2.45 ± 0.03	1.31 ± 0.02	138 ± 2
4	15-20	2.42 ± 0.03	1.35 ± 0.03	114 ± 2
5	20-25	2.45 ± 0.03	1.31 ± 0.03	96 ± 1
6	25-35	2.38 ± 0.08	1.39 ± 0.06	73 ± 1

Figure 6.16: *Pseudorapidity distributions of charged particles in* $40\,A\,GeV/c$ *Pb–Pb collisions obtained using* E_T *as centrality estimator.*

are in agreement for all the centrality classes defined with both E_{ZDC} and E_T with the expected value $\eta_{max} \approx 3.1$. For the 40 GeV/nucleon data, the values of η_{max} extracted from the gaussian fits to the charged particle pseudorapidity distributions are compatible with the VENUS based expectation ($\eta_{max} \approx 2.47$).

6.3.4 Gaussian width of particle pseudorapidity distributions

The width of the gaussian fit to our pseudorapidity distribution is lower at 40 than at 158 GeV/nucleon, reflecting the fact that the available phase space in rapidity increases with the center-of-mass energy.

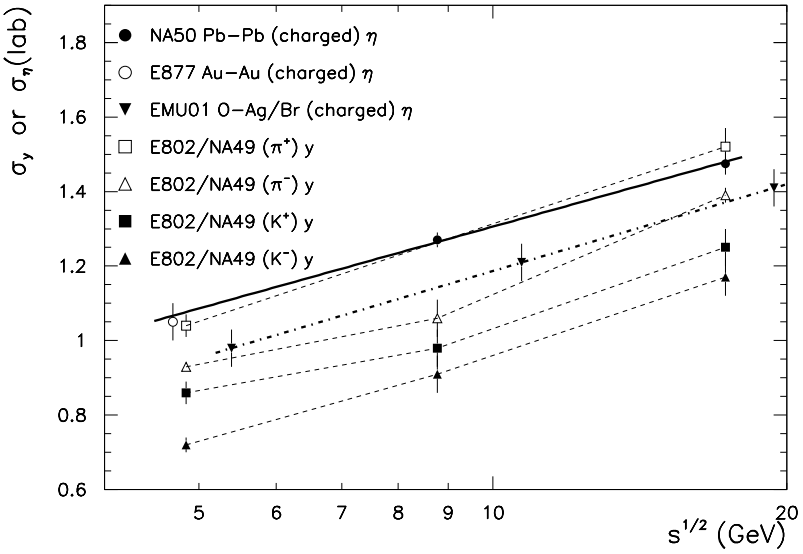

Figure 6.17: *Gaussian width of pseudorapidity or rapidity distributions as a function of center-of-mass energy for ion-ion collisions.*

In Fig. 6.17 we compare our results on the width in central Pb-Pb collisions with existing data at SPS and AGS energies. First, we present the evolution with $\sqrt{s}$ of the gaussian width of $dN_{ch}/d\eta$ for our most central class (0-5%) of Pb-Pb collisions at 40 and 158 GeV per nucleon, together

with the width measured in central Au-Au collisions by the E877 collaboration [5] at 10.8 GeV/c per nucleon. The fit of our results, taken together with the E877 one, to the simple scaling law $\sigma_\eta = a + b \times \ln\sqrt{s}$ [6, 7], gives $\sigma_\eta = (0.58 \pm 0.09) + (0.32 \pm 0.04) \times \ln\sqrt{s}$ (solid line), confirming the already observed fact that the width of the pseudorapidity distribution in central ion-ion collisions at AGS-SPS energies appears to follow a simple logarithmic scaling law independent of system size [1]. It is interesting to note [13] that at 158 GeV/nucleon the width of the rapidity distributions is about twice as large as the one expected from a single thermal source located at midrapidity.

We have also reported in Fig. 6.17 the widths of the rapidity distributions of identified π^+, π^-, K^+ and K^- measured by the E802 collaboration [14, 15, 16] in the 3%-5% most central Au-Au collisions at 11.6 GeV/c per nucleon and by the NA49 collaboration [17, 18, 19] in the 7% (resp. 5%) most central Pb-Pb collisions at 40 (resp. 158) GeV per nucleon (dashed lines connect σ_y values for the same particle species). We note that the widths of the rapidity distributions for identified produced hadrons follow the same scaling vs. $\sqrt{s}$ as the width of the pseudorapidity distribution, and furthermore $\sigma_\eta \approx \sigma_y(\pi^+)$, with $\sigma_y(\pi^+) > \sigma_y(\pi^-) > \sigma_y(K^+) > \sigma_y(K^-)$.

Finally, we have reported in Fig. 6.17 the width of the pseudorapidity distribution in the $\approx$ 10% most central O-Ag/Br collisions (between 14.6 and 200 GeV/c per nucleon) measured by the EMU01 collaboration [20] (triangles and dashed-dotted line), which have the same slope as our data but slightly smaller absolute values (note that slow protons are excluded from the EMU01 measurement).

In fig. 6.18, the width of the gaussian fits to the $dN_{ch}/d\eta$ distributions at 158 GeV/nucleon is plotted as a function of centrality for both centrality estimators. The behaviour of σ_{gaus} as a function of E_T for the 40 GeV/nucleon data is displayed in fig. 6.19. It can be observed that the gaussian widths

[1] A similar scaling law actually holds also for the width of the pion rapidity distribution measured in p-p collisions for the same energy range [8, 9, 10, 11]: $\sigma_y(\pi^+) \approx 0.59 \times \ln\sqrt{s}$ and $\sigma_y(\pi^-) \approx 0.54 \times \ln\sqrt{s}$. The gaussian width of $dN_{ch}/d\eta$ for particles having $\beta > 0.85$ (thus excluding slow protons) measured in p-p collisions at 100 and 200 GeV/c beam momentum [12] is within errors compatible with $\sigma_y(\pi^+)$ at the same energies, confirming a close relationship between pseudorapidity and rapidity widths. So, p-p collisions show a width (for π^+ and π^- rapidity distributions) which is similar to the one of central ion-ion collisions at AGS energy, but then rises slightly faster with $\sqrt{s}$, reaching $\approx$ 20% higher values at the highest SPS energy.

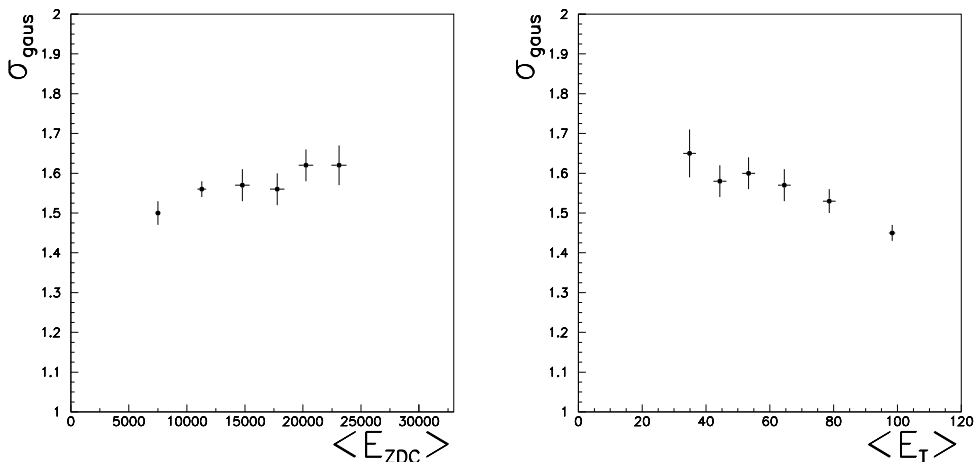

Figure 6.18: *Gaussian width of particle pseudorapidity distributions at 158 GeV/nucleon as a function of a) E_{ZDC} b) E_T.*

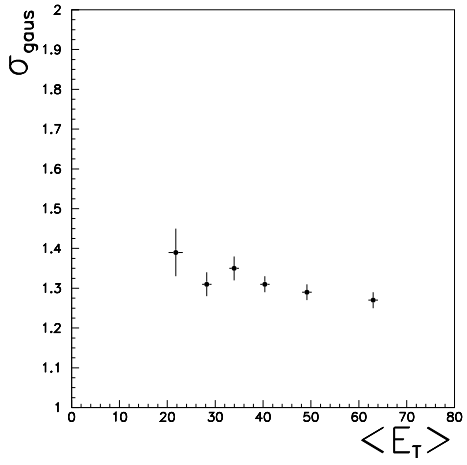

Figure 6.19: *Gaussian width of particle pseudorapidity distributions at 40 GeV/nucleon.*

show a slightly decreasing behaviour with increasing centrality at both energies. The narrowing of the shape of pseudorapidity distributions with increasing centrality has been observed by several other experiments, among which NA35 [21, 22], WA80 [23, 24], NA34/2 [25], HELIOS-Emulsion [26] and E802 [27] [2]. This narrowing can be associated with the higher degree of stopping reached in the interaction [28], and is mostly due to the decreasing contribution of protons from target and projectile fragmentation. In fact, emulsion experiments, which report the distribution of shower particles ($\beta > 0.7$) excluding therefore slow protons from the target fragmentation, usually find a weaker dependence of σ_η on centrality (see e.g. [29]).

6.3.5 Comparison with other SPS experiments

The values of $dN_{ch}/d\eta\ |_{max}$ extracted from the gaussian fits to our charged particle pseudorapidity distributions can be compared with the ones obtained by other SPS experiments.

In particular, particle multiplicities have been studied by NA45, NA49, NA57 and WA98 experiments with the Pb beam at 158 GeV/nucleon energy. At 40 GeV/nucleon, there exist, at the moment, only preliminary results from NA49 and NA45. In table 6.5, the the $dN/d\eta\ |_{max}$ measured by these experiments in the most central class of events are reported together with our results. It can be seen that, overall, our measurements at the two beam energies are within 15% of the other SPS results. The systematic error on our multiplicity evaluation amounts to 8% at 158 GeV/nucleon and to 10% at 40 GeV/nucleon, as explained above.

[2] For example, in the almost symmetric system S-Al at 200 GeV/c per nucleon WA80 measured a decrease of σ_η from 1.55 to 1.3 (16%) when going from peripheral to central events (see fig. 8 in ref. [24]).

158 GeV/nucleon

Experiment	System	σ/σ_{tot} %	$dN_{ch}/d\eta \mid_{max}$
NA50	Pb-Pb	0-5	$439 \pm 3 \pm 35$
NA45 [28]	Pb-Au	0-5	385
NA49 [17]	Pb-Pb	0-5	435[3]
WA97/NA57 [30, 31]	Pb-Pb	~0-4	397[4]
WA98 [32]	Pb-Pb	0-10	440

40 GeV/nucleon

Experiment	System	σ/σ_{tot} %	$dN_{ch}/d\eta \mid_{max}$
NA50	Pb-Pb	0-5	$211 \pm 4 \pm 21$
NA45 [33]	Pb-Au	0.1-4.8	268[5]
NA49 [18]	Pb-Pb	0-7	> 230[6]

Table 6.5: *Comparison of charged particle pseudorapidity density at the peak (for central events) in the laboratory system with the results of other SPS experiments.*

6.4 Evaluation of N_{part} and N_{coll}

An important test for models of particle production in heavy ion reactions is the study of its scaling properties with respect both to the number of participant nucleons (N_{part}) and to the number of binary collisions (N_{coll}). A scaling with N_{part} is expected in scenarios dominated by soft processes,

[3]The NA49 experiment has reported dN/dy measurements for negative hadrons. The $dN_{ch}/d\eta \mid_{max}$ value is calculated as $2.3 \cdot 0.97 \cdot (dN_{h^-}/dy)_{max}$ (where 2.3 is the ratio N_{ch}/N_{h^-} and 0.97 is the correction factor from dN_{ch}/dy to $dN_{ch}/d\eta$, both evaluated with VENUS).

[4]The yield of negative hadrons (see fig. 2 of Ref. [31]) in $\mid y - y_{cm} \mid < 0.5$ was converted to $dN_{ch}/d\eta \mid_{max} \simeq 2.3 \cdot 0.97 \cdot (dN_{h^-}/dy)_{max}$.

[5]The NA45/CERES experiment has reported the value $(dN_{h^-}/dy)_{max}$=120. The $dN_{ch}/d\eta \mid_{max}$ was evaluated as: $dN_{ch}/d\eta \mid_{max} \simeq 2.3 \cdot 0.97 \cdot (dN_{h^-}/dy)_{max}$.

[6]The NA49 experiment has reported at 40 GeV dN_{ch}/dy measurements for identified pions and kaons. The $dN_{ch}/d\eta \mid_{max}$ value is obtained by summing up the π^+, π^-, K^+, K^- and applying the factor 0.97. The contribution of protons is not included, so this is a lower limit.

while a scaling with N_{coll} is expected to be observed in a regime of nuclear reactions where hard processes dominate over the soft particle production. On this respect, the charged multiplicity information may help constrain different models of particle production, and quantify the relative importance of soft versus hard processes in the particle production mechanisms.

For each cross section interval, the average values of N_{part} and N_{coll} have been estimated in the framework of the Glauber model [34].

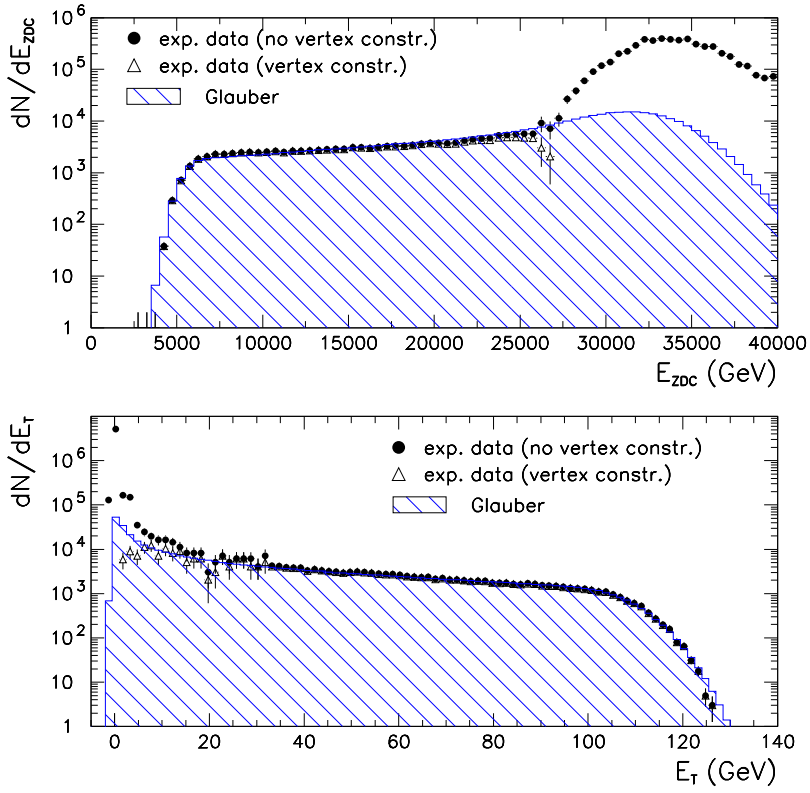

Figure 6.20: *Distributions of the forward energy E_{ZDC} and of the neutral transverse energy E_T in Pb–Pb collisions at 158 GeV per nucleon incident energy. Predictions of the Glauber model are superimposed (hatched histograms).*

The number of participant nucleons and of binary collisions as a function of the impact parameter b have been evaluated according to the formulae discussed in appendix A. Smearing effects due to the experimental resolution

of the calorimeters have also been included in the calculation by assuming that E_T is proportional to the number of participants and E_{ZDC} to the number of projectile spectators (see section A.3):

$$E_T = q \cdot N_{part} \tag{6.4}$$

$$\sigma^2_{E_T} = w \cdot q^2 \cdot N_{part}$$

$$E_{ZDC} = E_{beam} \cdot \left(208 - \frac{N_{part}}{2}\right) + \alpha N_{part} \tag{6.5}$$

$$\sigma^2_{E_{ZDC}} = \left(\beta\sqrt{E_{ZDC}} + \gamma E_{ZDC}\right)^2 + \delta^2$$

where $\beta = 3.39$ GeV$^{1/2}$, $\gamma = 0.062$ [35] and q, w, α and δ are adjusted to fit the Pb-Pb experimental MB spectra. In Fig. 6.20 we show a comparison between the E_T and E_{ZDC} Minimum Bias spectra calculated with the Glauber model and the experimentally measured ones with and without the NOCIMD vertex constraint [7]. The agreement between the data and the model is remarkable. The resulting fit parameters obtained from the 158 GeV/nucleon data sample are listed in table 6.6.

Parameter	Value
q	0.2788 ± 0.0003
w	1.49 ± 0.05
α	8.79 ± 0.04
δ	2.7 ± 11

Table 6.6: *Resulting parameters from a Glauber model fit to the E_T and E_{ZDC} MB spectra at 158 GeV/nucleon.*

Then, on the Glauber spectra, the E_{ZDC} and E_T values corresponding to the total inelastic cross-section fractions used to define the centrality classes listed in tab. 6.2 and 6.3, have been calculated and, in each E_{ZDC} and E_T interval, the distributions of N_{part} and N_{coll} have been built. In fig. 6.21 the distributions of the number of participants nucleons obtained for the 158 GeV/nucleon data sample for the 6 classes defined with E_T centrality selection are shown.

[7] The NOCIMD vertex constraint rejects the non interacting Pb ions whose contribution dominates the spectra at high E_{ZDC}-low E_T.

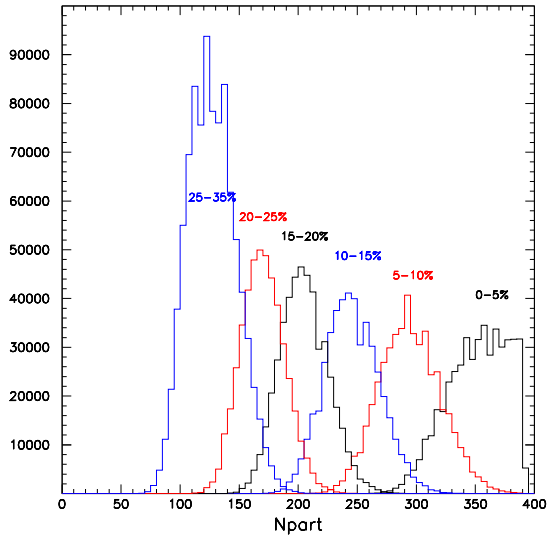

Figure 6.21: *Distributions of the number of participants nucleons at 158 GeV/nucleon beam energy with E_T centrality selection.*

The average values and the RMS of the distributions of N_{part} and N_{coll} at 158 GeV/nucleon for the different centrality classes are reported in table 6.7. It can be seen that the E_T and E_{ZDC} based calculations are generally in good agreement.

For the 40 GeV data sample, only E_T has been used as centrality estimator resulting in a larger uncertainty on the centrality interval definition. The E_T distribution at 40 GeV/nucleon (as it can be seen in fig 6.2) does not exhibit a sharp knee, as it does at 158 GeV/nucleon. This can be connected to the calorimeter resolution and to the fact that not all the data sample cleaning cuts were applied. In particular, it was not possible to use the halo counter cut and the diagonal selection on the E_T-E_{ZDC} correlation, so that the sample of events entering the E_T MB spectrum may be not perfectly cleaned up.

For this reason, we decided to use the N_{part} distributions calculated without including the experimental smearing extracted from the fit to the observed E_T distributions of MB events. The values of $< N_{part} >$ obtained in this way turn out to be in good agreement with the ones obtained at 158 GeV/nucleon energy where the calorimeter resolution is taken into account.

The average values of N_{part} and N_{coll} at 40 GeV per nucleon incident

E_{ZDC} centrality selection

Class	% of c.s.	$< N_{part} >$	RMS N_{part}	$< N_{coll} >$	RMS N_{coll}
1	0-5	354	22	802	66
2	5-10	294	23	634	63
3	10-15	246	25	501	64
4	15-20	205	26	395	65
5	20-25	173	28	316	66
6	25-35	129	35	214	74

E_T centrality selection

Class	% of c.s.	$< N_{part} >$	RMS N_{part}	$< N_{coll} >$	RMS N_{coll}
1	0-5	352	25	796	73
2	5-10	294	26	632	72
3	10-15	245	23	498	61
4	15-20	203	20	392	52
5	20-25	169	19	309	44
6	25-35	127	20	213	45

Table 6.7: *Number of participant nucleons and of binary collisions calculated for the 158 GeV/nucleon data sample for the different centrality classes defined by the two independent (E_{ZDC} and E_T) centrality variables.*

energy are reported in table 6.8.

6.5 Centrality dependence of particle production

To evaluate the centrality dependence of particle production, the scaling behaviour of the $dN_{ch}/d\eta \mid_{max}$ as a function of the number of participant nucleons N_{part} has been parametrized with the usual power law behaviour:

$$\left(\frac{dN_{ch}}{d\eta}\right)_{max} = a \cdot N_{part}^{\alpha}$$

Class	% of c.s.	$< N_{part} >$	RMS N_{part}	$< N_{coll} >$	RMS N_{coll}
1	0-5	356	20	808	58
2	5-10	295	16	635	43
3	10-15	245	13	501	34
4	15-20	204	11	396	27
5	20-25	170	9	310	22
6	25-35	127	15	213	33

Table 6.8: *Number of participant nucleons and of binary collisions calculated for the 40 GeV/nucleon data sample for the different centrality classes.*

The fit has been performed with the technique explained in [36] to take into account also the error on the independent variable N_{part}. The error on the average value of the number of participants has been assumed to be proportional to the RMS of the distribution (quoted in table 6.7 and 6.8), and tuned on the basis of the deviations observed on $< N_{part} >$ when varying the smearing parameters in the Glauber calculations. We thus assume $\delta N_{part} = 0.2 \cdot RMS$ for the 158 GeV sample and $\delta N_{part} = 0.4 \cdot RMS$ for the 40 GeV sample.

The value of the scaling exponent for the 158 GeV/nucleon data sample results to be $\alpha = 1.00 \pm 0.01$ with both the E_T and the E_{ZDC} centrality selections, as it can be seen in fig. 6.22. The systematic error on the α exponent due to the uncertainties on the number of participants has been estimated by a Monte Carlo simulation where the values of $< N_{part} >$ have been varied inside their error bars independently for the 6 centrality classes. The distribution of the α exponent obtained from this Monte Carlo simulation in the case of E_{ZDC} centrality selection is shown in fig. 6.23 and has a RMS $\Delta\alpha = 0.04$. A systematic error on α equal to the RMS of this distribution has thus been assumed.

We can therefore conclude that both centrality selections lead to a scaling of the charged particle production with the number of participants characterized by an exponent:

$$\alpha = 1.00 \pm 0.01(stat) \pm 0.04(syst)$$

This value of α is in agreement with the Wounded Nucleon Model assumption that the average multiplicity in a collision is proportional to the number of

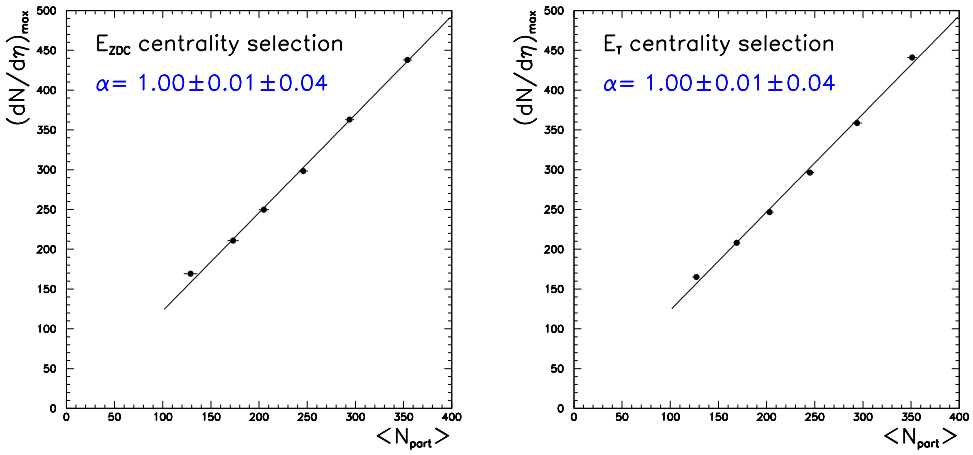

Figure 6.22: *Pseudorapidity density of N_{ch} at midrapidity as a function of the average number of participants ($< N_{part} >$) in 158 GeV/c per nucleon Pb–Pb collisions with the two independent centrality selections. Power-law fits are superimposed.*

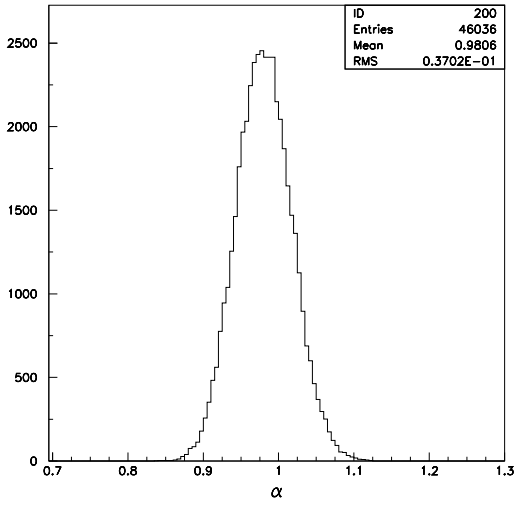

Figure 6.23: *Distribution of α exponent as given by Monte Carlo simulation where $< N_{part} >$ values have been varied inside they error bars.*

participant (wounded) nucleons.

It has to be stressed that the value of the exponent α is strongly dependent on the value of $< N_{part} >$ and may vary significantly as a consequence of slight variations of $< N_{part} >$. Also the $< N_{part} >$ definition plays an important role [37, 38]. For this reason we performed also power law fits using different $< N_{part} >$ evaluations. If the values of $< N_{part} >$ from VENUS 4.12 [3] are used, we obtain $\alpha = 1.08$ with the E_T centrality selection and $\alpha = 1.05$ with the E_{ZDC} selection. For the E_{ZDC} centrality selection we performed also the fit using a straightforward $< N_{part} >$ evaluation, namely $< N_{part} >= 2 \cdot 208 \cdot (1 - E_{ZDC}/E_{beam})$ for which we obtain $\alpha = 1.02$.

Our results for the α exponent of the power law fit to the N_{part} dependence of $dN_{ch}/d\eta \mid_{max}$ can be compared with the results of the WA98 [32] and WA97/NA57 [30] experiments at the SPS. The WA97/NA57 experiment used a Glauber calculation of the number of participants and finds $\alpha = 1.05 \pm 0.05$, which is compatible with our result. The WA98 result ($\alpha = 1.08 \pm 0.03$) has been obtained using a VENUS based estimation of N_{part} and is in agreement with what we find using N_{part} extracted from VENUS.

A fit to the power law $dN_{ch}/d\eta \mid_{max} \propto N_{coll}^{\beta}$ has also been performed, obtaining for the exponent the values $\beta = 0.74$ and $\beta = 0.76$ with E_{ZDC} and E_T centrality selections respectively. Therefore, we can conclude that N_{part} is well suited to describe the scaling of particle production with the centrality of the collision and that a scaling like N_{coll} is not observed at this energy.

Finally, a fit with the function $dN_{ch}/d\eta \mid_{max} = A \times N_{part} + B \times N_{coll}$ has been done, in order to verify the possible presence of a term proportional to the number of collisions. The results of the fits for both centrality selections lead to values of B compatible with zero, indicating that the contribution from hard processes to charged particle production is negligible at this energy.

The same power law fits have been performed to the data sample collected at 40 GeV per nucleon beam energy, obtaining $\alpha = 1.02 \pm 0.02$, as it can be seen in fig. 6.24. The systematic uncertainty on α, coming both from the same Monte Carlo evaluation used for the 158 GeV/nucleon data sample and from neglecting the experimental smearing in the Glauber calculations, is estimated to be 0.06. Therefore, the scaling exponent at 40 GeV/nucleon is determined to be:

$$\alpha_{40} = 1.02 \pm 0.02(stat) \pm 0.06(syst)$$

compatible with the value found at 158 GeV per nucleon. If the values of $< N_{part} >$ from VENUS 4.12 [3] are used instead, we obtain $\alpha = 1.10$,

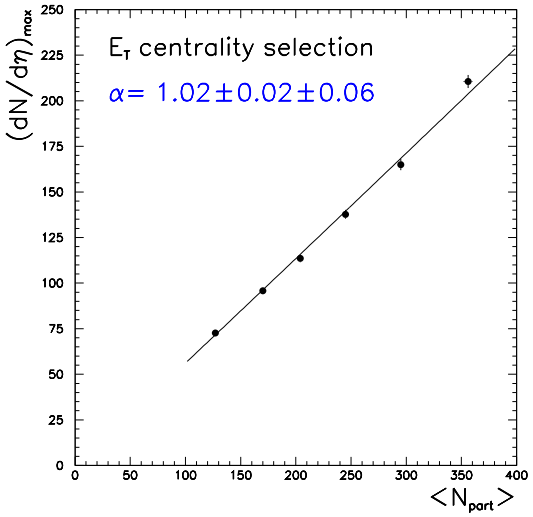

Figure 6.24: *Pseudorapidity density of N_{ch} at midrapidity as a function of the average number of participants ($< N_{part} >$) in 40 GeV/c per nucleon Pb–Pb collisions. Power-law fit is superimposed.*

what confirms the already known fact [38] that VENUS gives an α value systematically ~ 0.08 higher than the analytical Glauber calculation.

6.6 Energy dependence of charged particle production

Another information relevant for constraining particle production models is provided by the study of the scaling of charged particle multiplicity versus $\sqrt{s}$. Results from the analysis presented in this paper, at the two beam energies corresponding to $\sqrt{s} = 8.77$ and 17.3 GeV, are important to enrich the pattern outlined by the results of other experiments at the SPS and RHIC.

In order to examine the energy dependence of charged particle production and to compare our results with the ones obtained for other colliding systems, it is useful to introduce the charged particle pseudorapidity density

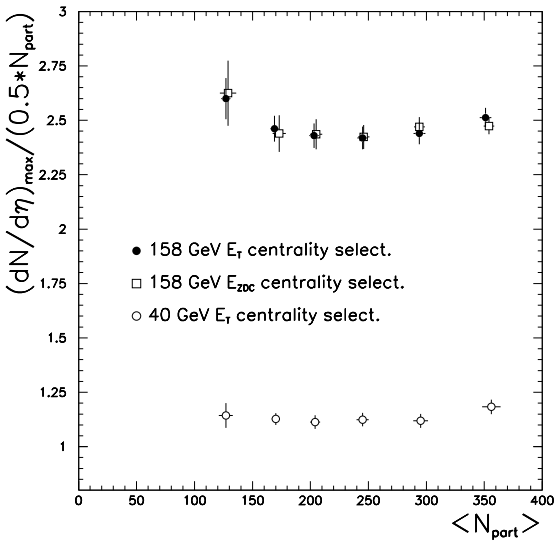

Figure 6.25: *Pseudorapidity density of N_{ch} at midrapidity per participant pair as a function of the average number of participants $< N_{part} >$ in 158·A GeV/c Pb–Pb collisions.*

at midrapidity per participant pair:

$$\left(\frac{dN_{ch}/d\eta \mid_{max}}{0.5 \cdot < N_{part} >} \right)$$

The results are plotted in figure 6.25 as a function of N_{part} (evaluated with Glauber calculations). The error bars take into account the statistical error on $dN_{ch}/d\eta_{max}$ as well as the uncertainty on $< N_{part} >$, while the 8% (resp. 10% at 40 GeV) systematic error on the multiplicity evaluation is not included. The flat behaviour of the charged particle density at midrapidity per participant pair with increasing N_{part} reflects the linear dependence of $dN_{ch}/d\eta_{max}$ on N_{part} pointed out by the power law fits described in the previous section.

In particular, at 158 GeV per nucleon for the 0-5 % centrality range we obtain:

$$\left(\frac{dN_{ch}/d\eta \mid_{max}}{0.5 \cdot < N_{part} >} \right) = 2.49 \pm 0.03(stat) \pm 0.20(syst)$$

which is the average of the values obtained with the E_T and E_{ZDC} centrality selections. The systematic error accounts for the 8% systematic uncertainty on the multiplicity evaluation.

At 40 GeV per nucleon, for the 0-5 % centrality range we obtain:

$$\left(\frac{dN_{ch}/d\eta\mid_{max}}{0.5\cdot < N_{part} >}\right) = 1.18 \pm 0.03(stat) \pm 0.15(syst)$$

The large systematic error bar is due both to the 10% systematic error on the multiplicity and to the uncertainty ($\approx 10\%$) on the evaluation of $< N_{part} >$ for the most central band.

The yield per participant pair thus obtained can be compared to the ones measured at higher energies by RHIC experiments PHOBOS [39, 40], BRAHMS [41] and PHENIX [42]. Since RHIC measurements are performed in the center-of-mass frame, to make a quantitative comparison we need to convert our results, obtained in the laboratory frame, to the center-of-mass frame. For our data at 158 GeV, assuming pions, kaons and protons relative yields as measured by NA49 [17, 43] and using the formula:

$$\frac{dN_{ch}}{d\mathbf{p}_T d\eta} = \sqrt{1 - \frac{m^2}{m_T^2 \cosh^2 y}}\ \frac{dN_{ch}}{d\mathbf{p}_T dy}$$

the measured yield of 2.49 translates into 2.14 ± 0.17. At 40 GeV we use the relative yields as obtained with VENUS 4.12 since the proton fraction has not been yet measured. We estimate that the measured yield of 1.18 translates into 0.97 ± 0.14 in the center-of-mass frame. In fig. 6.26, the pseudorapidity density per participant pair in the center-of-mass frame for the most central ion-ion collision at SPS and RHIC is shown together with some fits to $p\bar{p}$ data. It is important to point out that the yield per participant pair depends on the N_{part} calculation and therefore the comparison of our results with other experiments, which may use different models for the evaluation of N_{part}, is very delicate, even if N_{part} is not strongly model dependent for central collisions [37].

When comparing our results with the charged particle pseudorapidity density measured in nucleon-nucleon collisions we observe that our result at 40 GeV/nucleon is in agreement with the fit to data of inelastic $p\overline{p}$ interactions obtained by the UA5 experiment [44] assuming a logarithmic energy dependence, $dN/d\eta\mid_{max} = (0.01 \pm 0.14) + (0.22 \pm 0.02) \cdot \ln s$. It is also compatible with the UA5 fit obtained assuming a power law energy dependence, $dN/d\eta\mid_{max} = (0.74 \pm 0.04) \cdot s^{(0.105 \pm 0.006)}$. Therefore, we can conclude that the charged particle yield per participant pair at 40 GeV/nucleon is compatible with the one observed in nucleon-nucleon interactions at similar energies.

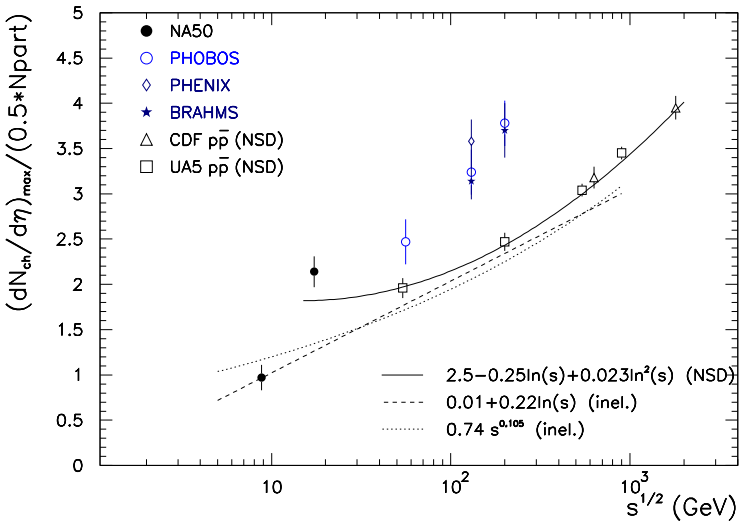

Figure 6.26: *Energy dependence of the pseudorapidity density per participant pair (in the center-of-mass frame) for the most central ion-ion collisions at SPS and RHIC. Fits to $p\bar{p}$ data are superimposed.*

On the opposite our result at 158 GeV/nucleon is more than 50% higher than any of the mentioned fits for the corresponding center-of-mass energy. In addition our result at 158 GeV is also $\sim 20\%$ higher than the fit ($dN/d\eta\mid_{max}= 2.5 - 0.25\ln s + 0.023\ln^2 s$) of the yield obtained by CDF [45] in $p\overline{p}$ non single diffractive interactions for much higher energies. The isospin effect ($\sim 10\%$ among pp, pn and nn interactions [46]) can not account for such a discrepancy as it can be argued also from the fact that our measurement at 158 GeV/nucleon results higher than the one obtained in pp interactions at 200 GeV [47] ($dN/d\eta_{CM} \approx 1.55 \pm 0.04$ after conversion from the measured dN/dy). This comparison suggests a steep increase of particle production in central ion-ion collisions between 40 GeV and 158 GeV which cannot be described by a simple energy scaling as observed in nucleon-nucleon collisions. Therefore, the particle production at 158 GeV/nucleon, although it scales approximately linearly with the number of participants, cannot be explained as an ordinary superposition of nucleon-nucleon interactions.

6.7 Summary and conclusions

The charged particle pseudorapidity distributions ($dN_{ch}/d\eta$) in Pb-Pb collisions at 158 GeV per nucleon ($\sqrt{s}$=17.3 GeV) and 40 GeV per nucleon ($\sqrt{s}$=8.77 GeV) beam energy have been measured in 6 centrality classes defined in terms of fractions of the total inelastic cross-section.

Data at 158 GeV/nucleon have been analyzed using two independent centrality estimators, namely the forward energy E_{ZDC} and the neutral transverse energy E_T. The results obtained are in agreement within $\simeq 1.5\%$ for the four most central classes of events and within 3% for the most peripheral events considered in this analysis.

The average charged particle pseudorapidity density in a η interval symmetric around the peak has been evaluated for each centrality class and shows an approximately linear correlation with both measured centrality-related variables (E_{ZDC} and E_T). No saturation or enhancement of the charged multiplicity is observed up to the most central E_T or E_{ZDC} interval considered in this analysis. This conclusion is also valid for the 40 GeV per nucleon data sample for which only the analysis in terms of E_T has been performed.

From the comparison of the data collected at the two energies it results that the charged multiplicity increases by a factor of $\simeq 2$ when going from $\sqrt{s}$=8.77 GeV to $\sqrt{s}$=17.3 GeV.

The $dN_{ch}/d\eta$ distributions have been fitted with gaussian functions, obtaining an estimate of the peak position, of the $dN_{ch}/d\eta$ value at maximum and of the gaussian width. The width of the distributions is larger at 158 GeV/nucleon than at 40 GeV/nucleon beam energy, reflecting the increase with energy of the available phase space in rapidity. Furthermore, it has been observed that the gaussian width at both energies decreases with increasing centrality, suggesting an increase with centrality of the degree of stopping reached in the interaction.

The charged particle pseudorapidity distributions $dN_{ch}/d\eta$ have been studied as a function of the number of participant nucleons N_{part} and of binary nucleon-nucleon collisions N_{coll}.

The charged particle pseudorapidity density at midrapidity scales as N_{part}^{α} with $\alpha = 1.00 \pm 0.01(stat) \pm 0.04(syst)$ at 158 GeV per nucleon beam energy, in agreement with the Wounded Nucleon Model predictions. The presence of a contribution scaling like N_{coll} is not observed, so that hard processes seem to play a negligible role in charged particle production at 158 GeV per nucleon. This is also supported by the fact that the value of the α

exponent is compatible with the one obtained from the data at 40 GeV per nucleon ($\alpha = 1.02 \pm 0.02 \pm 0.06$) where no contribution from hard processes is expected.

The increase of charged particle production at midrapidity between 40 and 158 GeV/nucleon can not be described by the simple energy scaling observed in nucleon-nucleon collisions at similar energies.

Bibliography

[1] H. Dekhissi et al., Nucl. Phys. A662 (2000) 207.

[2] E. Andersen et al. (NA36 collaboration) Phys. Lett. B220 (1989) 328.

[3] K. Werner, Phys. Rep. 32 (1993) 87.

[4] R. Brun et al., GEANT3, CERN/DD/cc/84-1.

[5] J. Barrette et al., *Phys. Rev.* **C 51** (1995) 3309.

[6] J. Stachel, *Nucl. Phys.* **A 525** (1991) 23c.

[7] Stachel and Young, *Ann. Rev. Nucl. Part. Sci.* **42** (1992) 537.

[8] V. Blobel et al., *Nucl. Phys.* **B 69** (1974) 454, report on π^+ and π^- production at 12 and 24 GeV/c.

[9] C. Bromberg et al., *Nucl. Phys.* **B 107** (1976) 82, report on positive and negative hadron production at 102 GeV/c.

[10] T. Kafka et al., *Phys. Rev.* **D 16** (1977) 1261, report on π^+ and π^- production at 205 GeV/c.

[11] M. Aguilar-Benitez at al., *Z. Phys.* **C 50** (1991) 405, report on π^+ and π^- production at 400 GeV/c.

[12] J.E. Elias et al., *Phys. Rev.* **D 22** (1980) 13.

[13] P. Senger and H. Ströbele, *J. Phys.* **G 25** (1999) R59.

[14] L. Ahle et al., *Phys. Rev.* **C 57** (1998) R466.

[15] L. Ahle et al., *Phys. Rev.* **C 58** (1998) 3523.

[16] L. Ahle et al., *Phys. Rev.* **C 59** (1999) 2173.

[17] H. Appelshäuser et al., NA49 Collaboration, *Phys. Rev. Lett.* **82** (1999) 2471.

[18] C. Blume et al. (NA49 collaboration), Quark Matter 01, Proc. Int. Conf. on Ultra-Relativistic Nucleus-Nucleus Collisions, Stony Brook, 2001, to appear on Nucl. Phys. A.

[19] F. Sikler et al., *Nucl. Phys.* **A 661** (1999) 45c and C. Höhne et al., *Nucl. Phys.* **A 661** (1999) 485c.

[20] M.I. Adamovich et al., *Z. Phys.* **C 56** (1992) 509.

[21] A. Bamberger et al., *Phys. Lett.* **B 184** (1987) 271.

[22] A. Bamberger et al., *Phys. Lett.* **B 205** (1988) 583.

[23] R. Albrecht et al., *Phys. Lett.* **B 202** (1988) 596.

[24] R. Albrecht et al., *Z. Phys.* **C 55** (1992) 539.

[25] T. Akesson et al., *Nucl. Phys.* **B 333** (1990) 48.

[26] T. Akesson et al., *Nucl. Phys.* **B 342** (1990) 279.

[27] T. Abbott et al., *Phys. Rev.* **C 45** (1992) 2933.

[28] F. Ceretto et al. (CERES collaboration), Nucl. Phys. A638 (1998) 467c
and F. Ceretto, Ph.D. thesis, Heidelberg 1998.

[29] M.I. Adamovich et al., *Nucl. Phys.* **A 566** (1994) 419c.

[30] F. Antinori et al., WA97 and NA57 Collaborations, Eur.Phys.J. C18 (2000) 57.

[31] E. Andersen et al., WA97 and NA57 Collaborations, Phys.Lett. B449 (1999) 401.

[32] M.M. Aggarwal et al, WA98 Collaboration, Eur. Phys. J. C18 (2001) 651.

[33] H. Appelshäuser et al. (CERES collaboration), Quark Matter 01, Proc. Int. Conf. on Ultra-Relativistic Nucleus-Nucleus Collisions, Stony Brook, 2001, to appear on Nucl. Phys. A.

[34] R.J. Glauber, Lectures in Theoretical Physics, Vol. 1, Interscience publishers, NY 1959, 315.

[35] R. Arnaldi, Ph.D. thesis, Dec. 2000, Universitè Blaise Pascal, Clermont-Ferrand.

[36] J.Orear, Am. J. Phys. 50 (1982) 912,
and Erratum, Am. J. Phys. 52 (1984) 278.

[37] Ben-Hao Sa et al., nucl-th/01080034, August 2001.

[38] N. Carrer, Heavy Ion Forum, CERN, Geneva, 18 June 1999.

[39] B.B. Back et al., PHOBOS Collaboration, Phys.Rev.Lett. 85 (2000) 3100.

[40] B.B. Back et al., PHOBOS Collaboration, nucl-ex/0108009, August 2001.

[41] I.G. Bearden et al., BRAHMS Collaboration, *Phys. Lett.* **B 523** (2001) 227, and I.G. Bearden et al., BRAHMS Collaboration, nucl-ex/0112001, submitted to Phys. Rev. Lett.

[42] K. Adcox et al., PHENIX Collaboration, Phys. Rev. Lett. 86 (2001) 3500.

[43] J. Bächler et al., NA49 Collaboration, *Nucl. Phys.* **A 661** (1999) 45c.

[44] G.J. Alner et al., *Z. Phys.* **C 33** (1986) 1.

[45] F. Abe et al., *Phys. Rev.* **D 41** (1990) 2330.

[46] M. Gazdzicki and O. Hansen, *Nucl. Phys.* **A 528** (1991) 754.

[47] C. De Marzo et al., *Phys. Rev.* **D 26** (1982) 1019.

Chapter 7

J/ψ suppression and the Quark Gluon Plasma

Since 1986, at the CERN SPS, the NA38 and NA50 experiments have studied J/ψ and ψ' production using the $\mu^+\mu^-$ decay channel with incident proton, oxygen, sulphur and lead ions on several targets. This experimental research is based on the Matsui and Satz prediction [1] that a suppression of charmonium yield would be a particularly interesting signature of the phase transition from ordinary nuclear matter to a state of matter in which quarks and gluons are no more confined into hadrons and behave as free particles. Such a state of matter is called Quark Gluon Plasma (QGP) and is expected to be observed in heavy-ion collisions if the critical temperature and energy density required for the phase transition are reached.

7.1 The Matsui and Satz prediction

In 1986 Matsui and Satz [1] predicted that the charmonium yield would be strongly suppressed in a deconfined medium due to the Debye screening of the attractive colour force which binds the c and $\bar{c}$ quarks together. Once the screening radius of the quark colour charge, $r_D(T)$, falls below the binding radius of the quark system, the confining force can not hold the quarks together: the charmonium state is dissolved into its c and $\bar{c}$ constituents, which separate and at hadronization combine mainly with light quarks to form a D and a $\bar{D}$ meson rather than a $c\bar{c}$ bound state. On a microscopic level, it has been argued that only a hot deconfined medium provides sufficiently

hard gluons to dissociate the most tightly bound charmonium states, i.e. the J/ψ (1S state) and the χ_c (1P state) [2, 3].

The main characteristics of some charmonium states are listed in table 7.1, together with their main decay modes (for the χ_c states, only the radiative decays to J/ψ are listed). Among them, the best candidate to probe the phase transition to QGP is the J/ψ meson because:

- The J/ψ probes the state of matter in the earliest stages of the collision, because the $c\bar{c}$ pairs necessary to form a charmonium state can only be produced in hard quark collisions, which occur very rarely and only in the initial instants of the collision evolution.
- The J/ψ is a tightly bound state that can not be easily broken by interactions with the hadronic medium and therefore it carries its original information through the different stages of the reacting medium.
- The J/ψ (as the ψ') has the quantum numbers of the photon and therefore can be studied via its $\mu^+\mu^-$ decay channel, with the advantage that muons are not affected by strong interactions and therefore bring to the detectors an undistorted image of the earliest stages of the collision.

	Quantum numbers	Mass (MeV)	FWHM (MeV)	Decay	B. R. (%)
J/ψ	$1\ ^3S_1$	3096.87 ± 0.04	0.087 ± 0.005	hadrons	87.7 ± 0.5
				e^+e^-	5.93 ± 0.10
				$\mu^+\mu^-$	5.88 ± 0.10
ψ'	$2\ ^3S_1$	3685.96 ± 0.09	0.277 ± 0.031	hadrons	98.1 ± 0.3
				J/ψ+X	55 ± 5
				e^+e^-	0.88 ± 0.13
				$\mu^+\mu^-$	1.03 ± 0.35
χ_{c0}	$1\ ^3P_0$	3415.0 ± 0.8	$14.9^{+2.6}_{-2.3}$	$J/\psi + \gamma$	0.66 ± 0.18
χ_{c1}	$1\ ^3P_1$	3510.51 ± 0.12	0.88 ± 0.14	$J/\psi + \gamma$	27.3 ± 1.6
χ_{c2}	$1\ ^3P_2$	3556.18 ± 0.13	2.00 ± 0.18	$J/\psi + \gamma$	13.5 ± 1.1

Table 7.1: *Characteristics of the charmonium bound states [4]. The quantum numbers are given in the form $n\ ^{2S+1}L_J$ where n is the radial quantum number and S, L and J define spin, orbital and total angular momentum respectively.*

The J/ψ production study is indeed complicated by the fact that, as it can be seen in table 7.1, higher charmonium excitations (such as the ψ' and the χ_c) decay into lower states, so that the J/ψ production in hadronic interactions occurs in a considerable extent through the production and subsequent decay of higher excited $c\bar{c}$ states. In particular the observed J/ψ's in hadron-hadron collisions originate from three different sources: about 62% are directly produced J/ψ's, while $\approx$ 30% come from radiative decay of χ_c mesons and the remaining $\approx$ 8% from ψ' decay [3, 5].

7.2 Absolute cross-section for charmonium production

NA38 and NA51 experiments collected an extensive set of measurements of J/ψ and ψ' production using p, O and S beams on several targets. Successively, the experimental apparatus has been upgraded and the experimental program has been carried on with the Pb beam as well as with proton beams by the NA50 experiment.

In order to compare charmonium production in different colliding systems it is useful to define a cross-section per nucleon-nucleon collision as:

$$\frac{B_{\mu\mu}\sigma_{J/\psi}}{A \times B} \tag{7.1}$$

where $B_{\mu\mu}$ is the branching ratio of J/ψ into two muons and A and B are the projectile and the target mass number respectively. This assumption is based on the fact that charmonium production is a hard process and therefore it should scale as $A \times B$.

The number of J/ψ events is determined by fitting the invariant mass spectrum of opposite sign muon pairs above 2.9 GeV/c^2. The fit is performed including 5 contributions: J/ψ, ψ', Drell-Yan, open charm (i.e. semileptonic decays of D and $\bar{D}$ mesons) and combinatorial background from π and K decays. The analysis method is described in detail in [6], an example of such a fit is shown in fig. 7.1. The shapes of charmonium resonances, open charm and Drell-Yan are extracted from Monte Carlo simulations including the resolution of the NA50 spectrometer, while the combinatorial background is evaluated from the sample of "Like-Sign" muon pairs (i.e. $\mu^-\mu^-$ and $\mu^+\mu^+$) according to the relation:

$$N_{bck} = 2 \cdot \sqrt{N^{++} \times N^{--}}$$

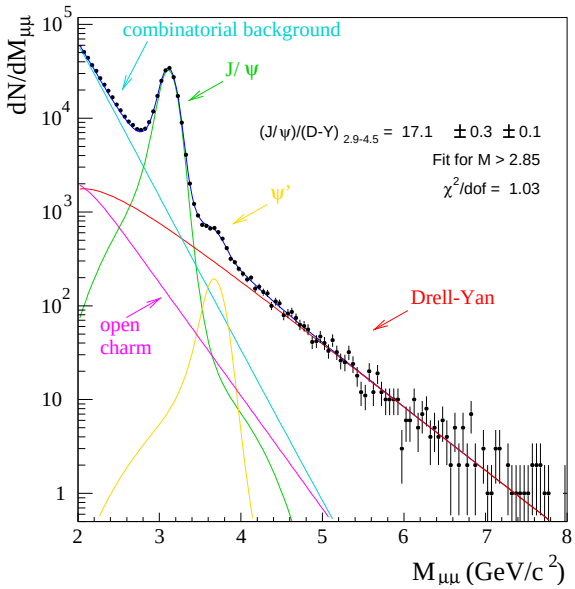

Figure 7.1: *Opposite sign muon pair invariant mass spectrum for Pb–Pb collisions.*

7.2.1 Charmonium production in proton-nucleus interactions

The systematics of J/ψ production measured by NA38 and NA51 in p-p and proton-nucleus can be parametrized as a function of the mass number A of the target nucleus by the simple law:

$$\sigma_A^{\psi} = \sigma_0 \cdot A^{\alpha}$$

with $\alpha = 0.918 \pm 0.015$ [7, 8] in the kinematical domain $0 < y^* < 1$, where y^* is the rapidity in the center-of-mass reference frame.

For a hard process, such as J/ψ production, one naively expects $\alpha = 1$. The deviation from this value, i.e. the less than linear scaling with A of the measured J/ψ yield in p-A collisions, indicates a "suppression" effect. This is commonly interpreted as due to final state interactions between the produced charmonium state and the surrounding matter, i.e. the nucleons of the target nucleus. The observation of a suppression effect depending on the presence of a bulk medium (the nucleus) which is a confined medium, indicates that J/ψ suppression does not generally mean deconfinement.

The A dependence of ψ' cross-section is remarkably similar to the one observed for the J/ψ and can be accounted for by the same exponent α. Since the ψ' has a much larger mean radius than the J/ψ and consequently a larger absorption cross section, the equally strong suppression indicates that the interactions with nuclear matter involve a charmonium state that is not the fully formed J/ψ nor the ψ', but rather a common precursor of them. The exact nature of this pre-resonant state is still debated; in fact, different models of charmonium production have been proposed, see for example [9, 10].

7.2.2 Charmonium production in light ion interactions

When turning to nucleus-nucleus collisions it has to be taken into account that, in addition to the target and projectile nuclei, there could be a substantial amount of produced "secondary" medium (confined or deconfined), which can contribute to the J/ψ absorption. In figure 7.2 the J/ψ cross-section per nucleon-nucleon collision as a function of A×B is shown: it can be seen that the production of J/ψ in ^{16}O and ^{32}S induced reactions follows the nuclear mass dependence of p–A collisions where the formation of a QGP is not expected. All the data from p-p up to central S-U collisions show a continuous and monotonic J/ψ suppression pattern from the lighter to the heavier interacting nuclei [7].

In order to appropriately parametrize the observed J/ψ yield, it is useful to introduce the L variable [11], defined as the length of nuclear matter traversed by the $c\bar{c}$ bound state while escaping from the interaction region. In particular, L is proportional to the number of nucleons that the $c\bar{c}$ pair can potentially interact with, which is given by $\rho \cdot L$, where ρ is the nuclear density. The path length L is evaluated in the framework of the Glauber model [12]. As a first approximation, the J/ψ cross section can be simply parametrized as:

$$\sigma^{\psi}_{AB} = \sigma_0 e^{-(\sigma^{\psi}_{abs}\rho L)}$$

which leads to a J/ψ absorption cross-section of 6.5 ± 1.0 mb. With a full Glauber calculation, a cross section $\sigma^{\psi}_{abs} = 7.2 \pm 1.2$ mb is found [7]. This result indicates that the J/ψ yield in nuclear collisions up to S-U can be understood in terms of ordinary nuclear absorption of a preresonant $c\bar{c}$ state meant to become later on, if not destroyed, the fully formed J/ψ.

On the contrary, the ψ' results to be more suppressed, in S-U reactions,

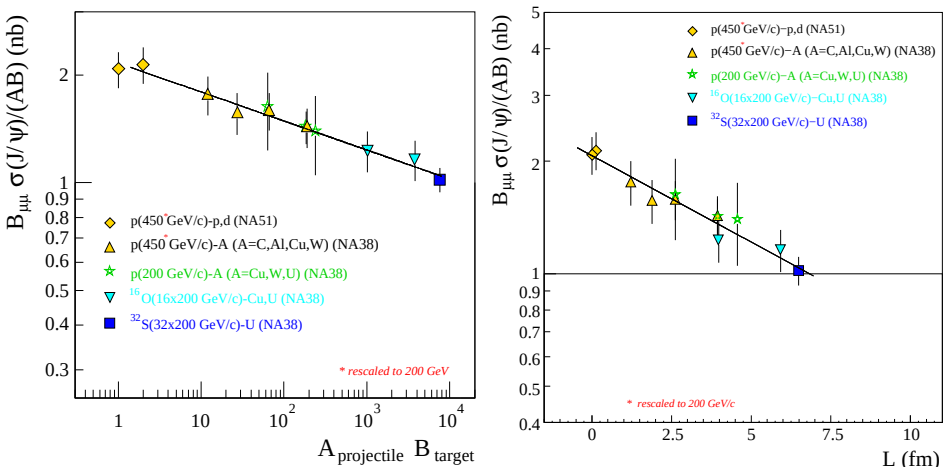

Figure 7.2: *J/ψ cross section as a function of a) $A\times B$ b) L from p–p to S-U interactions.*

than the J/ψ, in marked contrast to what is observed in p-A collisions where the ratio $\sigma_{\psi'}/\sigma_{J/\psi}$ is constant independently of the target mass number. The ψ' suppression beyond the expected pre-resonance nuclear absorption suggests the presence of a secondary medium which can distinguish a ψ' (which is suppressed) from a J/ψ (which remains unaffected). One candidate mechanism to explain this result is absorption by "comovers", i.e. secondary hadrons produced at about the same rapidity as the charmonium, which interact with the fully-formed ψ' state causing its dissociation. The fact that no evident comover absorption effect is present in the J/ψ data can be understood as due to the larger geometrical size of the ψ' and its lower threshold for dissociation with respect to the J/ψ. Therefore, the comover effect should set in much earlier for the ψ' than for the more tightly bound J/ψ resonance, exactly as observed.

Hence, a secondary medium is present, but it shows no indication for colour deconfinement: the phase transition to QGP should then occur at higher energy densities (temperatures) than the ones attained in S-U collisions at 200 GeV/nucleon incident energy. For this reason, data collected with heavier ions are required.

7.2.3 Anomalous J/ψ suppression in Pb–Pb collisions

The J/ψ suppression pattern observed in p-A and light ions interaction sets the baseline with respect to which the pattern of J/ψ production in Pb-Pb interactions should be compared. In fig. 7.3 it can be seen that the J/ψ cross-section measured in Pb–Pb collisions lies below the value expected from the fit to the data from p–p to S–U by a factor $R_K = 0.74 \pm 0.06$, i.e. $\sim$ 5 standard deviations [13]. This result indicates that the J/ψ suppression observed in Pb-Pb interactions cannot be anymore accounted for only by nuclear absorption effects: a new suppression mechanism is present.

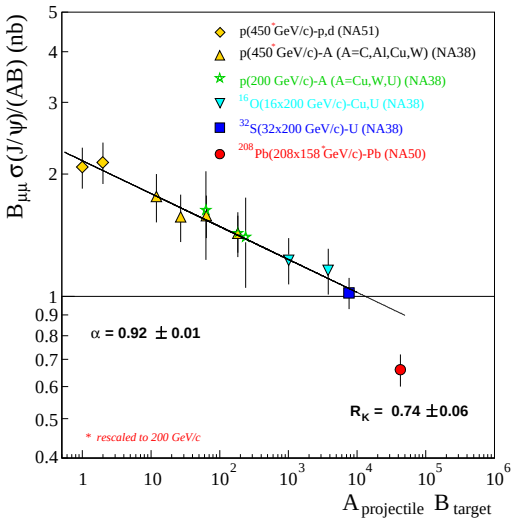

Figure 7.3: *J/ψ cross section as a function of $A \times B$ from p–p to Pb-Pb interactions.*

7.3 Centrality dependence of J/ψ suppression

The nature of the "anomalous" suppression mechanism could be clarified by means of a study of the J/ψ yield as a function of the energy density and/or the temperature reached in the interaction. Since the energy density and the temperature increase with increasing centrality of the collision, i.e. with decreasing impact parameter, it is interesting to study the J/ψ production as a function of the three centrality-related variables (namely the neutral

transverse energy E_T, the charged multiplicity N_{ch} and the forward energy E_{ZDC}) measured by the NA50 apparatus. The sudden onset of deconfinement should manifest itself as a critical behaviour in the J/ψ yield as a function of centrality in correspondence of the energy density (and/or temperature) value required for the phase transition to occur.

In order to perform a study of charmonium production as a function of the collision centrality, it is necessary to find a replacement for the A×B term in the definition (7.1) of the cross section per nucleon-nucleon collision. The best candidate to act as a "reference" is the Drell-Yan process which provides muons in the same mass range as the J/ψ.

7.3.1 The Drell-Yan reference

The Drell-Yan (DY) mechanism consists in the electromagnetic annihilation of a valence quark q of a nucleon with a sea antiquark $\bar{q}$ of a nucleon of the other nucleus. In the annihilation a lepton pair is created through a virtual photon, as shown in fig. 7.4.

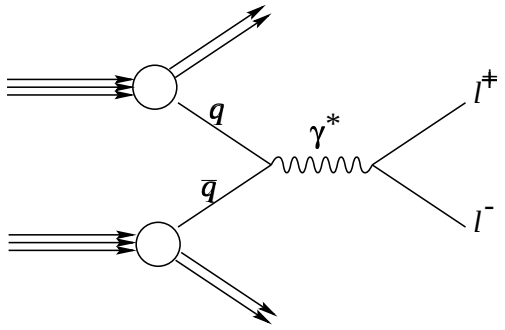

Figure 7.4: *The Drell-Yan process.*

Since leptons interact only electromagnetically, no final state interactions are expected to affect the DY sample. The DY production is a hard process and scales like the number of nucleon-nucleon collision, so that the DY cross-section in collisions between nuclei can be expressed as:

$$\sigma_{AB}^{DY} = \sigma_0 \cdot (A \times B)^1$$

where the exponent $\alpha = 1$ shows that no nuclear absorption is present. This theoretical expectation has been experimentally verified [6], proving that the

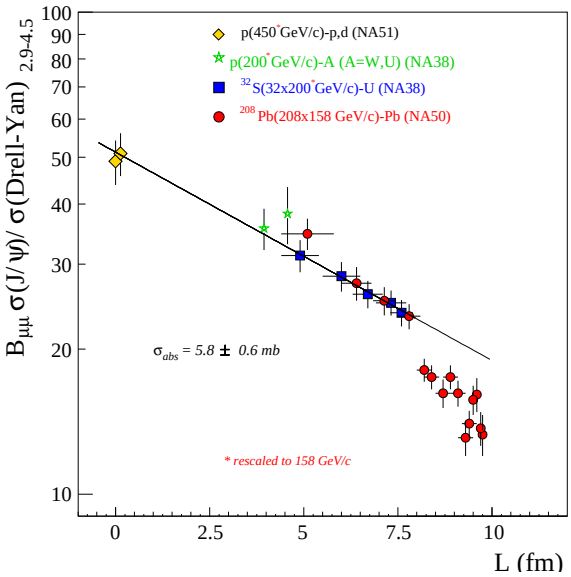

Figure 7.5: *$J/\psi/DY$ as a function of L from p–p to Pb-Pb interactions.*

DY cross section is proportional to the number of nucleon-nucleon collisions without any sizeable nuclear effect.

Hence, the DY mechanism provides a good reference for the study of the charmonium production and the ratio $B_{\mu\mu}\sigma_{J/\psi}/\sigma_{DY}$ can be used to study the centrality dependence of the J/ψ suppression [6], with the advantage that systematic errors related to detector inefficiencies and flux uncertainties are canceled in the ratio of the experimentally measured quantities $\sigma_{J/\psi}/\sigma_{DY}$.

7.3.2 The "standard" analysis

The "standard" analysis method is based on the evaluation of J/ψ and DY cross-sections by means of a fit to the invariant mass spectrum of the $\mu^+\mu^-$ pairs, as described above. The whole sample of muon pairs is divided into subsamples according to the transverse energy (or E_{ZDC} or N_{ch}) of the event; then in each of these subsamples the mass spectra are fitted and the J/ψ over DY ratio is calculated [14]. The result obtained using E_T as centrality estimator and expressed as a function of L is shown in fig. 7.5

The fit to the $\sigma_{J/\psi}/\sigma_{DY}$ data points from p-p to S-U with a simple exponential function ($e^{(-\sigma^{\psi}_{abs}\rho L)}$), which describes the effect of nuclear absorp-

tion, leads to $\sigma^{\psi}_{abs} = 5.9 \pm 0.6$ mb , while the Glauber calculation leads to $\sigma^{\psi}_{abs} = 6.4 \pm 0.8$ mb [7], in good agreement with the values found for the absolute J/ψ cross-section.

It is evident that the "peripheral" Pb-Pb data ($L < 8$ fm) agree with the nuclear absorption curve obtained from lighter systems and that there is a significative and abrupt departure from this behaviour at $L \approx 8$ fm. The anomalous suppression pattern can be seen within the same data sample.

7.3.3 The "Minimum Bias" analysis

The disadvantage of the "standard" analysis is that there are large statistical fluctuations in the $\sigma_{J/\psi}/\sigma_{DY}$ ratio, essentially due to the small statistics of the DY sample. In order to overcome this problem, an independent analysis method has been developed [15] in which the sample of DY events is replaced by the huge sample of events, collected with the Minimum Bias (MB) trigger.

In this analysis method the number of J/ψ events is obtained without any fitting procedure, simply by counting the number of opposite sign muon pairs in the mass range from 2.9 to 3.3 GeV/c^2, after combinatorial background subtraction. In order to compare the results of this analysis with the ones obtained with the standard method, the minimum bias reference has to be converted into the Drell-Yan reference. This is done by multiplying the measured E_T (E_{ZDC}) spectrum of the MB events by the ratio of the theoretical shapes of the E_T (E_{ZDC}) spectra of DY and MB, which can be evaluated in the framework of the Glauber model. The DY spectrum can thus be expressed as:

$$(dN/dE_T)_{DY^*} = (dN/dE_T)^{meas.}_{MB} \cdot \frac{(dN/dE_T)^{th}_{DY}}{(dN/dE_T)^{th}_{MB}} \tag{7.2}$$

where $(dN/dE_T)^{meas.}_{MB}$ is the measured spectrum of MB events, $(dN/dE_T)^{th}_{MB}$ and $(dN/dE_T)^{th}_{DY}$ are the theoretical shapes of transverse energy spectra for MB and DY events respectively. Because of the huge size of the minimum bias sample, this analysis is not affected by statistical fluctuations and a finer E_T (E_{ZDC}) binning is possible. It is also free from most inefficiencies as it is still computed from a ratio of experimental numbers.

The J/ψ over DY ratios obtained with the two independent analysis show a good agreement, as it can be seen in fig. 7.6 where the complete J/ψ suppression pattern obtained with the standard (closed circles) and the minimum

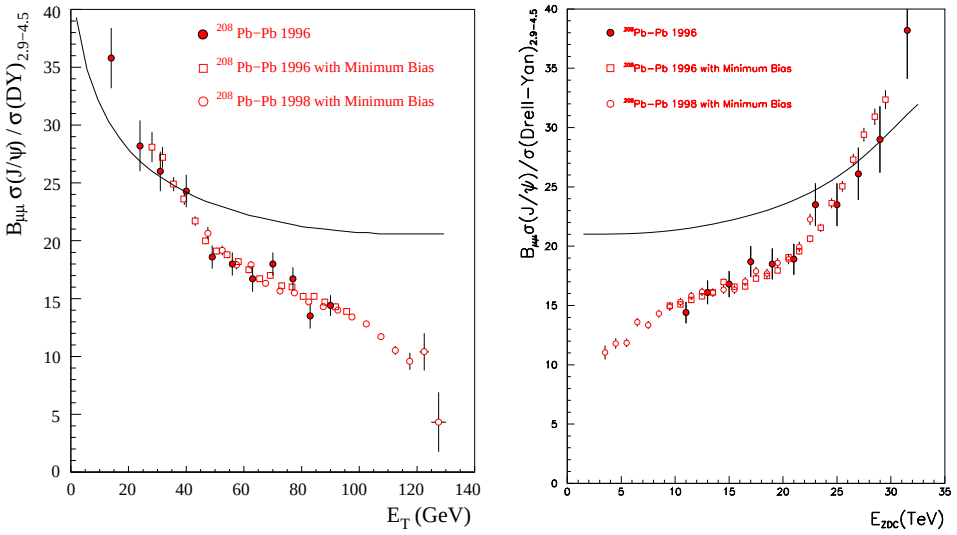

Figure 7.6: *$B_{\mu\mu}\sigma_{J/\psi}/\sigma_{DY}$ ratio as a function of E_T and E_{ZDC}, obtained with the standard and minimum bias analysis of the 1996 and 1998 data samples.*

bias (open points) analysis for the 1996 and 1998 data samples is plotted as a function of the transverse energy E_T [15] and of the forward energy E_{ZDC} [16].

The 1996 data points are plotted only for $E_T < 90$ GeV ($E_{ZDC} > 9$ TeV) because, due to the large thickness of the target (12 mm), the most central events could be affected by a not-negligible contamination from "re-interaction" events [14, 15, 16], i.e. events where a projectile spectator fragment from a first (peripheral) collision interacts again downstream (in a different subtarget) with a nucleus, leading to a measured E_T (E_{ZDC}) value typical of a central collision. If not properly identified and rejected, these events are incorrectly classified as central events inducing a systematic bias in the centrality measurement. In order to limit the effect of re-interactions and clarify the suppression pattern for the most central collisions, during 1998 data taking a thinner target (3 mm) has been used, with the drawback of a higher contamination from Pb-air events in the peripheral region. For this reason, 1998 data have been analyzed only for $E_T > 50$ GeV ($E_{ZDC} < 22$ TeV). In the intermediate centrality range the two data sets show a good agreement.

The solid line visible in figure 7.6 represents the "ordinary" nuclear ab-

sorption of the $c\bar{c}$ pair, which accounts for the J/ψ yield measured in lighter colliding systems (from p-p to S-U). It can be observed that for the most peripheral Pb–Pb collisions the J/ψ suppression can be accounted for by ordinary nuclear absorption while a clear departure from this trend can be seen at $E_T \approx 40$ GeV, ($E_{ZDC} \approx 26$ TeV) which approximately corresponds to an impact parameter $b \approx 8$ fm. It is also evident that there is no saturation of J/ψ suppression for the most central Pb–Pb collisions: a second change of slope in the J/ψ suppression pattern can be observed at $E_T \approx 90$ GeV ($E_{ZDC} \approx 10$ TeV).

7.4 Mechanisms for anomalous suppression

The combined results of the NA38 and NA50 experiments clearly indicate a step-wise J/ψ suppression pattern with no saturation for the most central collisions. A "new" suppression mechanism emerges in Pb-Pb collisions where the J/ψ yield deviates from the exponential behaviour, characteristic of nuclear absorption, which describes p-A and ion reactions up to the most central S-U interactions.

These results triggered a huge amount of theoretical work meant to clarify whether the observed J/ψ suppression pattern is or is not an unambiguous signature of the phase transition to QGP. In order to answer this question, all other conceivable mechanisms that could explain the observed suppression effect without invoking the phase transition need to be ruled out.

The mechanisms proposed to explain the observed "anomalous" J/ψ suppression can be grouped into three main categories:

1) Phase transition to QGP
For each charmonium bound state there exists a critical temperature T_D above which the "Debye" screening radius becomes smaller than the binding radius of the bound state, which consequently disappears. Quantitative calculations of this effect at finite temperature have been performed for charmonium (and bottonium) states in the framework of lattice gauge theory [17], the results are listed in table 7.2.

It can be seen that, while the higher excited states χ_c and ψ', with smaller binding energies and larger radii, break up at the critical deconfinement point, the more tightly bound J/ψ state requires higher temperatures (energies) to "melt". Furthermore, the ψ' has a mass only 50 MeV below the open

state	Binding energy (MeV)	T_D	ε_D
J/ψ(1S)	640	$1.2T_c$	$2\varepsilon_c$
χ_c(1P)	200-250	T_c	ε_c
ψ'(2S)	50	T_c	ε_c

Table 7.2: *Binding energy, critical values of temperature and energy density for Debye screening of charmonium resonances [3].*

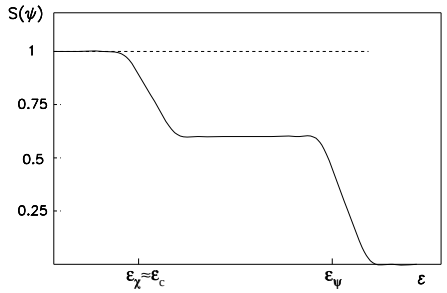

Figure 7.7: *J/ψ suppression pattern (normalized to ordinary nuclear absorption) predicted in the case of deconfinement.*

charm threshold, so that it should be easily dissociated in any (confined or deconfined) medium.

These considerations predict a sequential suppression pattern [3, 17]. First, any medium, confined or deconfined, can lead to ψ' suppression. When the energy density increases beyond the deconfinement point (ε_c), χ_c suppression will set in, and at even higher energies also the directly produced J/ψ will be suppressed. Therefore, apart from the small contribution coming from ψ', the J/ψ suppression pattern is expected to be like the one represented in fig. 7.7, showing two steps in correspondence of the melting of the χ_c and of the J/ψ respectively. This two-step pattern is well suited to explain the experimental result. In this scenario, the first step observed in charmonium suppression can be understood as due to the melting in deconfined matter of the χ_c and the second drop at more central collisions would be due to the dissolving of the more tightly bound J/ψ meson.

2) Quarkonium dissociation in hot media

This mechanism is based on the dissociation of charmonium states into open charm mesons in hot hadronic (confined) media and therefore has nothing to do with deconfinement: in this picture the J/ψ and the ψ' could disappear even if quarks and gluons would remain confined.

It is evident that charmonium states with a mass lower than twice the mass of the D meson (below the open charm threshold) can not dissociate in $D\bar{D}$. Nevertheless, at temperature $T >> 0$, a charmonium state which would be stable at $T = 0$ can be broken up if the gap between its mass and the open charm threshold is overcome, so that the decay into a $D\bar{D}$ pair becomes energetically favorable. This can occur if the energy of the $c\bar{c}$ pair increases due to the thermal motion (thermal dissociation) or if the open charm threshold decreases with temperature as a consequence of a decrease of the string tension term in the strong interaction potential (string breaking).

- *Thermal dissociation.* This model is based on the consideration that the internal states of the charmonium are occupied according to the Boltzman law and as the temperature rises, the probability that higher excited states are occupied increases. Since all those states above the $D\bar{D}$ threshold dissolve, the fraction of thermally dissociated states increases with temperature, leading to a charmonium suppression effect. It has been calculated [18] that, in the temperature range where a hadronic gas is likely to exist ($T < 170$ MeV), thermal dissociation is completely negligible.

- *String breaking dissociation.* In this approach it is considered that, when approaching the point of chiral symmetry restoration, the values of the quark masses and the string tension suffer dramatic modifications that can lead to the reduction of the open charm threshold. In other words, if the mass of the open charm meson decreases with temperature faster than the charmonium mass, at high enough T, the charmonium decay in $D\bar{D}$ becomes possible.

  Recent results from lattice QCD calculations [5, 19, 20] of this string-breaking effect are listed in table 7.3, where it can be seen that the χ_c and the ψ' dissolve well below the critical temperature T_c of the phase transition to QGP. Evidently, this result shows that the χ_c dissociation alone can not be used as a possible signal for the onset of deconfinement because it is dissociated for $T < T_c$ by hadronic in-medium effects. On

the contrary, the more tightly bound J/ψ state survives beyond T_c, so that the dissociation of the directly produced J/ψ mesons should occur only through color screening in a deconfined medium.

state	ΔE (MeV)	T_{diss}/T_c
J/ψ(1S)	640	1.10
χ_c(1P)	200-250	0.74
ψ'(2S)	50	0.1-0.2

Table 7.3: *Dissociation parameters (energy gap from open charm threshold and dissociation temperature) for different quarkonium states as obtained from color screening ($T > T_c$) and string breaking ($T < T_c$) [5, 20].*

3) Interaction with co-moving hadrons

In this scenario, the suppression of charmonium production is attributed to interactions with hadrons, called co-movers, produced along with the $c\bar{c}$ pair. Since co-moving hadrons are formed after a proper time $\tau_0 \sim$ 1-2 fm, much greater than the typical formation time of the J/ψ, the interaction with co-movers involves the final fully-formed charmonium state.

In the dense hadronic environment created after hadronization, the J/ψ can be destroyed through an inelastic reaction $J/\psi + h \rightarrow D\bar{D} + X$, where the involved hadrons (h) are mainly π, K and ρ mesons. The kinematical threshold for such a reaction to occur with pions is 640 MeV, while a lower threshold holds for J/ψ dissociation by ρ mesons [18]. At the typical temperatures of a hadron gas ($T \leq 170$ MeV), most of the produced pions do not have sufficient energy to destroy the J/ψ and ρ mesons are far less abundant than pions. So, hadrons above the kinematical threshold for J/ψ dissociation are rare (effective density < 0.1 fm^{-3} even at T=200 MeV [18]) and, consequently, the cross-section for J/ψ dissociation by comovers is expected to be small.

This suppression effect, if present, must be at work also with systems lighter than Pb-Pb and it should increase continuously with increasing the number of comovers, i.e. with the hadron multiplicity, which, according to the wounded nucleon model [21], is expected to scale as the number of wounded nucleons. Under this assumption, the data from p-A to S-U can be

fitted taking into account the combined effect of nuclear absorption and interaction with co-movers, obtaining $\sigma_{nucl.abs.} = 4.1$ mb and $\sigma_{co} = 0.46$ mb [22]. The values of the parameters are reasonable, but then the extrapolation to Pb-Pb fails to explain NA50 data [23], if the co-mover density continues to scale as the number of wounded nucleons (i.e. as E_T). A reasonable agreement with the Pb-Pb data would require a faster than linear rise of the co-mover density with E_T, such as $E_T^{5/3}$ [18], which can be understood by assuming a violation of the scaling of the multiplicity with the number of wounded nucleons and to the presence of an extra term proportional to the number of nucleon-nucleon collisions.

Finally, as it can be seen in fig. 7.8, the experimentally observed suppression is much steeper (when the experimental E_T resolution is taken into account) than the results of the predictions of presently available models of J/ψ suppression based on co-movers absorption, which can not account for a discontinuity in the J/ψ survival probability.

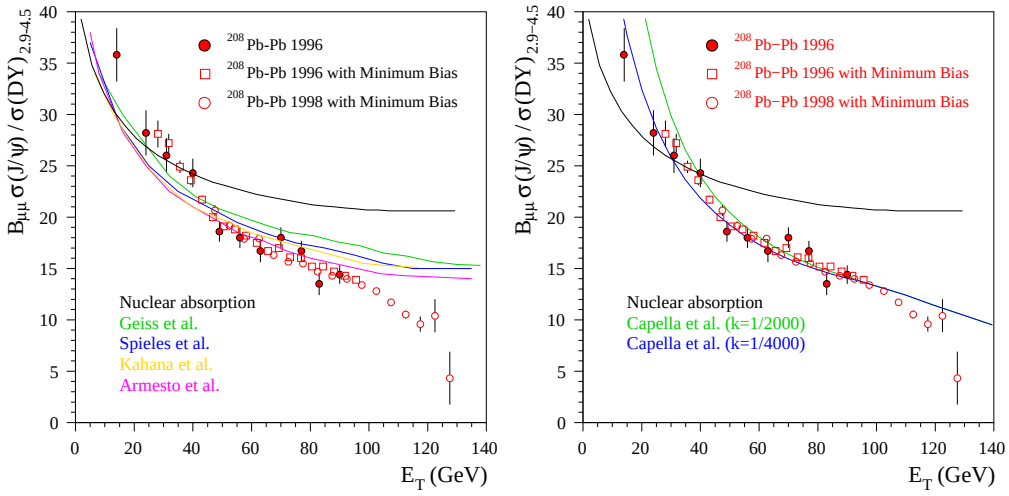

Figure 7.8: *Comparison of the J/ψ suppression pattern observed in Pb-Pb collisions with models assuming J/ψ absorption by interaction with comoving hadrons.*

Bibliography

[1] T. Matsui and H. Satz, Phys. Lett. B178 (1986) 416.

[2] D. Kharzeev and H. Satz, Phys. Lett. B334 (1994) 155.

[3] H. Satz, hep-ph/9711289.

[4] Review of particle physics, The Eur. Phys. Journal C15 (2000).

[5] S. Digal, P. Petreczky and H. Satz, hep-ph/0106017.

[6] M.C. Abreu et al., (NA50 coll.) Phys. Lett. B410 (1997) 327.

[7] M.C. Abreu et al., (NA38 coll.) Phys. Lett. B466 (1999) 408.

[8] M.C. Abreu et al., (NA51 coll.) Phys. Lett. B438 (1998) 35.

[9] R. Vogt, Phys. Rept. 310 (1999) 197.

[10] D. Kharzeev and H. Satz, Phys. Lett. B366 (1996) 316.

[11] C. Gerschel and J. Hufner, Phys. Lett. B207 (1988) 4253.

[12] R.J. Glauber, Lectures in Theoretical Physics, Vol. 1, Interscience publishers, NY 1959, 315.

[13] M.C. Abreu et al., (NA50 coll.) Phys. Lett. B410 (1997) 337.

[14] M.C. Abreu et al., (NA50 coll.) Phys. Lett. B450 (1999) 456.

[15] M.C. Abreu et al., (NA50 coll.) Phys. Lett. B477 (2000) 28.

[16] M.C. Abreu et al., (NA50 coll.) CERN-EP/2001-069, to appear in Phys. Lett.

[17] F. Karsch and H. Satz, Z.Phys. C51 (1991) 209.

[18] B. Muller, Talk given at CERN Heavy Ion Forum, Jun 1997, nucl-th/9806023.

[19] F. Karsch, E Laermann and A. Peikert, hep-lat/0012023 .

[20] S. Digal, P. Petreczky and H. Satz, Phys.Lett. B514 (2001) 57.

[21] Bialas, Bleszynski and Czyz, Nucl. Phys. B111 (1976), 461.

[22] A. Capella et al., Phys. Lett. B393 (1997) 431.

[23] Kharzeev, Lourenço, Nardi and Satz, Z. Phys C74 (1997) 307.

Chapter 8

J/ψ suppression as a function of the transverse energy E_T

The analysis presented hereafter is devoted to the study of the J/ψ production in Pb–Pb interactions as a function of the centrality of the collision, estimated by means of the measured transverse energy E_T. The study is performed on the data collected in 1998 using the MD based target identification (NOCIMD) presented in chapter 4. The use of NOCIMD allows to improve the efficiency of the quartz blade target recognition method for peripheral events and, at the same time, to eliminate the contamination coming from Pb-air interaction. We should therefore be able to extend to more peripheral (low E_T) events the 1998 J/ψ analysis which, as it has been explained in chapter 7, has been performed only for $E_T > 50$ GeV, because of the large contamination from Pb-air interactions which affects the peripheral region.

The analysis is performed using the "Minimum Bias" technique. The aim of this study is to measure the J/ψ/DY ratio for the 1998 data sample in the range $E_T > 15$ GeV where NOCIMD is expected to reject the contamination due to Pb-air events. In this way, the whole J/ψ suppression pattern in Pb–Pb interactions would be observed within a single year data sample.

8.1 The "Minimum Bias" analysis method

As it has been discussed in chapter 7, the "Minimum Bias" analysis has been developed to overcome the problem of the statistical fluctuations on the J/ψ over Drell-Yan ratio, essentially due to the low statistics of the Drell-Yan

(DY) sample. The small sample of directly measured DY events is replaced by the huge sample of Minimum Bias events (MB), which is then converted into the DY reference by means of Glauber model calculations [1], using the strictly related structure of MB and DY spectra in nucleus-nucleus collisions.

Minimum Bias events are the events generated by an incident Pb ion which interacts in the target, without any further requirement. These events are collected with a special trigger which is generated every time a minimum amount of energy is deposited in the ZDC. Even for the most central collisions, a few particles produced in the ZDC angular acceptance provide a signal, while for non-interacting Pb the signal is much bigger.

- The E_T spectrum of MB events in nucleus-nucleus collisions can be described as (see appendix A):

$$\left(\frac{dN}{dE_T}\right)^{th}_{MB} \propto \int 2\pi b\,(1 - P(0,b)) \cdot P(E_T, b) db \tag{8.1}$$

  where the term $2\pi b db$ comes from the collision geometry, $P(0,b)$ represents the probability that no nucleon-nucleon interaction occurs for a given impact parameter b and is evaluated in the framework of the Glauber model. Finally, $P(E_T, b)$ is the probability that a given E_T is measured in a collision with impact parameter b. As explained in section A.3, $P(E_T, b)$ is taken as a gaussian distribution around the mean value $< E_T(b) >$ which, according to the Wounded Nucleon Model [2], is assumed to be proportional to the number of participant nucleons:

$$< E_T(b) >= q \cdot N_{part}(b) \tag{8.2}$$

  with an enlargement due to the detector resolution given by:

$$\sigma_{E_T}(b) = w \cdot q < E_T(b) >= w \cdot q^2 N_{part}(b) \tag{8.3}$$

  The q and w parameters are obtained by means of a fit to the experimental E_T distribution of MB events, while $N_{part}(b)$ is calculated in the framework of the Glauber model.

- The E_T spectrum of DY events can be evaluated from the one of MB events taking into account that the production cross section for hard

processes is proportional to the number of nucleon-nucleon collisions (see appendix A). Hence:

$$\left(\frac{dN}{dE_T}\right)^{th}_{DY} \propto \int 2\pi b\,(1 - P(0,b)) \cdot N_{coll}(b) P(E_T, b) db \tag{8.4}$$

where $P(E_T, b)$ is fixed from the fit to MB spectrum, while $P(0, b)$ and $N_{coll}(b)$ are obtained by means of Glauber calculations.

On the basis of these relations, an estimator of the Drell-Yan spectrum can be obtained as:

$$\left(\frac{dN}{dE_T}\right)_{DY^*} = \left(\frac{dN}{dE_T}\right)^{exp}_{MB} \cdot \frac{\left(\frac{dN}{dE_T}\right)^{th}_{DY}}{\left(\frac{dN}{dE_T}\right)^{th}_{MB}} \tag{8.5}$$

- The E_T spectrum of J/ψ events is obtained simply by counting the number of opposite sign muon pairs in the mass range $2.9 < M_{\mu\mu} < 3.3$ GeV/c^2 after combinatorial background subtraction (see section 8.4.2), without any fit to the $\mu^+\mu^-$ mass spectrum.

Hence, the ratio J/ψ over DY can be estimated as:

$$\sigma_{J/\psi}/\sigma_{DY^*} = \frac{\left(\frac{dN}{dE_T}\right)^{exp}_{J/\psi}}{\left(\frac{dN}{dE_T}\right)_{DY^*}} = \frac{\left(\frac{dN}{dE_T}\right)^{exp}_{J/\psi}}{\left(\frac{dN}{dE_T}\right)^{exp}_{MB}} \cdot \frac{\left(\frac{dN}{dE_T}\right)^{th}_{MB}}{\left(\frac{dN}{dE_T}\right)^{th}_{DY}} \tag{8.6}$$

The cross-section ratio $\sigma_{J/\psi}/\sigma_{DY^*}$, based on the directly counted J/ψ and MB events, can be compared to the usual $\sigma_{J/\psi}/\sigma_{DY}$ ratio obtained from the fits to the invariant mass spectra ("standard" analysis), after adjustment with a free normalization constant. The advantage is that the ratio $\sigma_{J/\psi}/\sigma_{DY^*}$ is free from statistical fluctuations. It is also free from systematic errors connected to inefficiencies, as it is still calculated from a ratio of experimental numbers ($\sigma_{J/\psi}/\sigma_{MB}$). The drawbacks are due to potential systematic effects induced by the use of two data samples (the J/ψ and the MB) collected with different triggers and selected on the basis of different criteria (e.g. no dimuon based geometrical cuts are performed on the MB events).

8.2 Fixing the E_T scales

8.2.1 E_T scale of 1998 dimuon and Minimum Bias events

The MB analysis technique relies on the assumption that a theoretical DY spectrum (DY*) can be calculated from the measured MB spectrum. Since the calculation of the DY* spectrum from the measured MB spectrum is based on the $P(E_T, b)$ term extracted from the MB spectrum, the DY* has by construction the E_T scale of the MB events, which, as explained in appendix B, is not equal to one of the dimuon events, due to the presence of a problem in the trigger timing (Trigger Timing Bug, TTB).

In order to have consistent results, when calculating the ratio J/ψ/DY*, it is mandatory to have the same E_T scale for the J/ψ and the DY* spectra. This means that the E_T scale of dimuon events must be equal to the one of MB events, implying that it is necessary to introduce a correction for the TTB. This correction is based on two hypotheses:

1. Different E_T scales can be compared by means of simple multiplicative factors.

2. The E_T scale is described by the parameter q, which represents the average transverse energy released by each participant nucleon: q must have the same value for spectra collected with the dimuon and the MB trigger.

Practically, one needs to evaluate the q parameter both from the MB spectrum and from an E_T spectrum collected with the dimuon trigger.

For the MB events, q is easily extracted by fitting the E_T distribution of MB events with the Glauber formulae 8.1, 8.2 and 8.3 using the value of E_T written on the 1998 microDST. Due to the presence of distortions in the MB spectra, which will be addressed in the next sections, the fit has been performed only for the most central events, i.e. in the region $E_T > 80$ GeV. This limited range does not affect the evaluation of q because this parameter is determined by the position of the knee and the E_T region used for the fit is wide enough to obtain a good description of the knee, as it can be seen in fig. 8.1. The resulting fit parameters are:

$$q_{MB98} = 0.2809 \pm 0.0002 \text{ GeV} \qquad w_{MB98} = 1.45 \pm 0.03$$

To extract the q parameter which characterizes the dimuon E_T scale, there exist essentially three candidate spectra: the Like-Sign ($\mu^+\mu^+$ and

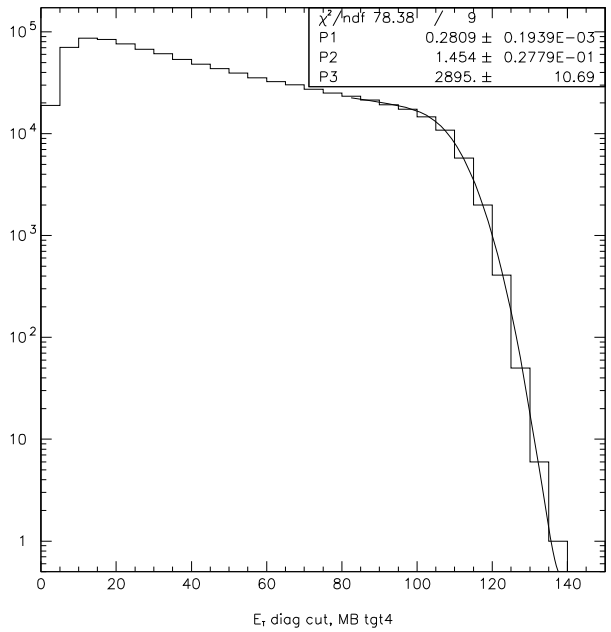

Figure 8.1: *Glauber model fit to the transverse energy distribution of MB events. The value of E_T is the one written on 1998 microDST.*

$\mu^-\mu^-$), the J/ψ and the Drell-Yan spectra. The best candidate would be the Like-Sign (LS) spectrum, because of its high statistics. Unfortunately it is not possible to define how many of the muons of the LS sample originate from decays of particles produced in soft processes (e.g. pions and kaons) and how many instead come from hard processes. For example, it is not easy to establish how big is the contamination from events in which the J/ψ decay generates one μ out of the spectrometer acceptance and one μ in the spectrometer acceptance which, together with another muon originating from a different source, may give rise to a LS muon pair. For this reason, a simple Glauber parametrization of LS spectrum allowing to extract the value of the q parameter is not feasible. On the other hand, the J/ψ distribution can not be used as a reference because it is affected by the anomalous suppression effect which can not be easily parametrized in the Glauber model.

Hence, the Drell-Yan spectrum must be used. The advantage is that there exist simple Glauber formulas (8.2, 8.3 and 8.4) which describe the DY spectrum and allow to extract the q parameter. The drawback is the lack of statistics of the Drell-Yan sample, which is obtained by simply counting

the opposite sign dimuons in the mass range $M_{\mu\mu} > 4$ GeV/c^2, where DY is expected to be the dominant source of muon pairs.

The result of the fit performed on the DY spectrum with the value of E_T written on the 1998 microDST is shown in fig. 8.2. The resulting value of the q parameter is:

$$q_{DY98} \quad = \quad 0.272 \pm 0.002 \text{ GeV}$$

The fit is performed on the interval $E_T > 70$ GeV with the w parameter fixed to the value extracted from the MB sample.

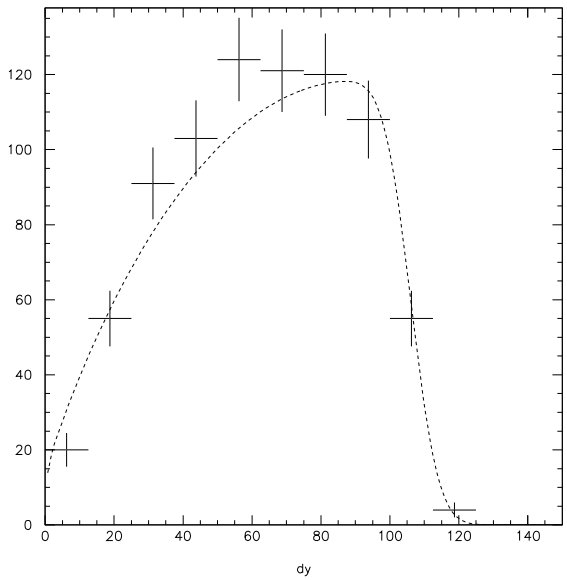

Figure 8.2: *Transverse energy distribution of DY events using the value of E_T written on 1998 microDST. The result of the Glauber fit is superimposed.*

The correction of the TTB therefore requires a rescaling of the 1998 MB E_T by a factor:

$$R(MB98 \rightarrow 2\mu 98) = \frac{q_{DY98}}{q_{MB98}} = \frac{0.272}{0.2809} = 0.968 \tag{8.7}$$

The error on this rescaling factor as given by the propagation of the errors on the fitted q_{MB98} and q_{DY98} is $\sim 1\%$. Possible systematics effects connected with this uncertainty will be discussed later, as well as the ones connected with the E_T range selected for the fits to the experimental spectra.

8.2.2 E_T scale of 1996 and 1998 dimuon events

Once the TTB is corrected, the Minimum Bias analysis can be consistently performed on 1998 data. Then, if the 1998 results are to be compared with the 1996 ones, the two year data samples must have the same E_T scale, which is conventionally chosen to be the one of 1996 dimuon events. As explained in appendix B, a further rescaling of the 1998 microDST E_T is therefore needed:

$$R(2\mu 98 \rightarrow 2\mu 96) = 1.085 \tag{8.8}$$

For 1998 MB events, the combination of the rescaling factor due to TTB correction (eq. 8.7) and of this factor which adjusts the 1998 scale on the 1996 one, gives rise to an overall rescaling:

$$R(MB98 \rightarrow 2\mu 96) = 0.968 \times 1.085 = 1.050 \tag{8.9}$$

8.3 The nuclear absorption curve

The measured J/ψ/DY ratio as a function of centrality in Pb-Pb collisions has to be compared with the result expected in the case that nuclear absorption were the only J/ψ suppression mechanism. A reference curve based on the NA38 p-p, p-A and S-U data is therefore needed. It is obtained by calculating, in the framework of the Glauber model, the ratio between the J/ψ and the DY cross-sections as a function of the impact parameter b and then including the smearing due to the features of the electromagnetic calorimeter.

The production cross-section of J/ψ and DY, both of them being hard processes, is proportional to the number of nucleon-nucleon collisions. For the J/ψ, which suffers from final state interactions, the survival probability to nuclear absorption has also to be taken into account. Hence:

$$\begin{aligned} N_{J/\psi} &\propto P_{int} \times N_{coll} \times \text{nuclear absorption effect} \\ N_{DY} &\propto P_{int} \times N_{coll} \end{aligned}$$

where $P_{int} = 1 - P(0, b)$ is the interaction probability. The charmonium nuclear absorption as a function of the impact parameter is evaluated in the framework of the Glauber model, as explained in section A.2.5. The absorption cross section and the normalization of the curve are fixed by the fit to the J/ψ/DY ratios measured in p-p, p-A and S-U [3]:

$$\sigma_{abs} = 6.4 \pm 0.8 \text{ mb} \qquad N_0 = 50 \pm 3$$

In fig. 8.3a, the curve representing the J/ψ/DY ratio expected from the Glauber calculation of the nuclear absorption is plotted as a function of the impact parameter b. The absorption curve can then be transposed as a function of the transverse energy taking into account the relation between E_T and b given by equations 8.2 and 8.3. The result is shown in fig. 8.3b.

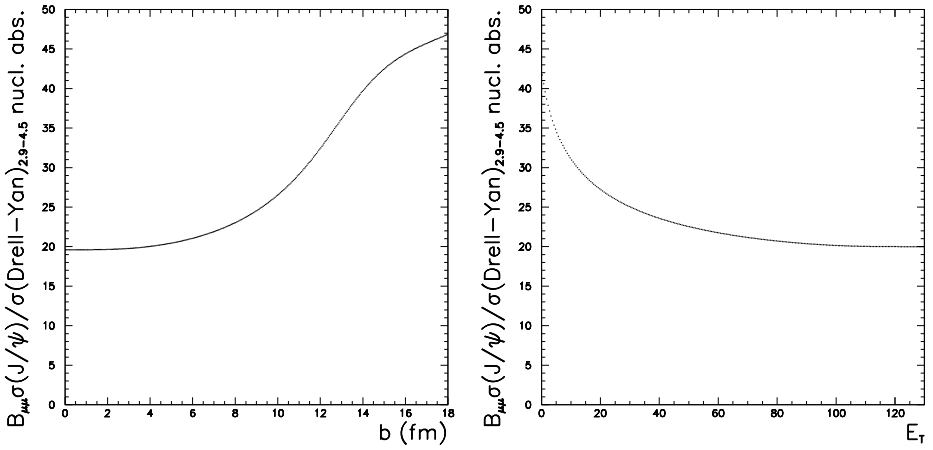

Figure 8.3: *J/ψ/DY ratio expected from the Glauber calculation of the nuclear absorption as a function of (a) impact parameter (b) E_T.*

Similarly, a curve describing the behaviour of the ratio J/ψ/MB expected if nuclear absorption were the only J/ψ suppression mechanism can also be built in the framework of the Glauber model:

$$\begin{aligned} N_{J/\psi} &\propto P_{int} \times N_{coll} \times \text{nuclear absorption effect} \\ N_{MB} &\propto P_{int} \end{aligned}$$

The curve as a function of both b and E_T is shown in fig. 8.4.

8.4 Data analysis

The analysis is performed according to the following procedure. First, events written on 1998 microDST are reprocessed and the E_T value is corrected event-by-event according to equations 8.8 and 8.9. Subsequently, quality cuts are applied. Next the transverse energy distributions of J/ψ and MB

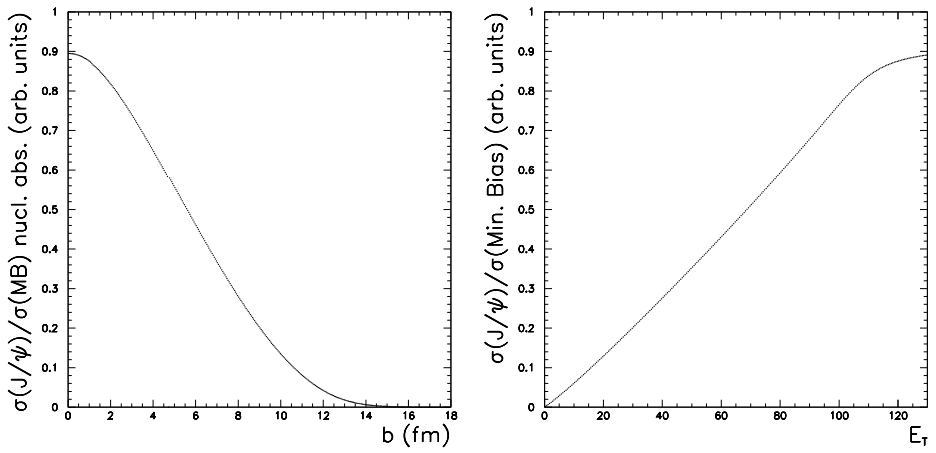

Figure 8.4: *J/ψ/MB ratio expected from the Glauber calculation of the nuclear absorption as a function of (a) impact parameter (b) E_T.*

events are built; the statistics collected in 1998 allows to perform the analysis in E_T bins of width $\Delta E_T = 5$ GeV.

The MB spectrum is then fitted with the Glauber formulae and the theoretical DY spectrum is calculated, allowing to obtain the ratio $\sigma_{J/\psi}/\sigma_{DY^*}$.

8.4.1 Event selection

The selection criteria discussed in chapter 4 are applied to obtain a clean sample of events. In particular, the following cuts are performed:

1. Beam cleaning cuts
2. Diagonal selection on the E_T versus E_{ZDC} correlation
3. Diagonal selection on the $MUL1$ versus E_T correlation
4. NOCIMD target identification
5. Kinematical cuts on muon tracks and 18% global cut (only for dimuon events)

It is important to emphasize that, thanks to the good efficiency of NOCIMD, no subtraction of the Pb-Air events based on empty target runs is needed, thus eliminating a possible source of systematic effects.

8.4.2 Dimuon combinatorial background subtraction

The sample of opposite sign dimuon pairs is the result of the superposition of signal dimuons (e.g. $J/\psi \to \mu^+\mu^-$) and of a certain amount of background originating essentially from uncorrelated decays of π and K mesons:

$$\begin{array}{ll} \pi^+ \to \mu^+\nu & \pi^- \to \mu^-\bar{\nu} \\ K^+ \to \mu^+\nu & K^- \to \mu^-\bar{\nu} \end{array}$$

These processes generate both opposite sign and like sign (LS) dimuons. Hence, the combinatorial background to the interesting opposite sign dimuon signals can be estimated from the LS events which are almost exclusively due to π and K decays.

The number of muon pairs originating from uncorrelated meson decays can be estimated via simple probability calculations, based on the assumptions that the production of positive and negative muons is completely uncorrelated and follows the Poisson statistics. [1]

Let us consider a sample of N_0 dimuon events and let N^+ (N^-) be the number of positively (negatively) charged mesons produced in the interaction and $P(N^+)$ ($P(N^-)$) the associated muon decay probability. The number of $\mu^+\mu^+$ muon pairs (positive Like-Sign dimuons) is given by:

$$N^{++} = N_0 \int A^{++} P(N^+) \frac{N^+(N^+-1)}{2} dN^+ = \frac{N_0}{2} \left(< (N^+)^2 > - < N^+ > \right) A^{++} \tag{8.10}$$

where A^{++} is the acceptance for positive LS dimuons. A similar formula holds for negative Like-Sign dimuons ($\mu^-\mu^-$):

$$N^{--} = N_0 \int A^{--} P(N^-) \frac{N^-(N^--1)}{2} dN^- = \frac{N_0}{2} \left(< (N^-)^2 > - < N^- > \right) A^{--} \tag{8.11}$$

where A^{--} is the acceptance for positive LS dimuons. Analogously, the number of opposite-sign dimuons resulting from π and K decays can be

[1] This is not always the case in the real physical situation where the number of positively and negatively charged mesons are correlated due to the total charge conservation law. However, when the particle multiplicity is high (such as in Pb-Pb collisions) the correlation does not play an important role and the above assumptions are certainly valid. On the contrary, at low multiplicity (such as in p-A collisions) some corrections are needed to take into account charge conservation.

expressed as:

$$N_{bck}^{+-} = N_0 \int A^{+-} P(N^+) P(N^-) N^+ N^- dN^+ dN^- = N_0 < N^+ >< N^- > A^{+-} \tag{8.12}$$

where A^{+-} is the acceptance for opposite sign dimuons. Since the meson multiplicity follows the Poisson law, it is $< N^2 > - < N >^2 = < N >$ and equations 8.10, 8.11 and 8.12 give:

$$N_{bck}^{+-} = 2\sqrt{N^{++} \cdot N^{--}} \cdot \frac{A^{+-}}{A^{++} \cdot A^{--}} \tag{8.13}$$

The application of the image cut (see section 4.1.2) assures that the NA50 spectrometer acceptance for positive and negative muons is the same ($A^{++} = A^{--} = A^{+-}$). Equation 8.13 therefore becomes:

$$N_{bck}^{+-} = 2\ \sqrt{N^{++} \cdot N^{--}} \tag{8.14}$$

Furthermore, during the data taking periods, the sign of the magnetic field in the spectrometer is periodically reversed, so that approximately half of the data is collected with positive and half with negative magnetic field. Since the μ^+ behave in a negative magnetic field like the μ^- in a positive one and viceversa, the reverse magnetic field allows to compensate possible acceptance asymmetries due to inefficiencies of the image cut, thus limiting possible systematic effects. Hence, the background is estimated from the LS sample as: [2]

$$N_{bck}^{+-} = 2\left(\sqrt{N_{(+)}^{++} \cdot N_{(+)}^{--}} + \sqrt{N_{(-)}^{++} \cdot N_{(-)}^{--}}\right) \tag{8.16}$$

where the bottom index between parentheses indicates the sign of the magnetic field.

[2] It is important to stress that this formula is valid only in the case of high multiplicity events, such as in Pb-Pb collisions. Otherwise, if it is necessary to correct for charge correlation effects, equation 8.16 has to be multiplied by a R_{bck} factor:

$$N_{bck}^{+-} = 2 \cdot R_{bck}\left(\sqrt{N_{(+)}^{++} \cdot N_{(+)}^{--}} + \sqrt{N_{(-)}^{++} \cdot N_{(-)}^{--}}\right) \tag{8.15}$$

where $R_{bck} = 1$ in Pb-Pb collisions, while it can be > 1 when the multiplicity is lower, such as in p-A collisions.

8.4.3 The J/ψ spectrum

The number of J/ψ in each E_T bin is obtained by simply counting the "good" opposite sign dimuon events in the mass range $2.9 < M_{\mu\mu} < 3.3$ GeV/c^2 after subtracting the combinatorial background:

$$N_{J/\psi} = \left(N^{+-}\right)_{2.9<M_{\mu\mu}<3.3} - \left(N^{+-}_{bck}\right)_{2.9<M_{\mu\mu}<3.3} \tag{8.17}$$

where N^{+-}_{bck} is given by eq. 8.16. The number of J/ψ events in each E_T bin is shown in fig. 8.5. The J/ψ spectrum extracted from the Glauber calculations (see appendix A) including charmonium nuclear absorption (with cross-section $\sigma_{abs} = 6.4 \pm 0.8$ mb [3]) is superimposed. [3]

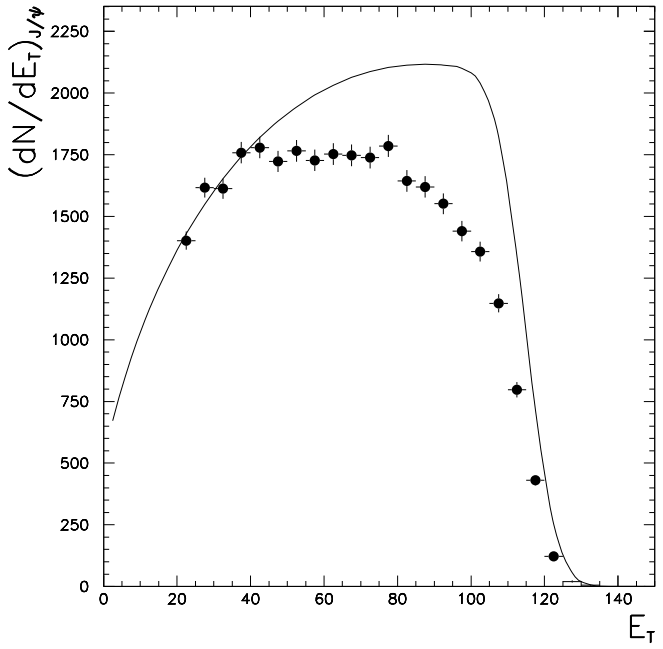

Figure 8.5: *Transverse energy distribution of J/ψ events. The J/ψ spectrum calculated in the framework of the Glauber model in the case of charmonium nuclear absorption with $\sigma_{abs} = 6.4 \pm 0.8$ mb is superimposed.*

[3] The normalization of the Glauber spectrum is tuned on the most peripheral E_T bins, where the nuclear absorption mechanism should account for the observed J/ψ suppression.

It can be seen that the ordinary nuclear absorption accounts for the measured J/ψ spectrum only for $E_T < 35$ GeV: a departure from the nuclear absorption expectation is observed at $E_T \approx 35 - 40$ GeV, in agreement with the J/ψ/DY results obtained from the 1996 data sample (see chapter 7).

8.4.4 The MB spectrum and the ratio ψ/MB

The E_T distribution of Minimum Bias events is shown in fig. 8.6.

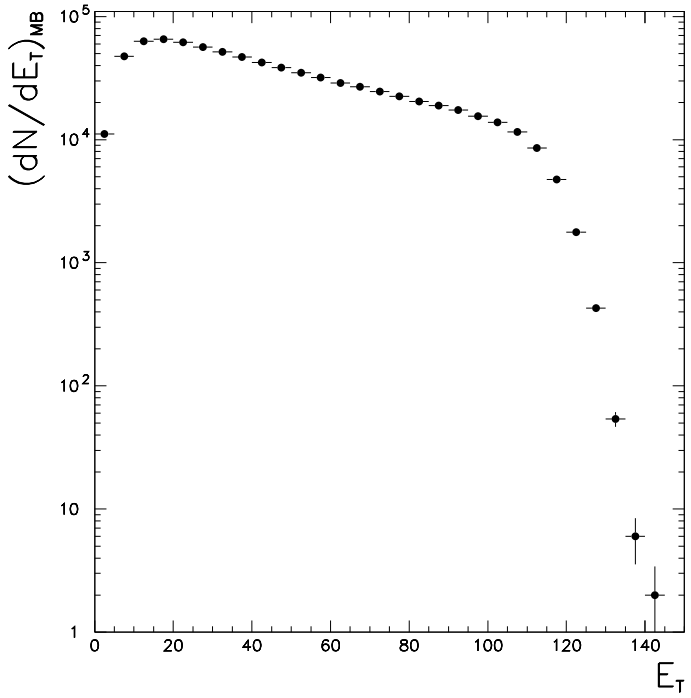

Figure 8.6: *Transverse energy distribution of Minimum Bias events.*

In fig. 8.7 the J/ψ distribution versus E_T directly divided by the measured Minimum Bias sample is shown. The comparison of the data with the continuous line representing the ordinary nuclear absorption [4] reveals the two typical features (the departure from the absorption curve at $E_T \approx 35 - 40$

[4]Since the J/ψ/MB is expressed in arbitrary units, the normalization of the absorption curve is not absolute, but is tuned on the most peripheral E_T bins in which the nuclear absorption mechanism accounts for the observed J/ψ suppression.

GeV and the change of slope at $E_T \approx 100$ GeV) observed in the published analyses (fig. 7.6) where the 1996 and 1998 data were used in limited E_T ranges.

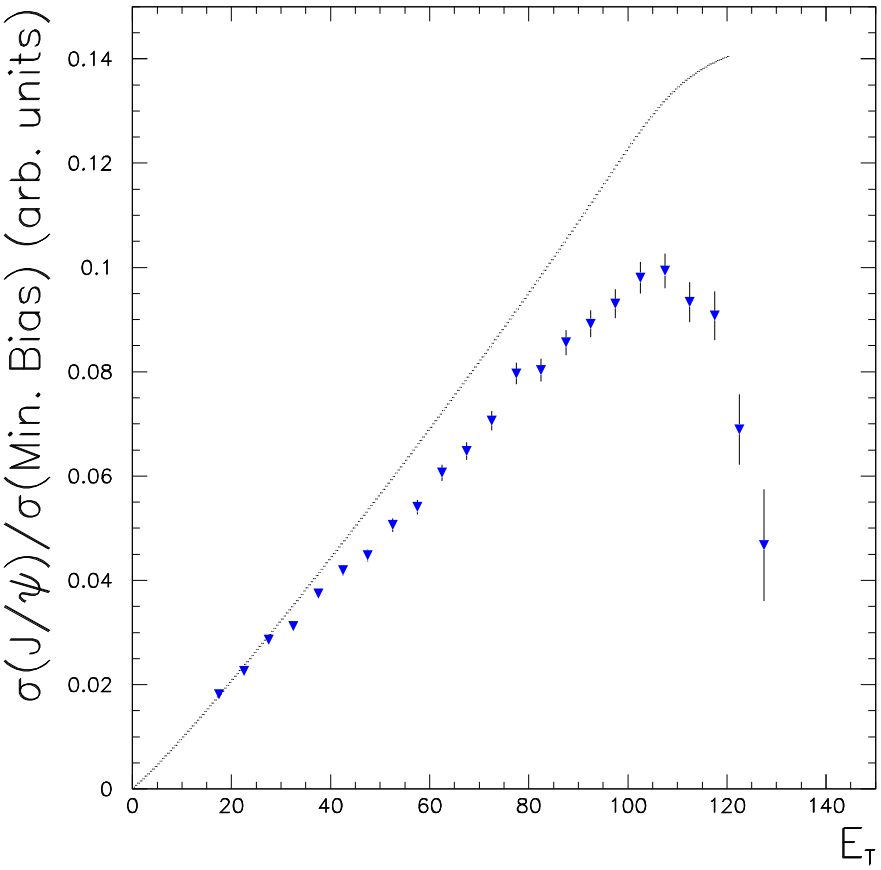

Figure 8.7: *The ratio $J/\psi/MB$ versus E_T. The curve corresponds to the Glauber calculations which accounts for ordinary nuclear absorption with $\sigma_{abs} = 6.4$ mb.*

8.4.5 Glauber fit to the MB distribution

The experimental MB distribution is fitted with the Glauber model formula 8.1 with the aim of extracting the $P(E_T, b)$ term which describes the probability of measuring a given E_T for a certain impact parameter b. The

fit obtained with the simple assumption:

$$< E_T(b) >= q \cdot N_{part}$$

using 3 free parameters (q, w and a normalization constant) is shown in fig. 8.8. It can be seen that the experimental MB spectrum is not satisfactorily described by the model, indicating that the simple assumption of linear E_T dependence on the number of participants is inadequate to fit the experimental data.

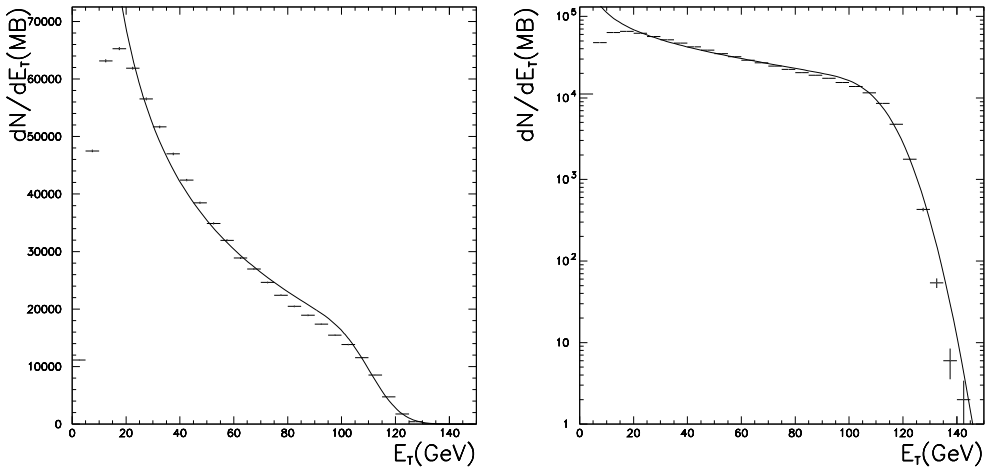

Figure 8.8: *Glauber fit to experimental MB spectrum with the assumption* $< E_T(b) >= q \cdot N_{part}$. *The plot is shown both in linear (left) and in logarithmic (right) scale.*

This non linearity, if not due to physics [5] , may be connected with distortions of the E_T spectra or to problems in the Minimum Bias trigger.

In order to obtain a good description of the experimental data, higher order terms in N_{part} are introduced in the E_T parametrization:

$$< E_T(b) >= q' \cdot N_{part} \cdot \left(1 + \beta q \cdot N_{part} + \gamma\ q^2 \cdot N_{part}^2\right) \qquad (8.18)$$

[5]The physical origin (such as contribution from hard processes) seems to be excluded by the fact that the simple wounded nucleon model assumption $< E_T(b) >= q \cdot N_{part}$ works well at SPS energies. In section 6.4, for example, it can be seen that the E_T and E_{ZDC} spectra of events collected in special low intensity runs is well described by the wounded nucleon model.

The fit is performed in the range $E_T > 30$ GeV where the efficiency of NOCIMD target identification is $\approx 100\%$ (see section 4.4.1) using 5 free parameters, namely q', w', β, γ and a normalization constant. The result of the fit is shown in fig. 8.9 in both linear and logarithmic scale; the quality of the fit is acceptable (χ^2/ndof $= 3.3$). The values obtained for the free parameters are:

$$\begin{aligned} q' &= 0.2912 \pm 0.0005 \text{ GeV} \\ w' &= 1.47 \pm 0.03 \\ \beta &= -0.218 \pm 0.004 \cdot 10^{-2} \text{ GeV}^{-1} \\ \gamma &= 0.199 \pm 0.004 \cdot 10^{-4} \text{ GeV}^{-2} \end{aligned}$$

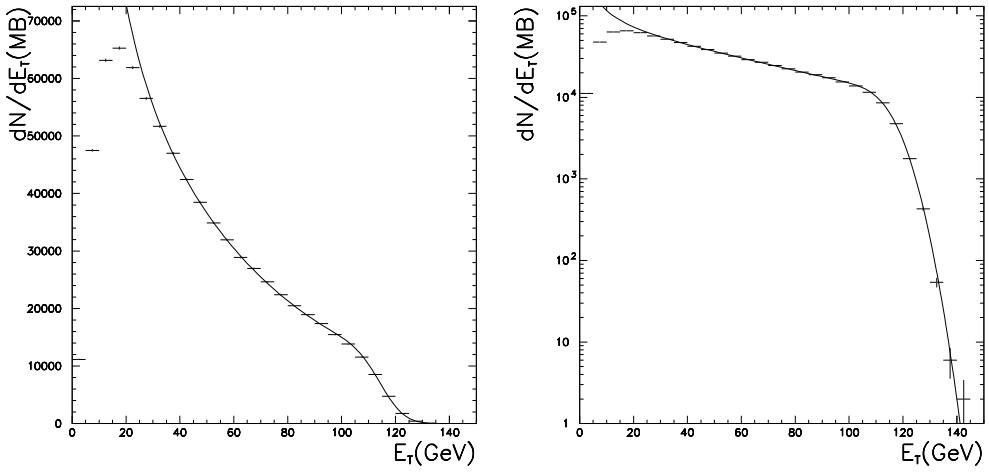

Figure 8.9: *Glauber fit to experimental MB spectrum with the assumption* $< E_T(b) >= q \cdot N_{part} \cdot (1 + \beta q \cdot N_{part} + \gamma\ q^2 \cdot N_{part}^2)$. *The plot is shown both in linear (left) and in logarithmic (right) scale.*

The presence of the higher order terms affects the values of the q' and w' parameters extracted from the fit, and consequently the evaluation of $P(E_T, b)$, which is used to calculated the Dell-Yan spectrum. In other words, q' and w' do not represent the same physical quantities (average E_T per participant and detector resolution) as q and w in the simpler parametrization. The values of q and w can be extracted by means of a fit to the most central region of the MB spectrum ($E_T \geq 90$ GeV) using the simple formula

$< E_T(b) >= q \cdot N_{part}$, as it has been done to correct the E_T scales (see section 8.2). The result of this fit is shown in fig. 8.10; the value of the fitting parameters are:

$$\begin{aligned} q &= 0.2934 \pm 0.0001 \text{ GeV} \\ w &= 1.50 \pm 0.03 \end{aligned}$$

slightly ($\sim 1\%$) different from q' and w'.

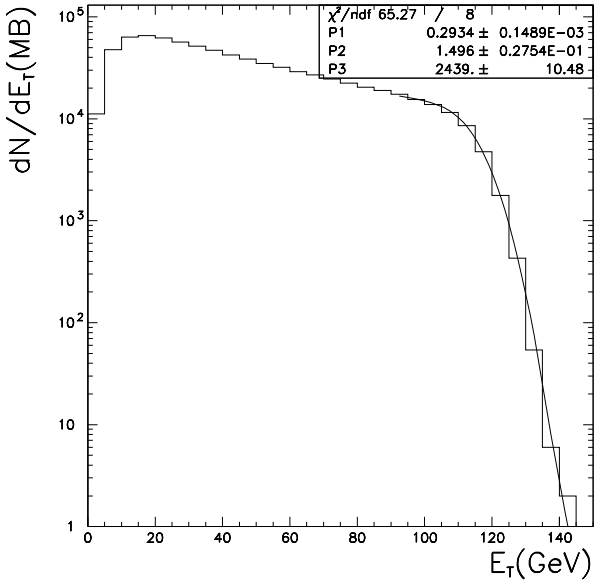

Figure 8.10: *Glauber fit to experimental MB spectrum with the assumption* $< E_T(b) >= q \cdot N_{part}$. *The fit is performed only in the range* $E_T \geq 90$ *GeV.*

8.4.6 The Drell-Yan theoretical spectrum

The theoretical description of the E_T distribution of Drell-Yan events is based on the $P(E_T, b)$ term extracted from the MB spectrum and on the assumption that the Drell-Yan, being a hard process, is proportional to the number of nucleon-nucleon collisions (see equation 8.4). The question that arises at this point concerns which of the two E_T parametrizations is better suited to describe the DY data. In other words, if the distortion of the transverse

energy MB distributions is due to problems in the Minimum Bias trigger timing, the problem should not affect the distributions of events collected with the dimuon trigger which would be well described with the simple assumption $< E_T >= q \cdot N_{part}$. On the contrary, if it is the performance of the electromagnetic calorimeter which causes the distortion of the MB spectra, the parametrization $< E_T(b) >= q' \cdot N_{part} \cdot (1 + \beta q \cdot N_{part} + \gamma\ q^2 \cdot N_{part}^2)$ should be used also for the DY calculation.

In fig. 8.11 the calculated DY spectra resulting from the two E_T parametrization are superimposed to the experimental DY spectrum obtained by simply counting the opposite sign dimuon events with $M_{\mu\mu} > 4$ GeV/c^2, where DY is expected to be the dominant source of muon pairs. Due to the low statistic of the DY sample, bins of $\Delta E_T = 10$ GeV have been considered. The parametrization $E_T = q \cdot N_{part}$ seems to describe better the experimental data, indicating that the distortion is present only in the MB sample.

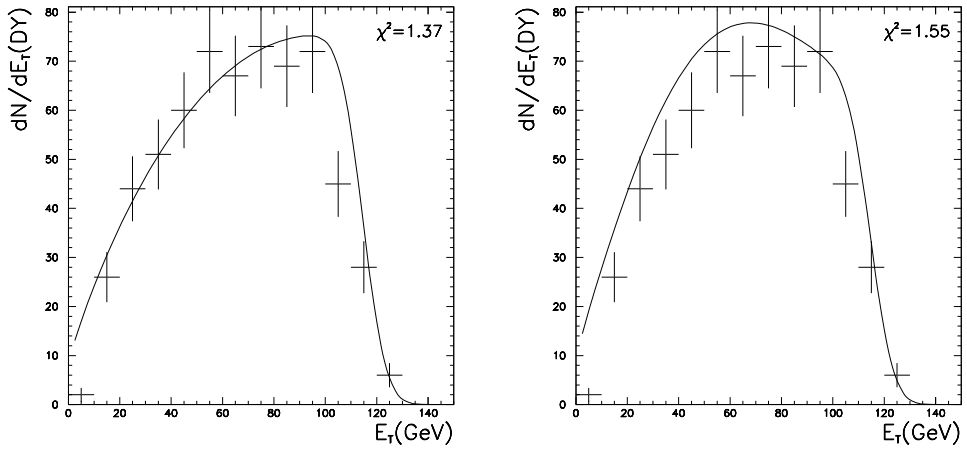

Figure 8.11: *Experimental DY spectrum with theoretical distributions obtained with the two different E_T parametrization superimposed. a) $E_T = q \cdot N_{part}$, b) $< E_T(b) >= q' \cdot N_{part} \cdot (1 + \beta q \cdot N_{part} + \gamma\ q^2 \cdot N_{part}^2)$.*

Subsequently, the ratio:

$$\Theta(E_T) = \frac{(dN/dE_T)^{th}_{DY}}{(dN/dE_T)^{fit}_{MB}} \tag{8.19}$$

is calculated. In principle, $\Theta(E_T)$ should show the behaviour of the number of

nucleon-nucleon collisions as a function of E_T ($N_{coll}(E_T)$) calculated within the Glauber model. The presence of distortions in the MB spectrum (i.e. of the higher-order terms in the E_T parametrization) causes $\Theta(E_T)$ to be different from the expected behaviour $N_{coll}(E_T)$, as it can be seen in fig. 8.12.

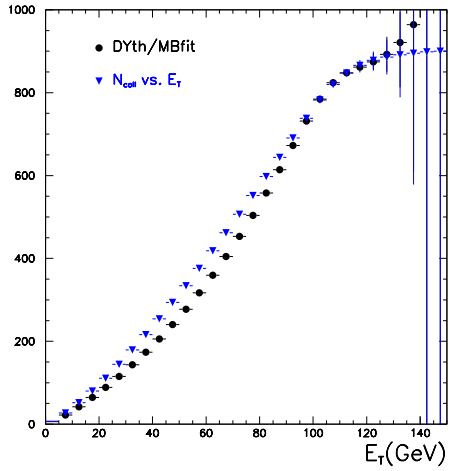

Figure 8.12: *Ratio of DY theoretical distribution to MB fit (closed circles). The calculated number of nucleon-nucleon collisions (triangles) is superimposed.*

Once the Θ function is calculated, the corresponding Drell-Yan estimator (DY^*) can be evaluated:

$$DY^* = \Theta(E_T) \cdot \left(\frac{dN}{dE_T}\right)^{exp}_{MB} \tag{8.20}$$

The comparison between the DY^* thus obtained and the experimental DY spectrum is shown in fig. 8.13: the agreement between the two distributions is good. The DY^* spectrum has much smaller error bars than the experimental DY and shows a smoother trend: the lack of statistic affecting the Drell-Yan sample is thus overcome.

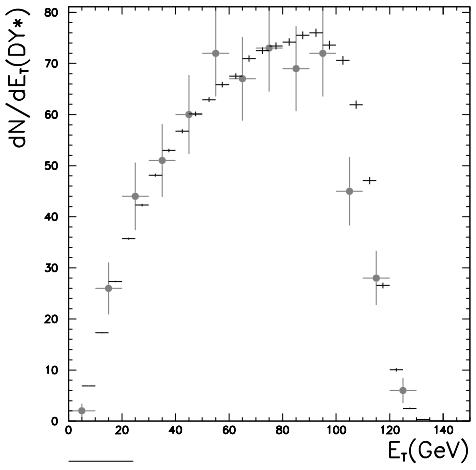

Figure 8.13: *Comparison between Drell-Yan experimental spectrum (closed circles) and the DY* estimator (crosses).*

8.4.7 The J/ψ/DY* ratio

The ratio J/ψ/DY is obtained by calculating:

$$\sigma_{J/\psi}/\sigma_{DY^*} = \frac{\left(\frac{dN}{dE_T}\right)^{exp}_{J/\psi}}{\left(\frac{dN}{dE_T}\right)^{exp}_{MB}} \cdot \frac{\left(\frac{dN}{dE_T}\right)^{fit}_{MB}}{\left(\frac{dN}{dE_T}\right)^{th}_{DY}} = \frac{\left(\frac{dN}{dE_T}\right)^{exp}_{J/\psi}}{\left(\frac{dN}{dE_T}\right)^{exp}_{MB}} \cdot \frac{1}{\Theta(E_T)}$$

Since the DY* spectrum gives the shape of the Drell-Yan distribution, but not its absolute normalization, the ratio $\sigma_{J/\psi}/\sigma_{DY^*}$ thus obtained needs to be normalized to the absolute value of the ratio $\sigma_{J/\psi}/\sigma_{DY}$. This is done by means of a normalization constant estimated from the result of the "standard" analysis of 1996 data in the range $60 < E_T < 100$ GeV, where the J/ψ/DY ratio is nearly flat.

The J/ψ/DY* result is shown in fig. 8.14. The solid line superimposed represents the ordinary nuclear absorption curve. It can be seen that for the most peripheral E_T bins ($E_T < 35$ GeV) the measured J/ψ/DY points are compatible with the expectation based on the charmonium absorption in ordinary nuclear matter. A clear departure from the absorption curve is visible at $E_T \approx 40$ GeV, in agreement with the result of the 1996 data analysis, shown in fig. 7.6. A second change of slope can be observed at

$E_T \approx 100$ GeV. This is compatible with what obtained from the 1998 data analysis with the quartz blades target recognition once the 8% rescaling of the 1998 measured E_T is included (see appendix B). It is important to emphasize again that, thanks to the good efficiency of NOCIMD, the whole J/ψ suppression pattern is obtained from a single year data sample.

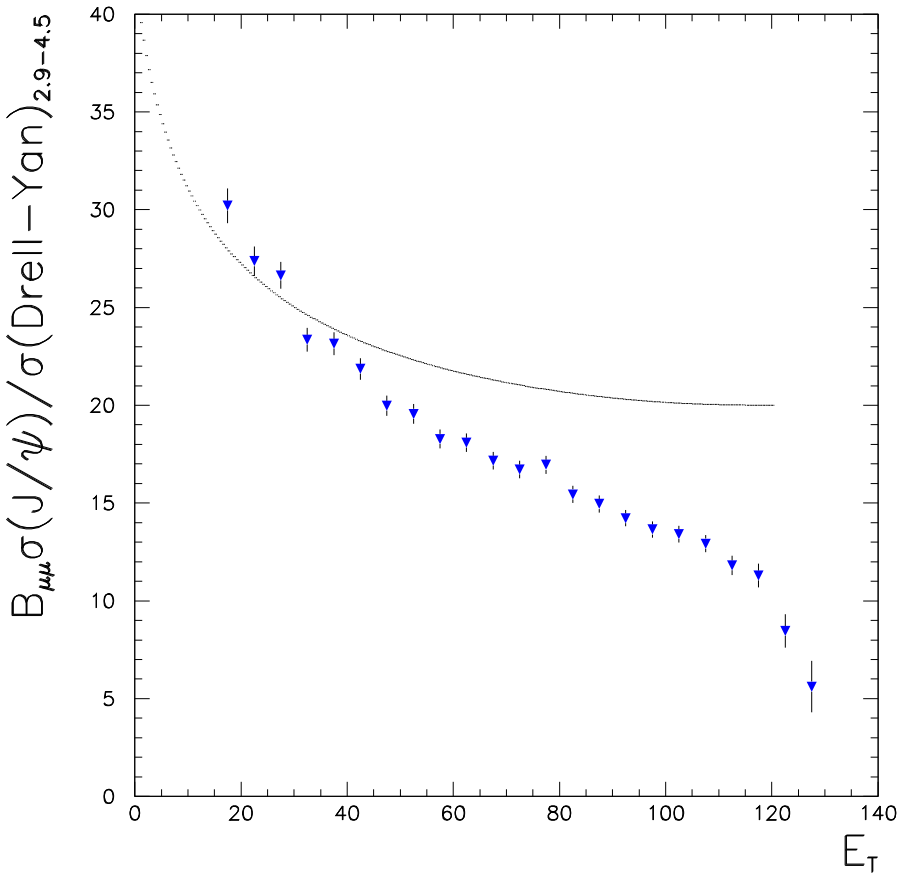

Figure 8.14: *$J/\psi/DY^*$ as a function of E_T with NOCIMD target recognition.*

8.5 Study of the systematic effects on the J/ψ/DY* result

In order to check the stability of the results obtained, various checks have been performed. In particular, four possible sources of systematic effects have been considered: the influence of the E_T binning, the uncertainty on the E_T scale correction, the choice of E_T range used for the normalization to the standard analysis and the inefficiencies of NOCIMD target identification.

8.5.1 E_T binning

In order to check the stability of the results and their possible dependence on the E_T binning used, the J/ψ/DY* ratios have been calculated also with E_T bins shifted by half a bin (i.e. 2.5 GeV). The comparison of the results obtained with the ones of fig. 8.14 is displayed in fig. 8.15. We can conclude that there is no important systematic effect due to the E_T binning.

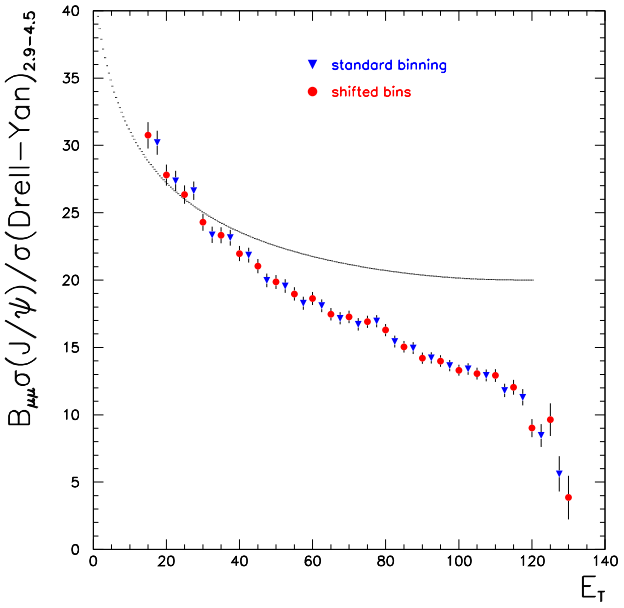

Figure 8.15: *J/ψ/DY* as a function of E_T with different E_T binnings.*

8.5.2 E_T rescaling

As it has been discussed in section 8.2.1, the correction of the Trigger Timing Bug for the 1998 data sample is based on the extraction of the q_{DY98} parameter from the E_T distribution of Drell-Yan events. In particular, the E_T rescaling of 1998 MB events is based on the value $q_{DY98} = 0.272$, extracted from a fit of the DY spectrum in the range $E_T > 70$ GeV. If a different E_T range is considered, the correspondent value of q varies in the range 0.269-0.273 GeV, as it can be seen in fig. 8.16, where four different fits to the DY spectrum are shown. This uncertainty on q_{DY98} ($\sim 1.5\%$) results to be of the same order of magnitude of the error on q resulting from the fit (i.e. ± 0.002).

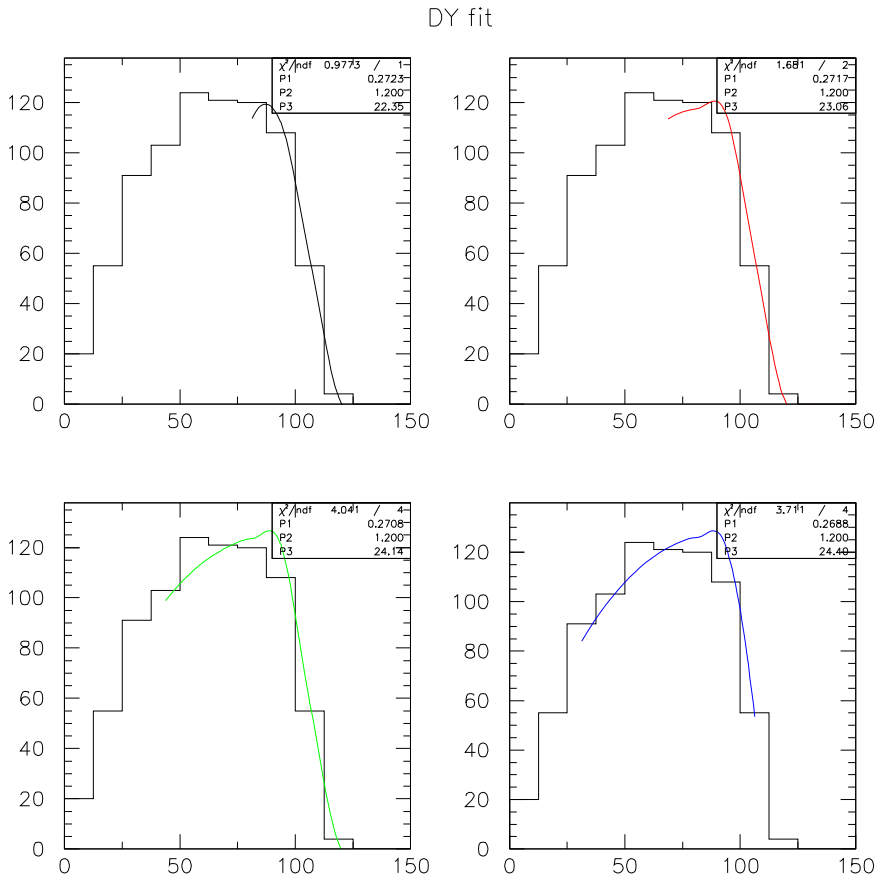

Figure 8.16: *Results of the fit to DY experimental spectra in different E_T range.*

The uncertainty on q_{DY98} is reflected in a correspondent uncertainty on the rescaling factor $R(MB98 \rightarrow 2\mu 96)$, which can take values in the range 1.039-1.054. The ratios J/ψ/MB and J/ψ/DY* obtained with the rescaling factors resulting from the different values of q_{DY98} extracted from the fits in fig. 8.16 are shown in fig. 8.17 and 8.18. It can be seen that a 1% modification of the rescaling factor causes a dramatic effect on the most central data points, i.e. for $E_T > 105$ GeV. For this reason, the evaluation of the cross-section ratios in the range $E_T > 105$ GeV is very delicate and a systematic error accounting for this effect must be included.

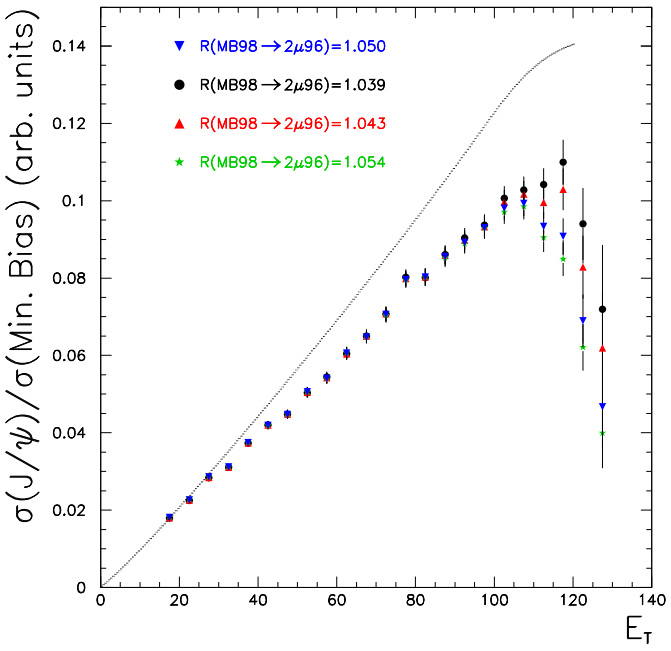

Figure 8.17: *J/ψ/MB ratios obtained with different values of the E_T rescaling factor $R(MB98 \rightarrow 2\mu 96)$.*

This result points out the main drawback of the Minimum Bias analysis technique, i.e. the presence of systematic effects due to the use of samples of events collected with different triggers. These systematics are not canceled in the ratio of the experimental J/ψ and MB spectra and therefore they affect the final result.

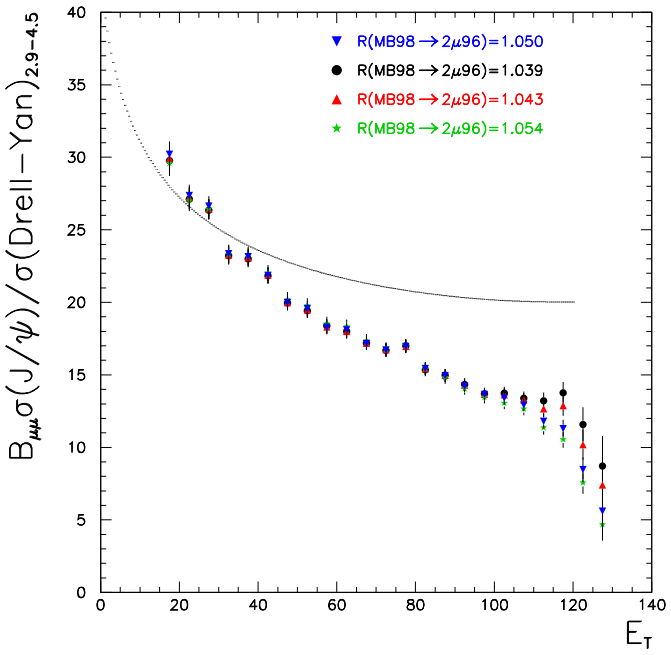

Figure 8.18: *$J/\psi/DY^*$ ratios obtained with different values of the E_T rescaling factor $R(MB98 \rightarrow 2\mu 96)$.*

8.5.3 Normalization range

The choice of the E_T range used to normalize the Minimum Bias analysis to the standard analysis of 1996 data may also influence the final result. In fig. 8.19 the ratio $J/\psi/\mathrm{DY}^*$ for four different normalization intervals is displayed. A 2% systematic uncertainty due to the E_T interval used for normalization to the standard analysis has therefore to be taken into account.

8.5.4 NOCIMD efficiency

The last source of systematic uncertainty considered are the inefficiencies of the NOCIMD target identification algorithm, which might play an important role for peripheral collisions. In particular, two effects are to be considered: the loss of peripheral (low multiplicity) in target events, and the mis-identification of Pb-air interactions as events occurring in the target.

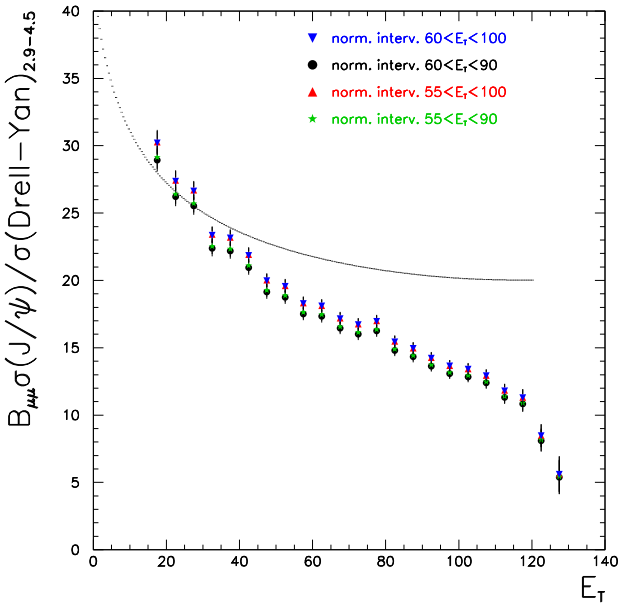

Figure 8.19: *Ratios J/ψ/MB (left) and J/ψ/DY* (right) obtained with different E_T intervals for normalization to the standard analysis.*

- As it has been discussed in section 4.4.1, the NOCIMD efficiency is $\approx 100\%$ for $E_T > 30$ GeV. Hence no systematic error is expected in this E_T region. In any case, the NOCIMD inefficiencies for E_T below 30 GeV should cancel in the ratio of the experimental J/ψ and MB spectra, provided that the efficiency is the same for the two trigger types.

- Data points with $E_T < 15$ GeV may be affected by residual Pb-air contamination, as pointed out by the Monte Carlo simulations discussed in section 4.4.1 and therefore they were not included in the analysis.

8.5.5 Conclusions

The inclusion of the systematic effects discussed in the previous sections leads to the plot of fig. 8.20, where the error bars represent the statistical errors, while the hatched band represents the systematic uncertainty. The error due to the choice of the normalization interval affects in the same way all the data points and is compatible with the statistical error. The most relevant effect is the one connected with the E_T rescaling and affects the most central bins.

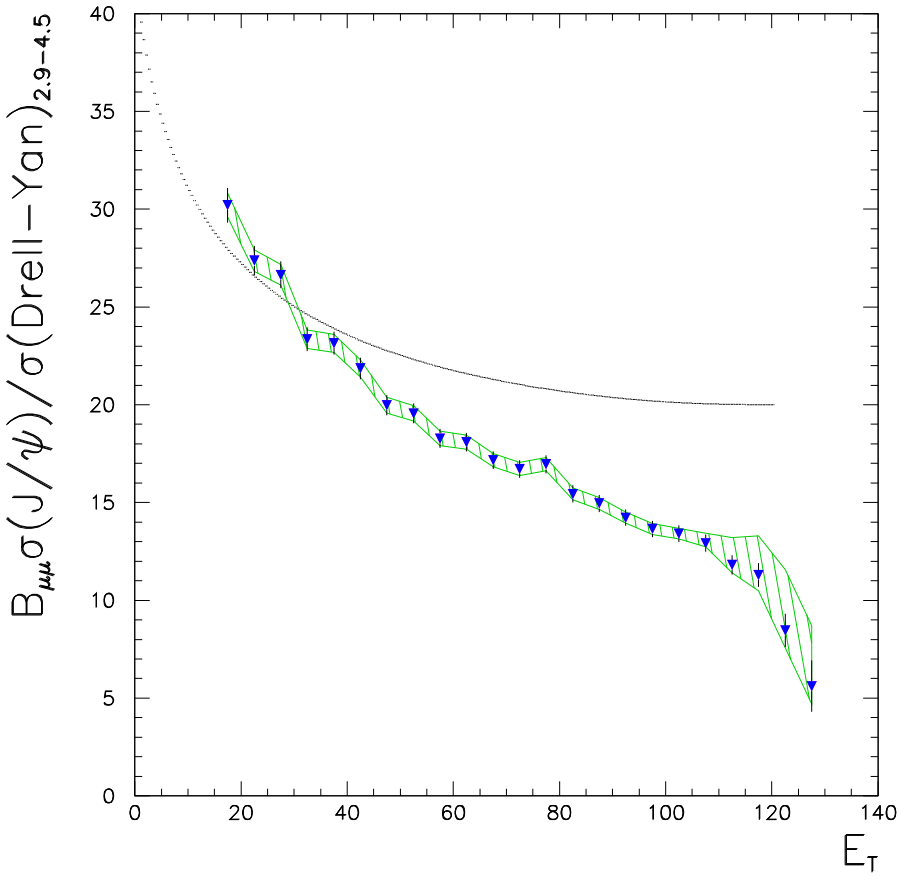

Figure 8.20: *$J/\psi/DY^*$ as a function of E_T with NOCIMD target recognition. The error bars represent the statistical errors, the hatched band represents the systematic error.*

8.6 Comparison with other Pb-Pb analyses

The J/ψ/DY* result obtained with the MD based target identification and the analysis method discussed in the previous sections (NOCIMD98 result) can be compared with other results published by NA50 collaboration, which were obtained with both the standard and Minimum Bias analysis [4, 5].

In fig. 8.21, the NOCIMD98 result is superimposed to the J/ψ/DY ratio obtained from the standard analysis of 1995 and 1996 data sample. It can clearly be seen that the use of the Minimum Bias technique reduces the fluctuations on the J/ψ/DY ratio and allows to obtain a smoother result with approximately twice of the E_T bins, as already pointed out in [4]. Our result is fully compatible with the 1995 data points and is in excellent agreement with 1996 standard analysis results in the range $E_T < 90$ GeV, where the 1996 data are free from the re-interaction bias. Nevertheless, when the correct E_T scale is used for the 1998 data and the consequent systematic error is taken into account as well as the fluctuations of the standard analysis data points, the 1996 analysis does not appear to be incompatible with our results also in the region $E_T > 90$ GeV, indicating that the contamination from re-interactions is probably smaller than expected.

The comparison of the NOCIMD98 result with the combined result of Minimum Bias analyses of 1996 and 1998 data is shown in fig. 8.22. It is important to recall that the 1998 data points of fig. 8.22 are different from the published ones (i.e. the ones in fig. 7.6) because of the E_T rescaling discussed in appendix B. The MD based target recognition leads to results which are in good agreement with both the 1996 and the 1998 MB analyses (based on the quartz blades target recognition) in the range $50 < E_T < 90$ GeV. For $E_T < 50$ GeV only 1996 data have been published and are compatible with our result which is extracted from the 1998 data sample collected with a different target setup (1 target instead of the 7 used in 1996). When looking at the most central region, it can be seen that in the range $90 < E_T < 105$ GeV our results are in excellent agreement with the 1998 rescaled data. Beyond $E_T = 105$ GeV, the J/ψ/DY* ratio must be considered carefully due to the presence of the large systematic errors intrinsic in the Minimum Bias analysis method. However, these data points appear to be compatible with the 1998 published data points and suggest the presence of a second change of slope in the J/ψ suppression pattern.

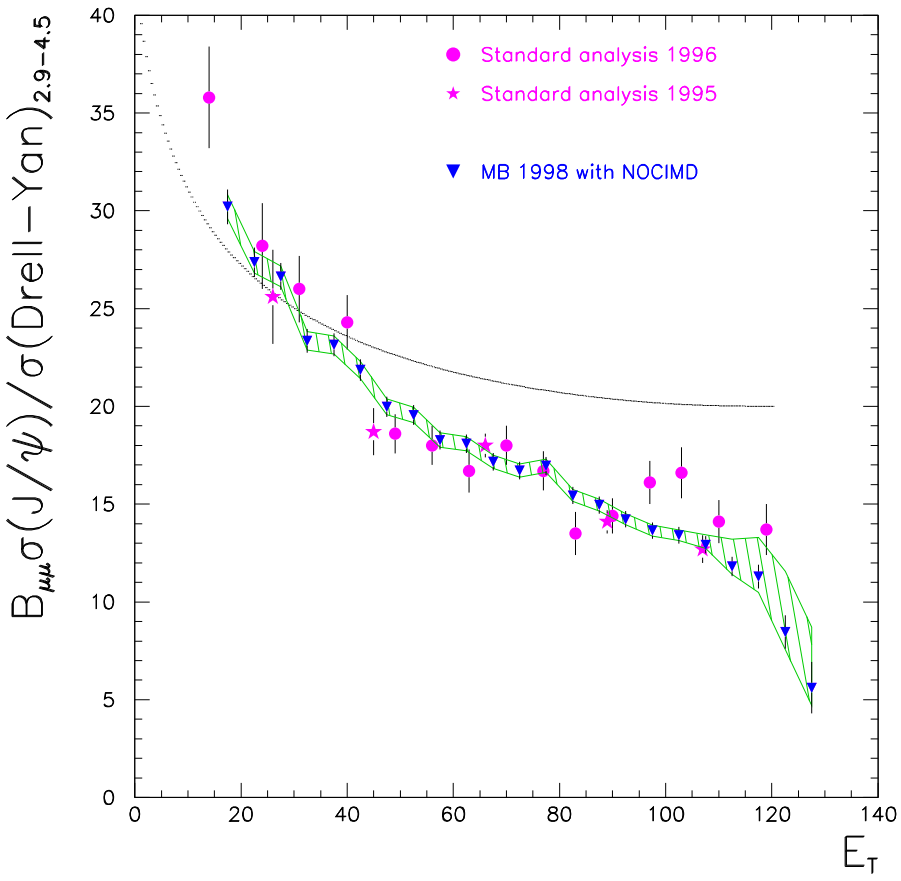

Figure 8.21: *Comparison between this analysis and the results of the standard analysis of 1996 data, published in [4].*

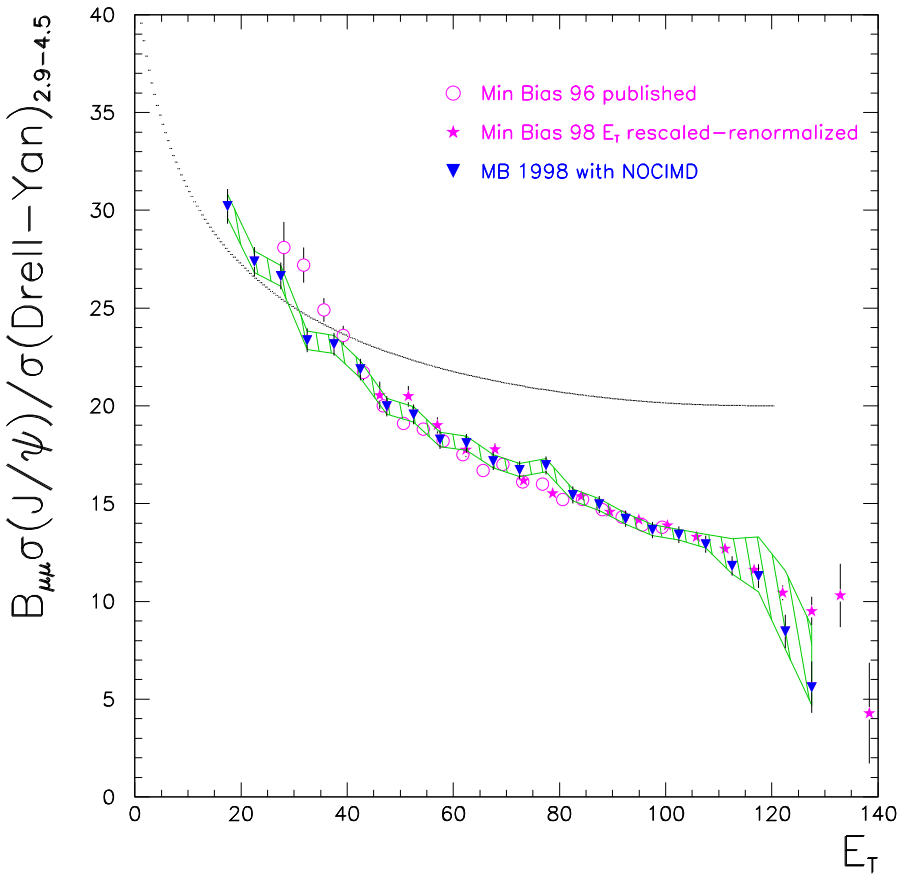

Figure 8.22: *Comparison between this analysis and the results of the MB analysis of 1996 and 1998 data [4, 5], after E_T rescaling of 1998 data (see appendix B).*

Bibliography

[1] R.J. Glauber, Lectures in Theoretical Physics, Vol. 1, Interscience publishers, NY 1959, 315.

[2] A. Bialas et al. Nucl. Phys. B 111 (1976) 461.

[3] M.C. Abreu et al., (NA38 coll.) Phys. Lett. B466 (1999) 408.

[4] M.C. Abreu et al., (NA50 coll.) Phys. Lett. B450 (1999) 456.

[5] M.C. Abreu et al., (NA50 coll.) Phys. Lett. B477 (2000) 28.

Chapter 9

J/ψ suppression as a function of charged multiplicity

The aim of the analysis presented in this chapter is the study of the centrality dependence of the J/ψ suppression in Pb–Pb collisions using, as centrality estimator, the number of charged particles per 10^o sector measured by the Multiplicity Detector (MD). The multiplicity variable used in this analysis is MDMUL1 which, as explained in chapter 4, is calculated in the pseudorapidity range $2.8 < \eta < 3.7$, approximately equal to the muon spectrometer acceptance. The "standard" analysis technique, based on the fit to the mass spectra of the opposite sign muon pairs, is used to evaluate the J/ψ over Drell-Yan ratio. The analysis is performed on the data collected in 1998 using the MD based target identification (NOCIMD variable), which allows to evaluate the J/ψ suppression over a broad centrality range, as it has been shown in chapter 8 where the J/ψ/DY ratio is studied as a function of E_T.

The most important feature of this analysis is that it allows to study the J/ψ suppression pattern as a function of a variable (MDMUL1) measured in the angular acceptance of the spectrometer. Furthermore, using the results discussed in chapter 6, concerning the charged particle pseudorapidity distributions, the J/ψ suppression pattern evaluated as a function of MDMUL1 can be displayed as a function of the particle pseudorapidity density at midrapidity ($dN/d\eta\ |_{max}$), which is directly related with the energy density attained in the collision.

9.1 The "standard" analysis method

The aim of the "standard" analysis is to evaluate in different centrality intervals the quantity $B_{\mu\mu}\sigma_{J/\psi}/\sigma_{DY}$, i.e. the ratio of J/ψ to Drell-Yan (DY) cross-sections multiplied by the branching ratio of the J/ψ decay into two muons. The number of J/ψ and Drell-Yan events is obtained from the analysis of the invariant mass spectra of opposite sign muon pairs ($\mu^+\mu^-$). In particular, the invariant mass spectra are fitted with a function accounting for the superposition of all known processes contributing to $\mu^+\mu^-$ production.

9.1.1 Contributions to the invariant mass spectrum

The main processes that contribute to the $\mu^+\mu^-$ invariant mass spectrum in the so-called high mass region ($M_{\mu\mu} \geq 2$ GeV/c^2) are:

- the Drell-Yan process;
- the open charm, i.e. semileptonic decays of $D\bar{D}$ mesons [1] ;
- the dimuon decay of J/ψ resonance;
- the dimuon decay of ψ' resonance;
- the combinatorial background, i.e. uncorrelated muons produced by π and K decays.

The experimental mass spectrum of opposite sign muon pairs is therefore fitted using the following function:

$$\frac{dN^{+-}}{dM} = N_{bck}\frac{dN_{bck}}{dM} + N_{DY}\frac{dN_{DY}}{dM} + N_{D\bar{D}}\frac{dN_{D\bar{D}}}{dM} + N_{J/\psi}\frac{dN_{J/\psi}}{dM} + N_{\psi'}\frac{dN_{\psi'}}{dM}$$

where $N_{J/\psi}$, $N_{\psi'}$, N_{DY}, $N_{D\bar{D}}$ and N_{bck} are normalization factors.

Apart from the combinatorial background (which is estimated from the sample of Like-Sign muon pairs), the mass spectra of the processes involved in the fit (J/ψ, ψ', open charm and Drell-Yan) are obtained via Monte

[1] According to the analysis of the intermediate mass region (between the ϕ and the J/ψ mass), the $D\bar{D}$ contribution includes also an excess explained as abnormally enhanced open charm production in nucleus-nucleus collisions with respect to the extrapolation of p-A results [1, 2]. The excess contribution results to have the same mass distribution of the $D\bar{D}$.

Carlo simulations. Muon pairs are generated according to the differential distributions of the various processes and tracked through the experimental apparatus by means of a dedicated program, called DIMUJET [3]. Then the simulated dimuons are reconstructed by means of the same program (DIMUREC [4]) used to reconstruct the experimental data and applying the same cuts as those used for the experimental data. The invariant mass spectra of the different dimuon sources are parametrized with ad-hoc functions which are tuned on the simulated data and then used in the fit to the experimental data.

The Drell-Yan

Drell-Yan events are generated using the leading order perturbative QCD DY cross section and the GRV-LO set of parton distribution functions [5]. The reconstructed mass distribution of the Monte Carlo DY events is then fitted with the following function [6]:

$$\frac{dN_{DY}}{dM} = a_1 \cdot \left\{ e^{-a_2 \cdot M} - a_3 \cdot e^{-(M-a_4)^2} \right\} \tag{9.1}$$

obtaining for the fit parameters the values listed in table 9.1 (a_1 is not reported because it is a normalization factor depending on the number of generated events).

Param.	Value
a_2	1.464 ± 0.004 $(\mathrm{GeV}/c^2)^{-1}$
a_3	0.239 ± 0.005 $(\mathrm{GeV}/c^2)^{-1}$
a_4	0.53 ± 0.01 (GeV/c^2)

Table 9.1: *Values of the parameters for the Monte Carlo Drell-Yan fitting function, taken from [6].*

The open charm

The $D\bar{D}$ events are generated using PYTHIA 5.7 [7], according to the procedure explained in [1]. The Monte Carlo mass distribution of open charm dimuons is then parametrized as [1]:

$$\frac{dN_{D\bar{D}}}{dM} = c_1 \cdot e^{-0.5\left(\frac{M-c_2}{\sigma_{cc}}\right)^2} \tag{9.2}$$

where:

$$\sigma_{cc} = \begin{cases} c_3 & \text{if } M < c_5 \\ c_3\,[1 + c_4(M - c_5)] & \text{if } M > c_5 \end{cases}$$

The values of the fit parameters c_2-c_5 are shown in table 9.2, c_1 is a normalization factor and therefore it is not reported.

Param.	Value
c_2	1.80 ± 0.01 (GeV/c^2)
c_3	0.30 ± 0.04 (GeV/c^2)
c_4	0.42 ± 0.06 (GeV/c^2)$^{-1}$
c_5	1.5 ± 0.3 (GeV/c^2)

Table 9.2: *Values of the parameters for the Monte Carlo open charm fitting function, taken from [1].*

The J/ψ and the ψ'

The charmonium bound states J/ψ and ψ' are generated as Dirac distribution functions centered on their nominal mass values ($M_{J/\psi} = 3.097$ GeV/c^2 and $M_{\psi'} = 3.686$ GeV/c^2 [8]). The widths of the two resonances ($\sigma_{J/\psi} = 87$ KeV and $\sigma_{\psi'} = 277$ KeV) are neglected because they result to be much smaller than the mass resolution of the NA50 spectrometer, which is $\sim 3\%$ for both the charmonium states. For further details about J/ψ and ψ' generation see [1, 6]

The mass shape of the reconstructed J/ψ and ψ' resonances is described by "pseudo-gaussian" functions [6]:

$$\frac{dN_{\psi,\psi'}}{dM} = p_1 \cdot e^{-0.5\left(\frac{M-p_2}{\sigma}\right)^2} \tag{9.3}$$

where:

$$\sigma = \begin{cases} p_3 \cdot [1 + p_4 \cdot (M_1 - M)]^{[p_5 - p_6 \cdot (M_1 - M)]} & \text{if } M < M_1 \\ p_3 & \text{if } M_1 < M < M_2 \\ p_3 \cdot [1 + p_7 \cdot (M - M_2)]^{[p_8 - p_9 \cdot (M - M_2)]} & \text{if } M > M_2 \end{cases}$$

and:

$$\begin{aligned} M_1 &= p_2 \cdot p_{10} \\ M_2 &= p_2 \cdot p_{11} \end{aligned}$$

parameters $p_4 - p_{11}$ describe the deviation from a simple gaussian. The values of the resulting fit parameters $p_2 - p_{11}$ are listed in table 9.3. [2]

Param.	J/ψ	ψ'
p_2	3.1276 ± 0.0003	3.7203 ± 0.0002
p_3	0.0907 ± 0.0002	0.1027 ± 0.0002
p_4	2.16 ± 0.02	2.03 ± 0.01
p_5	1.43 ± 0.03	1.37 ± 0.01
p_6	0.44 ± 0.02	0.298 ± 0.007
p_7	1.39 ± 0.05	0.74 ± 0.06
p_8	1.54 ± 0.06	1.57 ± 0.05
p_9	1.62 ± 0.09	2.15 ± 0.02
p_{10}	0.976 ± 0.002	0.9708 ± 0.0007
p_{11}	1.067 ± 0.002	1.053 ± 0.003

Table 9.3: *Values of the parameters for the Monte Carlo J/ψ and ψ' fitting functions, taken from [6].*

The combinatorial background

The combinatorial background contribution (dN_{bck}/dM) originating from uncorrelated decays of π and K mesons is estimated from the sample of Like-Signs muon pairs ($\mu^+\mu^+$ and $\mu^-\mu^-$), as explained in section 8.4.2:

$$N_{bck}^{+-} = 2\sqrt{N^{++} \cdot N^{--}} \tag{9.4}$$

where N^{++} is the number of $\mu^+\mu^+$ pairs and N^{--} the number of $\mu^-\mu^-$ pairs.

9.1.2 Acceptances

The acceptance of the apparatus for a given physical process is defined as the number of Monte Carlo reconstructed events divided by the number of generated events in the kinematical window:

$$0 < y^* < 1 \qquad -0.5 < \cos(\vartheta_{CS}) < 0.5$$

[2] p_1 is a normalization factor depending on the number of generated events and therefore it is not reported in table 9.3.

For example, the acceptance for a process P in the invariant mass region $M_1 < M < M_2$ is given by:

$$A = \frac{\int_{M_1}^{M_2} \frac{dN_{rec}^P}{dM}}{\int_{M_1}^{M_2} \frac{dN_{gen}^P}{dM}} \tag{9.5}$$

The values of acceptance for the physical processes considered in this analysis, calculated taking into account the selection criteria discussed in section 9.2.1 (in particular the global cut and the image cut) are listed in table 9.4.

Process	Mass range GeV/c^2	Acceptance %
J/ψ	-	7.44 ± 0.01
ψ'	-	8.69 ± 0.01
DY	$2.9 \leq M_{\mu\mu} \leq 4.5$	8.40 ± 0.01
$D\bar{D}$	$M_{\mu\mu} \geq 1.5$	1.08 ± 0.02

Table 9.4: *Calculated acceptances for the different processes contributing to the invariant mass spectrum of opposite sign dimuons.*

9.2 Data analysis

The analysis is performed on the data sample collected in 1998 according to the following procedure.

1. Quality cuts on dimuon events are applied.
2. Events are grouped in centrality bins according to the value of MDMUL1.
3. In each centrality bin the invariant mass spectrum of opposite sign muon pairs is fitted and the ratio J/ψ/DY is calculated.

9.2.1 Data selection

Dimuon events selected for the analysis have to fulfill the standard selection criteria discussed in chapter 4. Beam cleaning cuts and diagonal selections on the E_T versus E_{ZDC} and MDMUL1 vs E_T correlations are applied. Only

muon pairs satisfying the image cut selection and lying in the kinematical domain defined by $0 < y^* < 1$ and $-0.5 < \cos(\vartheta_{CS}) < 0.5$ are accepted. A 18% global cut on the data is applied. Target identification is done with the NOCIMD variable which provides a good efficiency also for peripheral events allowing, at the same time, to reject the contamination due to Pb-Air events.

9.2.2 Centrality selection

The events of the whole Pb-Pb sample are subdivided into 5 subsamples of events according to the number of charged particles produced in the interaction and measured by the Multiplicity Detector (MD). The multiplicity variable chosen as centrality estimator for this analysis is MDMUL1, which is the number of charged "tracks" per 10^o sector measured in the pseudo-rapidity range $2.8 < \eta < 3.7$. The method used to evaluate MDMUL1 is explained in detail in chapter 4. In fig. 9.1 the MDMUL1 distribution of the opposite sign dimuon events in the J/ψ mass region ($2.9 < M_{\mu\mu} < 3.3$ GeV/c^2) is displayed. It is important to recall that MDMUL1 is measured in a 10^o azimuthal angle, so that the total number of charged particles produced in the Pb-Pb interaction is approximately given by:

$$N_{ch} = 36 \cdot \text{MDMUL1}$$

The limits of the 5 multiplicity bins are listed in table 9.5 and plotted as lines superimposed on the MDMUL1 spectrum of fig. 9.1. The average MDMUL1 value and the number of $\mu^+\mu^-$ events in the J/ψ mass region for each centrality bin are also reported in table 9.5.

Bin	MDMUL1 range	$<$ MDMUL1 $>$	# of $\mu^+\mu^-$ ($2.9 < M_{\mu\mu} < 3.3$ GeV/c^2)
1	$0 \leq$ MDMUL1 < 3.0	1.89	6566
2	$3.0 \leq$ MDMUL1 < 4.5	3.63	6018
3	$4.5 \leq$ MDMUL1 < 6.0	5.13	6476
4	$6.0 \leq$ MDMUL1 < 8.0	6.87	8862
5	$8.0 \leq$ MDMUL1 < 15.0	9.19	6718

Table 9.5: *Definition of the multiplicity bins used for this analysis.*

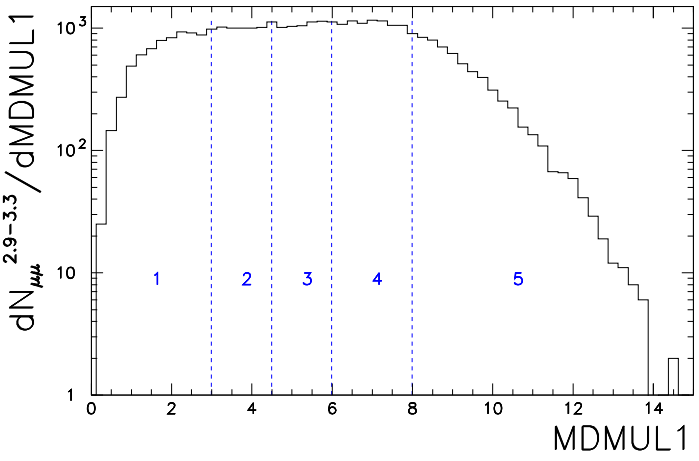

Figure 9.1: MDMUL1 *distribution of $\mu^+\mu^-$ events in the J/ψ mass region ($2.9 < M_{\mu\mu} < 3.3$ GeV/c^2). The limits of the centrality bins used in this analysis are superimposed.*

9.2.3 Fit to the mass spectra

The fit to the invariant mass spectra of opposite sign dimuons is performed in each centrality bin with a multi-step method sketched in fig. 9.2 and detailed hereafter. All the fits are performed using the likelihood method because it takes better into account the low statistics bins.

1. Fit to the combinatorial background invariant mass spectrum dN_{bck}^{+-}/dM (as given by equation 9.4) in the region $2.1 < M_{\mu\mu} < 3.6$ GeV/c^2 with a gaussian function:

$$\frac{dN_{bck}}{dM} = k_1 \cdot e^{-0.5\left(\frac{M-k_2}{k_3}\right)^2}$$

   with k_1, k_2 and k_3 free parameters.

2. Fit to the opposite sign dimuon invariant mass spectrum in the range $M_{\mu\mu} > 3.05$ GeV/c^2 with the following contributions:

$$\frac{dN^{+-}}{dM} = N_{bck}\frac{dN_{bck}}{dM} + N_{J/\psi}\frac{dN_{J/\psi}}{dM} + N_{\psi'}\frac{dN_{\psi'}}{dM} + N_{DY}\frac{dN_{DY}}{dM}$$

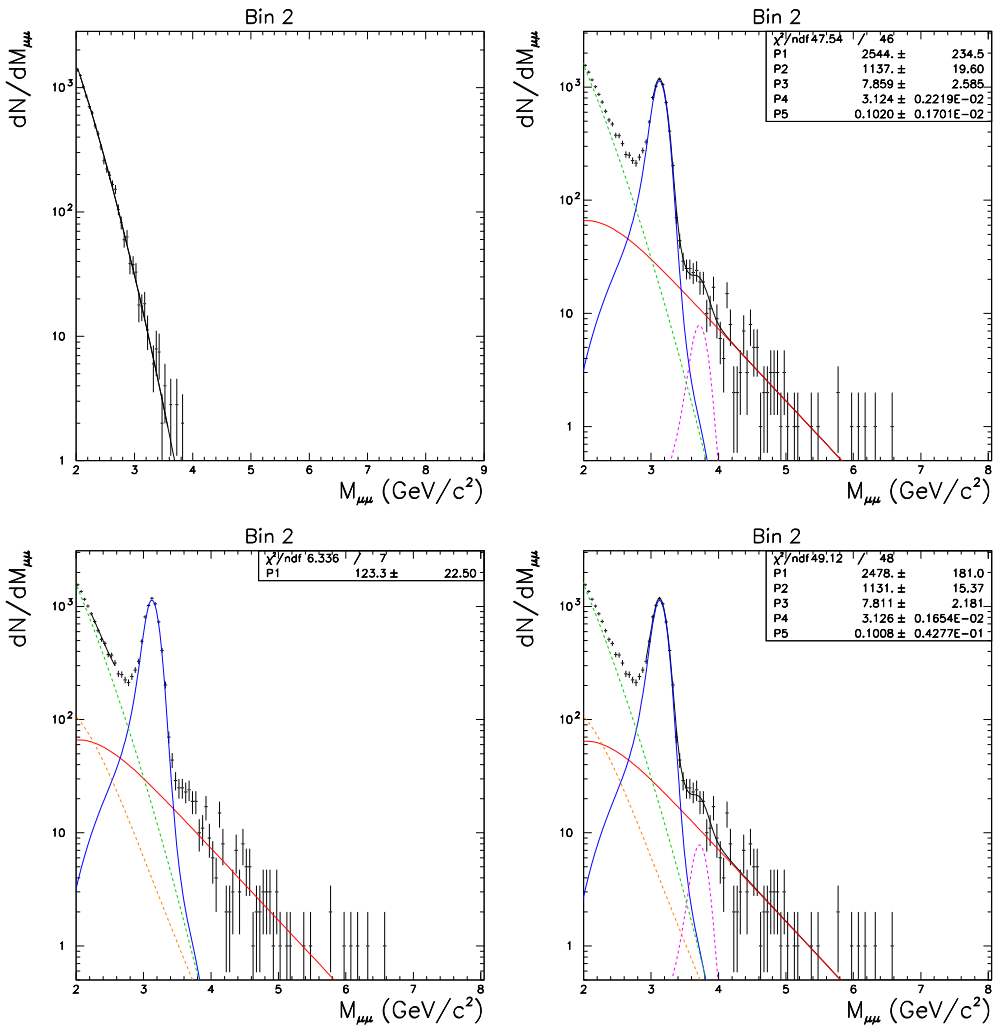

Figure 9.2: *Four step procedure used to fit the $\mu^+\mu^-$ invariant mass spectra.*

with the background fixed to the result obtained from step 1) and $N_{J/\psi}$, $N_{\psi'}$ and N_{DY} kept as free parameters. The $D\bar{D}$ contribution is not included. To obtain a better fit quality, since the Monte Carlo generated shape does not reproduce the mass and the width of the measured J/ψ, also the J/ψ mass and width ($M_{J/\psi}$ and $\sigma_{J/\psi}$, corresponding to parameters p_2 and p_3 of the pseudo-gaussian resonance parametrization) are treated as free parameters of the fit. The mass and the width of the ψ' are related to those of the J/ψ according to the results of Monte Carlo simulations:

$$M_{\psi'}^{data} = M_{J/\psi}^{data} + (M_{\psi'}^{MC} - M_{J/\psi}^{MC}) \tag{9.6}$$

$$\sigma_{\psi'}^{data} = \sigma_{J/\psi}^{data} \cdot \frac{\sigma_{\psi'}^{MC}}{\sigma_{J/\psi}^{MC}} \tag{9.7}$$

The total number of free parameters in the fit is therefore equal to 5.

3. Fit to the $\mu^+\mu^-$ invariant mass spectrum in the range $2.2 < M_{\mu\mu} < 2.6$ GeV/c^2 with the following contributions:

$$\frac{dN^{+-}}{dM} = N_{bck}\frac{dN_{bck}}{dM} + N_{D\bar{D}}\frac{dN_{D\bar{D}}}{dM} + N_{J/\psi}\frac{dN_{J/\psi}}{dM} + N_{DY}\frac{dN_{DY}}{dM}$$

The background is the one fixed in step 1) and the DY and J/ψ are fixed to the results of step 2). The only free parameter is the normalization of the open charm contribution ($N_{D\bar{D}}$). The ψ' is not included because the fit is performed in a mass region where its contribution is completely negligible. The aim of this step is to evaluate the $D\bar{D}$ contribution in a mass region where the open charm is expected to play an important role. In the next step of the procedure, the open charm contribution is fixed to the result obtained in this step. This allows to reduce the systematic error on the J/ψ/DY ratio due to the $D\bar{D}$ evaluation.

4. Final fit to the opposite sign dimuon mass spectrum in the range $M_{\mu\mu} > 2.9$ GeV/c^2 including all the dimuon sources:

$$\frac{dN^{+-}}{dM} = N_{bck}\frac{dN_{bck}}{dM} + N_{D\bar{D}}\frac{dN_{D\bar{D}}}{dM} + N_{J/\psi}\frac{dN_{J/\psi}}{dM} + N_{\psi'}\frac{dN_{\psi'}}{dM} + N_{DY}\frac{dN_{DY}}{dM}$$

with the background fixed in step 1) and the open charm fixed in step 3). The lower limit of the fitting range ($M_{\mu\mu} = 2.9$ GeV/c^2) is chosen to

reduce possible unknown contributions and to minimize the systematics connected with the background evaluation. The free parameters are 4: the three normalizations ($N_{J/\psi}$, $N_{\psi'}$ and N_{DY}) and the mass of the J/ψ. The J/ψ width on the contrary is fixed for all the multiplicity bins to the value extracted from a fit to the high statistic sample of semi-central and central (MDMUL1> 3) events with $\sigma_{J/\psi}$ kept as a free parameter. The width of the J/ψ resonance is then fixed to the same value ($\sigma_{J/\psi} = 100.8$ MeV) for all the centrality bins. [3] The ψ' mass and width are fixed according to equations 9.6 and 9.7

9.2.4 Fit results

In each of the 5 multiplicity bins, the ratio J/ψ/DY is calculated from the result of the 4th step of the fitting procedure. The results of the final fit are shown in fig. 9.3 for 4 different centrality bins (the bin not included is the one shown in fig. 9.2).

The total number of J/ψ ($N^{tot}_{J/\psi}$) is obtained by integrating in the mass range $M_{\mu\mu} \geq 1.5$ the J/ψ invariant mass spectrum estimated from the fit. The Drell-Yan spectrum is integrated in the mass range $2.9 \leq M_{\mu\mu} \leq 4.5$ GeV/c^2 obtaining the number of DY events in this mass interval ($N^{2.9-4.5}_{DY}$). The acceptance correction is also taken into account. Hence:

$$\frac{B_{\mu\mu} \cdot \sigma_{J/\psi}}{\sigma_{DY}} = \frac{N^{tot}_{J/\psi}}{A_{J/\psi}} \cdot \frac{A_{DY}}{N^{2.9-4.5}_{DY}} \tag{9.8}$$

In table 9.6 the number of J/ψ and Drell-Yan events obtained in the 5 multiplicity bins are reported, together with the ratio J/ψ/DY corrected for the acceptances and the χ^2 of the final fit. The error quoted on the J/ψ/DY ratio is purely statistical. The systematic error is expected to be negligible since this quantity is calculated as the ratio of experimentally measured quantities and consequently most of the systematics (such as flux uncertainties affecting the luminosity determination and detector inefficiencies) should cancel.

[3] In the 1996 data analysis the J/ψ width was fixed to values increasing when going from central to peripheral collisions, because for peripheral collisions there was a high number of events which were not assigned to the right subtarget and therefore reconstructed from the central subtarget (target 4), resulting in a worse mass resolution [6]. This is not the case in 1998 data sample where only one subtarget is present and therefore the mass resolution should be constant and independent of centrality.

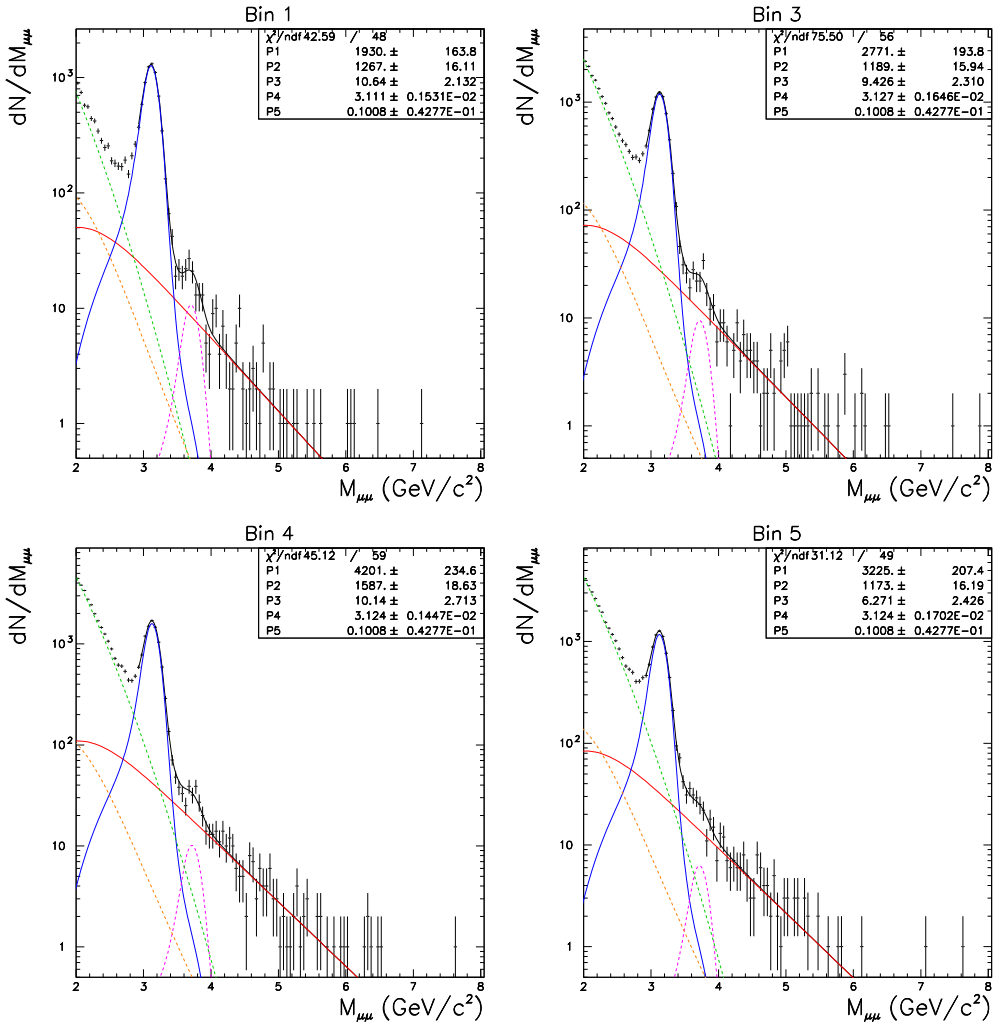

Figure 9.3: *Final fit to the $\mu^+\mu^-$ invariant mass spectra for four different centrality bins, from the most peripheral (1) to the most central (5) bin. The result of the final fit for bin 2 is shown in fig. 9.2.*

N. bin	$N_{J/\psi}^{tot}$ ($M_{\mu\mu} \geq 1.5$)	$N_{DY}^{2.9-4.5}$ ($2.9 \leq M_{\mu\mu} \leq 4.5$)	J/ψ/DY accept. corr.	χ^2
1	7317 ± 126	335 ± 28	24.7 ± 2.1	0.89
2	6529 ± 117	430 ± 31	17.1 ± 1.3	1.02
3	6866 ± 122	481 ± 34	16.1 ± 1.2	1.35
4	9163 ± 152	729 ± 41	14.2 ± 0.8	0.76
5	6773 ± 122	559 ± 36	13.7 ± 0.9	0.64

Table 9.6: *Results of the final fit to the $\mu^+\mu^-$ invariant mass spectra for the 5 multiplicity bins. The total number of J/ψ's, the number of DY events in the range $2.9 \leq M_{\mu\mu} \leq 4.5$ GeV/c^2 as well as the J/ψ/DY ratio and the χ^2 of the fit are listed.*

The systematic effect connected with the mass range chosen for the 4th step of the fitting procedure can be evaluated by varying the starting point (lower mass limit) of the fit. The values of the ratio J/ψ/DY obtained for different starting points of the 4th step fit (namely 2.5, 2.8 and 2.9 GeV/c^2) are listed in table 9.7. All the values result to be within statistical error bars, so that it can be concluded that the mass interval chosen for the fit does not substantially affect the evaluation of the J/ψ/DY ratio.

N. bin	starting point of step 4 fit		
	2.5 GeV/c^2	2.8 GeV/c^2	2.9 GeV/c^2
1	25.4 ± 1.9	26.0 ± 2.2	24.7 ± 2.1
2	16.0 ± 1.0	16.9 ± 1.2	17.1 ± 1.3
3	15.4 ± 1.0	15.7 ± 1.1	16.1 ± 1.2
4	14.8 ± 0.8	14.7 ± 1.0	14.2 ± 0.8
5	13.3 ± 0.8	13.5 ± 0.9	13.7 ± 0.9

Table 9.7: *Values of J/ψ/DY ratio obtained when the 4th step fit is performed in different mass intervals.*

9.3 The ordinary nuclear absorption curve

The reference curve accounting for charmonium absorption in ordinary nuclear matter as a function of the impact parameter is calculated in the framework of the Glauber model as explained in section 8.3 and appendix A. The value $\sigma_{abs} = 6.4 \pm 0.8$ mb [9] is used for the absorption cross-section.

The curve thus obtained has to be transposed as a function of MDMUL1 variable. This is done by taking into account the relation between the charged multiplicity and the impact parameter b, which is based on the assumption that, for a given b, MDMUL1 is gaussian distributed around its average value $<$ MDMUL1 $>$:

$$P(\text{MDMUL1}, b) \propto e^{-0.5 \cdot \left(\frac{\text{MDMUL1} - <\text{MDMUL1}>}{\sigma_{\text{MDMUL1}}} \right)^2}$$

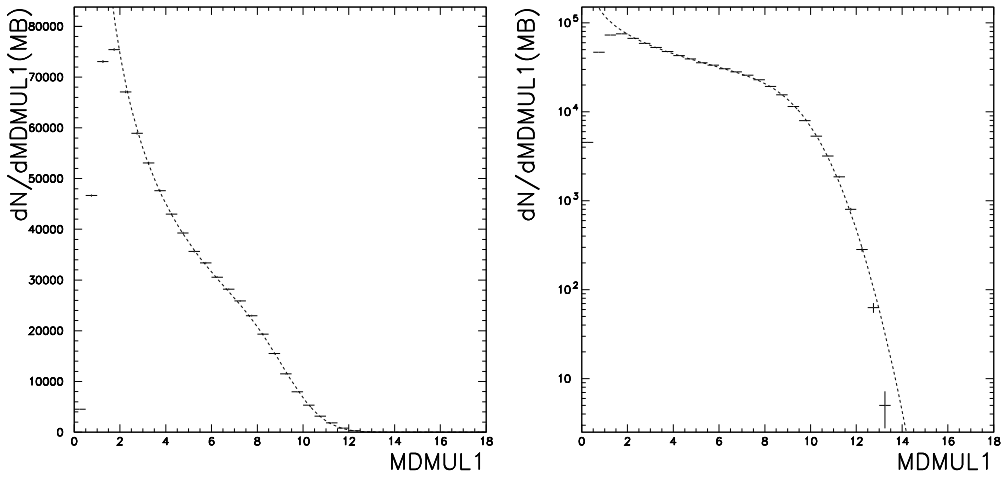

Figure 9.4: *Glauber model fit to the* MDMUL1 *distribution of MB events, shown in both linear (left panel) and logarithmic (right panel) scale.*

According to the wounded nucleon model [10], $<$ MDMUL1 $>$ is assumed to be proportional to the number of participant (wounded) nucleons: [4]

$$< \text{MDMUL1}(b) >= q_N \cdot N_{part}(b) \tag{9.9}$$

[4]This assumption is confirmed by the results of the analysis discussed in chapter 6 concerning the scaling of charged particle production as a function of N_{part}.

The enlargement due to the detector resolution is given by:

$$\sigma^2_{\mathrm{MDMUL1}}(b) = w_N \cdot q_N < \mathrm{MDMUL1}(b) >= w_N \cdot q_N^2 \cdot N_{part}(b) \qquad (9.10)$$

The q_N and w_N parameters are extracted from a fit to the MDMUL1 distribution of MB events (see fig. 9.4) obtaining:

$$q_N = 0.02427 \pm 0.00002 \qquad w_N = 7.4 \pm 0.1$$

The resulting absorption curve is shown in fig. 9.5.

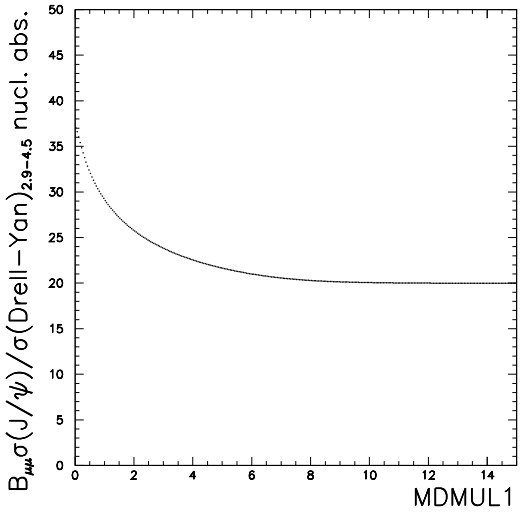

Figure 9.5: *J/ψ/DY ratio expected from the Glauber calculation of nuclear absorption as a function of* MDMUL1.

9.4 J/ψ suppression as a function of MDMUL1

The J/ψ/DY ratio in the 5 centrality bins is plotted as a function of MDMUL1 in fig. 9.6 where the solid curve represents the charmonium absorption in nuclear matter (see fig. 9.5). It can be seen that the most peripheral bin is in agreement with the J/ψ suppression expected in the case of ordinary nuclear absorption. For collisions with MDMUL1>3 the nuclear absorption

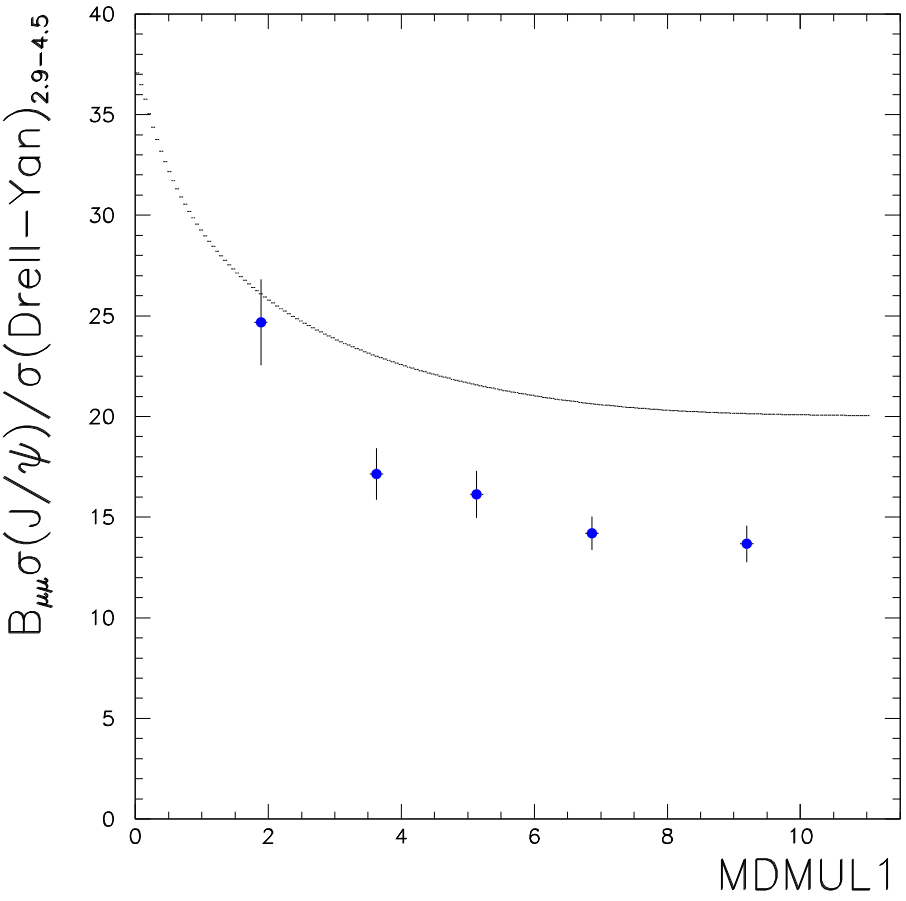

Figure 9.6: *$J/\psi/DY$ ratio as a function of* MDMUL1.

does not account for the measured J/ψ/DY ratio: an "anomalous" suppression mechanism is at work.

The departure from the nuclear absorption behaviour can be quantified using the ratio:

$$R_K^{J/\psi/DY} = \frac{(\sigma_{J/\psi}/\sigma_{DY})_{measured}}{(\sigma_{J/\psi}/\sigma_{DY})_{expected}} \tag{9.11}$$

which is given for each multiplicity bin in table 9.8.

The value obtained in the first multiplicity bin:

$$R_K^{J/\psi/DY}(0 \leq \text{MDMUL1} < 3) = 0.94 \pm 0.08$$

N. bin	$B_{\mu\mu}\sigma_{J/\psi}/\sigma_{DY}$ measured	$J/\psi/DY$ nucl. absorpt.	R_K
1	24.7 ± 2.1	26.17	0.94 ± 0.08
2	17.1 ± 1.3	23.03	0.74 ± 0.06
3	16.1 ± 1.2	21.60	0.75 ± 0.05
4	14.2 ± 0.8	20.65	0.69 ± 0.04
5	13.7 ± 0.9	20.15	0.68 ± 0.04

Table 9.8: *Ratio between the measured $J/\psi/DY$ ratio and the nuclear absorption expectation in the 5 multiplicity bins.*

is fully compatible with what expected in the case that nuclear absorption is the only J/ψ suppression mechanism. This result implies that no anomalous mechanism is at work in peripheral Pb-Pb collisions, confirming the result already observed as a function of E_T and E_{ZDC} [11, 12]. Bins from 2 to 5 lie more than 4 standard deviations from the absorption curve. The amount of "anomalous" suppression ($\approx 40\%$) is quantitatively in agreement with the results of the analyses as a function of both E_T and E_{ZDC}. It can also be seen that the anomalous suppression keeps increasing with increasing multiplicity (centrality).

9.5 Comparison with results obtained using E_T as centrality estimator

The result obtained using MDMUL1 as centrality estimator can be compared with the ones obtained with an E_T based centrality selection. This comparison requires the evaluation of a transverse energy value ($< E_T^{calc} >$) for each of the 5 centrality bins defined by MDMUL1. This is done by calculating in each of the 5 multiplicity bins the average value of the E_T distribution of the opposite sign dimuon events in the J/ψ mass region ($2.9 < M_{\mu\mu} < 3.3$ GeV/c^2). [5] An error on $< E_T^{calc} >$ equal to 0.67 of the RMS of the E_T distribution (corresponding to 50% of distribution contents) is considered.

In fig. 9.7 the J/ψ/DY ratio evaluated as a function of MDMUL1 and

[5] The value of E_T extracted from the 1998 microDST is multiplied by 1.085 to have the E_T scale coherent with the 1996 one (see appendix B).

transposed in the E_T variable is superimposed to the results of the standard analyses performed on 1995 and 1996 data samples [11, 13]. The agreement among the different results, obtained from three different data samples with two different centrality estimators, is satisfactory.

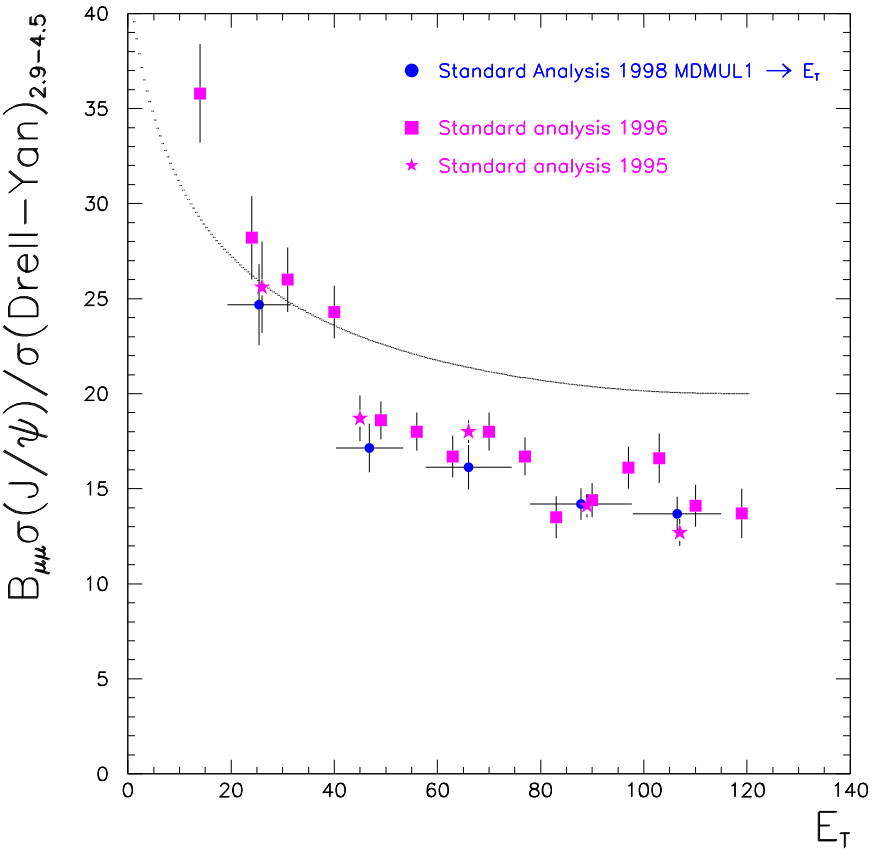

Figure 9.7: *J/ψ/DY ratio as a function of MDMUL1 transposed in E_T and compared with the results of 1995 and 1996 standard analyses.*

The MDMUL1 result converted into E_T can also be compared with the J/ψ/DY* ratio obtained in chapter 8 from the 1998 data sample using the Minimum Bias analysis technique and NOCIMD target identification. The comparison is shown in fig. 9.8 where it can be seen that, except for the 2nd multiplicity bin (corresponding to $E_T \approx 45$ GeV), the two analyses agree. The discrepancy observed for the 2nd bin can be understood when

considering the error implicit in the conversion from MDMUL1 to E_T and the larger smearing resulting from the Minimum Bias analysis, which is also visible in fig. 8.21.

It can therefore be concluded that the result obtained using the charged multiplicity MDMUL1 as centrality estimator is fully compatible with the ones obtained using the E_T based centrality selection.

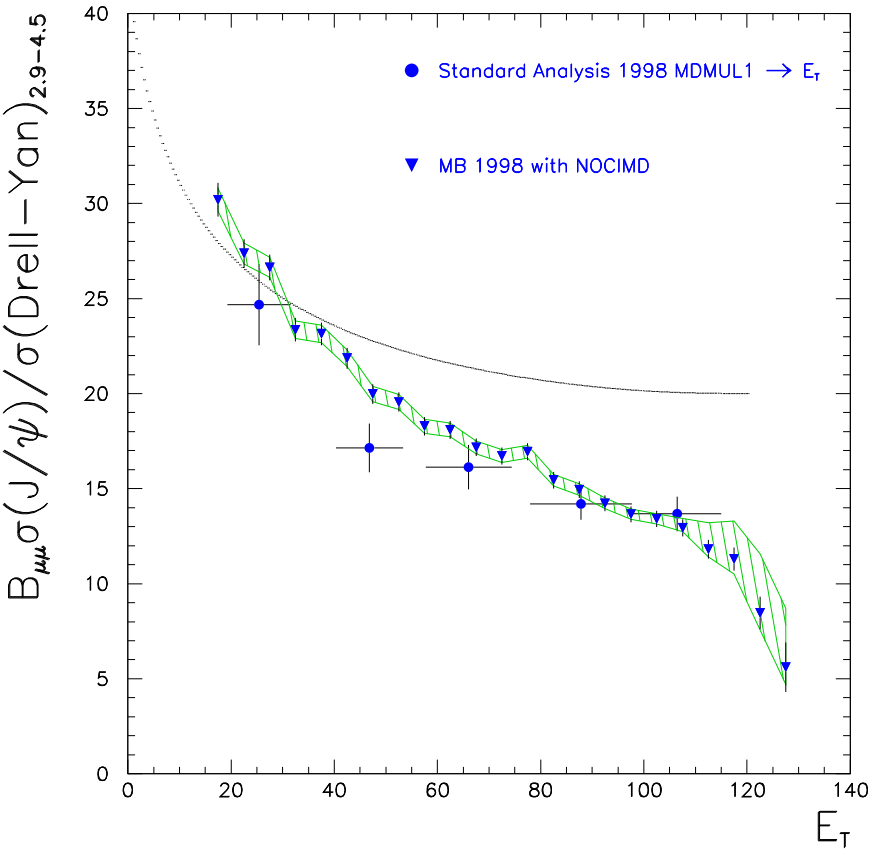

Figure 9.8: *$J/\psi/DY$ ratio as a function of MDMUL1 transposed in E_T and compared with the result of 1998 Minimum Bias analysis with NOCIMD (see chapter 8).*

9.6 J/ψ/DY as a function of $dN_{ch}/d\eta\ |_{max}$

The results of the study concerning the charged particle pseudorapidity distributions ($dN_{ch}/d\eta$) can be used to translate the horizontal scale of the J/ψ suppression plot into an absolute multiplicity scale. This is done according to the following procedure. In each of the 6 E_T classes used for the $dN_{ch}/d\eta$ analysis (see chapter 6), corresponding to a 5% (or 10%) interval of total inelastic cross-section, the average value of MDMUL1 is evaluated. The results are summarized in table 9.9. [6] For each centrality class, the particle pseudorapidity density at midrapidity ($dN_{ch}/d\eta\ |_{max}$) value extracted from the gaussian fits to the $dN_{ch}/d\eta$ distributions (see section 6.3.3) is also reported.

% of c.s.	$E_T^{min} - E_T^{max}$	< MDMUL1 >	$dN_{ch}/d\eta\ \|_{max}$
0-5	87.2-140.	8.64	441 ± 4
5-10	71.5-87.2	7.29	359 ± 4
10-15	58.7-71.5	6.16	296 ± 3
15-20	48.9-58.7	5.17	247 ± 3
20-25	40.9-48.9	4.36	208 ± 2
25-35	29.6-40.9	3.43	165 ± 3

Table 9.9: *Correspondence between* MDMUL1 *and* $dN_{ch}/d\eta\ |_{max}$.

On the basis of the data listed in table 9.9 a plot of the charged particle pseudorapidity density at midrapidity as a function of MDMUL1 can be built. As it can be seen in fig. 9.9, a linear fit reproduces quite well the correlation between $dN_{ch}/d\eta\ |_{max}$ and MDMUL1:

$$dN_{ch}/d\eta\ |_{max} = (52.2 \pm 0.8) \cdot \text{MDMUL1} \ - \ (20 \pm 4) \qquad (9.12)$$

The non-zero value of MDMUL1 at $dN_{ch}/d\eta\ |_{max} = 0$ is probably due to residual beam pile–up [7] which might be recovered by means of some refinements in MDMUL1 calculation.

[6] The E_T values reported in table 9.9 are based on the E_T scale of the 1998 microDST and are not corrected with the 1.085 factor (see appendix B). In this case the rescaling is not important because we are interested in the correlation between MDMUL1 and $dN/d\eta\ |_{max}$ and E_T is used only to define the centrality classes.

[7] To minimize pile–up contamination, $dN_{ch}/d\eta\ |_{max}$ has been evaluated in special low-intensity runs. In these runs < MDMUL1 > results slightly lower (by ~ 0.3 units) with respect to the values quoted in table 9.9 which are extracted from standard intensity runs.

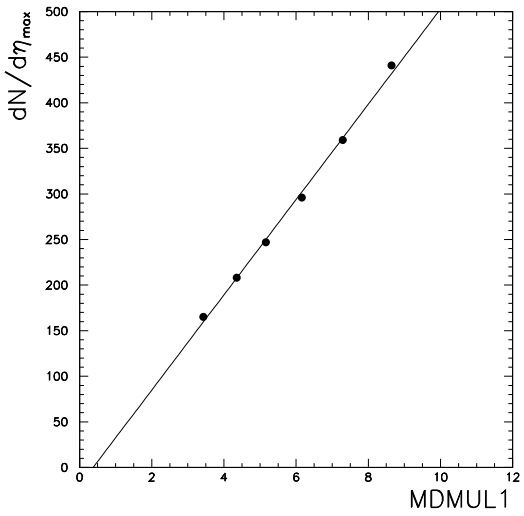

Figure 9.9: $dN_{ch}/d\eta\ |_{max}$ *as a function of* MDMUL1. *The result of the linear fit is superimposed.*

Equation 9.12 allows to simply transform the measured MDMUL1 variable into the $dN_{ch}/d\eta\ |_{max}$, providing an absolute scale for the horizontal axis of the J/ψ suppression plot as a function of charged multiplicity.

The J/ψ/DY ratio as a function of $dN_{ch}/d\eta\ |_{max}$ is shown in fig. 9.10 where it can be seen that the onset of the "anomalous" suppression occurs at $dN_{ch}/d\eta\ |_{max} \sim 100 - 160$.

It is important to recall that the particle rapidity density at midrapidity is strictly related with the energy density attained in the collision. As it has been discussed in chapter 1, in the case of transparency regime and purely longitudinal expansion of the system, the energy density can be calculated by means of the Bjorken formula [14]:

$$\varepsilon_{BJ} = \frac{< m_T >}{\mathcal{A} c \tau_o} \left(\frac{dN}{dy} \right)_{y=y_{cm}} \approx \frac{< m_T >}{\mathcal{A} c \tau_o} \frac{3}{2} \left(\frac{dN_{ch}}{dy} \right)_{y=y_{cm}}$$

where $\mathcal{A}$ is the transverse overlapping area in the collision of the two nuclei, τ_o is the formation time and m_T is the transverse mass. Hence, in fig. 9.10, the J/ψ suppression pattern is plotted as a function of a variable directly connected with the energy density reached in the Pb-Pb collision.

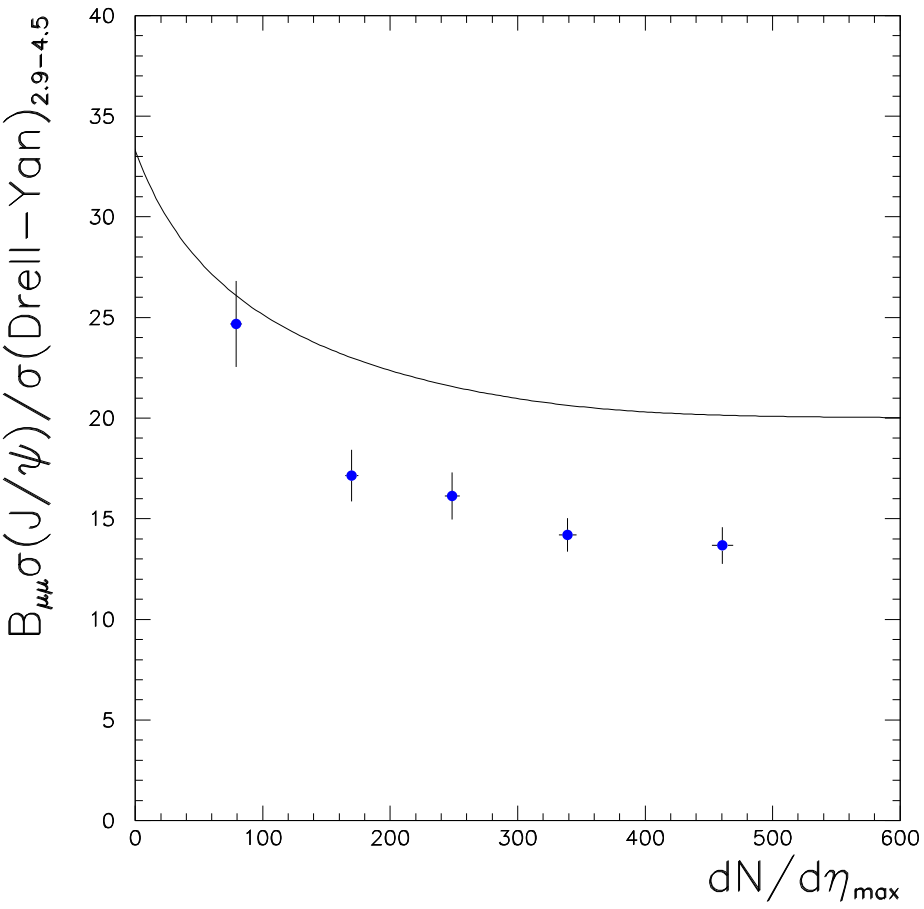

Figure 9.10: *$J/\psi/DY$ ratio as a function of $dN_{ch}/d\eta\ |_{max}$.*

Bibliography

[1] C. Soave, Ph.D. thesis, Università di Torino, 1998.

[2] M.C. Abreu et al., (NA50 coll.) Eur. Phys. J. C14 (2000) 443.

[3] DIMUJET USER GUIDE 2.00/02 (1997).

[4] DIMUREC USER GUIDE 2.00/02 (1997).

[5] PDFLIB 7.09, User's manual, CERN/PPE (1997).

[6] R. Arnaldi, Ph.D. thesis, Dec. 2000, Universitè Blaise Pascal, Clermont-Ferrand.

[7] T. Sjostrand, Pythia 5.7 and Jetset 74 (1993).

[8] Review of particle physics, The Eur. Phys. Journal C15 (2000).

[9] M.C. Abreu et al., (NA38 coll.) Phys. Lett. B466 (1999) 408.

[10] Bialas, Bleszynski and Czyz, Nucl. Phys. B111 (1976), 461.

[11] M.C. Abreu et al., (NA50 coll.) Phys. Lett. B410 (1997) 337.

[12] M.C. Abreu et al., (NA50 coll.) CERN-EP/2001-069, to appear in Phys. Lett.

[13] M.C. Abreu et al., (NA50 coll.) Phys. Lett. B450 (1999) 456.

[14] J.D. Bjorken, Phys. Rev. D 27 (1983) 140.

Appendix A

Glauber model of nucleus-nucleus collisions

The Glauber model [1] provides a quantitative geometrical description of nucleus-nucleus collisions, treated as a superposition of nucleon-nucleon collisions. The projectile nucleons traverse the target nucleus following straight line trajectories and undergoing several collisions with the nucleons of the target. The only physical inputs are the elementary nucleon-nucleon inelastic cross-section and the density distribution inside the nuclei.

The Glauber model assumes that the basic nucleon-nucleon cross-section is the same throughout the passage of a nucleon through the other nucleus. This is clearly an approximation because a nucleon, after a collision, may become excited and subsequently interact with other nucleons with a different cross-section. The total nucleon-nucleon cross-section in the range 3 GeV$< \sqrt{s} <$ 100 GeV (including the SPS energies) is approximately 40 mb, and the inelastic part is about 30 mb [2]. A small fraction of the inelastic cross-section ($\simeq 6\%$) is due to diffractive dissociation processes. Since elastic or diffractive dissociation collisions lead to a small loss of energy, a nucleon suffering elastic or diffractive collisions can be treated as undergoing no collision at all. Therefore only non-diffractive inelastic collisions are considered and it is assumed $\sigma = \sigma_{in} = 30$ mb.

The density distribution ρ inside the nuclei is assumed to follow a Woods-Saxon distribution:

$$\rho(r) = \frac{\rho_0}{1 + e^{(r-r_0)/C}}$$

where r is the distance from the center of the nucleus. For the Pb nucleus

(see fig. A.1), it is assumed $r_0 = 6.624$ fm, $C = 0.549$ fm and $\rho_0 = 0.16$ fm^{-3} as obtained from electron-nucleus scattering experiments [3].

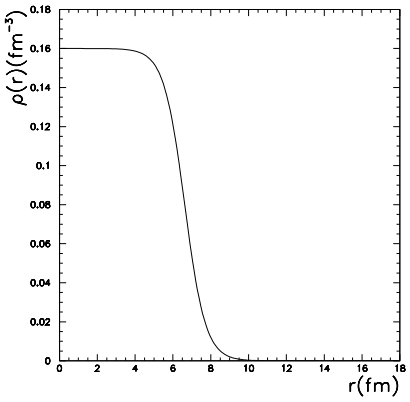

Figure A.1: *Nuclear density profile of a Pb nucleus as a function of the distance r from the nucleus center.*

A.1 Nucleus-Nucleus collisions: formalism

We consider the collision between two nuclei of mass numbers A (projectile) and B (target). A schematic view of the geometry of the collision and of the variables used in the following is shown in figure A.2 and A.3.

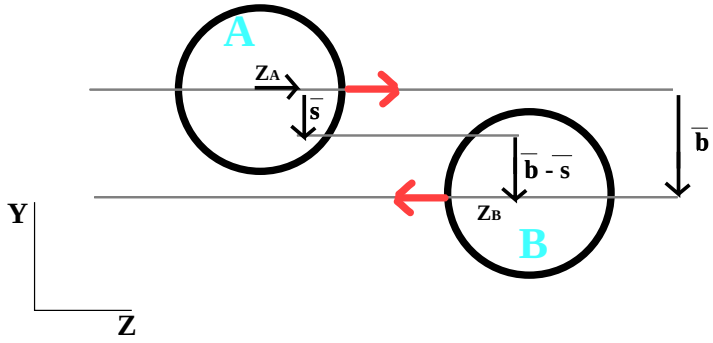

Figure A.2: *Longitudinal view of a collision between a projectile nucleus A and a target nucleus B.*

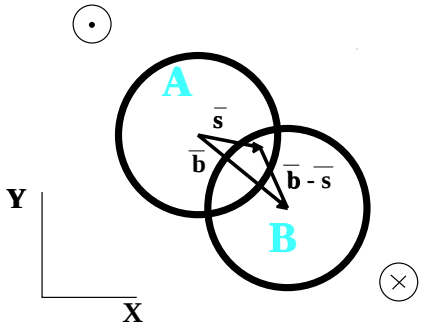

Figure A.3: *Transverse view of a nucleus-nucleus collision.*

The probability of finding a baryon in the volume element $d\vec{s}\,dz_A$ in nucleus A at the position $(\vec{s}, z_A)$ is given by $\rho_A(\vec{s}, z_A)\,d\vec{s}\,dz_A$, where $\rho_A(\vec{s}, z_A)$ is the nuclear density in the $(\vec{s}, z_A)$ position. Therefore the nucleon density per surface unit in the transverse plane perpendicular to the collision axis is:

$$T_A(\vec{s}) = \int_{-\infty}^{\infty} \rho_A(\vec{s}, z_A)\, dz_A \tag{A.1}$$

ρ_A is normalized to the total number of nucleons of the nucleus, so as to have:

$$\int T_A(\vec{s})\, d^2s = \int d^2s \int_{-\infty}^{\infty} \rho_A(\vec{s}, z_A)\, dz_A = 1$$

An analogous formula gives for the nucleus B:

$$T_B(\vec{b} - \vec{s}) = \int_{-\infty}^{\infty} \rho_B(\vec{b} - \vec{s}, z_B)\, dz_B \tag{A.2}$$

which is related to the probability of finding a target nucleon in the volume element $d(\vec{b} - \vec{s})dz_B$ at the position $(\vec{b} - \vec{s}, z_B)$, and is normalized according to:

$$\int T_B(\vec{b} - \vec{s})\, d^2(b - s) = \int d^2(b - s) \int_{-\infty}^{\infty} \rho_B(\vec{b} - \vec{s}, z_B)\, dz_B = 1$$

$T_A(\vec{s})$ and $T_B(\vec{b} - \vec{s})$ are called "nucleus thickness functions".

The probability element for the occurrence of a nucleon-nucleon collision when the nuclei A and B collide with an impact parameter $\vec{b}$ is the product of:

i) the probability element $\rho_A(\vec{s}, z_A)\, d\vec{s}_A\, dz_A$
ii) the probability element $\rho_B((\vec{b} - \vec{s}), z_B)\, d\vec{s}_B\, dz_B$
iii) the cross-section σ_{in} for a nucleon-nucleon inelastic collision
Hence:

$$dP = \rho_A(\vec{s}, z_A)\, d\vec{s}_A\, dz_A \;\cdot\; \rho_B((\vec{b} - \vec{s}), z_B)\, d\vec{s}_B\, dz_B \;\cdot\; \sigma_{in} \tag{A.3}$$

The total probability for the occurrence of one nucleon-nucleon collision when the nuclei A and B are located at an impact parameter $\vec{b}$ from each other, given by $P(1, \vec{b}) = \int dP$, is usually written as:

$$P(1, \vec{b}) = T_{AB}(\vec{b})\, \sigma_{in}$$

where T_{AB} is the nucleus-nucleus thickness function, i.e. the nucleon density per surface unit:

$$T_{AB}(\vec{b}) \;= \int d^2s\, T_A(\vec{s})\, T_B(\vec{b} - \vec{s}) \tag{A.4}$$

If nuclei are not deformed or oriented, $T_{AB}(\vec{b})$ depends only on the magnitude of $\vec{b}$ and hence $T_{AB}(\vec{b}) = T_{AB}(b)$ In fig. A.4 the Pb-Pb thickness function T_{AB} is plotted as a function of the impact parameter.

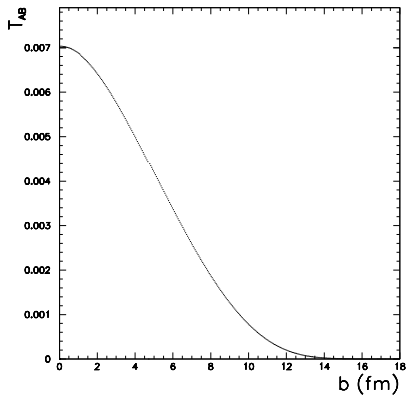

Figure A.4: *T_{AB} as a function of the impact parameter b for Pb-Pb collisions.*

A.2 Interesting physical quantities as a function of b

Having defined the thickness function, the probability for various events can be calculated, as well as other interesting physical quantities, such as the total number of nucleon-nucleon collisions and the number of nucleons which undergo a collision with another nucleon.

A.2.1 Interaction probability

The probability for the occurrence of n inelastic baryon-baryon collisions at an impact parameter $\vec{b}$ is given by the binomial law:

$$P(n,\vec{b}) = \left(\begin{array}{c} AB \\ n \end{array} \right) (T_{AB}(\vec{b})\,\sigma_{in})^n\,[1 - T_{AB}(\vec{b})\,\sigma_{in}]^{AB-n} \qquad \text{(A.5)}$$

where the first factor on the right hand side represents the number of combinations for finding n collisions out of AB possible nucleon-nucleon encounters, the second factor gives the probability of having exactly n collisions and the third factor gives the probability of having exactly AB-n misses.

The total probability for the occurrence of at least one inelastic event in the collision of the nuclei A and B, at an impact parameter $\vec{b}$, is given by the sum of eq. A.5 from n=1 to n=AB:

$$\frac{d\sigma_{in}^{AB}}{d\vec{b}} = \sum_{n=1}^{AB} P(n,\vec{b}) = 1 - P(0,\vec{b}) \qquad \text{(A.6)}$$

where:

$$P(0,\vec{b}) = [1 - T_{AB}(\vec{b})\,\sigma_{in}]^{AB}. \qquad \text{(A.7)}$$

is the probability of having no collisions between nucleons. In fig. A.5, σ_{in}^{AB} is plotted as a function of $\vec{b}$ in the case of Pb-Pb collisions. It can be seen that the probability of the occurrence of at least one nucleon-nucleon collision is =1 up to $b \approx 14$ fm and it decreases for larger values of impact parameter, where only the tails of the nuclear density distributions superimpose.

Finally, from eq. A.6, the total inelastic cross section σ_{in}^{AB} for an AB collision can be calculated:

$$\sigma_{in}^{AB} = \int d^2b\{1 - [1 - T_{AB}(\vec{b})\,\sigma_{in}]^{AB}\}$$

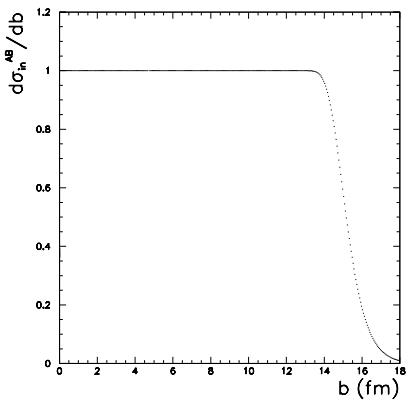

Figure A.5: *Probability of at least one inelastic nucleon-nucleon collision as a function of the impact parameter b for Pb-Pb collisions.*

A.2.2 Number of participant and spectator nucleons

The nucleons of the projectile and of the target which have undergone at least one inelastic collision with the surrounding nucleons are called "participant nucleons" ("wounded nucleons" [4]). In the framework of the Glauber model, the number of participant nucleons N_{part} as a function of the impact parameter b can be obtained from the following equation [5, 6]:

$$N_{part}(\vec{b}) = \int d^2s \left\{ AT_A(\vec{s})[1-(1-\sigma_{in}T_B(\vec{b}-\vec{s}))^B] + \right.$$
$$\left. + BT_B(\vec{b}-\vec{s})[1-(1-\sigma_{in}T_A(\vec{s}))^A] \right\} \qquad \text{(A.8)}$$

The impact parameter dependence of N_{part} in Pb-Pb collisions is shown in fig. A.6a: the higher the centrality, the larger the number of nucleons of the projectile and target nuclei involved in the interaction.

The number of projectile spectators is defined as the number of nucleons of the projectile nucleus which do not participate in the interaction. For symmetrical systems (A=B), it can be obtained, once the number of participants is known, from the relation:

$$N_{proj.spec.} = A - \frac{N_{part}}{2} \qquad \text{(A.9)}$$

where A is the projectile mass number. The centrality dependence of $N_{proj.spec.}$ for Pb-Pb collisions is shown in fig. A.6b.

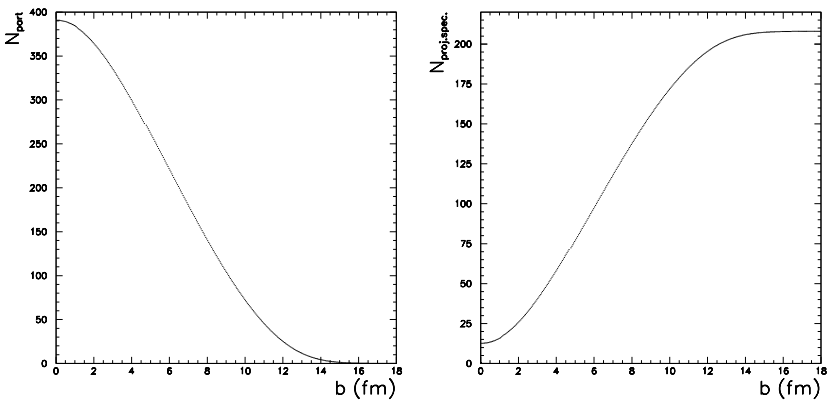

Figure A.6: *(a) Number of participant nucleons and (b) number of spectator nucleons versus the impact parameter b for Pb-Pb collisions.*

A.2.3 Number of elementary nucleon nucleon collisions

Given the probability of having n baryon-baryon collisions, as defined by eq. A.5, the mean number of elementary nucleon-nucleon collisions N_{coll} as a function of the impact parameter b is given by:

$$< N_{coll}^{AB}(b) >= \sum_{n=0}^{AB} n \cdot P(n,b) = AB\ T_{AB}(b)\sigma_{in} \tag{A.10}$$

The plot of N_{coll} as a function of b in the case of Pb-Pb collisions is shown in fig. A.7

A.2.4 Hard process cross-section

Once the total probability of occurrence of an inelastic event, as given by eq. A.6, is known, the production cross section for hard processes, such as Drell-Yan or charmonia production, can also be calculated in the framework of the Glauber model. This is done by simply replacing in eq. A.6 the inelastic nucleon-nucleon cross-section (σ_{in}) by the production cross-section for hard processes in nucleon-nucleon collisions (σ_{hard}^{NN}):

$$\frac{d\sigma_{hard}^{AB}}{d\vec{b}} = \sum_{n=1}^{AB} P(n,\vec{b}) = \sum_{n=1}^{AB} \left(\begin{array}{c} AB \\ n \end{array} \right) (T_{AB}(\vec{b})\ \sigma_{hard}^{NN})^n\ [1 - T_{AB}(\vec{b})\ \sigma_{hard}^{NN}]^{AB-n} \tag{A.11}$$

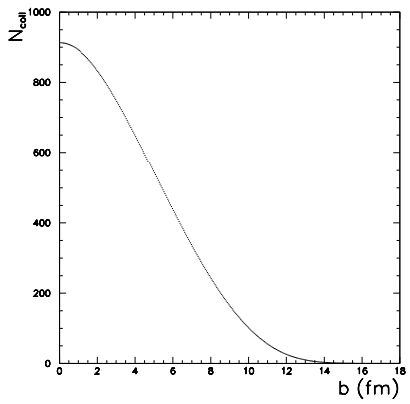

Figure A.7: *Number of elementary nucleon-nucleon collisions as a function of the impact parameter b in Pb-Pb collisions.*

Since σ_{hard}^{NN} is very small, it is $\sigma_{hard}^{NN} T_{AB}(\vec{b}) << 1$, which means that the probability of a hard process to occur in nucleus-nucleus collisions is very small. Therefore equation A.11 can be approximated by (see also eq. A.10):

$$\frac{d\sigma_{hard}^{AB}}{d\vec{b}} \approx AB\ T_{AB}(\vec{b})\ \sigma_{hard}^{NN} \propto N_{coll}\sigma_{hard}^{NN} \tag{A.12}$$

Hence, the differential cross-section for hard processes is approximately proportional to the number of elementary nucleon-nucleon collisions.

By integrating over the impact parameter, the total production cross-section for hard processes in A-B collisions can be obtained:

$$\sigma_{hard}^{AB} = \int d^2b\ AB\ T_{AB}(\vec{b})\sigma_{hard}^{NN} = AB\sigma_{hard}^{NN} \tag{A.13}$$

which is proportional to the product of the projectile and target mass numbers.

A.2.5 J/ψ production and nuclear absorption

Charmonium production occurs via hard processes and therefore the J/ψ production cross-section can be written as:

$$\sigma_{J/\psi}^{AB} = AB\ \sigma_{J/\psi}^{pp} = AB\ \sigma_{J/\psi}^{pp} \int d^2b\ d^2s\ T_A(\vec{s})\ T_B(\vec{b}-\vec{s}) \tag{A.14}$$

since $\int d^2b\, d^2s\, T_A(\vec{s})\, T_B(\vec{b}-\vec{s}) = \int d^2b\, T_{AB}(\vec{b}) = 1$.

Once the charmonium has been produced, it can be destroyed by strong interactions while moving through the nuclear environment, resulting in a suppression of the charmonium yield in proton-nucleus and nucleus-nucleus collisions. Consequently, on its way out, the J/ψ is attenuated by an exponential damping. The survival probability $S^{AB}_{J/\psi}$ can be expressed as:

$$\begin{aligned} S^{AB}_{J/\psi} &= e^{-(\text{number of nucleons per unit of surface along the trajectory})\cdot\sigma_{abs}} = \\ &= e^{-(A-1)\int_{-\infty}^{z_A} dz \rho_A(\vec{s},z_A)\sigma_{abs}} \times e^{-(B-1)\int_{-\infty}^{z_B} dz' \rho_B(\vec{b}-\vec{s},z_B)\sigma_{abs}} \end{aligned} \quad \text{(A.15)}$$

where σ_{abs} is the cross-section for J/ψ break-up by nuclear absorption and $(\vec{s}, z_A)$ and $(\vec{b}-\vec{s}, z_B)$ give the position of the charmonium production point within nucleus A and within nucleus B respectively. Therefore, in presence of interactions with nuclear matter, the J/ψ production cross-section becomes:

$$\begin{aligned} S^{AB}_{J/\psi} &= \frac{\sigma^{AB}_{J/\psi}}{AB\,\sigma^{pp}_{J/\psi}} = \int d^2b d^2s \int_{-\infty}^{\infty} dz_A \rho_A(\vec{s},z_A) e^{-(A-1)\int_{-\infty}^{z_A} dz \rho_A(\vec{s},z_A)\sigma_{abs}} \cdot \\ &\cdot \int_{-\infty}^{\infty} dz_B \rho_B(\vec{b}-\vec{s},z_B) e^{-(B-1)\int_{-\infty}^{z_B} dz' \rho_B(\vec{b}-\vec{s},z_B)\sigma_{abs}} \end{aligned} \quad \text{(A.16)}$$

Integrating on z, it results [7, 8]:

$$\begin{aligned} \frac{\sigma^{AB}_{J/\psi}}{AB\,\sigma^{pp}_{J/\psi}} &= \frac{1}{(A-1)(B-1)\sigma^2_{abs}} \cdot \\ &\cdot \int d^2b d^2s \left(1 - e^{-(A-1)T_A(\vec{s})\sigma_{abs}}\right)\left(1 - e^{-(B-1)T_B(\vec{b}-\vec{s})\sigma_{abs}}\right) \end{aligned} \quad \text{(A.17)}$$

Using this formula, the J/ψ nuclear absorption effect as a function of the impact parameter b can be calculated, using the value of charmonium nuclear absorption cross-section (σ_{abs}) extracted from the fit to NA38 and NA51 pp, p-A and S-U data [9], which is:

$$\sigma_{abs} = 6.4 \pm 0.8 \text{ mb}$$

The result obtained is displayed in fig. A.8.

As long as σ_{abs} is sufficiently small, equation A.18 can be developed as:

$$\begin{aligned} \frac{\sigma^{AB}_{J/\psi}}{\sigma^{pp}_{J/\psi}} &= AB\left[1 - \sigma_{abs}\int d^2b d^2s T_A(\vec{s}) T_B(\vec{b}-\vec{s}) \frac{(A-1)T_A(\vec{s}) + (B-1)T_B(\vec{b}-\vec{s})}{2} + \ldots\right] = \\ &= (AB)^{\alpha} \end{aligned} \quad \text{(A.18)}$$

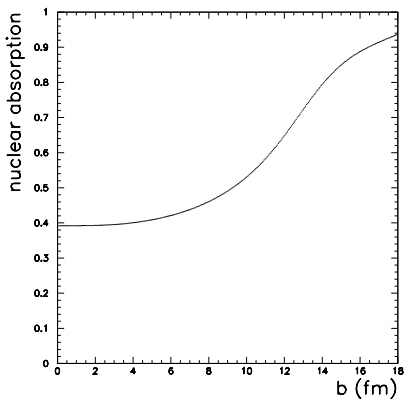

Figure A.8: *J/ψ nuclear absorption (eq. A.18) as a function of the impact parameter b.*

where the exponent α is < 1, and therefore it is:

$$\frac{\sigma^{AB}_{J/\psi}}{\sigma^{pp}_{J/\psi}} = (AB)^{\alpha} < AB \tag{A.19}$$

as a consequence of J/ψ nuclear absorption.

An appropriate variable to parametrize the measured J/ψ absorption cross-section is the number of nucleons that the created charmonium state can potentially interact with. This number is equivalent to the product $< \rho L >$, where ρ is the nuclear density distribution and L is the length of nuclear matter traversed by the $c\bar{c}$ state. If we define:

$$< \rho L >= \frac{\int d^2b d^2s T_A(\vec{s}) T_B(\vec{b}-\vec{s}) \frac{(A-1)T_A(\vec{s})+(B-1)T_B(\vec{b}-\vec{s})}{2}}{\int d^2b d^2s T_A(\vec{s}) T_B(\vec{b}-\vec{s})} \tag{A.20}$$

equation A.18 can be written as:

$$\sigma^{AB}_{J/\psi} \approx AB \cdot \sigma^{pp}_{J/\psi}\, e^{-\sigma'_{abs}<\rho L>} \tag{A.21}$$

where the term $AB \cdot \sigma^{pp}_{J/\psi}$ accounts for charmonium production cross-section and $e^{-\sigma'_{abs}<\rho L>}$ for the nuclear absorption effect. In this case, the value $\sigma'_{abs} = 5.9 \pm 0.6$ mb, extracted from the simple exponential fit to NA38 data [9] and different from σ_{abs}, should be used.

A.2.6 Minimum Bias cross-section

Events in which the projectile nucleus interacts in the target, without any further requirement, are called Minimum Bias (MB) events.

Since the projectile interacts in the target if at least one inelastic nucleon-nucleon collision occurs, the probability of a MB event is given by $[1 - P(0, b)]$, where $P(0, b)$ is the probability that no nucleon-nucleon interaction occurs at a given impact parameter b, as defined in eq. A.7.

In fact, the impact parameter distribution in MB events is not uniform, but it is distributed according to:

$$dN = 2\pi b[1 - P(0, b)]db \tag{A.22}$$

where the term $2\pi bdb$ comes from the collision geometry (there are $2\pi b$ possibilities of having the center of the nucleus A at a distance b from the center of the nucleus B). This implies that up to $b \approx 13 - 14$ fm the higher impact parameters are favored respect to the lower ones, as shown in Fig. A.9. For higher values of b, the term $[1 - P(0, b)]$ cuts off the integral as a consequence of the decreasing of the probability of having a nucleon-nucleon collision at large b.

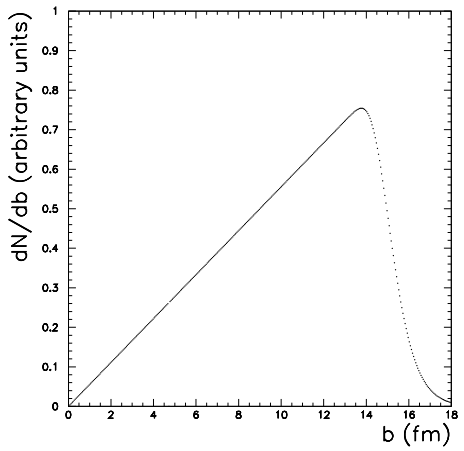

Figure A.9: *Minimum bias impact parameter distribution.*

A.3 Centrality-related experimental variables

In order to find the link between the centrality of the collision (defined by the impact parameter b) and the experimentally measured variables (namely the neutral transverse energy E_T, the charged multiplicity N_{ch} and the forward energy E_{ZDC}) the detector features must be taken into account.

Neutral transverse energy
The estimation of the E_T spectrum in the framework of the Glauber model goes through the calculation of the probability $P(E_T, b)$ of measuring a given E_T in a collision with an impact parameter b. Such a probability should follow a gaussian distribution around the mean value $< E_T(b) >$.

$$P(E_T, b) = \frac{1}{\sqrt{2\pi} \cdot \sigma_{E_T}(b)} \; e^{-\frac{1}{2}\frac{(E_T - < E_T(b) >)^2}{2\sigma^2_{E_T}(b)}}$$

It is assumed that E_T is proportional to the number of participant nucleons and that the width of the gaussian reflects the detector experimental resolution (sampling fluctuations and other instrumental effects):

$$< E_T(b) >= q \cdot N_{part}(b) \tag{A.23}$$

$$\sigma_{E_T}(b) = w \cdot q < E_T(b) >= w \cdot q^2 N_{part}(b) \tag{A.24}$$

where q represents the average neutral transverse energy released by each participant nucleon and w the detector resolution. The q and w parameters should be adjusted to reproduce the experimental E_T distributions, while $N_{part}(b)$ is calculated in the framework of the Glauber model, according to eq. A.8.

Charged multiplicity
As E_T, also the charged multiplicity is expected to be proportional to the number participant nucleons. Consequently, formulae analogous to the ones used for the E_T parametrization are used:

$$< N_{ch}(b) >= q_N \cdot N_{part}(b) \tag{A.25}$$

$$\sigma_{N_{ch}}(b) = w_N \cdot q_N < N_{ch}(b) >= w_N \cdot q_N^2 N_{part}(b) \tag{A.26}$$

Forward energy
The mean energy detected by the Zero-Degree Calorimeter (ZDC) in Pb-Pb

collisions at 158 GeV incident energy is expressed as a function of the impact parameter b by:

$$\begin{aligned} < E_{ZDC}(b) > &= 158 \cdot N_{proj.spec.}(b) + \alpha \cdot N_{part}(b) = \\ &= 158 \cdot \left(208 - \frac{N_{part}(b)}{2} \right) + \alpha \cdot N_{part}(b) \end{aligned} \quad \text{(A.27)}$$

where $N_{proj.spec.}$ is the number of projectile spectator nucleons, and N_{part} is the number of participant nucleons, as given by equations A.8 and A.9. The α factor accounts for the fraction of secondary particles (mostly pions) entering the ZDC and it depends on the characteristics of the detector, playing an important role only for very central collisions [10].

The calorimeter resolution is described by:

$$\sigma_{E_{ZDC}}(b) = \sqrt{(\beta \cdot \sqrt{E_{ZDC}(b)} + \gamma \cdot E_{ZDC}(b))^2 + \delta^2} \quad \text{(A.28)}$$

where $\beta = 3.39$ GeV$^{1/2}$, $\gamma = 0.062$ [10] have been extracted from special data taking periods with low intensity beam, while the δ term accounts for the smearing of the signal due to pedestal width and calibration uncertainties. The α and δ parameters are adjusted to fit the experimental spectra.

The probability of measuring a given E_{ZDC} in a collision at an impact parameter b can thus be expressed as:

$$P_{AB}(E_{ZDC}, b) = \frac{1}{\sqrt{2\pi}\sigma_{E_{ZDC}}(b)} \, exp\left(-\frac{(E_{ZDC} - < E_{ZDC}(b) >)^2}{2\sigma^2_{E_{ZDC}}(b)} \right) \quad \text{(A.29)}$$

Bibliography

[1] R. J. Glauber in Lectures in Theoretical Physics, NY, 1959, Vol. 1, 315.

[2] D.E. Groom et al., Review of Particle Physics, Eur. Phys. Journ. C15 (2000), 1.

[3] C.W. de Jager et al., Atomic Data and Nuclear Data Tables 14 (1974) 485.

[4] A. Bialas et al. Nucl. Phys. B 111 (1976) 461.

[5] D. Kharzeev, Nucl. Phys. A610 (1996) 418c.

[6] M. Nardi, Proceedings of CERN Heavy Ions Physics School CERN, Geneva, Switzerland; 21 - 25 Jun 1999

[7] J.P. Blaizot and J.Y. Ollitrault, Phys. Rev. Lett. 77 (1996) 1703.

[8] C. Gerschel and J. Hufner, Phys. Lett. B207 (1988) 253.

[9] M.C. Abreu et al., (NA38 coll.) Phys. Lett. B466 (1999) 408.

[10] R. Arnaldi, Ph.D. thesis, Dec. 2000, Universitè Blaise Pascal, Clermont-Ferrand.

Appendix B

E_T scales in 1996 and 1998

The scale of the measured E_T varies for the different data taking periods, and for different triggers, dimuon (2μ) and Minimum (MB).

Due to the ageing of the detector, to the different calibration of the calorimeter response and to different experimental setup (target configuration) the E_T value measured in 1998 differs from the 1996 one.

Moreover, both in 1996 and 1998 data taking periods, the triggers delivered by the Zero Degree Calorimeter (ZDC) were affected by a timing problem, the so called Trigger Timing Bug (TTB). As a consequence, the transverse energy (E_T) obtained with dimuon triggers differs systematically from the E_T measured with ZDC (or MB — minimum bias) triggers. This problem has been solved starting from 1999 replacing the old ZDC discriminator with a constant fraction discriminator.

Summarizing, there exist four different scales of measured E_T:

1. $(E_T)^{\mu\mu}_{96}$: 1996 data, dimuon trigger

2. $(E_T)^{MB}_{96}$: 1996 data, minimum bias trigger

3. $(E_T)^{\mu\mu}_{98}$: 1998 data, dimuon trigger

4. $(E_T)^{MB}_{98}$: 1998 data, minimum bias trigger

As a first approximation, it can be assumed that these different scales can be compared with the aid of simple multiplicative factors, neglecting in this

way the non-linear higher-order effects that can induce a distortion of the E_T spectra. [1] The four scales are thus connected via 4 constants, as follows:

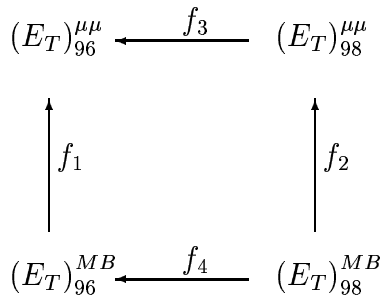

$$
\begin{aligned}
(E_T)^{\mu\mu}_{96} &= f_1\ (E_T)^{MB}_{96} \\
(E_T)^{\mu\mu}_{98} &= f_2\ (E_T)^{MB}_{98} \\
(E_T)^{\mu\mu}_{96} &= f_3\ (E_T)^{\mu\mu}_{98} \\
(E_T)^{MB}_{96} &= f_4\ (E_T)^{MB}_{98}
\end{aligned}
$$

Let us stress that f_3 and f_4 should be different due to the TTB. It should be:

$$f_4 \cdot f_1 = f_2 \cdot f_3$$

Since the Psi/DY standard analysis of is performed with 2μ triggers only, the E_T scale used in the plot of 1996 Psi/DY ratio (figure 5 in ref. [1]) is the one of 1996 2μ triggers $[(E_T)^{\mu\mu}_{96}]$.

To perform a MB analysis, it is mandatory to rescale the 1996 MB E_T scale $[(E_T)^{MB}_{96}]$ to $(E_T)^{\mu\mu}_{96}$ using the formula:

$$(E_T)^{\mu\mu}_{96} = f_1\ (E_T)^{MB}_{96}$$

this means that, for MB triggers only, the E_T extracted from the 1996 microDST must be multiplied by f_1 in order to express it in the 2μ E_T scale.

[1] Such a distortion is present in 1998 MB data sample. Therefore higher order terms have to be added to the simple relation $E_T = q \cdot N_{part}$ to fit the distorted MB E_T spectrum.

The factor f_1 in the 1996 published data (fig. 8 of [1]) has been chosen to be 1.020 as explained in detail in [3]. In this way, for central events, the Psi/DY ratio evaluated from MB sample is in agreement with the values obtained from the standard analysis. It has to be stressed that a slight modification on this factor f_1 has a dramatic influence on the final results: if for example f_1 is fixed to 1.000 (no rescaling between $(E_T)^{\mu\mu}_{96}$ and $(E_T)^{MB}_{96}$) the Psi/DY ratio increases for central events, while if $f_1 = 1.029$ is used, the Psi/DY ratio decreases.

If then one wants to compare data from different years (1996 and 1998), since there are differences in the measured E_T from year to year, the 1998 E_T scale must be fixed on the 1996 one. This has been done via a "calibration" factor that was applied to the measured 1998 E_T in order to have the knee of the 1998 MB spectrum coincident with the knee of the 1996 MB distribution [4, 5]. So the value of 1998 E_T (for any trigger) existing in the standard microDST available at CERN and Lyon is the one obtained applying this "calibration" factor to the measured E_T both for MB events and for 2μ events. In this way the 1996 MB spectrum and the 1998 MB spectrum are put on the same E_T scale, as it can be seen in figure B.1, which is also figure 1 of [2] and this implies that $(E_T)^{MB}_{96} = (E_T)^{MB}_{98}$, which means $f_4 = 1$. The ratio MB1996/MB1998 is flat for $E_T < 110$ GeV, as it can be seen in figure B.2.

Since the scale of the Psi/DY plots (like the one in figure 7.6, which corresponds to fig. 4 of [2]) is fixed by $(E_T)^{\mu\mu}_{96}$, the dimuon spectra of 1998 and 1996 must have the same E_T scale when comparing 1998 and 1996 Psi/DY results.

In figure B.3 the 1996 and 1998 Like-Sign spectra (collected with the dimuon trigger) are compared, [2] and it can be clearly seen that there is not a good agreement between the two years for the 2μ trigger events.

There are two main possibilities that can explain why these two spectra are so different: this effect may be due to physics or to a hardware problem. If the difference is mostly due to physics (i.e. it is an effect of the 1996 thick target which causes much more re-interactions than in 1998 and therefore can lead to higher values of measured E_T), a rescaling of E_T does not make sense. On the contrary, if the difference in the LS spectra is mostly due to hardware, as a first approximation it should be recovered by applying

[2] These are LS events with $M_{\mu\mu} > 1.5$ GeV/c^2

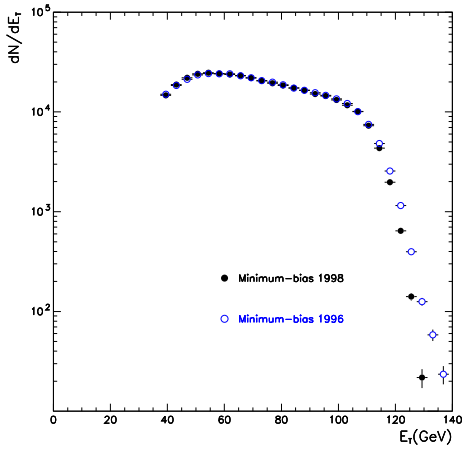

Figure B.1: *MB 1996 and 1998*

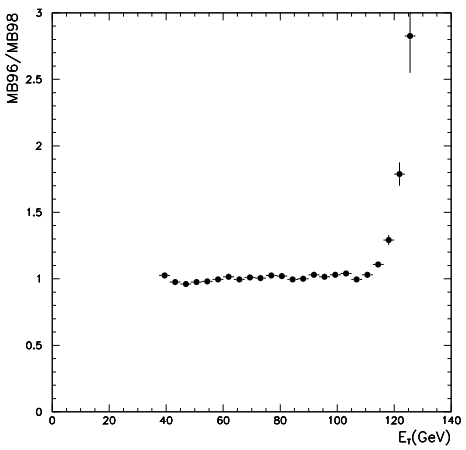

Figure B.2: *ratio between 1996 and spectra comparison (fig. 1 of [2]) 1998 MB spectra*

a rescaling factor. It can be told if it is mainly physics or hardware by looking at the ratio LS1996/LS1998 after the rescaling: if this ratio is flat, the rescaling factor accounts for the difference between the spectra. If not, it means that the LS can not be used as a reference to fix the E_T scales.

At this point, it should be evaluated a rescaling factor that accounts for the observed difference in the 1996 and 1998 LS E_T spectra. This factor allows a rescaling from $(E_T)^{\mu\mu}_{98}$ to $(E_T)^{\mu\mu}_{96}$ (which is the scale of the published plots).

$$(E_T)^{\mu\mu}_{96} = f_3 \cdot (E_T)^{\mu\mu}_{98}$$

Comparing the knee of the histograms it results:

$$(E_T)^{\mu\mu}_{96} = 1.086\,(E_T)^{\mu\mu}_{98}$$

while, if the maxima of the fitting functions are compared, it is:

$$(E_T)^{\mu\mu}_{96} = 1.085\,(E_T)^{\mu\mu}_{98}$$

These two values are compatible with the one found by B. Chaurand [6]:

$$(E_T)^{\mu\mu}_{98} = 0.922\,(E_T)^{\mu\mu}_{96}$$

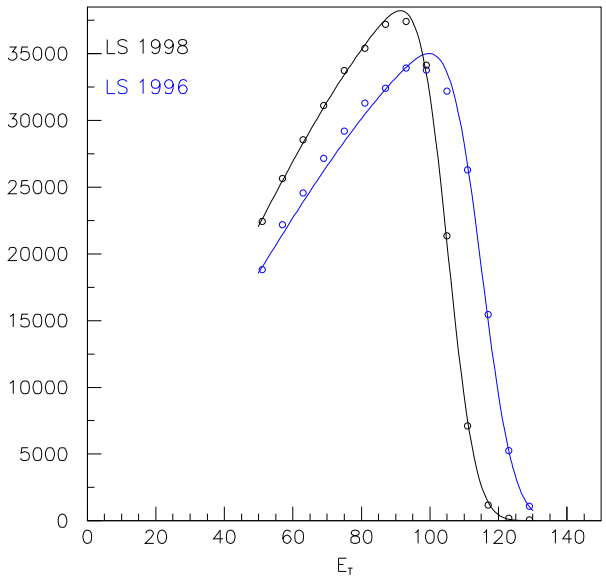

Figure B.3: *Comparison of 1996 and 1998 LS spectra and fitting functions (1996: runs 1800-2042, 1998: all runs); E_T taken from respective microDSTs.*

which means:

$$(E_T)^{\mu\mu}_{96} \quad = \quad 1.084\,(E_T)^{\mu\mu}_{98}$$

It is important to stress that these rescaling factors have been evaluated on runs 1800-2042 of 1996 data sample, and so they are correct only for runs 1801-3386, while they might be slightly different for the other runs.

In figures B.4 and B.5 the comparison between the 1996 and 1998 LS spectra and their ratio after rescaling the 1998 E_T by 1.085 are shown. It can be seen that the ratio LS1996/LS1998 is flat in the region 60< E_T <110, while the 1996 spectrum is a little bit higher for more central events, and this may be due to the different resolution (a similar effect is visible also for the MB distributions in figure B.2). This result supports the hypothesis that the disagreement between the 1996 and 1998 LS spectra is mostly due to a difference in the E_T scales that can be corrected with the help of a rescaling factor.

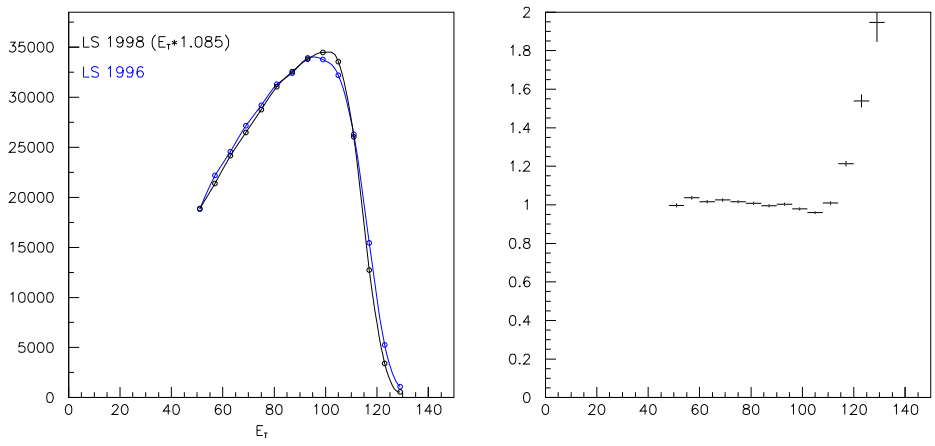

Figure B.4: *comparison between 1996 and 1998 LS spectra after 1.085 rescaling of 1998 E_T*

Figure B.5: *ratio between 1996 and 1998 LS spectra after 1.085 rescaling of 1998 E_T*

These results point out that in the plot in figure 7.6 (fig. 4 of [2]) two different E_T scales are used, namely $(E_T)^{\mu\mu}_{96}$ (for 1996 standard and minimum bias analysis) and $(E_T)^{\mu\mu}_{98}$ (for 1998 points). In order to have a correct comparison between 1996 and 1998 data, the new rescaling factor $f_3 = 1.085$ must be included. This affects the Psi/DY results as shown in figures B.6 and B.7 in which respectively published data and rescaled 1998 E_T points are presented. It is important to recall that:

- In figures B.6 and B.7, the normal absorption curve has been calculated using a $\sigma_{abs}(J/\psi) = 6.4$ mb and normalized to the asymptotic value of 20.0 at high E_T and therefore it is different from the one published in [1] [2] which is normalized to the asymptotic value of 21.0.

- The Psi/DY values (y coordinates of the points in the plots) are normalized to the 1996 standard analysis in a fixed E_T range (chosen in the flat region of middle E_T, i.e. 60-100). The normalization factor might be slightly different after the rescaling of E_T according to $(E_T)^{\mu\mu}_{96} = 1.085\,(E_T)^{\mu\mu}_{98}$. This re-normalization is NOT included in the plot in fig. B.7. This re-normalization factor has been evaluated in the 60-100 GeV $(E_T)^{\mu\mu}_{96}$ range and it turned out to be 0.992. The Psi/DY ratio after re-normalization is plotted in fig. B.8.

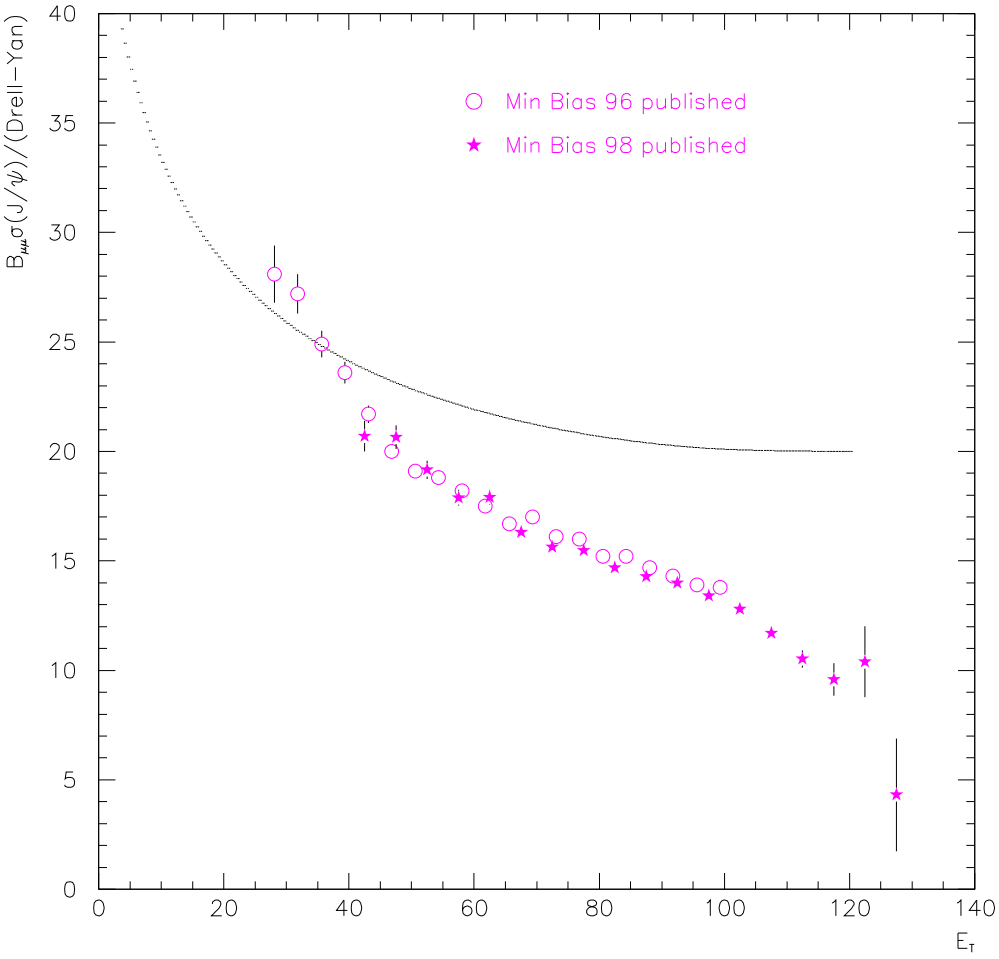

Figure B.6: *Published data*

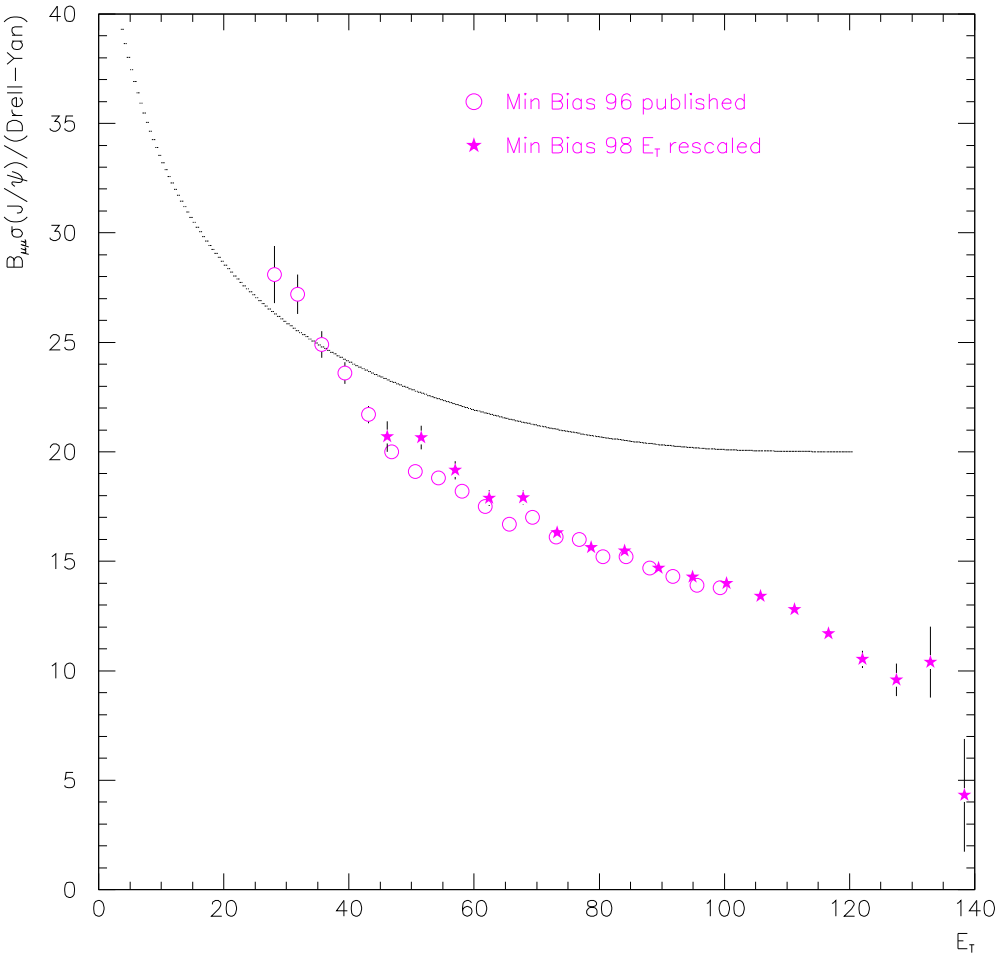

Figure B.7: *Data with new rescaling factor* $(E_T)^{\mu\mu}_{96} = 1.085\,(E_T)^{\mu\mu}_{98}$

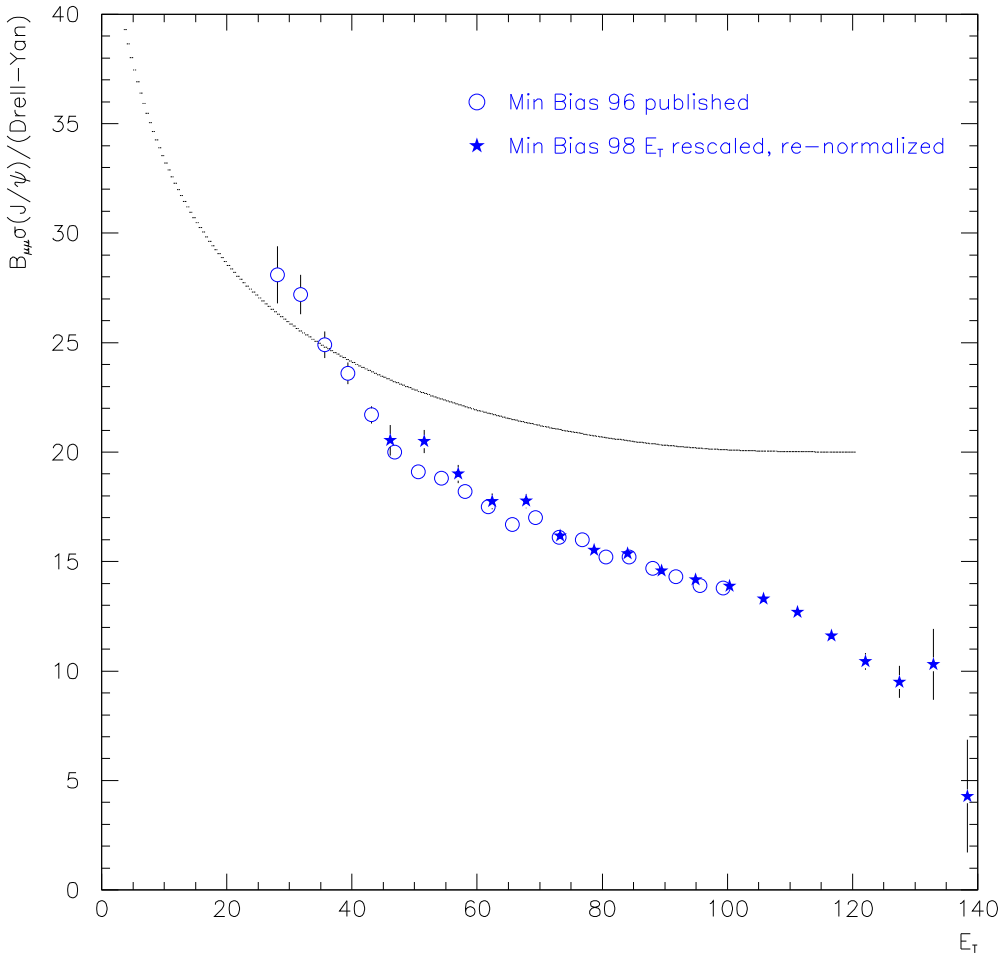

Figure B.8: *Data with new rescaling factor* $(E_T)^{\mu\mu}_{96} = 1.085\,(E_T)^{\mu\mu}_{98}$ *and re-normalization*

Bibliography

[1] M.C. Abreu et al. (NA50 coll.), Phys. Lett. B450 (1999) 456.

[2] M.C. Abreu et al. (NA50 coll.), Phys. Lett. B477 (2000) 28.

[3] B. Chaurand, NA50 meeting 98/04, Jul 1998 (paper 3).

[4] M. Gonin, NA50 meeting 99/01, Mar 1999 (paper 9).

[5] B. Chaurand, M. Gonin, NA50 meeting 99/02, Apr 1999 (paper 13).

[6] B. Chaurand, private communication

Acknowledgments

It is now time to thank all the people who helped me during these PhD years and in the preparation of this thesis.

I would start by thanking my advisors Alberta Marzari Chiesa and Luciano Ramello who offered me the opportunity to work in their group and guided and directed my efforts.

I'm especially grateful also to Bernard Chaurand who gave me many precious suggestions for the data analysis and accepted to report on my thesis in the final examination.

Thanks also to all the members of the NA50 collaboration, in particular L. Kluberg for his valuable advice and constant encouragement, R. Arnaldi and E. Scomparin for many important discussions and contributions.

The work presented here has been carried on in strict and continuous collaboration with the people of the Torino MD group, among them let me mention (in alphabetical order) S. Beolè, M. Idzik, M. Masera, M. Monteno and L. Ramello. Without their practical help and support I couldn't have made it.